



Provided by the author(s) and University of Galway in accordance with publisher policies. Please cite the published version when available.

Title	Seismic Design of Concentrically Braced Steel Frames
Author(s)	Salawdeh, Suhaib
Publication Date	2012-03-01
Item record	http://hdl.handle.net/10379/3045

Downloaded 2024-04-18T10:49:58Z

Some rights reserved. For more information, please see the item record link above.



Seismic Design of Concentrically Braced Steel Frames

by Suhaib Salawdeh

Supervisor: Dr. Jamie Goggins



A thesis submitted in partial fulfilment of the requirements for the degree of
Doctor of Philosophy
in the College of Engineering and Informatics

31/01/2012

Abstract

Concentrically braced frames (CBFs) are widely employed as structural systems in many seismic regions around the world, including Europe. They are frequently relied upon to provide adequate earthquake resistance for buildings and other structures. This implies that their design, construction and seismic performance play an important role in ensuring public safety during seismic events. However, recent research has shown that current design practice for these structures may lead to unsatisfactory seismic performance. This has implications for new construction and for the assessment of existing buildings.

The aim of this project is to develop a robust numerical model that accurately replicates the behaviour of CBFs during earthquakes. This numerical model is then used to validate a codified performance based design approach for CBFs, known as the direct displacement based design (DDBD) procedure. Numerical models and design guidelines have not always been validated using data and findings from real-time physical tests. This research addresses this need.

When analysing the performance of whole building systems during earthquakes, macro-numerical models, such as physical theory models, are often used in both research and design practice. This is due to their ability to represent the salient features of the system, while being computationally efficient and simple to construct. However, there are a limited number of physical theory models that reliably predict the behaviour of CBFs when subjected to strong earthquakes. Specifically, very few of these models take into account low cyclic fatigue. Furthermore, to the author's knowledge, none have been calibrated using real-time full scale shake table tests. One of the main objectives of this work is to fulfil this requirement. This is carried out in several stages. Firstly, a study of the behaviour of cold-formed square and rectangular structural hollow section brace elements is carried out. These are the main elements in CBF system that dissipates energy during seismic actions. Then, a robust numerical model incorporating a fatigue model for braces is developed with adequate fatigue parameters. A set of pseudo-static cyclic tests is used to calibrate the numerical model for braces, after which another independent set

of pseudo-static cyclic tests is used to validate the model for both hot-rolled and cold-formed square and rectangular hollow sections. This numerical model is extended and used to develop a single storey CBF numerical model, which is validated by shake table tests and a large range of nonlinear time history analysis (NLTHA). The comparative assessments presented in this work indicate that these developed numerical models can accurately capture the salient features related to the seismic behaviour of CBFs.

The DDBD methodology is well-developed for reinforced concrete structures. However, further research and development is required for steel structures and in particular for CBFs with diagonal bracing. Thus, there is a pressing need to validate a DDBD methodology for these systems using full scale real-time shake table tests and NLTHA. In this work, a DDBD procedure for single storey CBFs is developed. The performance of the DDBD methodology is verified by comparing its design values with experimental results obtained from the shake table tests and a large range of NLTHA. The DDBD procedure is then applied to multi-storey CBFs and its design values are compared to predictions obtained from the NLTHA of both 4-storey and 12-storey CBF buildings. It is shown that the DDBD gives on average slightly conservative storey drifts. On the other hand, the total shear resisted by the system was higher than the design value due to both compression and tension brace members resisting the lateral forces in NLTHA. The main reason for the difference in design values and those obtained from NLTHA is that only the tension member was assumed to contribute to the lateral resistance in the DDBD as recommended by Eurocode 8.

The numerical model presented in this thesis gave accurate simulations of the response of CBFs to strong earthquake loading. It can be used by researchers and designers to predict the real behaviour of CBF systems. Furthermore, this model can be used to represent different configurations of CBFs. The DDBD procedure validated in this work can be used by engineers to design CBFs in seismic regions. This design methodology is simple to apply and provides reliable displacement solutions to seismic design problems.

Table of contents

Table of contents.....	i
List of tables.....	viii
List of figures.....	xi
Declarations.....	xxix
Acknowledgments.....	xxx
Dedication.....	xxxii
List of Abbreviations and Symbols.....	xxxiii
Chapter 1 Introduction.....	1
1.1 General introduction.....	1
1.2 Introduction to seismology and earthquake engineering.....	2
1.2.1 Introduction to seismology.....	2
1.2.2 Introduction to earthquake engineering.....	3
1.3 Earthquake design principles.....	7
1.3.1 Fundamental requirements.....	7
1.3.2 Limit states.....	7
1.3.3 Basic principles of conceptual design.....	8
1.3.4 Importance classes and importance factors.....	8

1.3.5	Capacity design.....	9
1.3.6	Structural material and types	10
1.4	Current design philosophies.....	14
1.4.1	Force based design (FBD) procedure	15
1.4.2	Direct displacement based design (DDBD).....	16
1.5	Scope and objectives of the current research	18
1.6	Organisation of the thesis.....	20
Chapter 2 Literature review		22
2.1	Introduction.....	22
2.2	Performance of CBF buildings in past earthquakes.....	23
2.3	Hysteretic behaviour of brace elements	32
2.3.1	Physical tests of brace members	35
2.3.2	Numerical models for brace members	44
2.3.2.1	Phenomenological models	44
2.3.2.2	Physical theory models	44
2.3.2.3	Finite element models.....	46
2.4	Physical tests on CBFs.....	46
2.5	Response analysis procedures.....	52
2.5.1	Linear static analysis.....	52
2.5.2	Linear dynamic analysis	53
2.5.3	Non-linear static (pushover) analysis.....	53
2.5.4	Non-linear dynamic analysis.....	54
2.6	Design procedure in Eurocode 8 (EC8).....	55

2.6.1	Ground conditions.....	55
2.6.2	Seismic zones.....	55
2.6.3	Basic representation of the seismic action.....	58
2.6.3.1	Horizontal elastic response spectrum.....	58
2.6.3.2	Design spectrum for elastic analysis.....	60
2.6.4	Design procedure for CBFs in Eurocode 8.....	61
2.7	Direct displacement based design (DDBD) procedure for CBFs.....	65
2.8	Summary.....	66
Chapter 3 Numerical model for steel brace members incorporating a fatigue model		69
3.1	Introduction.....	69
3.2	Cyclic tests of steel brace specimens.....	70
3.3	Numerical modelling of steel brace elements.....	75
3.4	Low cyclic fatigue modelling.....	87
3.5	Verification of the numerical model.....	93
3.5.1	Buckling and tensile loads.....	107
3.5.2	Fracture.....	108
3.5.3	Energy dissipated.....	109
3.6	Summary and conclusion.....	111
Chapter 4 Ground motions.....		113
4.1	Introduction.....	113
4.2	Ground motion parameters.....	114
4.3	Choice of accelerograms for NLTHA.....	114
4.3.1	Artificially adjusted earthquakes.....	116

4.3.1.1 Artificially adjusted accelerograms with spectra scaled to match shake table tests accelerograms spectra.	118
4.3.1.2 Artificially adjusted accelerograms with spectra scaled to match EC8 type 1 spectrum, soil type C.....	120
4.3.2 Real earthquakes	121
4.4 Generation of inelastic displacement spectra.....	125
4.5 Summary and conclusion.....	130
Chapter 5 Validation of non-linear time history analysis models for single storey concentrically braced frames using full scale shake table tests	131
5.1 Introduction.....	131
5.2 Shake table tests	132
5.2.1 Test set-up.....	132
5.2.2 Specimen properties.....	133
5.3 Non-linear time-history analysis (NLTHA).....	136
5.4 Comparison between shake table tests and NLTHA	138
5.4.1 Displacement and axial force time history response.....	141
5.4.2 Equivalent viscous damping	148
5.5 Sensitivity of frame response to different earthquake excitation.....	151
5.6 Summary and conclusion	157
Chapter 6 Direct displacement based seismic design for single storey CBFs	159
6.1 Introduction.....	159
6.2 Direct displacement based design (DDBD).....	160
6.2.1 Design displacement	160
6.2.2 Yield displacement.....	161

6.2.3	Design displacement ductility.....	162
6.2.4	Equivalent viscous damping.....	162
6.2.5	Effective period of the structure.....	164
6.2.6	Effective stiffness of substitute structure.....	165
6.2.7	Design base shear force.....	165
6.2.8	Brace cross-section size.....	166
6.3	Comparison of DDBD with shake table tests.....	167
6.4	Verification of DDBD methodology using NLTHA.....	168
6.5	Summary and conclusion.....	172
Chapter 7 DDBD for multi-storey CBFs.....		173
7.1	Introduction.....	173
7.2	DDBD procedure for multi-storey CBFs.....	174
7.2.1	Design storey displacements.....	174
7.2.2	Equivalent SDOF system characteristics.....	176
7.2.3	Design displacement ductility.....	177
7.2.4	Equivalent viscous damping.....	177
7.2.5	Effective period.....	178
7.2.6	Effective stiffness of substitute structure.....	179
7.2.7	Design base shear force.....	179
7.3	Case studies for DDBD for CBFs.....	180
7.3.1	Braces design.....	185
7.3.2	Columns and beams capacity design.....	188
7.4	Verification of the DDBD procedure.....	190

7.4.1	Numerical model.....	191
7.4.2	Ground motions used in the study	191
7.4.3	Comparison of results from NLTHA and DDBD.....	192
7.4.3.1	Using artificially adjusted earthquakes.....	192
7.4.3.2	Using real earthquakes	199
7.5	Design of CBFs according to FBD	206
7.5.1	Design response spectrum and seismic forces	207
7.5.2	Design of braces.....	208
7.5.3	Beams and columns design.....	210
7.5.4	Inter-storey drift limitation	210
7.5.5	P- Δ effect	211
7.6	Comparison of FBD approach with DDBD and NLTHA	212
7.7	Summary and conclusion.....	218
Chapter 8 Summary, conclusions and future work.....		220
8.1	Introduction.....	220
8.2	Summary and conclusions	220
8.2.1	Validating of a numerical model for steel brace members incorporating a fatigue model	220
8.2.2	Validation of NLTHA model for single storey CBFs.....	221
8.2.3	DDBD for single storey CBFs	222
8.2.4	DDBD for multi-storey CBFs.....	223
8.2.5	Potential impact of this research project.....	224
8.3	Future work.....	225
References.....		227

Appendix A NLTHA results for shake table tests	236
Appendix B DDBD for 12-storey CBF case study.....	258
B.1 Calculation of design displacement and effective height	260
B.2 Columns and beams capacity design	267
Appendix C OpenSees input files	269
C.1 OpenSee input file for a brace element.....	269
C.2 OpenSees input file for SDOF CBF.....	276

List of tables

Table 1.1: Importance classes for buildings (CEN 2004).....	9
Table 2.1: Summary of observed damage of selected CBF structures during seismic actions	33
Table 2.2: Nonlinear regression of the post-buckling compression resistance of the braces (Tremblay 2002).	41
Table 2.3: Ground types according to EC8 (CEN 2004).....	56
Table 2.4: Values of the parameters describing the recommended Type 1 elastic response spectra EC8 (CEN 2004).	59
Table 2.5: Values of the parameters describing the recommended Type 2 elastic response spectra EC8 (CEN 2004).	60
Table 3.1: Parameters and results for the specimens used to calibrate the numerical model.....	72
Table 3.2: Parameters and results for the specimens used to calibrate the numerical model.....	95
Table 3.3: Parameters and results for the specimens used to validate the numerical model.	96
Table 4.1: Properties of the first set ground motions.....	116
Table 4.2: Second set of ground motions used in the study.....	122

Table 5.1: Shake table and specimen parameters.	136
Table 5.2: Comparison of the results between the physical shake table tests and the numerical models in OpenSees.	141
Table 5.3: Properties of ground motions used.	153
Table 5.4: Numerical model results using eight different accelerograms compatible to displacement spectrum for ST2-E50H test and comparison with the results from physical test.	154
Table 5.5: Numerical model results using eight different accelerograms compatible to displacement spectrum for ST5-E20H test and comparison with the results from physical test.	154
Table 5.6: Numerical model results using eight different accelerograms compatible to displacement spectrum for ST5-E20H-B test and comparison with the results from physical test.	155
Table 5.7: Numerical model results using eight different accelerograms compatible to displacement spectrum for ST8-E40H test and comparison with the results from physical test.	155
Table 6.1: Results from DDBD and comparison to physical experimental results	168
Table 6.2: Comparison of displacements and base shear obtained from NLTHA and DDBD.	171
Table 7.1: Calculations for design displacements, effective height and yield displacement.	184
Table 7.2: Initial calculation of forces, shear and the design of brace elements ($n = 1$).	186
Table 7.3: Calculation of overstrength factor and the new equivalent viscous damping ($n = 1$)	187
Table 7.4: Final trial results of designing the braces ($n = 2$)	188
Table 7.5: Column and Beam designed sections from capacity design principles.	189

Table 7.6: Structural member sizes for 12-storey building estimated using DDBD.	190
Table 7.7: Values of the parameters describing the recommended Type 1 elastic response spectra for ground type C, EC8 (CEN 2004).	207
Table 7.8: Storey forces and design shear for the 4-storey case study structure.	208
Table 7.9: Calculation of brace axial forces and the design of brace elements.	209
Table 7.10: Column and Beam designed sections from capacity design principles.	210
Table 7.11: Calculations of elastic displacement, design displacement and drift.	211
Table 7.12: Calculation of the inter-storey drift sensitivity coefficient.....	212
Table B.1: Calculations for design displacement and effective height.....	261
Table B.2: Calculations for yield displacement.....	262
Table B.3: Base shear distribution and brace section selection (n =1).	265
Table B.4: Equivalent viscous damping calculations (n =1)	266
Table B.5: Revised base shear distribution and brace section selection (n = 2).....	267
Table B.6: Column and Beam designed sections from capacity design principles.	268

List of figures

Figure 1.1: Subduction zone, spreading ridge, and transform fault boundaries (Kramer 1996).	3
Figure 1.2: Single-degree-of-freedom-system (SDOF).	4
Figure 1.3: Graphical description of acceleration response spectrum (Bungale 2004).	5
Figure 1.4: a) Fundamental mode of a multi-mass system. b) Equivalent single mass system. Adapted from (Bungale 2004).	6
Figure 1.5: Principle of strength limitation illustrated with ductile chain (Paulay and Priestley 1992)	10
Figure 1.6: Moment resisting frames (dissipative zones in beams and at bottom of columns) (CEN 2004).	12
Figure 1.7: Frames with concentric diagonal bracings (dissipative zones in tension diagonals only) (CEN 2004).	12
Figure 1.8: Frames with concentric V-bracings (dissipative zones in tension and compression diagonals) (CEN 2004).	12
Figure 1.9: Frame with K bracings (not allowed in EC8 (CEN 2004)).	13
Figure 1.10: Frames with eccentric bracings (dissipative zones in bending or shear links) (CEN 2004).	13

Figure 1.11: Inverted pendulum: a) dissipative zones at the column base; b) dissipative zones in columns (CEN 2004).	13
Figure 1.12: Structures with concrete cores or concrete walls(CEN 2004).....	14
Figure 1.13: Moment resisting frame combined with concentric bracing (dissipative zones in moment frame and in tension diagonals) (CEN 2004).	14
Figure 1.14: Moment resisting frame combined with infill (CEN 2004).	14
Figure 1.15: Fundamentals of DDBD adapted from (Priestley et al. 2007).	17
Figure 1.16: Flow chart of the primary objectives of the thesis.	19
Figure 2.1: Unbalanced arrangement of braces in ground floor for a CBF building due to functional reasons (Tanaka et al. 1980).	24
Figure 2.2: Pino Suarez complex (Ger et al. 1993).....	25
Figure 2.3: Configuration of Pino Suarez complex (Ger et al. 1993).....	25
Figure 2.4: Wreckage of the 21-storey steel-constructed building in the Pino Suarez apartment complex during Mexico City earthquake in September 19 th 1985 (Encyclopædia Britannica 2010).....	26
Figure 2.5: Oviatt library building at the California State University at Northridge: failure of the overhanging roof. (California State University Northridge 1994)	27
Figure 2.6: Global view of the four storey Los Angeles building elevation that suffered damage during the 1994 Northridge earthquake (Kelly et al. 2000).	28
Figure 2.7: Brace fracture (Kelly et al. 2000).....	29
Figure 2.8: CBF building with fracture of bracing members during 1995 Hyogo-ken-Nanbu earthquake (Kitagawa and Hiraishi 2004).....	30
Figure 2.9: Fracture of the welds between a brace and a column in a parking garage building after Christchurch earthquake occurred in February 22, 2011 (Bruneau et al. 2011).	31

Figure 2.10: Residual buckling due brace elongation in a parking garage building after Christchurch earthquake occurred in February 22, 2011 (Bruneau et al. 2011).....	31
Figure 2.11: Hysteretic behaviour of a brace member (Bruneau et al. 1998).....	34
Figure 2.12: Normalised slenderness ratio vs. total ductility reached at fracture (Tremblay 2002).	39
Figure 2.13: Definition of brace response parameters showing the total ductility reached at fracture, μ_f , (Tremblay 2002).....	40
Figure 2.14: Typical plan and elevation of US-Japan Joint Research Programme full-scale test frame: (a) Typical floor plan, (b) Frame B elevation, (c) Frame A and C elevation, and (d) Frame 1 and 3 elevation (Foutch et al. 1987).....	50
Figure 2.15: Seismic zone map for Italy, showing the peak ground accelerations that have a 10% probability of exceedance in 50 years (return period of 475 years) (INGV 2004).57	
Figure 2.16: Shape of the elastic response spectrum from EC8 (CEN 2004).....	59
Figure 2.17: Lateral resistance of CBF where the symmetry should be satisfied (CEN 2004).	64
Figure 2.18: Flow chart of the DDBD procedure for CBFs adapted from (Wijesundara 2009).	67
Figure 3.1: Cyclic displacement waveform for ECCS procedure.....	71
Figure 3.2: (a) Specimen diagram and (b) experimental load-displacement response of the Specimen 40X40X.2.5X1100-CS-CF-G1 (Goggins 2004).	74
Figure 3.3: Failure of specimen 40X40X2.5X1100-CS-CF-G1. (a) Lateral and local buckling. (b) Fracture across local buckled area near top stiffener. (c) Fracture across local buckled are at mid-height of the specimen (Goggins 2004).	74
Figure 3.4: Pushover curves of braced moment resisting frame while using lumped and distributed plasticity, adapted from Lotfollahi and Alinia (2009).	76
Figure 3.5: Setup and loading direction of the numerical model used in OpenSees.	77

Figure 3.6: Monotonic envelop for uniaxial Giuffre-Menegotto-Pinto steel material (McKenna et al. 2000).	78
Figure 3.7: Effect on the force displacement response of changing the number of fibres across the thickness of the cross section of the brace in the numerical model.	80
Figure 3.8: Effect on the force displacement response of changing the number of fibres along the perimeter of the cross section of the brace in the numerical model.....	80
Figure 3.9: Experimental force-displacement response of specimen 50X25X2.5X1100-CS-CF-G5 compared to the hysteretic model found from OpenSees with (a) 0.05% initial camber and (b) 0.1% initial camber.	81
Figure 3.10: Effect on the force displacement response of changing the number of non-linear beam column elements to represent the unstiffened length for the brace in the numerical model using 3 integration points per element.	82
Figure 3.11: Effect on the force displacement response of changing the number of integration points for the brace in the numerical model using eight non-linear beam-column elements per brace over the unstiffened length.....	84
Figure 3.12: Effect on the force displacement response of changing both the number of elements and integration points for the unstiffened brace in the numerical model.	85
Figure 3.13: Effect on the force displacement response of changing the number of integration points for the brace in the numerical model using two non-linear beam-column elements per brace over the unstiffened length.....	86
Figure 3.14: Comparison of response of numerical model to monotonic and cyclic loading.....	87
Figure 3.15: Effect on the force displacement response of changing the number of non-linear beam column elements for the brace in the numerical model while using the fatigue model and 6 integration points per element.	91

Figure 3.16: Effect on the force displacement response of changing the number of non-linear beam-column elements for the brace in the numerical model while using the fatigue model and 10 integration points per element.....	92
Figure 3.17: Experimental force-displacement response of the specimen 50X25X2.5X1100-CS-CF-G6 compared to the hysteretic model in OpenSees using parameters suggested by Uriz (2005).	93
Figure 3.18: (a) Physical test and (b) numerical model load displacement hysteretic loops for Specimen 40X40X2.5X1100-CS-CF-G1.....	96
Figure 3.19: (a) Physical test and (b) numerical model load displacement hysteretic loops for Specimen 40X40X2.5X1100-CS-CF-G2.....	97
Figure 3.20: (a) Physical test and (b) numerical model load displacement hysteretic loops for Specimen 20X20X2.0X1100-CS-CF-G3.....	97
Figure 3.21: (a) Physical test and (b) numerical model load displacement hysteretic loops for Specimen 20X20X2.0X1100-CS-CF-G4.....	97
Figure 3.22: (a) Physical test and (b) numerical model load displacement hysteretic loops for Specimen 50X25X2.5X1100-CS-CF-G5.....	98
Figure 3.23: (a) Physical test and (b) numerical model load displacement hysteretic loops for Specimen 50X25X2.5X1100-CS-CF-G6.....	98
Figure 3.24: (a) Physical test and (b) numerical model load displacement hysteretic loops for Specimen 40X40X2.5X3300-CS-CF-G7.....	98
Figure 3.25: (a) Physical test and (b) numerical model load displacement hysteretic loops for Specimen 40X40X2.5X3300-CS-CF-G8.....	99
Figure 3.26: (a) Physical test and (b) numerical model load displacement hysteretic loops for Specimen 40X40X2.5X3300-CS-CF-G9.....	99
Figure 3.27: (a) Physical test and (b) numerical model load displacement hysteretic loops for Specimen 20X20X2.0X3300-CS-CF-G10.....	99

Figure 3.28: (a) Physical test and (b) numerical model load displacement hysteretic loops for Specimen 20X20X2.0X3300-CS-CF-G11.....	100
Figure 3.29: (a) Physical test and (b) numerical model load displacement hysteretic loops for Specimen 20X20X2.0X3300-CS-CF-G12.....	100
Figure 3.30: (a) Physical test and (b) numerical model load displacement hysteretic loops for Specimen 50X25X2.5X3300-CS-CF-G13.....	100
Figure 3.31: (a) Physical test and (b) numerical model load displacement hysteretic loops for Specimen 50X25X2.5X3300-CS-CF-G14.....	101
Figure 3.32: (a) Physical test and (b) numerical model load displacement hysteretic loops for Specimen 50X25X2.5X3300-CS-CF-G15.....	101
Figure 3.33: (a) Physical test and (b) numerical model load displacement hysteretic loops for Specimen 60X60X3X2050-CS-HR-N16.....	101
Figure 3.34: (a) Physical test and (b) numerical model load displacement hysteretic loops for Specimen 40X40X3X2050-CS-HR-N17.....	102
Figure 3.35: (a) Physical test and (b) numerical model load displacement hysteretic loops for Specimen 40X40X3X1250-CS-HR-N18.....	102
Figure 3.36: (a) Physical test and (b) numerical model load displacement hysteretic loops for Specimen 60X60X3X2050-CS-CF-N19.....	102
Figure 3.37: (a) Physical test and (b) numerical model load displacement hysteretic loops for Specimen 40X40X4X2050-CS-CF-N20.....	103
Figure 3.38: (a) Physical test and (b) numerical model load displacement hysteretic loops for Specimen 40X40X3X2050-CS-CF-N21. Specimen failed at end connection.....	103
Figure 3.39: (a) Physical test and (b) numerical model load displacement hysteretic loops for Specimen 40X40X3X1250-CS-CF-N22.....	103
Figure 3.40: (a) Physical test and (b) numerical model load displacement hysteretic loops for Specimen 60X60X3X2850-SS-CF-N23.....	104

Figure 3.41: (a) Physical test and (b) numerical model load displacement hysteretic loops for Specimen 50X50X3X2850-SS-CF-N24.	104
Figure 3.42: (a) Physical test and (b) numerical model load displacement hysteretic loops for Specimen 60X40X3X2850-SS-CF-N25. Specimen failed at end connection.	104
Figure 3.43: (a) Physical test and (b) numerical model load displacement hysteretic loops for Specimen 60X60X3X2050-SS-CF-N26.	105
Figure 3.44: (a) Physical test and (b) numerical model load displacement hysteretic loops for Specimen 50X50X3X2050-SS-CF-N27.	105
Figure 3.45: (a) Physical test and (b) numerical model load displacement hysteretic loops for Specimen 60X40X3X2050-SS-CF-N28.	105
Figure 3.46: (a) Physical test and (b) numerical model load displacement hysteretic loops for Specimen 60X60X3X1250-SS-CF-N29.	106
Figure 3.47: (a) Physical test and (b) numerical model load displacement hysteretic loops for Specimen 50X50X3X1250-SS-CF-N30.	106
Figure 3.48: (a) Physical test and (b) numerical model load displacement hysteretic loops for Specimen 60X40X3X1250-SS-CF-N31.	106
Figure 3.49: Comparison of displacement ductility, μ , values obtained from the expressions established by Nip et al. (2010) to the numerical model results.	109
Figure 3.50: Energy dissipated by specimens in physical tests (Goggins et al. 2005; Nip et al. 2010) and the numerical models.	110
Figure 3.51: Energy index versus slenderness for the first cycle at a ductility of 4 measured in physical tests (Goggins et al. 2005; Nip et al. 2010) and obtained from numerical models.	111
Figure 4.1: Northridge earthquake, January 17, 1994, EQ3a.	116
Figure 4.2: Northridge earthquake, January 17, 1994, EQ3b.	117
Figure 4.3: Imperial Valley earthquake, October 15, 1979, EQ4a.	117

Figure 4.4: Imperial Valley earthquake, October 15, 1979, EQ4b.	117
Figure 4.5: Hector earthquake, October 16, 1999, EQ5a.....	117
Figure 4.6: Hector earthquake, October 16, 1999, EQ5b.	117
Figure 4.7: Landers earthquake, June 28, 1992, EQ6a.	118
Figure 4.8: Landers earthquake, June 28, 1992, EQ6b.	118
Figure 4.9: Displacement response spectrum for eight different earthquakes scaled to be compatible with the displacement spectrum for the earthquake used in ST2 test.	118
Figure 4.10: Displacement response spectrum for eight different earthquakes scaled to be compatible with the displacement spectrum for the earthquake used in ST5-20H test. .	119
Figure 4.11: Displacement response spectrum for eight different earthquakes scaled to be compatible with the displacement spectrum for the earthquake used in ST5-20HB test.	119
Figure 4.12: Displacement response spectrum for eight different earthquakes scaled to be compatible with the displacement spectrum for the earthquake used in ST8 test.	120
Figure 4.13: 5% design spectrum compared to the scaled displacement spectra for eight accelerograms used to verify the design procedure using NLTHA.	121
Figure 4.14: 5% design spectrum compared to the scaled displacement spectra for the average of eight accelerograms used to verify the design procedure using NLTHA.	121
Figure 4.15: Denali earthquake, Nov. 3, 2002, LA1.....	122
Figure 4.16: Chi-Chi earthquake, Sep. 9, 1999, LA2.	122
Figure 4.17: Chi-Chi earthquake, Sep. 9, 1999, LA3.	122
Figure 4.18: Chi-Chi earthquake, Sep. 9, 1999, LA4.	123
Figure 4.19: Darfield earthquake, Sep. 4, 2010, LA5.....	123
Figure 4.20: Loma Prieta earthquake, Oct. 17, 1989, LA6.....	123
Figure 4.21: Loma Prieta earthquake, Oct. 17, 1989, LA7.....	123

Figure 4.22: Irpinia, Nov. 23, 1980, LA8.	123
Figure 4.23: 5% design spectrum compared to the scaled displacement spectra for real eight accelerograms used to verify the design procedure using NLTHA.	124
Figure 4.24: 5% design spectrum compared with the average of scaled displacement spectra for real eight accelerograms used to verify the design procedure using NLTHA.	124
Figure 4.25: Design displacement response spectrum of 16.4% damping compared with the displacement spectra for the artificially adjusted accelerograms of 16.4% damping.	126
Figure 4.26: Design displacement response spectrum of 18.54% damping compared with the displacement spectra for the artificially adjusted accelerograms of 18.54% damping.	126
Figure 4.27: Design displacement response spectrum of 16.4% damping compared with the displacement spectra for the real accelerograms of 16.4% damping.	127
Figure 4.28: Design displacement response spectrum of 18.54% damping compared with the displacement spectra for the real accelerograms of 18.54% damping.	127
Figure 4.29: Design displacement response spectrum of 16.4% damping compared with the mean of displacement spectra for the artificially adjusted accelerograms of 16.4% damping.	128
Figure 4.30: Design displacement response spectrum of 18.54% damping compared with the mean of displacement spectra for the artificially adjusted accelerograms of 18.54% damping.	128
Figure 4.31: Design displacement response spectrum of 16.4% damping compared with the mean of displacement spectra for the real accelerograms of 16.4% damping.	129
Figure 4.32: Design displacement response spectrum of 18.54% damping compared with the mean of displacement spectra for the real accelerograms of 18.54% damping.	129

Figure 5.1: Diagram of the experimental set-up for the shake table test (all dimensions are in mm) (Elghazouli et al. 2005).....	133
Figure 5.2: Photo of the experimental set-up for the shake table test (Goggins 2004)...	134
Figure 5.3: Shake table model used in OpenSees.....	138
Figure 5.4: Comparison for the displacement time-history response of test ST2-E50H and the numerical model in OpenSees.....	143
Figure 5.5: Comparison for the displacement time-history response of test ST8-E40H and the numerical model in OpenSees.....	143
Figure 5.6: Comparison for the axial load time-history response of the first brace specimen of test ST2-E50H and the numerical model in OpenSees.	144
Figure 5.7: Comparison for the axial load time-history response of the second brace specimen of test ST2-E50H and the numerical model in OpenSees.	144
Figure 5.8: Comparison for the axial load time-history response of the first brace specimen of test ST8-E40H and the numerical model in OpenSees.	145
Figure 5.9: Comparison for the axial load time-history response of the second brace specimen of test ST8-E40H and the numerical model in OpenSees.	145
Figure 5.10: (a) Physical test and (b) numerical model base shear-lateral displacement hysteretic response of test ST2-E50H.....	146
Figure 5.11: (a) Physical test and (b) numerical model axial force- axial displacement response of a brace element from test ST2-E50H.	146
Figure 5.12: (a) Physical test and (b) numerical model base shear-lateral displacement hysteretic response of test ST8-E40H.....	146
Figure 5.13: (a) Physical test and (b) numerical model axial force- axial displacement response of a brace element from test ST8-E40H.	147
Figure 5.14: Comparison for the displacement time-history response of test ST1-R50H and the numerical model in OpenSees.....	147

Figure 5.15: Comparison for the axial load time-history response of the first brace specimen of test ST1-R50H and the numerical model in OpenSees.	148
Figure 5.16: Comparison of equivalent viscous damping values.	149
Figure 5.17: Displacement response spectrum for eight different earthquakes scaled to be compatible with the displacement spectrum for the table excitation employed in test ST2-E50H.	152
Figure 5.18: Lateral frame displacement-time history response of ST2-E50H frame using EQ3b earthquake.....	156
Figure 5.19: Axial load-time history response of braces for frame ST2-E50H using EQ3b.	156
Figure 5.20: Displacement-time history response of ST8-E40H frame using EQ4a earthquake.	157
Figure 5.21: Axial load-time history response of braces for frame ST8-E40H using EQ4a earthquake.	157
Figure 6.1: Yield deformation of the CBF due to brace elongation.	162
Figure 6.2: Comparison of equivalent viscous damping values.	164
Figure 6.3: Displacement spectrum for design of frame ST2-50H.....	165
Figure 6.4: Measured displacement time-history response of test ST2-E50H in (a) physical test and (b) numerical model.	169
Figure 6.5: Comparison for the axial load time-history between the physical test ST2-E50H and the numerical model for (a) first brace and (b) second brace.	169
Figure 6.6: Measured displacement time-history response of test frame ST8-E40H in shake table test.	171
Figure 7.1: Displacement response spectrum.	179
Figure 7.2: Flow chart of the DDBD procedure for CBFs adapted from (Wijesundara 2009).	181

Figure 7.3: Plan view of the four storey CBF case study.	182
Figure 7.4: Elevation of the 4-storey CBF case study.	183
Figure 7.5: Displacement response spectra for the 5% and 17.3% damping.....	185
Figure 7.6: Maximum recorded displacements for eight spectrum compatible accelerograms compared with the design displacements for a 4-storey CBF.	193
Figure 7.7: Maximum recorded displacements for eight spectrum compatible accelerograms compared with the design displacements for a 12-storey CBF.	193
Figure 7.8: Average of the maximum recorded displacements for eight spectrum compatible accelerograms compared with the design displacements for the 4-storey CBFs.	194
Figure 7.9: Average of the maximum recorded displacements for eight spectrum compatible accelerograms compared with the design displacements for the 12-storey CBFs.	194
Figure 7.10: Average of the maximum recorded storey drifts for eight spectrum compatible accelerograms compared with the design storey drifts for the 4-storey CBF.	195
Figure 7.11: Average of the maximum recorded storey drifts for eight spectrum compatible accelerograms compared with the design storey drifts for the 12-storey CBF.	195
Figure 7.12: Maximum recorded ductility for eight spectrum compatible accelerograms compared with the design ductility for (a) 4-storey CBF and (b) 12-storey CBF.	196
Figure 7.13: Average of the maximum recorded ductility for eight spectrum compatible accelerograms compared to the design ductility, ductility expressions of Nip et al (2010) for cold-formed and hot-rolled carbon steel and ductility expression of Tremblay (2002) for (a) 4-storey CBF and (b) 12-storey CBF.....	197
Figure 7.14: 4-storey CBF shear force design values compared to shear at the maximum displacement from NLTHA using artificially adjusted earthquakes resisted by (a) first	

brace and (b) second brace. Negative sign represents compression resistance and positive sign represents tension.	198
Figure 7.15: 12-storey CBF shear force design values compared to shear at the maximum displacement from NLTHA using artificially adjusted earthquakes resisted by (a) first brace and (b) second brace. Negative sign represents compression resistance and positive sign represents tension.	198
Figure 7.16: Average total shear forces resisted by both compression and tension braces from NLTHA using artificially adjusted earthquakes compared to the design shear forces of (a) 4-storey CBF (b) 12-storey CBF.	199
Figure 7.17: Maximum recorded displacements for real eight spectrum compatible accelerograms compared with the design displacements for the 4-storey CBF.	201
Figure 7.18: Maximum recorded displacements for real eight spectrum compatible accelerograms compared with the design displacements for the 12-storey CBF.	201
Figure 7.19: Average of the maximum recorded storey drifts for real eight spectrum compatible accelerograms compared with the design storey drifts for the 4-storey CBF.	202
Figure 7.20: Average of the maximum recorded storey drifts for real eight spectrum compatible accelerograms compared with the design storey drifts for the 12-storey CBF.	202
Figure 7.21: Average of the maximum recorded storey drifts for real eight spectrum compatible accelerograms compared with the design storey drifts for the 4-storey CBF.	203
Figure 7.22: Average of the maximum recorded storey drifts for real eight spectrum compatible accelerograms compared with the design storey drifts for the 12-storey CBF.	203

Figure 7.23: Maximum recorded ductility for real eight spectrum compatible accelerograms compared with the design ductility for (a) 4-storey CBF and (b) 12-storey CBF.	204
Figure 7.24: Average of the maximum recorded ductility for real eight spectrum compatible accelerograms compared with the design ductility, ductility expression of Nip et al (2010) for cold-formed and hot-rolled steel and ductility expression of Tremblay (2002) for (a) 4-storey CBF and (b) 12-storey CBF.	205
Figure 7.25: 4-storey CBF shear force design values compared to shear at the maximum displacement from NLTHA using real earthquakes resisted by (a) first brace and (b) second brace. Negative sign represents compression resistance and positive sign represents tension.	205
Figure 7.26: 12-storey CBF shear force design values compared to shear at the maximum displacement from NLTHA using artificially adjusted earthquakes resisted by (a) first brace and (b) second brace. Negative sign represents compression resistance and positive sign represents tension.	206
Figure 7.27: Average total shear forces resisted by both compression and tension braces from NLTHA using artificially adjusted earthquakes compared to the design shear forces of (a) 4-storey CBF (b) 12-storey CBF.	206
Figure 7.28: Maximum recorded displacements for eight spectrum compatible accelerograms compared with the design displacements used for the DDBD and the displacements obtained from FBD approach for a 4-storey CBFs.	213
Figure 7.29: Average of the maximum recorded displacements for eight spectrum compatible accelerograms compared with the design displacements used for the DDBD and the displacements obtained from FBD approach for a 4-storey CBFs.	214
Figure 7.30: Average of the maximum recorded storey drifts for eight spectrum compatible accelerograms compared with the design storey drifts used for the DDBD and the drifts obtained from FBD approach for the 4-storey CBFs.	215

Figure 7.31: Maximum recorded ductility for eight spectrum compatible accelerograms compared with the design ductility from DDBD and FBD method for the 4-storey CBFs.	216
Figure 7.32: Average of the maximum recorded ductility for eight spectrum compatible accelerograms compared to the design ductility from DDBD and FBD approach, ductility expressions of Nip et al (2010) for cold-formed and hot-rolled carbon steel and ductility expression of Tremblay (2002) for the 4-storey CBFs.	216
Figure 7.33: 4-storey CBF shear force design values compared to shear at the maximum displacement from NLTHA using artificially adjusted earthquakes resisted by (a) first brace and (b) second brace. Negative sign represents compression resistance and positive sign represents tension.	217
Figure 7.34: Average total shear forces resisted by both compression and tension braces from NLTHA using artificially adjusted earthquakes compared to the design shear forces obtained from FBD approach for the 4-storey CBF.	217
Figure A.1: Comparison for the displacement time-history response of test ST1-R50H and the numerical model in OpenSees.	237
Figure A.2: Measured displacement time-history response of test ST1-R50H in (a) physical test and (b) numerical model.	237
Figure A.3: Comparison for the axial load time-history response of the first brace specimen of test ST1-R50H and the numerical model in OpenSees.	238
Figure A.4: Axial load time-history response of the first brace of test ST1-R50H in (a) physical test and (b) numerical model.	238
Figure A.5: Comparison for the axial load time-history response of the second brace specimen of test ST1-R50H and the numerical model in OpenSees.	239
Figure A.6: Axial load time-history response of the second brace of test ST1-R50H in (a) physical test and (b) numerical model.	239

Figure A.7: Comparison for the displacement time-history response of test ST2-E50H and the numerical model in OpenSees.....	240
Figure A.8: Measured displacement time-history response of test ST2-E50H in (a) physical test and (b) numerical model.	240
Figure A.9: Comparison for the axial load time-history response of the first brace specimen of test ST2-E50H and the numerical model in OpenSees.	241
Figure A.10: Axial load time-history response of the first brace of test ST2-E50H in (a) physical test and (b) numerical model.	241
Figure A.11: Comparison for the axial load time-history response of the second brace specimen of test ST2-E50H and the numerical model in OpenSees.	242
Figure A.12: Axial load time-history response of the second brace of test ST2-E50H in (a) physical test and (b) numerical model.	242
Figure A.13: Comparison for the displacement time-history response of test ST4-R20H and the numerical model in OpenSees.....	243
Figure A.14: Measured displacement time-history response of test ST4-R20H in (a) physical test and (b) numerical model.	243
Figure A.15: Comparison for the axial load time-history response of the first brace specimen of test ST4-R20H and the numerical model in OpenSees.	244
Figure A.16: Axial load time-history response of the first brace of test ST4-R20H in (a) physical test and (b) numerical model.	244
Figure A.17: Comparison for the axial load time-history response of the second brace specimen of test ST4-R20H and the numerical model in OpenSees.	245
Figure A.18: Axial load time-history response of the second brace of test ST4-R20H in (a) physical test and (b) numerical model.	245
Figure A.19: Comparison for the displacement time-history response of test ST5-E20H and the numerical model in OpenSees.....	246

Figure A.20: Measured displacement time-history response of test ST5-E20H in (a) physical test and (b) numerical model.	246
Figure A.21: Comparison for the axial load time-history response of the first brace specimen of test ST5-E20H and the numerical model in OpenSees.	247
Figure A.22: Axial load time-history response of the first brace of test ST5-E20H in (a) physical test and (b) numerical model.	247
Figure A.23: Comparison for the axial load time-history response of the second brace specimen of test ST5-E20H and the numerical model in OpenSees.	248
Figure A.24: Axial load time-history response of the second brace of test ST5-E20H in (a) physical test and (b) numerical model.	248
Figure A.25: Comparison for the displacement time-history response of test ST5-E20H-B and the numerical model in OpenSees.	249
Figure A.26: Measured displacement time-history response of test ST5-E20H-B in (a) physical test and (b) numerical model.	249
Figure A.27: Comparison for the axial load time-history response of the first brace specimen of test ST5-E20H-B and the numerical model in OpenSees.	250
Figure A.28: Axial load time-history response of the first brace of test ST5-E20H-B in (a) physical test and (b) numerical model.	250
Figure A.29: Comparison for the axial load time-history response of the second brace specimen of test ST5-E20H-B and the numerical model in OpenSees.	251
Figure A.30: Axial load time-history response of the second brace of test ST5-E20H-B in (a) physical test and (b) numerical model.	251
Figure A.31: Comparison for the displacement time-history response of test ST7-E40H and the numerical model in OpenSees.	252
Figure A.32: Measured displacement time-history response of test ST7-E40H in (a) physical test and (b) numerical model.	252

Figure A.33: Comparison for the axial load time-history response of the first brace specimen of test ST7-E40H and the numerical model in OpenSees.	253
Figure A.34: Axial load time-history response of the first brace of test ST7-E40H in (a) physical test and (b) numerical model.	253
Figure A.35: Comparison for the axial load time-history response of the second brace specimen of test ST7-E40H and the numerical model in OpenSees.	254
Figure A.36: Axial load time-history response of the second brace of test ST7-E40H in (a) physical test and (b) numerical model.	254
Figure A.37: Comparison for the displacement time-history response of test ST8-E40H and the numerical model in OpenSees.	255
Figure A.38: Measured displacement time-history response of test ST8-E40H in (a) physical test and (b) numerical model.	255
Figure A.39: Comparison for the axial load time-history response of the first brace specimen of test ST8-E40H and the numerical model in OpenSees.	256
Figure A.40: Axial load time-history response of the first brace of test ST8-E40H in (a) physical test and (b) numerical model.	256
Figure A.41: Comparison for the axial load time-history response of the second brace specimen of test ST8-E40H and the numerical model in OpenSees.	257
Figure A.42: Axial load time-history response of the second brace of test ST8-E40H in (a) physical test and (b) numerical model.	257
Figure B.1: Plan view of the 12-storey CBF case study.	258
Figure B.2: Elevation of the 12-storey CBF.	259
Figure B.3: Displacement response spectra for the 5% and 17.3% damping.	263

Declarations

This thesis or any part thereof, has not been, or is not currently being submitted for any degree at any other university.

Suhaib Salawdeh

The work reported herein is as a result of my own investigations, except where acknowledged and referenced.

Suhaib Salawdeh

Acknowledgments

I would like to express my deepest gratitude to my supervisor, Dr. Jamie Goggins, for his support, understanding, patience, guidance and most importantly, his friendship. During my studies, his door was always open anytime I needed him and he was always there to offer advice during the hard times. Without his extensive knowledge, direction, and endless encouragement, this thesis would not have been completed.

I would also like to extend my appreciation to my Graduate Research Committee members: Prof. Padraic O'Donoghue and Dr. Michael Hartnett for their advice during my research. I am very grateful to the NUIG College of Engineering and Informatics fellowship which helped to fund me during my studies. The help provided from Dr. Bryan McCabe and Daithi Byrne is greatly appreciated.

I would like to thank all my friends and colleagues at National University of Ireland, Galway, my friends in Europe and Palestine for their endless support. The advice, support and friendship from Dr. Kushan Wijesundara are also highly appreciated.

Finally, I would like to thank my parents, who deserve my sincerest appreciation, but also my siblings for their love and support.

Dedication

This work is dedicated to my parents. Their support and confidence in me gave me courage and strength to accomplish this work.

List of Abbreviations and Symbols

A	area of the member
A_b	brace cross sectional areas
a_g	design ground acceleration
A_g	gross cross sectional area
a_{gR}	reference peak ground acceleration on type A ground as defined by Eurocode 8 (EN 1998-1) (CEN 2004)
a,b, and c	constants
B	the bay width
BRB	buckling restrained brace
c	damping coefficient
C	overstrength ratio
CBF	centrically braced frame
CF	cold-formed
c_{eq}	equivalent viscous damping coefficient
CS	carbon steel
C_r	first buckling load of the brace

C_r'	reduced buckling capacity
c_u	undrained shear strength of the soil
C_v	coefficient of variation
DDBD	direct displacement based design
DI	damage from cyclic loading
DI_i	damage for each amplitude of cycling
E	Young's modulus
EC1	Eurocode 1 (EN1991-1) (CEN 2004)
EC3	Eurocode 3 (EN 1993-1) (CEN 2005)
EC8	Eurocode 8 (EN 1998-1) (CEN 2004)
EVD	equivalent viscous damping
E_{nc}	energy dissipated
e_y	axial yield displacement
F	applied force
F_b	base shear force as defined by Eurocode 8
FBD	force based design
F_c	initial buckling load
F_i	horizontal forces
F_{max}	the maximum tensile force
$F_{P-\Delta}$	increase in the lateral force required to account for P- Δ effects
f_y	yield stress of the brace
f_{ya}	the increased average yield strength due to cold working
f_{yb}	the basic yield strength value of sheet obtained from coupon tests

f_u	the basic ultimate tensile strength of sheet taken from coupon test
g	acceleration due to gravity = 9.81m/s^2
h_i	the storey height
H_e	effective height
H_n	the roof height
HR	hot-rolled
HSS	hollow structural section
i	radius of gyration
K	effective length factor
K	numerical coefficient that depends on the type of forming
K	stiffness
K_e	effective stiffness
K_i	initial stiffness
L	the overall length
L_b	brace length
m	mass
m	fatigue ductility exponent
M	earthquake magnitude
MRF	moment resisting frame
$M_{Ed,E}$	bending moment in the beam or in the column due to the design seismic action
$M_{Ed,G}$	bending moment in the beam or in the column due to the non-seismic actions

$M_{pl,Rd}$	moment resistance
M_s	surface-wave magnitude
n	the number of 90° bends in the cross-section
n	current number of cycles
n	number of integration points per element
n_i	number of cycles at an amplitude
N_f	fatigue life
N_{fi}	number of constant amplitude cycles of that amplitude necessary to cause failure
NLTHA	non-linear time history analysis
$N_{Ed,E}$	the axial force in the beam or in the column due to the design seismic action
$N_{Ed,G}$	the axial force in the beam or in the column due to the non-seismic actions
$N_{pl,Rd}$	the design buckling resistance of the beam or the column
$N_{pl,Rd,i}$	the design resistance of diagonal i
$N_{Ed,i}$	the design value of the axial force in diagonal i in the seismic design situation
N_{cr}	the elastic critical force for the relevant buckling mode based on the gross cross section properties as defined in EC3
$NSPT_{(blows/30cm)}$	standard penetration test blow count
P	axial load
PGA	peak ground acceleration
PGD	peak ground displacement
PGV	Peak ground velocity

q	behaviour factor as defined in EC8
Q	restoring force
r	radius
r	second slope stiffness ratio
r	epicentre distance
r	radius of root fillet
RHS	rectangular hollow sections
R_{ξ}	damping modifier
S	soil factor
S_a	stress amplitude
$S_d(T)$	design response spectrum
$S_e(T)$	elastic response spectrum
SDOF	single degree of freedom
SHS	square hollow sections
s_i	lateral relative displacement of the mass m_i as defined in EC8 (CEN 2004)
SS	stainless steel
t	the design core thickness of the steel material before cold forming
T	total time
T	period
T_B	the lower limit of the period of the constant spectral acceleration branch
T_C	the upper limit of the period of the constant spectral acceleration branch
T_D	the value defining the beginning of the constant displacement response range of the spectrum

T_e	effective period
u	relative lateral frame displacement
$u(t)$	structure's lateral displacement relative to the ground at an instant time t
$\dot{u}(t)$	structure's lateral velocity relative to the ground at an instant time t
$\ddot{u}(t)$	structure's lateral acceleration relative to the ground at an instant time t
$\ddot{u}_g(t)$	the horizontal acceleration of the ground at an instant time t
$V_{\text{compression}}$	shear force resisted by the compression brace
$V_{\text{Ed,E}}$	shear force in the beam or in the column due to the design seismic action
$V_{\text{Ed,G}}$	shear force in the beam or in the column due to the non-seismic actions
$V_{\text{pl,Rd}}$	shear resistance of the beam or the column
V_{Tension}	shear force resisted by the tension brace
$v_{s,30}$	shear wave velocity
W_D	work done; energy dissipated by a viscous dashpot in a linear SDOF system
W_{tot}	total energy dissipated
$W_{\mu=4}$	energy dissipated at the first cycle of ductility of 4
z_i	height of the mass m_i
α	the angle of the brace with the horizontal axis
β	flag-shaped hysteretic rule constant
β	the lower bound factor for the horizontal design spectrum
γ	importance factor
γ_{ov}	overstrength factor
δ	axial deflection

δ_1	the normalised inelastic mode shape of the critical storey
δ_i	the normalised inelastic mode shape
Δ_1	the displacement of the critical storey
Δ_C	the displacement at the corner period
Δ_D	lateral design displacement of frame at effective height
Δ_{Di}	lateral design storey displacements
Δ_{max}	lateral maximum displacement of frame at effective height
Δt_i	time step
Δu_i	change in relative lateral displacement of the frame
Δ_y	lateral yield displacement of frame at effective height
$\Delta \varepsilon_p$	plastic strain amplitude
$\varepsilon_{br,y}$	the brace axial yield strain
$\varepsilon_{col,y}$	the column axial yield strain
ε_y	the yield strain
ε_o	fatigue ductility coefficient
$\varepsilon_{C,i,d}^r$	the right column axial strains at the i^{th} storey
$\varepsilon_{C,i,d}^l$	the left column axial strains at the i^{th} storey
$\varepsilon_{i,d}^{tension}$	the tension brace axial strain at the i^{th} storey
η	damping correction factor
θ_C	design drift limit
$\theta_{i,d}$	the design drift for floor i
λ	correction factor

λ	effective slenderness ratio
$\bar{\lambda}$	non-dimensional slenderness ratio as defined in EC3
μ	ductility
μ_f	ductility at fracture
$v_{b,i,d}$	the beam mid-span vertical deflection at the i^{th} storey
$v_{i,d}^r$	vertical displacement at the base of the i^{th} storey right column due to elongation or shortening of columns from the first to the $(i-1)^{\text{th}}$ storey
$v_{i,d}^l$	vertical displacement at the base of the i^{th} storey left column due to elongation or shortening of columns from the first to the $(i-1)^{\text{th}}$ storey
ξ	viscous damping
ξ_{eq}	equivalent viscous damping
ξ_{hyst}	hysteresis damping ratio
ξ_o	elastic damping ratio
Ω	the brace overstrength taken as minimum value of $\Omega_i = N_{p1,Rd,i}/N_{Ed,i}$ over all the diagonals of the braced frame system
ω_n	natural circular frequency

Chapter 1

Introduction

1.1 General introduction

In 2004, the United Nations Development Programme (UNDP) found that every year, on average, about 130 million people are exposed to the risk of earthquakes (UNDP 2004). The damage done to the lives of people all around the world due to earthquakes is almost incomprehensible. Over the last decade, more than 815,000 deaths and substantial economic losses have occurred as a result of earthquakes (PEER 2011). For example, the 2011 Tōhoku earthquake in Japan led to over 15,800 deaths and an economic loss of approximately €156 billion (EM-DAT 2011). It is apparent that, safer and more reliable buildings need to be provided taking into account the initial cost and longer economic effects. This can be achieved by reducing maintenance and minimising repair costs after an earthquake. This requires new improved design methodologies and codified approaches for new buildings.

The 1994 Northridge earthquake and the 1995 Hyogoken-Nabu earthquake resulted in unanticipated damage to moment resisting frames. These were a popular steel lateral resisting system at that period. The subsequent damage led many engineers to seek out simpler and more economical systems that would promise good seismic performance with minimised drifts. As a result, concentrically braced frames (CBFs) have been commonly used as an alternative lateral resisting system for structures located in seismically active regions.

Previous research into the earthquake response behaviour of CBFs has mostly employed cyclic testing of brace members and sub-frames. Considering the widespread use of

concentrically-braced frames throughout the world, there have been relatively few shake table tests that investigated the ultimate response of full-scale models using real-time earthquake loadings. This is partially attributable to the global shortage of experimental facilities with sufficient seismic force capacity to match the inherent strength and structural efficiency of the CBFs. Furthermore, various numerical models exist for this type of systems. However, very few have been calibrated using real-time full scale shake table tests. This research addresses these issues, as well as developing a performance based design methodology for CBFs. The objective and the scope of the work can be found in Section 1.5.

In this chapter, a brief introduction to seismology and earthquake engineering will be presented followed by a summary of important earthquake design principles and current design philosophies. At the end of this chapter a summary outlining the structure of the thesis will be provided.

1.2 Introduction to seismology and earthquake engineering

1.2.1 Introduction to seismology

The Earth's surface consists of a series of large plates called tectonic plates. Beneath these plates there are convection currents that move the plates in different directions in constant motion. The boundaries of these plates are normally locked and do not move most of the time, even though the plates are in continuous movement. This causes the gradual accumulation of stresses and strains along the boundaries of the plates. When this stored elastic strain energy within the boundaries becomes sufficient to create a fracture, a sudden release of the energy will occur which creates the seismic waves causing earthquakes. This gradual accumulation and release of stress and strain is referred to as the “elastic rebound theory” of earthquakes. Most earthquakes are the result of the sudden elastic rebound of previously stored energy, with most earthquakes occurring at the boundaries where the tectonic plates either converge, diverge or transform. Plate convergence occurs where two plates move toward each other, resulting in one plate subducting under the other and the area of that plate decreasing. Divergence, on the otherhand, arises when two plates move away from each other with mantle rising to fill the space vacated by the plates. This causes new plate area to be created. Transform of plates occurs when plates move side-by-side past each

other and the area is conserved. The three types of plate movements are shown in Figure 1.1. Earthquakes that occur at the boundary of the tectonic plates are called interplate earthquakes and are the most common form of earthquakes. However, some earthquakes do occur in the interior part of tectonic plates and these are called intraplate earthquakes.

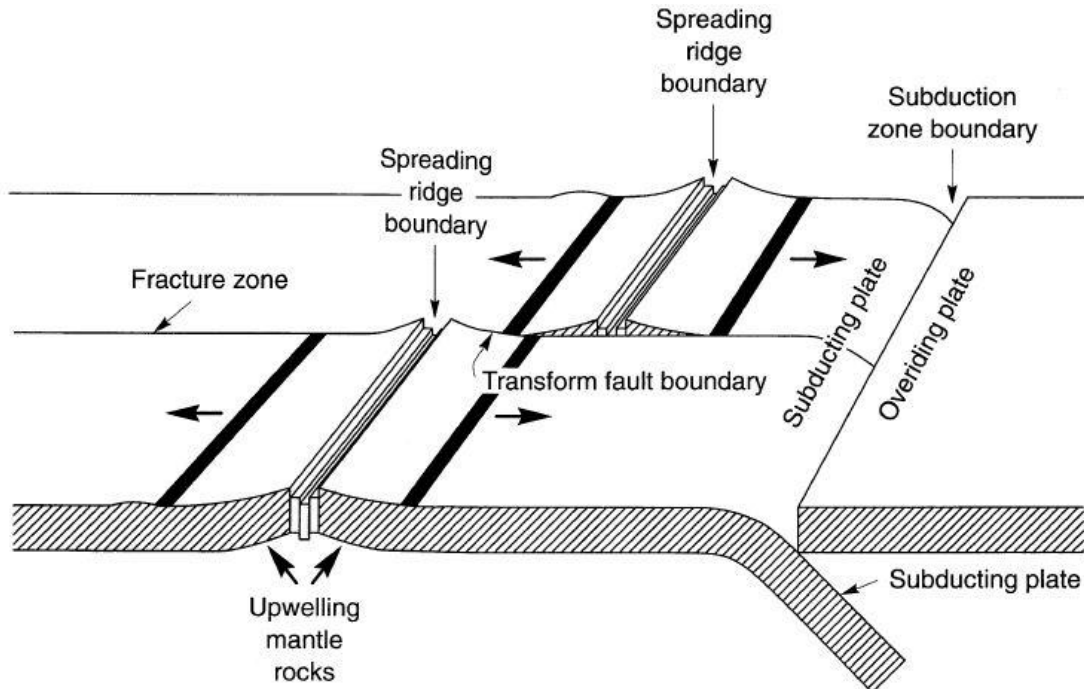


Figure 1.1: Subduction zone, spreading ridge, and transform fault boundaries (Kramer 1996).

The size of an earthquake can be quantified in two ways: intensity and magnitude. Intensity is a qualitative description of the effect of the earthquake at a particular site, as evidenced by observed damage and human reactions at that location. Magnitude is an objective and quantitative measure of earthquake size that is used to characterize the amount of energy released by an earthquake event. This was made possible with the development of modern instrumentation for measuring ground motion during earthquakes.

1.2.2 Introduction to earthquake engineering

In any seismic area, every structure should be designed to withstand the applied seismic forces in the event of seismic activity. This help to prevent human losses and minimise economic losses, while structures important for civil protection should remain operational. These seismic forces result directly from the motion of the ground on which the structure

rests. The magnitude and distribution of forces and displacements resulting from ground motion are influenced by the characteristics of the ground and the properties of the structure. To understand the dynamic properties of the structures, a single-degree-of-freedom (SDOF) structure is presented in Figure 1.2. It is an example of the SDOF system which is a single-column structure with a mass at its top or a single-storey frame with flexible columns and a rigid beam.

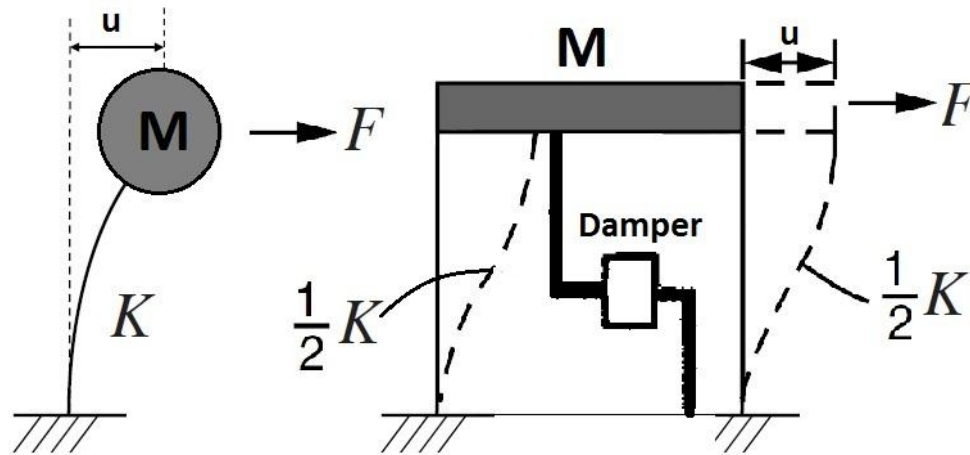


Figure 1.2: Single-degree-of-freedom-system (SDOF).

Any structure can be expressed by three linear dynamic properties. These are mass, m , stiffness, K , and damping, c . The stiffness of the system represents the horizontal force F divided by the corresponding lateral displacement u . Damping is an internal mechanism for dissipating energy when the structure moves. This energy dissipated is proportional to the velocity of the structure at any instant of time and causes vibrations of the structure to diminish over time and eventually stop. Sources of damping in any structure depend upon construction materials, frictional dissipation of energy at bolted connections, yielding of structural members and influence of non-structural elements on the stiffness characteristics of the building. The equation of motion can be given as the dynamic equilibrium between external forces and internal forces, which includes the inertia force, damping force and stiffness force as in the following:

$$m\ddot{u}(t) + c\dot{u}(t) + Ku(t) = m\ddot{u}_g(t) \quad [1.1]$$

where m is the mass, c is the damping, K is the stiffness, $u(t)$, $\dot{u}(t)$ and $\ddot{u}(t)$ are the structure's horizontal displacement, velocity and acceleration relative to the ground at an instant time t , $\ddot{u}_g(t)$ is the horizontal acceleration of the ground at an instant time t .

If a horizontal force or displacement is applied to the mass of the structure in Figure 1.2 and released, the mass will vibrate at a certain frequency called the natural frequency of vibration, which can be determined by the number of cycles per unit of time. The duration of one cycle while the motion repeats itself is called the period. It is the reciprocal of frequency, and given by the following formula:

$$T = 2\pi\sqrt{\frac{m}{K}} \quad [1.2]$$

where K is the stiffness of the system which represents the force F divided by the corresponding displacement u and m is the mass.

The response of buildings with different ranges of periods can be summarised in a single graph called spectrum. This graph can be constructed by subjecting a specific earthquake ground motion to a series of structures having different periods, T , and obtaining the maximum response each structure will experience. An example of constructing an acceleration response spectrum is shown in Figure 1.3.

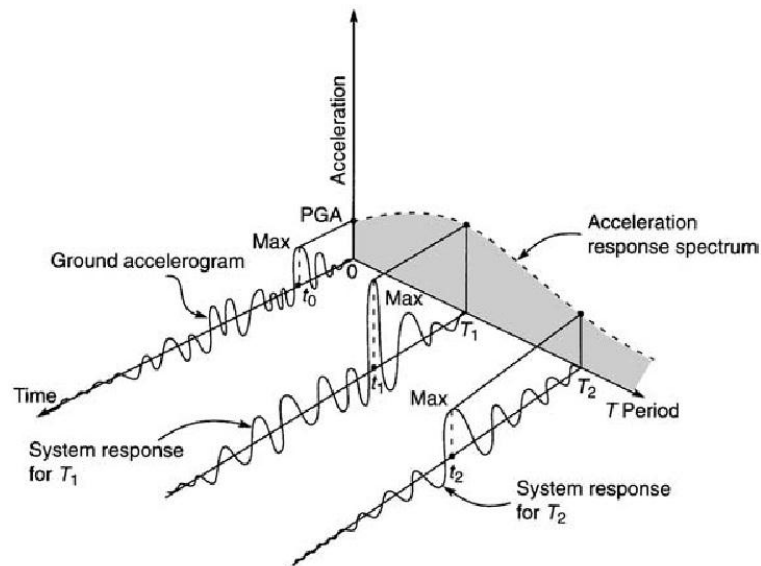


Figure 1.3: Graphical description of acceleration response spectrum (Bungale 2004).

Multi-storey structures may be analysed as multi-degree-of-freedom (MDOF) systems by lumping storey-masses at intervals along the length of a vertically cantilevered pole (stick model with the mass in each storey lumped at a single point) and the stiffness of the seismic load resisting system at each storey can be represented by a single translational spring. Each mass will be deflected in one direction or another during vibration. Some masses may move in opposite directions for higher modes of vibration. In the fundamental mode, all masses may deflect at the same time in the same direction. An idealised MDOF system has a number of modes equal to the number of masses. Each mode of vibration will have a unique natural period with a unique mode shape represented by a line connecting the deflected masses. Each mode of a MDOF system can be represented by an equivalent SDOF system with generalized values m and K for mass and stiffness, respectively. These values represent the equivalent combined effects of storey masses and stiffnesses as shown in Figure 1.4, which provides a computational basis for using response spectra based on SDOF systems for analysing MDOF buildings. In other words, by knowing the period, mode shape, and mass distribution of a multi-storey building, the response spectra of a single-degree-of-freedom (SDOF) system can be used for computing the deflected shape, storey accelerations, forces, and overturning moments.

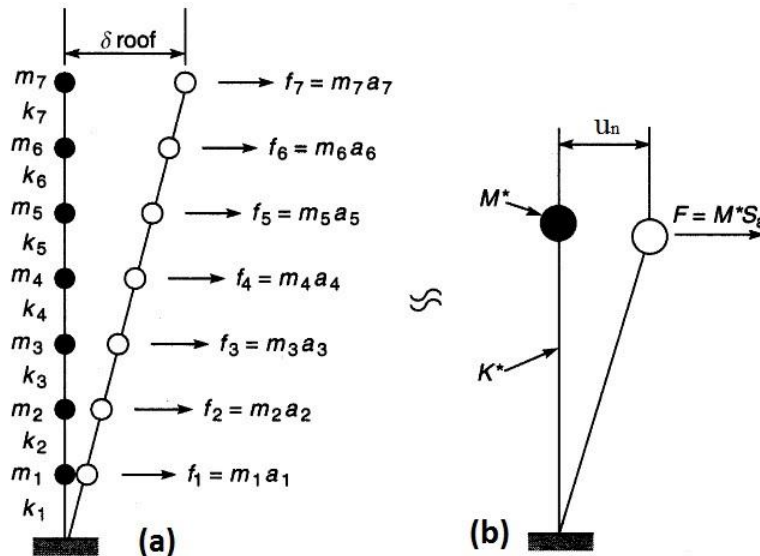


Figure 1.4: a) Fundamental mode of a multi-mass system. b) Equivalent single mass system. Adapted from (Bungale 2004).

1.3 Earthquake design principles

This section outlines earthquake design principles with particular reference to Eurocode 8 (CEN 2004), henceforth identified as EC8.

1.3.1 Fundamental requirements

EC8 (CEN 2004) has two fundamental requirements for designing and constructing every structure in a seismic region. These are:

- No-collapse requirement: where the structure is designed and constructed to withstand the design seismic actions without local or global collapse, and to retain full load bearing capacity after the seismic events. After the earthquake, there should be sufficient lateral strength and stiffness to protect the structure from collapse if aftershocks occur, taking into account the importance of the structure. For normal structures, a design life of 50 years is utilised, with an earthquake of a return period of 475 years resulting in ground motion parameters that carry a 10% probability of being exceeded.
- Damage limitation requirement: where the structure is designed and constructed to withstand a seismic action with a larger probability of occurrence than the design seismic actions. The cost of damage and the associated limitations of use should not be disproportionately high in comparison with the cost of the structure itself. The damage limitation requirement has a 10% probability of being exceeded in 10 years with a return period of 95 years.

1.3.2 Limit states

A limit state is the state beyond which the structure no longer fulfils the relevant design criteria. In order to satisfy the fundamental requirements for designing and constructing structures explained in Section 1.3.1, EC8 (CEN 2004) suggests to check the following limit states:

1. Ultimate limit states: those associated with collapse or with other similar forms of structural failure that might put the safety of people at risk. Verification of these states should be carried out under design seismic actions.

2. Damage limitation states: those associated with damage beyond which specified service requirements are no longer met. Verification of these states should be carried out for important structures, ensuring that the structure has sufficient resistance and stiffness to maintain the function of the vital services in the facilities for a seismic event associated with an appropriate return period.

1.3.3 Basic principles of conceptual design

EC8 (CEN 2004) sets out some aspects for buildings in seismic regions that should be taken into account in the early stages of the conceptual design of the building, thus enabling the achievement of a structural system which, within acceptable costs, satisfies the ‘no-collapse’ and ‘damage limitation’ requirements. The guiding principles governing this conceptual design are the following:

- Structural simplicity.
- Uniformity, symmetry and redundancy.
- Bi-directional resistance and stiffness.
- Torsional resistance and stiffness.
- Diaphragmatic behaviour at storey level.
- Adequate foundation.

Reliability differentiation is implemented by classifying structures into different importance categories (CEN 2004).

1.3.4 Importance classes and importance factors

EC8 (CEN 2004) classifies buildings in 4 importance classes with different importance factors, γ , depending on the consequences of collapse for human life, on their importance for public safety and civil protection in the immediate post-earthquake period, and on the social and economic consequences of collapse. The definitions of the importance classes are given in Table 1.1. The recommended values of γ for the importance classes I, II, III and IV are

equal to 0.8, 1.0, 1.2 and 1.4, respectively. The importance factor γ is used to alter the seismic event reference return period. In other words, those buildings in higher importance classes have greater reference return periods for seismic design. In order to limit the consequences of the seismic event, National Authorities may specify restrictions on the height or other characteristics of a structure depending on local seismicity, importance category, ground conditions, city planning and environmental planning.

Table 1.1: Importance classes for buildings (CEN 2004).

Importance class	Buildings
I	Buildings of minor importance for public safety, e.g. agricultural buildings, etc.
II	Ordinary buildings, not belonging in the other categories.
III	Buildings whose seismic resistance is of importance in view of the consequences associated with a collapse, e.g. schools, assembly halls, cultural institutions etc.
IV	Buildings whose integrity during earthquakes is of vital importance for civil protection, e.g. hospitals, fire stations, power plants, etc.

1.3.5 Capacity design

EC8 (CEN 2004) defines the capacity design method as a method in which elements of the structural system are chosen and suitably designed and detailed for energy dissipation under severe deformations, while all other structural elements are provided with sufficient strength so that the chosen means of energy dissipation can be maintained.

To illustrate the capacity design concept in a simple way, a ductile chain introduced by Paulay and Priestley (1992) shown in Figure 1.5 is used. The strength of the chain is assumed to equal the strength of the weakest link which is assumed to provide adequate ductility for the entire chain. The other stronger links are presumed to be brittle. Examples for capacity

design in buildings are to make columns stronger than beams in moment resisting frames and making beams and columns stronger than braces in concentrically braced frames.

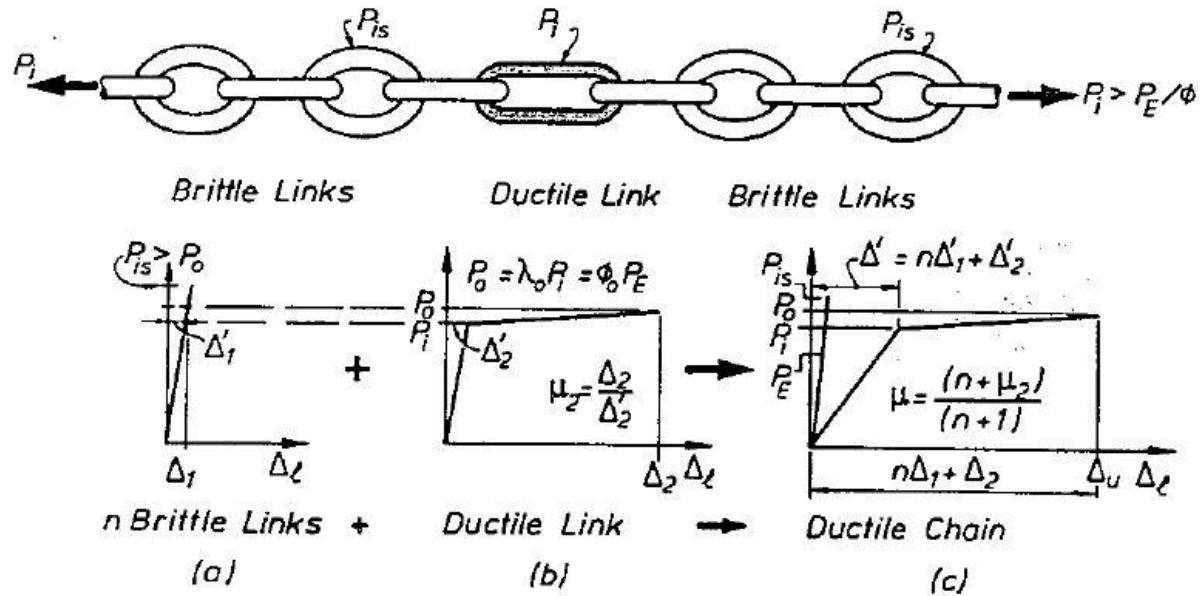


Figure 1.5: Principle of strength limitation illustrated with ductile chain (Paulay and Priestley 1992)

1.3.6 Structural material and types

According to EC8 (CEN 2004), the structure should have a capacity adequate to dissipate energy without substantial reduction of its overall resistance against horizontal and vertical loading. The requirements of both the ‘no-collapse’ and ‘damage limitation’ should be applied. In other words, adequate resistance of all structural elements shall be provided and non-linear deformation demands in critical regions should be proportionate with the overall ductility assumed in calculations.

Structural material and form used in buildings are influenced by many factors, such as relative cost, environment, locally available skills, functional and aesthetic considerations.

For concrete buildings, EC8 (CEN 2004) classifies them into one of the following structural types according to their behaviour under horizontal seismic actions:

- Frame systems.
- Dual systems (frame or wall equivalent).

- Ductile wall systems (coupled or uncoupled).
- Systems of large lightly reinforced walls.
- Inverted pendulum systems.
- Torsionally flexible systems.

For steel buildings, EC8 (CEN 2004) classifies them into one of the following structural types according to the behaviour of their primary resisting structure under horizontal seismic actions:

- Moment resisting frames, in which the horizontal forces are mainly resisted by members acting in an essentially flexural manner as shown in Figure 1.6. Energy is assumed to be dissipated by plastic hinges in beams and at the base of the bottom columns. All other columns are supposed to behave elastically (weak beams-strong columns).
- Frames with concentric bracings, in which the horizontal forces are mainly resisted by braces subjected to axial forces. Energy is assumed to be dissipated by tension diagonals only neglecting the compression diagonals for the configurations shown in Figure 1.7 and by both tension and compression diagonals for the V-bracings shown in Figure 1.8. EC8 (CEN 2004) does not allow K-bracings in which the intersection of the diagonals lies on a column as shown in Figure 1.9.
- Frames with eccentric bracings, in which the horizontal forces are mainly resisted by axially loaded members. Energy is assumed to be dissipated by seismic links by cyclic bending or cyclic shear as shown in Figure 1.10.
- Inverted pendulum structures, in which energy is assumed to be dissipated by plastic hinges located at the bases of columns as shown in Figure 1.11a, or at both ends of the columns as shown in Figure 1.11b.
- Structures with concrete cores or concrete walls, in which horizontal forces are mainly resisted by cores or walls as shown in Figure 1.12.

- Moment resisting frames combined with concentric bracings shown in Figure 1.13.
- Moment resisting frames combined with infill shown in Figure 1.14.

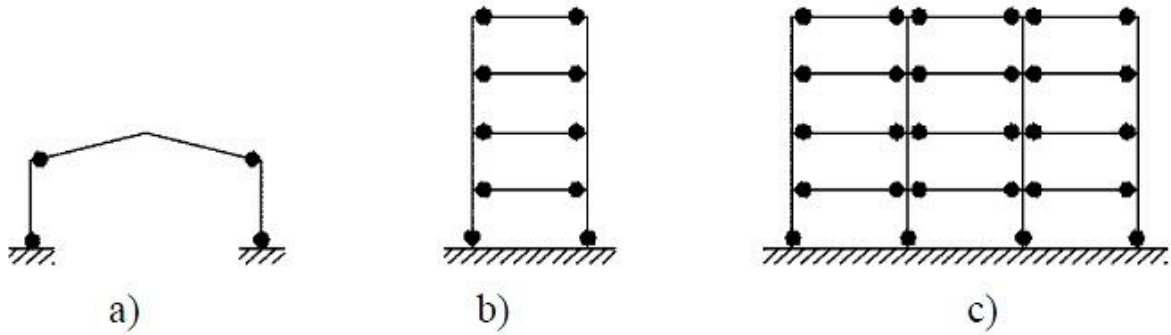


Figure 1.6: Moment resisting frames (dissipative zones in beams and at bottom of columns) (CEN 2004).

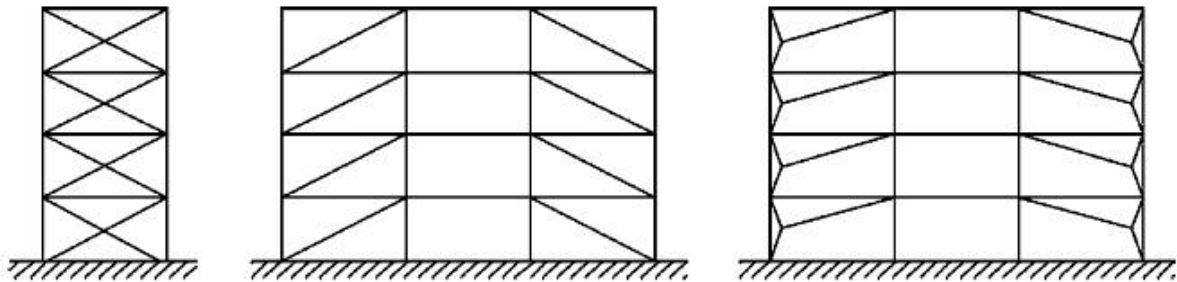


Figure 1.7: Frames with concentric diagonal bracings (dissipative zones in tension diagonals only) (CEN 2004).

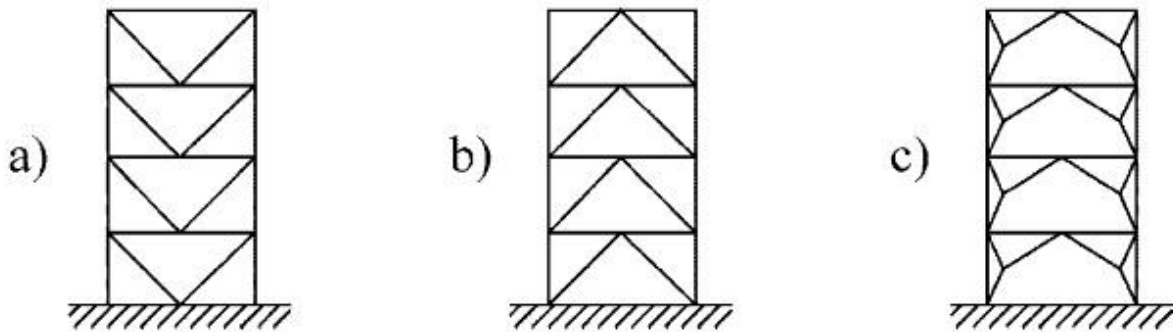


Figure 1.8: Frames with concentric V-bracings (dissipative zones in tension and compression diagonals) (CEN 2004).

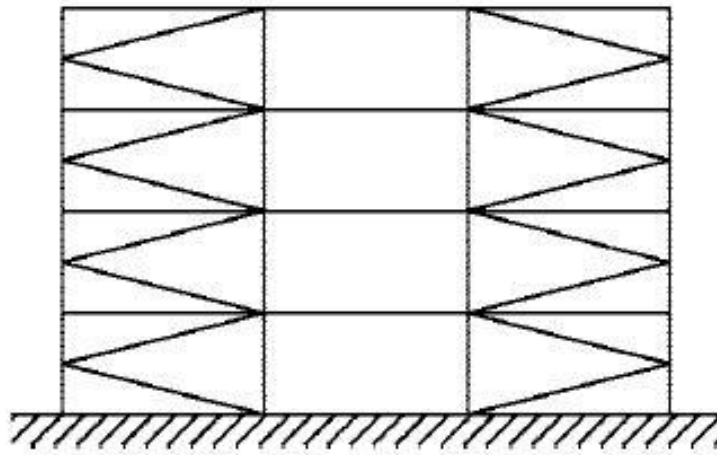


Figure 1.9: Frame with K bracings (not allowed in EC8 (CEN 2004)).

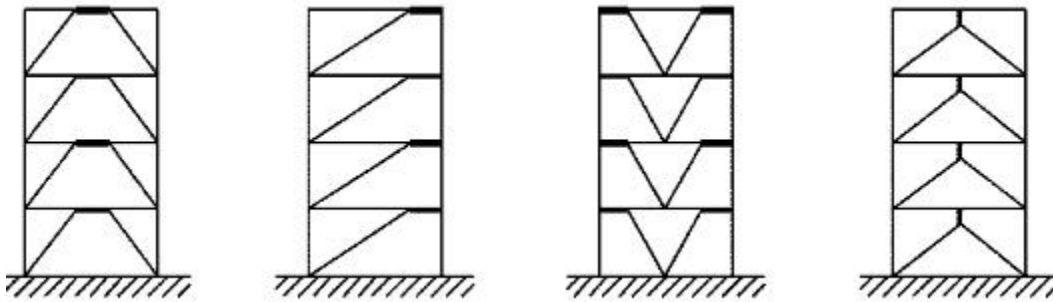


Figure 1.10: Frames with eccentric bracings (dissipative zones in bending or shear links) (CEN 2004).

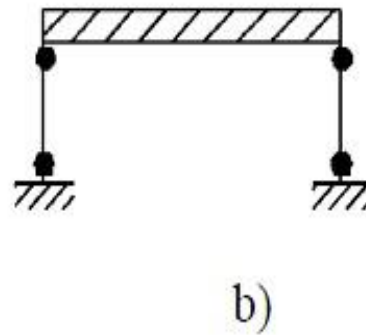


Figure 1.11: Inverted pendulum: a) dissipative zones at the column base; b) dissipative zones in columns (CEN 2004).

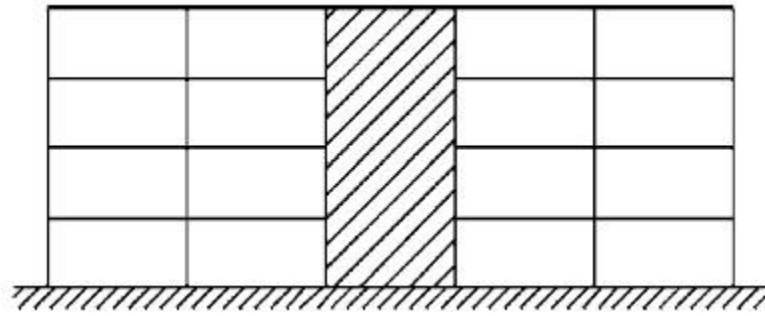


Figure 1.12: Structures with concrete cores or concrete walls(CEN 2004).

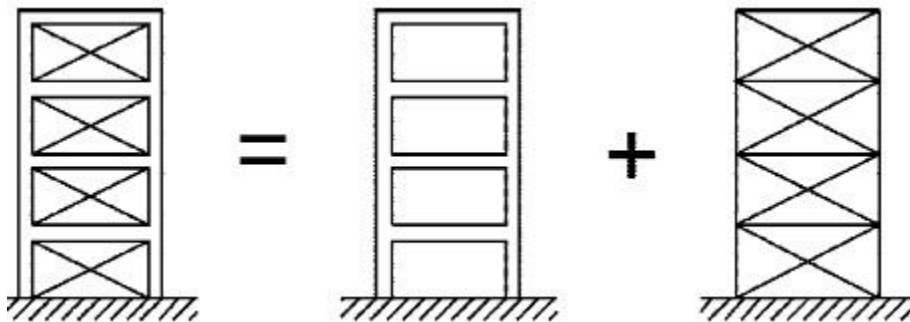


Figure 1.13: Moment resisting frame combined with concentric bracing (dissipative zones in moment frame and in tension diagonals) (CEN 2004).

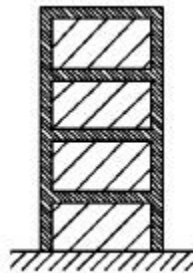


Figure 1.14: Moment resisting frame combined with infill (CEN 2004).

1.4 Current design philosophies

Two design philosophies exist in seismic design of structures. They are force based design (FBD) and direct displacement based design (DDBD). Current design procedures such as EC8 (CEN 2004) use FBD. Calvi and Sullivan (2009) published codified provisions for DDBD and work is on-going for extending the DDBD methodology. Each of these seismic design philosophies will be discussed in the following subsections.

1.4.1 Force based design (FBD) procedure

In FBD preliminary estimates of member sizes should be carried out at the start of the design in order to estimate the elastic stiffness needed to find the fundamental period using Equation [1.2]. Seismic codes use empirical expressions for the period based on a general description of the structural system and its geometry. EC8 (CEN 2004) approximates the period, T in seconds, for buildings with heights of up to 40 m by the following expression:

$$T = C_t H^{\frac{3}{4}} \quad [1.3]$$

where C_t is 0.085 for moment resistant space steel frames, 0.075 for moment resistant space concrete frames and for eccentrically braced steel frames and 0.050 for all other structures, H is the height of the building, in metres, from the foundation or from the top of a rigid basement.

To take into account the capacity of the structure to dissipate energy, FBD uses the design spectrum, S_d . This can be obtained by reducing the ordinates of the reference elastic spectrum, S_e , by means of a behaviour (reduction) factor, q , which allows for the ductility expected for the structural system. Seismic codes specify values for the behaviour factor, q , depending upon the material of construction and the type of structural system used. However, these values appear to be arbitrary and difficult to justify.

By finding the design spectrum, S_d , the design base shear can be found and distributed to the floors. Then the structure can be analysed under the lateral distributed seismic forces and the structural design of members that are meant to dissipate energy can be carried out and the displacements under the seismic actions can be estimated.

If the calculated displacements exceed the code limits, redesign is required. If the calculated displacements are satisfactory, the members that are not meant to dissipate energy and remain elastic can be designed using the capacity design methodology.

Priestley (1993; 2003) critically examined the force based seismic design procedure. He suggested that the current emphasis on strength-based seismic design, based on elastic structural characteristics, modified by behaviour factors leads designers in directions that are

not always rational. Some of the problems associated with force based design outlined by Priestley et al. (2007) are summarised as follows:

- Force based design relies on estimates of initial stiffness to determine the period and the distribution of design forces between different structural elements. Since the stiffness is dependent on the strength of the elements, this cannot be ascertained until the design process is complete.
- Allocating seismic force among elements based on initial stiffness (even if accurately known) is illogical for many structures, because it incorrectly assumes that the different elements can be forced to yield simultaneously.
- Force based design is based on the assumption that unique force reduction factors (based mainly on system ductility demand) are appropriate for a given structural type and material. However, ductility demand for individual structural members significantly differs from the system ductility depending upon geometry of the structure, flexibility of the capacity protected elements and foundation flexibility.

1.4.2 Direct displacement based design (DDBD)

As a result of the shortcoming of the force based design approach identified by Priestley (1993; 2003), Priestley et al. (2007) published a book on displacement based seismic design (DDBD) of structures in order to mitigate the deficiencies in current force based design. This has led to codified provisions for DDBD being published by Calvi and Sullivan (2009). The fundamental property of the DDBD is characterising the structure to be designed by a single degree of freedom (SDOF) model with a peak displacement response. This representation is based on the substitute structure approach carried out by Gulkan and Sozen (1974) and Shibata and Sozen (1976).

Figure 1.15 shows the basic formulation of the DDBD method, which applies to all type of structures. The methodology for the DDBD outlined by Priestley et al. (2007) is summarised in the following paragraphs:

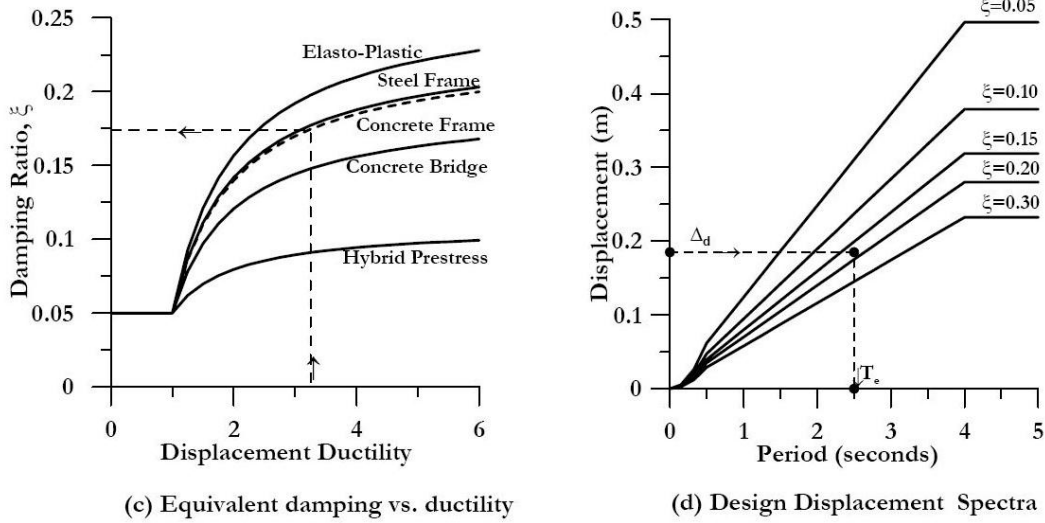
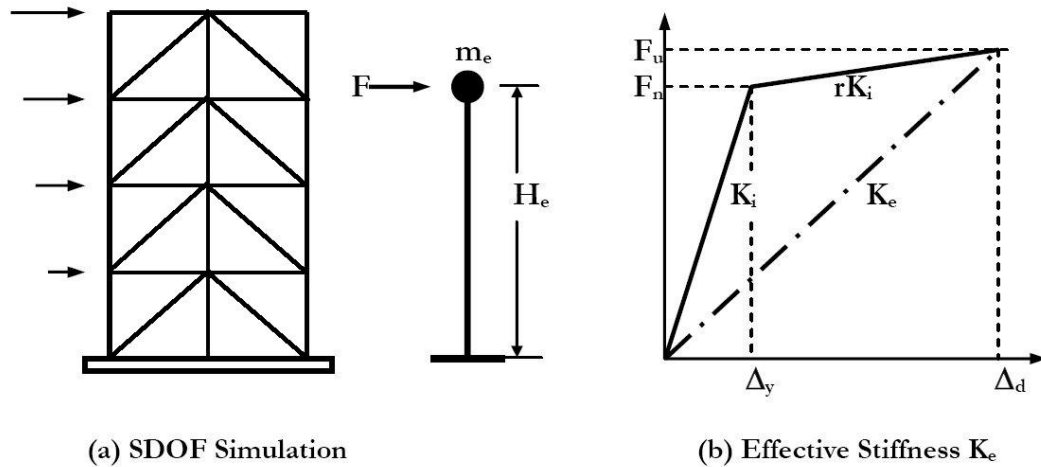


Figure 1.15: Fundamentals of DDBD adapted from (Priestley et al. 2007).

The direct displacement based design (DDBD) method characterises the structure to be designed by a single degree of freedom (SDOF) representation of performance at peak displacement response, as shown in Figure 1.15 (a).

While force-based seismic design characterises the structure in terms of elastic, pre-yield, properties (initial stiffness, K_i , elastic damping), direct displacement based design (DDBD) characterises the structure by the secant stiffness, K_e , at maximum displacement Δ_D , as shown in Figure 1.15 (b).

For a given level of ductility demand, DDBD characterises the structure with a level of equivalent viscous damping, ξ_{eq} , representative of the combined elastic damping and the hysteretic energy absorbed during inelastic response, as shown in Figure 1.15 (c).

After determining the design displacement at maximum response, and the corresponding damping estimated from the expected ductility demand, the effective period, T_e , at maximum displacement response, measured at the effective height, H_e , can be read from a set of displacement spectra for different levels of damping, as shown in Figure 1.15 (d). Then the effective stiffness, K_e , of the equivalent SDOF system at maximum displacement can be found and the design based shear can be estimated.

The research into the displacement based design of steel structures has focused on three types of steel structures: (i) steel moment resisting frame structures, (ii) steel frames incorporating buckling-restrained braces, and (iii) concentrically braced steel frames that utilise inverted V bracing (Calvi and Sullivan 2009). In this work, a DDBD procedure for CBFs with diagonal bracing system will be carried out. This DDBD methodology will be validated using physical full scale structural systems subjected to real earthquake loadings and robust numerical models.

1.5 Scope and objectives of the current research

The objective of the current work is to study the seismic design for concentrically braced frames and improve current design methodologies. The steps taken to achieve this goal are outlined in Figure 1.16 and can be summarised as follows:

- To create improved numerical models that can capture the salient performance features of structural steel hollow section members that are subjected to cyclic axial loading by calibrating, and later validating, the models using pseudo-static cyclic tests.
- To validate a fatigue model that simulates fracture to be used for structural steel hollow section bracing members in low cyclic fatigue applications.
- To employ the improved numerical model in non-linear time history analyses for single-storey concentrically braced frames (CBFs) subjected to earthquakes and prove

its applicability by comparing its predictions to measured performance of CBFs in shake table tests.

- Develop a direct displacement based design (DDBD) procedure for single-storey tension yielding CBFs and validate it using shake table tests and non-linear time history analyses.
- Develop a DDBD procedure for multi-storey tension yielding CBFs and validate it using non-linear time history analysis (NLTHA).

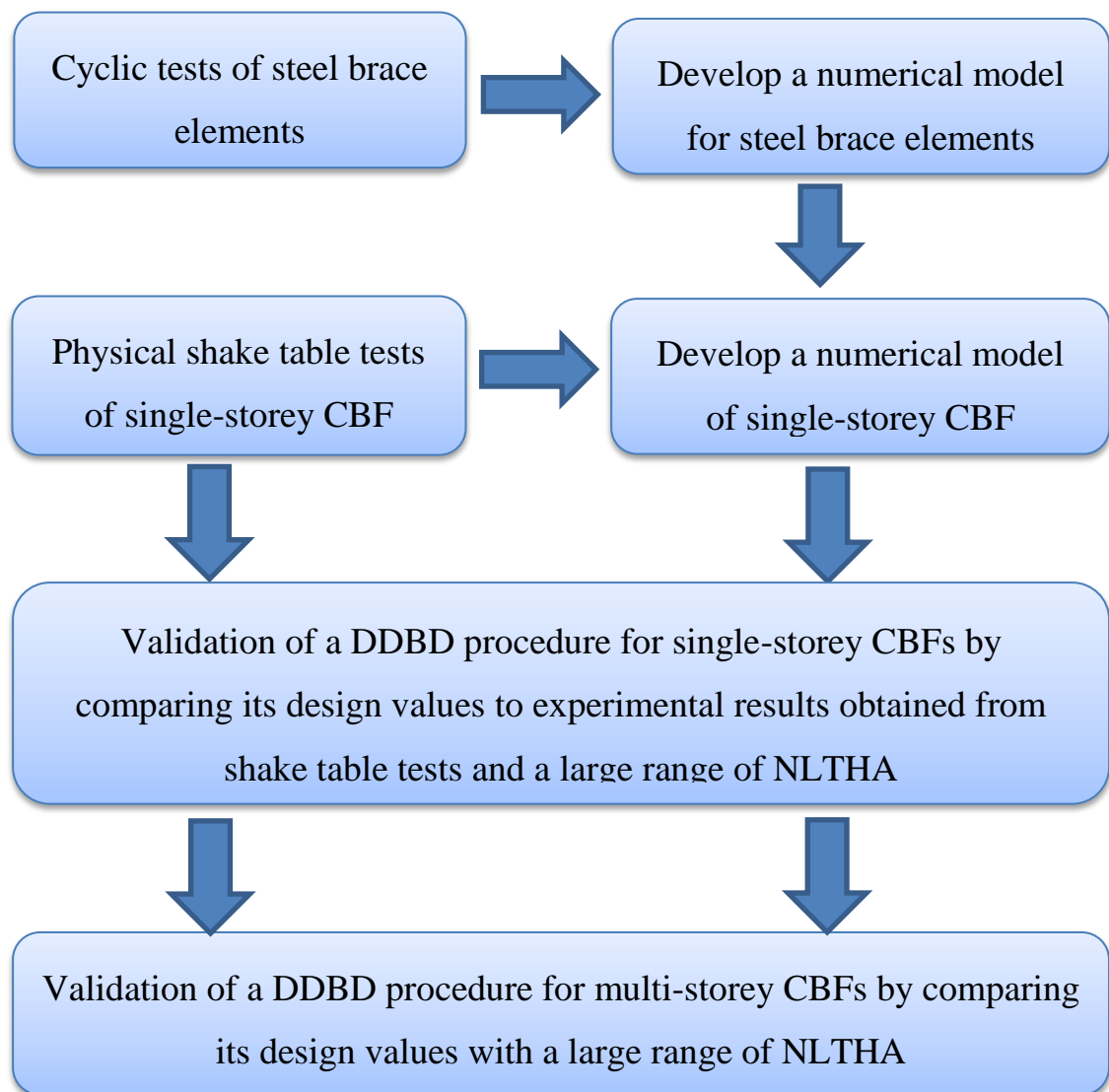


Figure 1.16: Flow chart of the primary objectives of the thesis.

1.6 Organisation of the thesis

The study of the seismic design for concentrically braced steel frames is discussed in the following chapters:

Chapter two gives an extensive literature review for concentrically braced frames (CBFs), where the performance of CBFs is assessed during past earthquakes, in laboratory experiments and through numerical models. A study of the behaviour of brace elements and CBFs during physical tests is carried out. Furthermore, a review of existing numerical models representing braces and CBFs is conducted, and a brief summary of current design philosophies is given.

In Chapter three, a study of the behaviour of cold-formed square and rectangular structural hollow section brace elements, which is the main element in CBF systems that dissipates energy during seismic actions, is carried out. A robust numerical model incorporating a fatigue model for braces is developed. A set of pseudo-static cyclic tests are used to calibrate the numerical model for braces, after which another independent set of pseudo-static cyclic tests are used to validate the model for cold-formed as well as hot-rolled steel square and rectangular hollow sections.

The spectrum compatible accelerograms are presented in Chapter four. They are scaled to have a displacement spectrum matching different displacement spectra and are used to verify the performance of CBFs.

Chapter five extends the numerical model developed in Chapter 3 to be used in a single storey CBF numerical model, which is employed in non-linear time history analyses (NLTHA). This numerical model is validated by comparing its predicted performance to that measured in full scale physical shake table tests. The sensitivity of the response parameters of the model to the characteristics of the earthquake inputs is determined by carrying out a large range of NLTHA that employ ground accelerograms that matches the displacement response spectra employed in the shake table tests.

In Chapter six, a direct displacement based design (DDBD) procedure for single degree of freedom (SDOF) CBFs is presented by using an appropriate equivalent viscous damping model specifically for CBFs. The performance of the DDBD methodology is verified by comparing its design values with experimental results obtained from shake table tests and a large range of NLTHA.

Chapter seven discusses the application of DDBD for multi-storey CBFs. The DDBD procedure is validated by comparing predictions from NLTHA of multi-storey CBFs to design values obtained from DDBD methodology. However, the research presented here does not develop or investigate guidelines for the capacity design of CBF systems.

A summary of the work undertaken during the current research programme is given in Chapter eight. This is followed by a series of conclusions and recommendations for future work in the area of numerically modelling and designing structural systems containing CBFs that are located in seismically active regions.

Chapter 2

Literature review

2.1 Introduction

Extensive research has been carried out on the behaviour of concentrically braced frames (CBFs) over the last two decades. Major concerns surfaced following the 1994 Northridge and the 1995 Hyogoken-Nabu earthquakes, where the lateral resistance systems that were most commonly employed before these events were steel moment resisting frames (MRFs). After the occurrence of these earthquakes, significant damages were found in a number of the MRFs. Specifically, this was due to failure in the beam-column connections, causing excessive economic losses in steel MRF buildings, as noted in the surveys conducted by Tremblay et al. (1995) and Nakashima et al. (1998). These damages and economic losses were the main reason for the increase in use of CBF systems in seismically active regions.

Advantages of CBF systems are that they are easy to design and construct, providing a relatively high stiffness that minimises drifts leading to less damage in the non-structural elements during earthquakes and also providing the high strength required to resist the lateral loads at a low cost. In CBFs, gravity loads are carried by beams and columns, while the lateral loads are resisted by brace elements through their inelastic behaviour. Beams and columns are designed to behave elastically. Inelastic behaviour is not commonly permitted in the beams and columns of CBF systems during earthquakes in

order to sustain their strength to carry the gravitational loads. To allow rotation and transfer of the lateral loads to the braces, simple beam-column connections are used.

The literature review presented in this chapter will cover the following subjects:

- Performance of CBF buildings in past earthquakes.
- Behaviour of brace elements and CBFs.
- Physical tests of brace members and CBFs.
- Numerical models representing braces and CBFs behaviour.
- Current design philosophies.

2.2 Performance of CBF buildings in past earthquakes

The study of the performances of buildings containing CBF systems in past earthquakes affords the opportunity to illustrate the behaviour of CBFs during seismic actions and illustrate problems associated with this type of lateral resistance system, focusing on typical detailing and proportioning details. Many researchers (for example, Tanaka et al. 1980; Oстераas and Krawinkler 1989; Ger et al. 1993; Tremblay et al. 1995; Tremblay et al. 1996; Nakashima et al. 1998; Kelly et al. 2000; Kitagawa and Hiraishi 2004; Bruneau et al. 2011) studied in detail the performance of many steel structures during earthquakes. Some examples of CBF structural behaviour during past earthquakes that were investigated by the aforementioned authors are discussed here.

Tanaka et al. (1980) carried out a survey for the 1978 Miyagiken-oki earthquake in Sendai city, where eight steel buildings were destroyed and 20 steel buildings leaned more than 1/30 in drift angle. Furthermore, dozens of steel buildings were subjected to damage for the following reasons:

1. Unbalanced arrangements of braces (see Figure 2.1) due to a lack of understanding of the effects of the nonlinear response of individual braces on the behaviour of the overall braced steel frame.

2. The strength of the effective area of the braces at the bolted parts of angles was insufficient to permit overall yielding.
3. The strength of the fasteners was too low.
4. The strength of the gusset plate was not sufficient to transfer ultimate loads from bracing members to the supporting framing members.

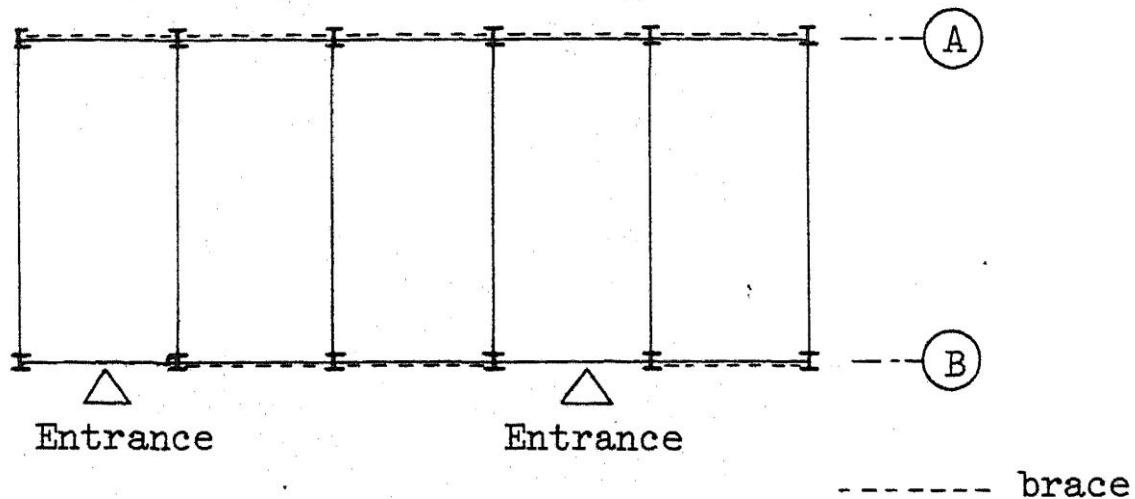


Figure 2.1: Unbalanced arrangement of braces in ground floor for a CBF building due to functional reasons (Tanaka et al. 1980).

Osteraas and Krawinkler (1989) and Ger et al. (1993) surveyed the performance of one of the most interesting steel buildings that collapsed in Mexico City after the 8.1 magnitude earthquake, which occurred in the coast of Lazaro Cardenas in September 19th 1985. The structure was called Pino Suarez complex. This complex consisted of five high-rise steel buildings in a line. That is, two identical 14 storey buildings were constructed at both ends and three identical 21 storey buildings were constructed in between, as shown in Figure 2.2. The structural design and details were the same for the five buildings. In the N-S direction, the lateral resistance system consisted of moment-resisting frames and two chevron concentric V-bracing frames. In the E-W direction the lateral resistance system consisted of moment-resisting frames and two concentric X-diagonal bracing frames. The configuration of the 21-storey buildings is shown in Figure 2.3

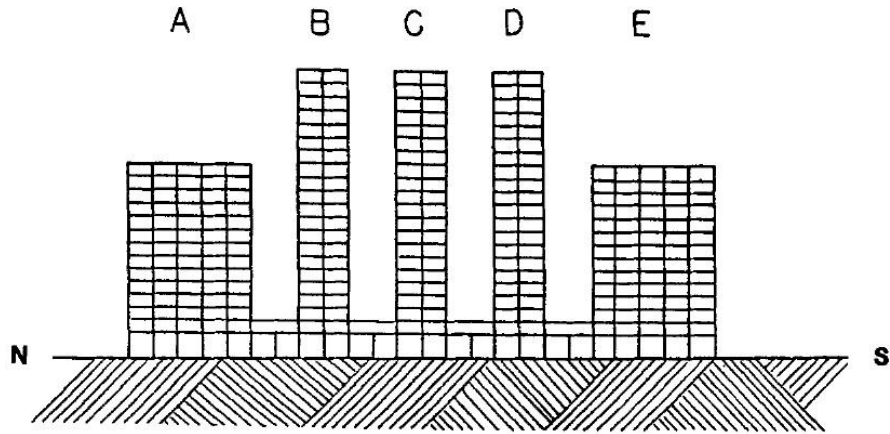


Figure 2.2: Pino Suarez complex (Ger et al. 1993).

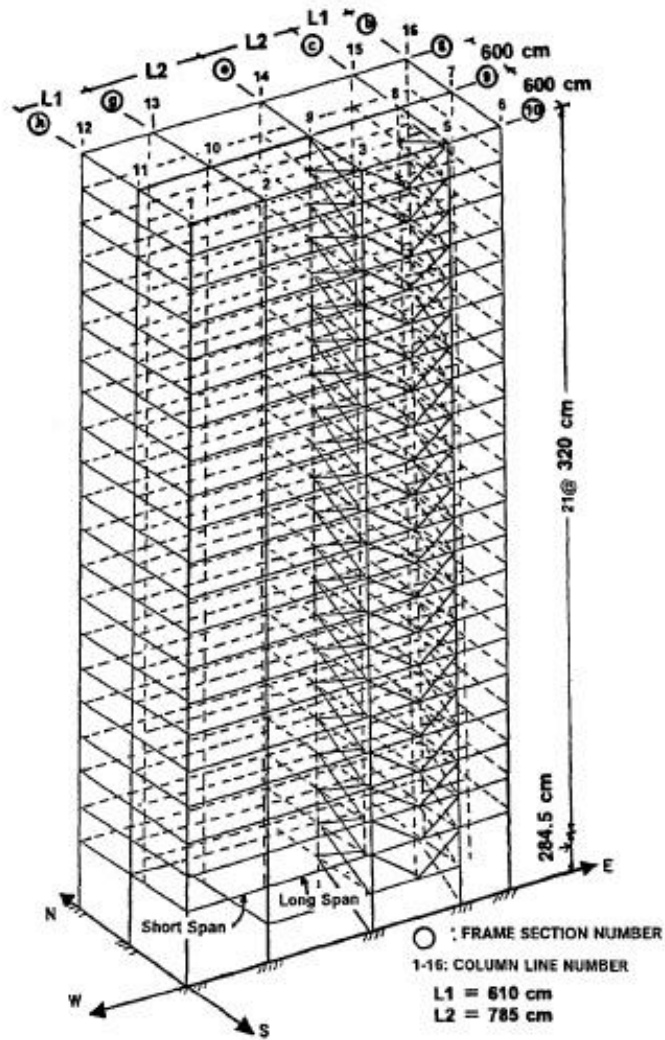


Figure 2.3: Configuration of Pino Suarez complex (Ger et al. 1993).

During the earthquake one of the 21-storey buildings (Building D) collapsed and fell on top of the adjacent 14-storey building (Building E), leading to its subsequent collapse, as shown in Figure 2.4. The remaining two 21-storey buildings (Buildings B and C) were severely damaged, with Building C close to collapse. Diagonal X-bracing members were spliced at their midspan and several locally-buckled columns were observed on the fourth floor to which large clamps were added after the earthquake to prevent collapse of Building C. Furthermore, many beams containing the chevron concentric V-bracings failed prematurely where they were not capable of withstanding forces from the braces.



Figure 2.4: Wreckage of the 21-storey steel-constructed building in the Pino Suarez apartment complex during Mexico City earthquake in September 19th 1985 (Encyclopædia Britannica 2010).

During the 1994 Northridge earthquake, which had a magnitude of 6.9, significant damage occurred to the Oviatt library serving the California State University, Northridge. The lateral resistance frames were CBFs added at the east and west ends. According to Tremblay et al. (1995), the inspection engineer indicated that the preliminary damage assessment of the structure indicated that the steel braced frames had managed to resist

the shaking caused by the earthquake with no noticeable damage. After removing the interior finishes, a brittle failure of the welded connection between the brace gusset plates and base plates was found, as well as fracture of the base plates themselves at the bottom of approximately 75% of the columns located within the braced bays. Anchor bolts used for these columns suffered inelastic elongation up to 12 mm and the bolt failed in tension in one case. The braced frame did not undergo inelastic action during the earthquake because the welds between the brace gusset plates and base plates failed, where the capacity of the welds was below the actual strength of the bracing members. This resulted in large drifts that may have caused the collapse of the overhanging roof, as shown in Figure 2.5.



Figure 2.5: Oviatt library building at the California State University at Northridge: failure of the overhanging roof. (California State University Northridge 1994)

Tremblay et al. (1995) and Kelly et al. (2000) described the damage that occurred in a four-storey office building located in the outskirts of Los Angeles after the occurrence of the 1994 Northridge earthquake. A global view of the building is shown in Figure 2.6.

CBFs were used as the lateral resisting system for this building. In each direction six bays of chevron-configured hollow square steel braces were used with a total of 12 braces in each direction for each storey. Following the earthquake, damage was observed at the second floor, where premature fracture of the hollow square section braces was initiated by local buckling of the thin walls. Fractures were located near the end connections and at the middle of the brace length, as shown in Figure 2.7. Some beams were twisted out-of-plane at beam midspan-brace connections and some brace end connections also failed.



Figure 2.6: Global view of the four storey Los Angeles building elevation that suffered damage during the 1994 Northridge earthquake (Kelly et al. 2000).



Figure 2.7: Brace fracture (Kelly et al. 2000).

Tremblay et al. (1996), Nakashima et al. (1998) and Kitagawa and Hiraishi (2004) presented an overview of damage to steel buildings observed from the 1995 Hyogo-ken-Nanbu earthquake in Kobe city, which had a magnitude of 7.2. CBFs mainly consisted of X-bracings and chevron bracing types with different bracing cross sections, such as rods, angles, flat plates, round tubes, square tubes, wide flanges and channels. An example of a damaged CBF building is shown in Figure 2.8. Damage to tension-only bracing members were found to be more severe in smaller cross-sections (rods, angles and flat plates), which generally were used more frequently in older buildings. Brace fracture and fracture of connections where bolt holes were located decreased the lateral load resistance of frames. This caused large inter-storey drifts and induced total collapse of the frame in some cases. Damage to braces with larger cross-sections was concentrated mostly in their connections with adjoining beams or columns. Fracture occurred to bolted brace-to-gusset connections at net area. In other instances, low cyclic fatigue fracture of brace members was observed at plastic hinge locations after the occurrence of local buckling. For chevron configurations, some beams connected to a pair of braces sustained significant web-plate buckling and out-of-plane distortion. In general, damage to braces having large cross-sections was strongly correlated with the connection details, with poor connection details suffering more severe damage.



Figure 2.8: CBF building with fracture of bracing members during 1995 Hyogo-ken-Nanbu earthquake (Kitagawa and Hiraishi 2004).

Bruneau et al. (2011) carried out a field study of selected steel structures in Christchurch after a 6.3 magnitude earthquake occurred in February 22, 2011. In general, they noticed that most of steel structures performed relatively well during this earthquake and reported some damage that occurred in selected steel buildings. A single suspended level parking garage using concentrically braced frames (CBFs) as a lateral resistance system was found to perform poorly. On one side, a failure of welds between a brace and a column occurred under tension loads (see Figure 2.9). These welds did not appear to be designed according to the capacity design principles to sustain the tension capacity of the brace.

The CBF at the other side performed better, without fractures. However, a visible post-earthquake residual buckling was found in a brace as a consequence of brace elongation, as shown in Figure 2.10.



Figure 2.9: Fracture of the welds between a brace and a column in a parking garage building after Christchurch earthquake occurred in February 22, 2011 (Bruneau et al. 2011).

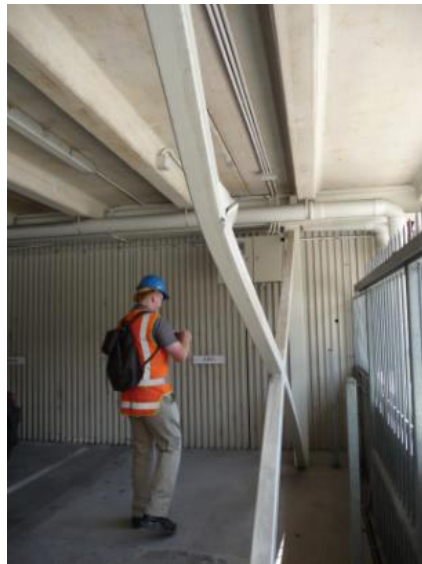


Figure 2.10: Residual buckling due brace elongation in a parking garage building after Christchurch earthquake occurred in February 22, 2011 (Bruneau et al. 2011).

A summary of the observed damage of selected CBF structures during seismic action is given in Table 2.1. In general, the main types of failure patterns observed during previous earthquakes for CBF buildings are (i) fracture of the braces at their ends or mid-length due to low cyclic fatigue and after the occurrence of local buckling, (ii) insufficient strength of the braces at the bolted parts to permit overall yielding, (iii) fracture of bolts and welding at connections between braces and other structural members, (iv) insufficient strength of the gusset plate to transfer ultimate loads from bracing members to the supporting framing members, (v) unbalanced arrangement of braces causing concentration of forces and failures in the weak side and (vi) failure of beams and columns that were not designed to have adequate capacity. In many of these failures, large residual inter-storey drifts were observed, sometimes resulting in the collapse of the building.

2.3 Hysteretic behaviour of brace elements

Brace members in CBFs are the main elements to dissipate energy during seismic actions. They dissipate energy in lateral force resisting systems, while resisting axial forces induced from seismic actions, through yielding in tension and buckling in compression. The hysteretic behaviour of a brace element with pinned end conditions is shown in Figure 2.11, where the brace behaviour is described by the hysteretic response of applied axial load (P) plotted against resulting axial deflection (δ). The area under the P - δ curve indicates the amount of hysteretic energy the member dissipates. Figure 2.11 shows the stages the brace experiences during cyclic loading. From Point O to Point A, the brace is compressed (shortened) elastically. Buckling is assumed to occur at Point A. If the brace is sufficiently slender, the brace may buckle elastically, where P equals the Euler (elastic) buckling load C_r , in which the applied axial load may be sustained as the brace deflects laterally. The buckling stage is shown from Point A to Point B. From Point B to Point C, the plastic hinge rotation stage in compression occurs and the brace capacity falls. From Point C to Point D, elastic elongation in compression unloading and subsequently in tension occurs. From Point D to Point E, the plastic hinge rotation stage in tension occurs

Table 2.1: Summary of observed damage of selected CBF structures during seismic actions

CBF structure	Earthquake	Location	M	Structural damage	References
Different buildings	1978 Miyagiken-oki earthquake	Sendai city-Japan	7.4	<ul style="list-style-type: none"> - Failure of connections joining braces together or braces to frame elements. - Failures of some buildings due to unbalanced arrangement of braces. 	(Tanaka et al. 1980)
Pino Suarez complex	1985 coast of Lazaro Cardenas earthquake	Mexico City	8.1	<ul style="list-style-type: none"> - Collapse of 21-storey buildings and fell on top of the adjacent 14-storey building. - Diagonal X-bracing members were spliced at their midspan. - Several columns buckled locally. - Many beams containing the chevron concentric V-bracings failed. 	(Osteraas and Krawinkler 1989) and (Ger et al. 1993)
Oviatt Library	1994 Northridge earthquake	Northridge	6.9	<ul style="list-style-type: none"> - Failure of the welded connection between brace gusset plates and base plates. - Fracture of base plates. - Yielding of anchor bolts. 	(Tremblay et al. 1995)
Four-story office building	1994 Northridge earthquake	Northridge	6.9	<ul style="list-style-type: none"> - Fracture of brace members. - Beams were twisted out-of-plane at beam midspan-brace connections. - Failure of end connections of braces. 	(Tremblay et al. 1995) and (Kelly et al. 2000)
Different buildings	1995 Hyogo-ken-Nanbu earthquake	Kobe city - Japan	7.2	<ul style="list-style-type: none"> - Premature fracture of small cross section braces. - Fracture to bolted brace to gusset connection at net area. - Failure of connections of braces with adjoining beams or columns. - Low cyclic fatigue fracture of braces at plastic hinge locations after the occurrence of local buckling. 	(Tremblay et al. 1996) (Nakashima et al. 1998) and (Kitagawa and Hiraishi 2004)
A parking garage	2011 Christchurch earthquake	Christchurch	6.3	<ul style="list-style-type: none"> - Failure of welds between a brace and a column. - Post-earthquake residual buckling was found in a brace. 	(Bruneau et al. 2011)

where the moments on the hinge are reversed and the element gradually deforms to its straight position and the lateral deflection is recovered. From Point E to Point F, plastic elongation occurs, where the tensile capacity of the brace is achieved and maintained. In subsequent cycles of the same or lower displacement demand, residual lateral deformations will occur. However, these lateral residual deformations are eliminated after the displacement demand of the previous cycle in tension is exceeded and up until the moment of load reversal. From Point F to Point G, the elastic shortening stage in tension unloading and compression occurs. The compression buckling capacity of the brace occurs at point G. This buckling capacity is reduced due to the residual lateral displacement and the Baushinger effect. It is known as the residual buckling capacity of the brace, C_r' .

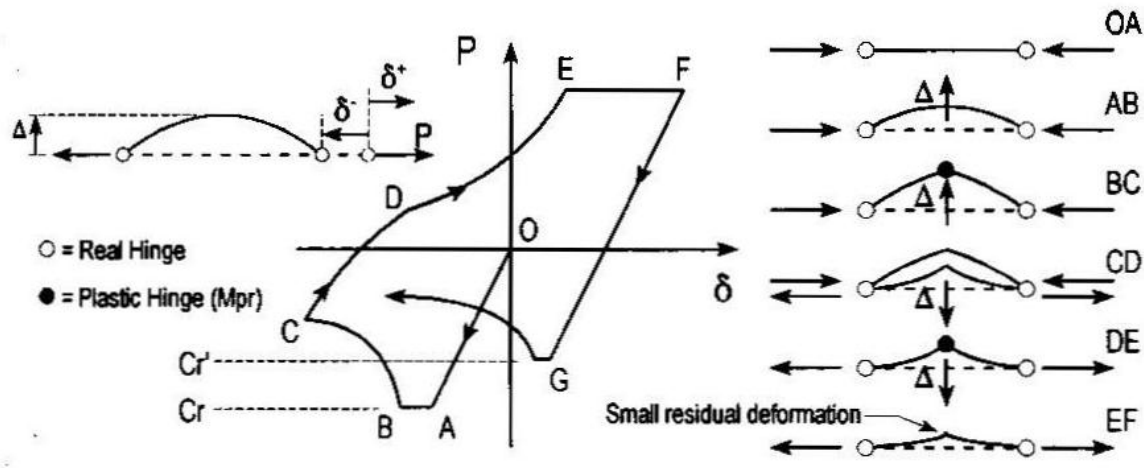


Figure 2.11: Hysteretic behaviour of a brace member (Bruneau et al. 1998).

The cyclic response of braces depends principally upon its effective slenderness ratio, $\lambda = KL/i$, where K is the effective length factor, L is the overall specimen length and i is the radius of gyration about the relevant axis. EC3 (CEN 2005) specifies a non-dimensional slenderness ratio, $\bar{\lambda}$, as the following

$$\bar{\lambda} = \frac{KL}{i} \sqrt{\frac{f_y}{\pi^2 E}} = \frac{\lambda}{\lambda_1} \quad [2.1]$$

where f_y is the yield strength, E is the Young's modulus and λ_1 is 93.9ε , where $\varepsilon = \sqrt{235/f_y}$. Concentric braces are often described as either slender (large $\bar{\lambda}$), intermediate, or stocky (small $\bar{\lambda}$). The hysteretic behaviour of braces with different slenderness ratios varies significantly. The area under the P- δ curve indicating the energy dissipated is greater for stocky members than for slender members. The ratio of the capacity of the brace in tension to that in compression is dependent on its slenderness ratio. The more slender the brace the larger the ratio (Bruneau et al. 1998).

Bruneau et al. (1998) proposed for braces with Grade S235 steel to be stocky if it has an effective slenderness ratio less than or equal to 60 (equivalent to normalised slenderness ratio, $\bar{\lambda}$, of 0.64), slender if it is more than or equal to 130 ($\bar{\lambda} = 1.38$) and intermediate if it is between these values. For Grade S355 steel, the lower and upper limits of effective slenderness ratios are 50 and 110, respectively ($0.65 \leq \bar{\lambda} \leq 1.44$). Bruneau et al. (1998) defined slender braces as those braces for which the elastic buckling stress is less than or equal to half of the yield stress, f_y . They defined stocky braces as those braces for which yielding and local buckling dominate the response and for the intermediate braces they proposed that local buckling phenomena are less critical than inelastic buckling, which is the same as the observation of Khatib et al. (1988).

2.3.1 Physical tests of brace members

Results of some cyclic tests conducted by many researchers on brace members are summarised in the following paragraphs. These tests provide experimental data that can help in formulating provisions in design codes for brace members, such as slenderness ratio, section shapes, material properties, end conditions and overstrength ratios.

Additionally, these tests are useful for mathematical modelling of hysteretic behaviour of braces under cyclic loading.

Kahn and Hanson (1976) tested 16 hot-rolled small steel bars with rectangular cross section of 25.4X12.7 mm and effective member slenderness ratios, KL/i , ranging from 85 to 210. Axial loading regimes were applied cyclically to these bars at both dynamic and quasi-static rates. It was found that the maximum compressive load reduced progressively

with increasing number of cycles and the maximum reduction was between the first and second cycles. All specimens suffered from a net elongation after a complete cycle of deformation. The dynamic and static loading cases produced hysteretic behaviour of the bars with no appreciable difference for all the specimens with a given effective slenderness ratio.

Jain et al. (1977; 1978; 1980) carried out a series of cyclic tests on small tubes with square sections, angles and rectangular bar specimens. The square tubes were cold formed with dimension of 25X25X2.67 mm with effective member slenderness ratios, KL/i , ranging from 30 to 140. The angle sections were hot-rolled single angles of sizes ranging from 25X25X6 mm to 40X40X3 mm with effective slenderness ratios, KL/i , ranging from 85 to 120. The most important parameter that influenced the hysteretic behaviour of the specimens was found to be the effective member slenderness ratio, KL/i , similar to the observation of Kahn and Hanson (1976); they found that the maximum compressive load decreased with each successive cycle of load. They concluded that differences in the hysteresis loop characteristics of different section types can be attributed to the shape of the cross section, heat treatment, strain hardening, residual stresses, Bauschinger effect, wall thickness, and local buckling.

Black et al. (1980) and Popov and Black (1981) carried out twenty four tests on specimens with different effective member slenderness ratios, KL/i , which ranged from 40 to 120, different cross section shapes (wide flange, structural T, thick and thin walled circular pipe and tube sections, and built-up double angle and double channel sections), and different boundary conditions to study the inelastic behaviour of members used as struts. The main finding from these tests was that the member slenderness ratio is the main parameter that influences the inelastic behaviour of the specimens for any cross sectional shape and that cyclic loading reduces the buckling strength of braces, proving the observations of Kahn and Hanson (1976) and Jain et al. (1977; 1978; 1980). They found that the end conditions of the specimen had a minor effect on the hysteresis loop for the same KL/i ratio. Although the experimental results focused more on compressive strength degradation rather than on fracture events, an important finding was that the

braces with larger width to thickness ratios experienced local buckling faster than braces with smaller width to thickness ratios. Thus, these studies gave an indication of the importance of width-to-thickness ratio as a parameter affecting fracture life.

Gugerli and Goel (1982) tested a series of wide-flange shapes and structural tubes with different member slenderness, KL/i , ranging from 95 to 175, under cyclic loading. They found that the effective member slenderness ratio, which is the most important parameter for determining the shape of axial load-displacement hysteresis loops, was found to also affect the fracture life. They found that the hysteresis loops of both section types were similar, but that fracture was more critical than local buckling in limiting the resistance and energy dissipating capacity of braces. Additionally, they found in their experiments that the fracture life of members with wide flanges was greater than that of tubes and that ductility was improved with increasing member slenderness and decreasing width to thickness ratio. Similar observations were found in the results of experimental tests carried out by Popov and Black (1981).

Astaneh-Asl and Goel (1984) and Astaneh-Asl et al. (1985) carried out 17 cyclic tests on a series of double angle specimens to investigate the effectiveness of gusset plates in restraining the double angle braces. The effective slenderness ratios, KL/i , of the specimens ranged from 44 to 186. The angles were connected together with welded or bolted stitches along the length and were connected to end gusset plates with bolts or fillet welds. Some specimens were designed to buckle in-plane and others out-of-plane. The direction of buckling had a significant influence on the cyclic behaviour and the failure mode. The in-plane buckling specimens behaved as fixed-ended columns. Plastic hinges formed in the braces at midspan and at their connections with the gusset plates. The out-of-plane buckling specimens behaved as pin-ended columns. Plastic hinges formed at midspan in the braces and in the gusset plates. They proposed better detailing specifications for the gusset plates to avoid local buckling and fracture, providing an adequate free length of gusset plate to allow for the formation of the plastic hinge and to improve the ductility of the gusset, and improved stitching details for built-up members.

Tang and Goel (1989) studied six cyclic tests on brace specimens with slenderness ratio, KL/i , ranging from 60 to 79. They found that fracture ductility is controlled by a combination of effective member slenderness ratios and width to thickness ratios. They also documented that increasing member slenderness ratios have beneficial effects on brace member performance, which is similar to the observation of Gugerli and Goel (1982).

Walpole (1995) carried out three cyclic tests on cold-formed 150X100X6 mm rectangular hollow steel sections. The effective member slenderness ratios were 40, 60, and 80. He found that stockier members exhibited larger hysteretic loops. The specimens formed a local buckle relatively quickly in the plastic hinge at mid-span and the corners of the section and fracture followed. Local buckling was more significant with the less slender specimen. He recommended more attention should be given to width to thickness ratio for cold-formed sections in high seismic zones where high ductility is required.

Remennikov and Walpole (1998) found that the post-buckling compression capacity of steel bracing members can vary between 20% and 100% of that in the first cycle depending upon the effective slenderness ratio of the brace. This reduction increases as the brace slenderness ratio increases. Results were checked by tests on tube, universal column (UC) and cold-formed rectangular hollow sections, with effective slenderness ratios, KL/i , ranging from 30 to 110, carried out by several researchers (Wakabayashi et al. 1977; Jain and Goel 1979; Shibata and Wakabayashi 1984; Walpole 1995; Walpole and Leowardi 1995).

Tremblay (2002) carried out a review of 76 cyclic loading tests on bracing members from nine different test programmes. Different brace section type, cross sectional area, end conditions, effective slenderness ratio, material properties and several displacement histories were used. Normalised slenderness ratios, $\bar{\lambda}$, ranged from 0.5 to 2.1, which is approximately equivalent to effective slenderness ratio, KL/i , ranged from 38 to 160.

Tremblay (2002) found that fracture of rectangular hollow section bracing members depends primarily upon the slenderness ratio of the bracing members and, to a lesser extent, on the width-to-thickness ratio of the cross-section and the imposed displacement

history. He found that the strain demand in the plastic hinge reduces with the brace slenderness causing slender braces to sustain higher ductility levels prior to fracture, as shown in Figure 2.12. He proposed a simple approach in which the total ductility reached at fracture, μ_f , is related only to the normalised slenderness parameter, $\bar{\lambda}$, and is given by:

$$\mu_f = 2.4 + 8.3\bar{\lambda} \quad [2.2]$$

where μ_f is the sum of the peak ductility reached in tension and the peak ductility attained in compression in any cycle before the half-cycle in tension in which failure of the brace is observed, as shown in Figure 2.13. The convenience of this approach for design is that only the maximum expected ductility needs to be known, not the complete time history. The effects of width-to-thickness ratio were more pronounced for less slender braces. Short braces with higher width-to-thickness ratio experienced more severe local buckling at large deformation, resulting in a larger reduction in the flexural capacity at the plastic hinge and, therefore, in a more significant loss in compression strength. All tests were of the quasi-static-cyclic type and possible strain rate effects on the brace compressive and tensile resistance could not be assessed.

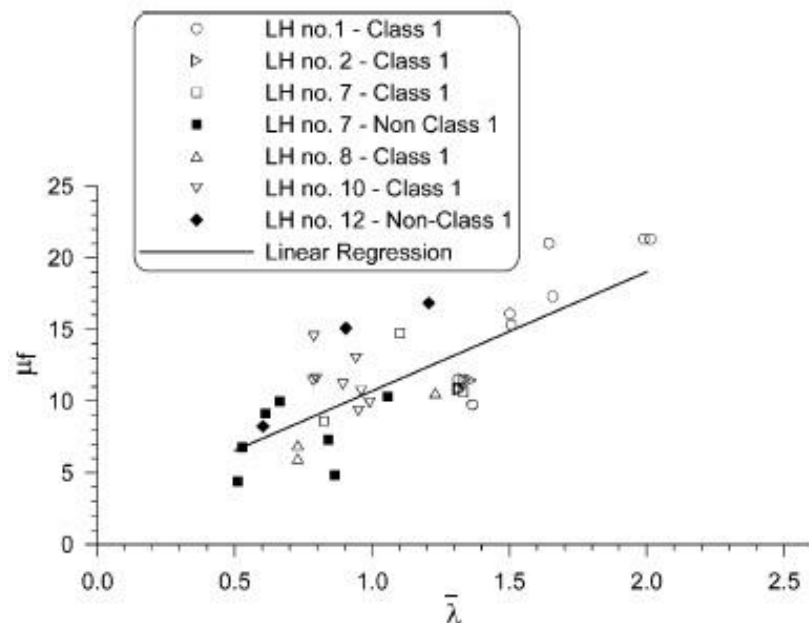


Figure 2.12: Normalised slenderness ratio vs. total ductility reached at fracture (Tremblay 2002).

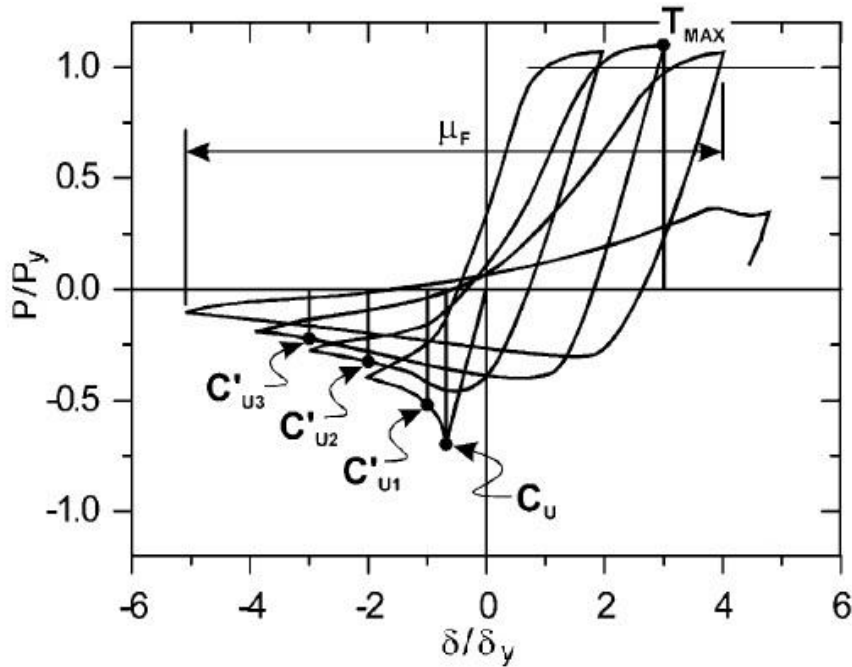


Figure 2.13: Definition of brace response parameters showing the total ductility reached at fracture, μ_F , (Tremblay 2002).

Tremblay (2002) studied the post-buckling resistance, C_r' , under compression load that a brace can sustain at a peak ductility level. Such a brace has been elongated in tension to the specified ductility level and, therefore, has larger lateral deformation and lower strength when loaded subsequently in compression for this ductility level. Three ductility levels of 2, 3, and 5 were selected. The value of C_r' for the three ductility levels is expressed with the following nonlinear regression equation

$$C_r' = A_g F_y (a + b \bar{\lambda}^{-c}) \leq C_r \quad [2.3]$$

where C_r' is the reduced buckling capacity, A_g is the cross sectional area, F_y is the yield stress of the brace, $\bar{\lambda}$ is the normalised slenderness ratio, C_r is the first buckling load of the brace member and a , b , and c are constants. Table 2.2 gives, for each ductility level, the number of data points considered, n , the values of the parameters a , b , and c for the mean-value function and the conditional standard deviation assuming the variance is constant within the range of the test data.

Table 2.2: Nonlinear regression of the post-buckling compression resistance of the braces (Tremblay 2002).

Ductility level	n	a	b	c	Conditional standard deviation
2	39	0.058	0.23	1.4	0.07
3	37	0.084	0.12	1.61	0.06
5	42	0.095	0.046	2.22	0.036

Shaback and Brown (2003) investigated the hysteretic behaviour of nine various sized square hollow structural steel sections with effective slenderness ratios, KL/i , ranging from 52 to 66. They found that the fracture life of the square hollow section brace is affected mainly by the width to thickness ratio of the section brace walls, and that the effective slenderness ratio, KL/i , has a less significant effect on the fracture life, but was the most important parameter influencing the hysteretic behaviour of the specimens tested. This is in contrast to the observations of Tremblay (2002). This is because most of the test specimens of Shaback and Brown (2003) are stocky with low member slenderness ratios. However, the more slender specimens experience less severe local buckling as found by many researchers, such as Gugerli and Goel (1982) and Tang and Goel (1989).

Lee and Bruneau (2005) collected and reviewed experimental data of cyclic tests on brace specimens, carried out by several researchers, to quantify the energy dissipation of braces in compression and loss of compression strength at various magnitudes of compressive axial displacements. The effective slenderness ratios, KL/i , for the specimens ranged from 25 to 189. They found that bracing members with hollow cross-section suffered less degradation of compressive strength and normalised energy dissipation in compression at a given level of normalised inelastic displacements compared to other cross sections, such as W-shape, double angles back-to-back, angles, and structural tees. However, it was recognised that structural hollow sections with large width-to-thickness ratios are sensitive to fracture due to cyclic local buckling.

Goggins et al. (2006) investigated the behaviour of cold-formed square and rectangular hollow steel bracing members when subjected to pseudo static cyclic axial loading. The normalised slenderness ratios, $\bar{\lambda}$, used were between 0.4 to 3.2, which is equivalent to effective slenderness ratio between 38 and 300. They found that the ductility capacity of the cyclically loaded specimens was affected by yield strength, member slenderness and to a lesser extent section width-to-thickness ratio. Similar observations were found by Tremblay (2002). Goggins et al. (2006) advanced Equation [2.2] with their test data and developed new relationships expressing the displacement ductility, μ_f , in terms of global slenderness, $\bar{\lambda}$, and width to thickness ratio (b/t) as the following:

$$\mu_f = -0.68 + 26.2\bar{\lambda} \quad [2.4]$$

$$\mu_f = 29.1 - 1.07(b/t) \quad [2.5]$$

The tests of Goggins et al. (2006) will be discussed in more detail in Chapter 3 and will be used in this work to develop a numerical model that represents the behaviour of brace elements under cyclic loading.

Fell et al. (2009) carried out 18 cyclic tests on steel bracing members, including square hollow sections, pipes, and wide-flange sections, with different width to thickness ratios and effective slenderness ratios ranging from 63 to 153, to study their inelastic buckling and fracture behaviour. They found that loading history, width to thickness ratio and member slenderness ratio have the largest influence on brace ductility. Effects of loading rate were found to be insignificant. Similar to Shaback and Brown (2003), they found that brace fracture ductility is a function of section compactness and to a lesser extent member slenderness and loading history. In particular, they found that the tendency for local buckling and fracture initiation increases with increasing width–thickness ratios, resulting in reduced drift capacity at fracture. They found that fracture ductility increases slightly with increasing member effective slenderness ratios. The brace buckling is more elastic as the slenderness ratio increases, and the smaller cross-section dimensions relative to the brace length lead to smaller strain demands at the central plastic hinge. Additionally, the standard loading protocols were found to be more damaging than loading protocols developed to represent pulse-like near-field ground motions. In contrast to the findings of

Gugerli and Goel (1982), they found that local buckling in hollow square sections was more severe than other sectional shapes, leading to fracture initiation near the corners of the braces. On the other hand, pipe and wide-flange sections exhibited more gradual local buckling modes which delayed fracture initiation.

Nip et al. (2010) carried out cyclic axial tests on 16 square and rectangular hollow section members of three materials: hot-rolled carbon steel, cold-formed carbon steel and cold-formed stainless steel. Normalised member slenderness ratios of these members were between 0.34 and 1.4, equivalent to effective slenderness ratios between 32 and 131. After applying the cyclic tests, the cold-formed stainless steel members were found to be capable of sustaining more cycles of loading than both cold-formed and hot-rolled carbon steel members, especially for stocky (low width to thickness ratio) sections and members with high global slenderness. Hot-rolled carbon steel and cold-formed stainless steel specimens were more ductile than cold-formed carbon steel specimens, particularly for high global slenderness and low local slenderness. Stainless steel specimens exhibit higher tensile and compressive resistances than the carbon steel specimens. However, the areas under the hysteretic loops of specimens at the same amplitude of loading of the three materials were found to be relatively similar. Nip et al. (2010) proposed predictive expressions for the displacement ductility with different expression for each material as follows:

Hot-rolled carbon steel:

$$\mu_f = 3.69 + 6.97\bar{\lambda} - 0.05(b/t\varepsilon) - 0.19(\bar{\lambda})(b/t\varepsilon) \quad [2.6]$$

Cold-formed carbon steel:

$$\mu_f = 6.45 + 2.28\bar{\lambda} - 0.11(b/t\varepsilon) - 0.06(\bar{\lambda})(b/t\varepsilon) \quad [2.7]$$

Cold-formed stainless steel:

$$\mu_f = -3.42 + 19.86\bar{\lambda} + 0.21(b/t\varepsilon) - 0.64(\bar{\lambda})(b/t\varepsilon) \quad [2.8]$$

where $\bar{\lambda}$ is the normalised slenderness ratio, b is the width of the wider face of the section, t is the thickness of the section and $\varepsilon = \sqrt{235/f_y}$ where f_y is the yield strength.

Physical tests carried out by Nip et al. (2010) will be used to validate the numerical model used in this work for brace members.

2.3.2 Numerical models for brace members

Many numerical models have been developed and used to predict the cyclic behaviour of brace members. These models can be classified into one of the following categories: a) Phenomenological models. b) Physical theory models. c) Finite element models. (Ikeda and Mahin 1986). They are categorised as either macro-models or micro-models according to their resolution in modelling the nonlinear behaviour of beam-column elements. Macro-models emphasise generalised stress versus generalised strain behaviour. Micro-models emphasise pointwise stress versus strain response. As a result, macro-models are more computationally efficient than micro-models and form the basis of most large-scale analyses of two- and three-dimensional frames (Jin and El-Tawil 2003). Phenomenological and physical theory models are characterised as macro-models, while finite element models are characterised as micro-models.

2.3.2.1 Phenomenological models

Phenomenological models, which are normally truss or spring element models, are used to represent the brace element hysteretic behaviour by many researchers (for example, Jain et al. (1980), Maison and Popov (1980), Zayas et al. (1980), Khatib et al. (1988), Andreaus and Gaudenzi (1989), Sabelli (2001), McCormick et al. (2007)). These models are governed by a set of parameters and empirical rules derived from real experimental data to replicate the hysteretic behaviour of brace elements. The advantages are their simplicity and computational efficiency. However, models are restricted in use to conditions similar to those from which the rules and parameters were derived and they are difficult to generalise to different materials, cross-sectional shapes or loading histories.

2.3.2.2 Physical theory models

Physical theory models overcome some of the limitations of phenomenological models as they are theoretically less dependent on empirical parameters. The input parameters of

these models are based on brace material, cross-section, the distribution and characteristics of fibres at various critical sections, and brace engineering properties.

Material non-linearity in physical theory models can be incorporated in two ways, lumped or distributed plasticity. In the lumped plasticity models, the inelastic behaviour of the beam-column member, in general, follows the concept of the Giberson one-component model (Sharpe 1974) which has the location of the plastic hinges pre-determined. They are usually located at one or both ends of the elastic beam-column element and possibly at the midspan. Brace elements are often modelled with pinned ends using two elastic beam column elements connected to a plastic hinge at midspan. This approach has been used by several researchers to generalise the behaviour of buckling braces (Wakabayashi et al. 1973; Higginbotham and Hanson 1976; Gugerli and Goel 1982; Ikeda and Mahin 1986; Hassan and Goel 1991; Remennikov and Walpole 1997b). It was shown that for general cyclic loading, the behaviour of the bracing elements at the global force deformation level is captured fairly accurately. The main limitations of these models are that they do not account for the spread of plasticity along the member length, the transition from elastic to plastic behaviour is abrupt and does not account for the Bauschinger effect, degradation of axial stiffness with cycling is not simulated and boundary conditions are pinned–pinned (Jin and El-Tawil 2003). However, Ikeda and Mahin (1986) and Remennikov and Walpole (1997a) accounted for the Bauschinger effect and the degradation in axial brace stiffness with cyclic loading in their models.

Jin and El-Tawil (2003) proposed a beam-column model that can be used to account for the inelastic brace buckling. This model accounts for spread of plasticity along the length and cross section of the brace element. It simulates the degradation of axial stiffness with cycling and has no restrictions on the boundary conditions. In this model, the cross-sectional shape can vary along the length of the element and is defined by fibres. Each fibre can have different constitutive characteristics. The main limitation of the fibre-element model is that it cannot explicitly model localized effects along the length of the brace. Uriz (2005) implemented a scheme to track a critical strain measure at the cross-section level of a fibre-element to predict fracture. The approach relies on empirical

calibration to account for the effects of local buckling and low cyclic fatigue. This fatigue calibration has only been performed for 6x6x3/8" elements and further refinement should be carried out. For the current research the empirical parameters will be calibrated to provide reasonably accurate fracture predictions in the bracing element, as will be discussed in Chapter 3.

2.3.2.3 Finite element models

In finite element models, the brace is discretised into a number of elements with elastic or elastic-plastic constitutive laws. They can employ one-, two- or three-dimensional elements. These models can provide realistic representations of brace behaviour by simulating local as well as global imperfections. These simulations can directly model several complex phenomena, such as local buckling, that lead to fracture. Some researchers (for example, Haddad et al. (2004), Yoo et al. (2006), and Nip et al. (2010)) used finite element models to model braces as it can overcome the limitations in the physical theory models using different software packages, such as ANSYS (2002), RAM-Perform 3D (2003) and ABAQUS (2006). Finite element models have many advantages compared to fibre-based element models, as they evaluate directly the inelastic brace response at each point along the length of the member, as well as through the depth of the cross-section and allow localised deformation effects to develop along the length the cross-section of the bracing member. However, they are computationally expensive for practical analyses of large structures. Because of that, their use had been restricted to analysis of individual brace members and end connections.

2.4 Physical tests on CBFs

In this section, a summary of experimental studies on CBFs is carried out to highlight the important parameters that affect the behaviour of these lateral resisting systems.

Ghanaat (1980) conducted shake table tests to study the effect of adding braces to moment resisting frames for lateral loading resistance. A three-storey 3/5 scale steel moment resisting frame structure was tested without brace elements and compared to the frame when different bracings were added. A range of brace member sectional shapes and slenderness were employed, such as rod X-braces with a slenderness ratio, KL/i , of

370, pipe X-braces with a slenderness ratio, KL/i , of 125, and double angle X-braces with a slenderness ratio, KL/i , of 86. The shake table tests were subjected to a scaled acceleration history from the 1940 El Centro and 1971 Pacoima Dam earthquake records. He concluded from the tests that the addition of braces is effective in resisting lateral forces. It tends to limit the storey drifts and, thus, reduces damage to both structural and non-structural components. However, he had different recommendations for each bracing type. He recommended that braces with slenderness ratios greater than 200 can be used for wind resistance and very low intensity earthquakes. Ghanaat (1980) concluded that the most important feature in the response behaviour with rod braces is that pre-tension is lost during moderate earthquakes, leading to an impacting type response in the resulting slack rod system. However, there was no evidence from the presented data of impact type behaviour causing amplification in tensile loads on the system. For moderate earthquakes, he had suggested to use braces with slenderness ratios less than 200 to resist moderate earthquakes, as members in this slenderness range were found to be quite effective in limiting storey drifts and significant energy was absorbed by the braces in post-buckling displacement cycles. Furthermore, he had suggested using braces with slenderness ratios less than 100 for moderate to strong earthquakes. It was noted that the effectiveness of the brace members in this slenderness range to limit storey drift was reduced only for rather strong earthquakes as a “pinching” effect developed in the force displacement loops because of accumulated tensile yield deformation.

Goel and El-Tayem (1986) conducted quasi-static cyclic loading tests on six full-scale specimens made from carbon steel single and double angles. Five of these specimens were made of equal leg single angles, with slenderness ratio ranged from 87 to 143. One specimen was made of unequal leg double angles with slenderness ratio of 62. It was found that the change of the brace type did not greatly affect the shape of the hysteresis loop. However, local buckling was found to be more severe in X-bracing made with double angles in which buckling occurred in the out-of plane direction. The larger width-to-thickness ratio and smaller slenderness ratio caused more severe local buckling. Failure mechanisms occurred at locations of local buckling in the braces. In two cases, failure of gusset plates occurred.

Ballio and Perotti (1987) carried out reduced-scale tests on single storey X-braced configurations using either double angles or double channels placed back-to-back to develop and validate numerical models for inelastic behaviour of braces. The two braces were connected at the centre with a pin connection in the X-configured specimens. It was found that this pinned middle connection allowed for in-plane buckling of the members in a second fundamental mode shape, which spread damage over both halves of the brace in compression.

Foutch et al. (1987), Roeder et al. (1987), Yamanouchi et al. (1989), and Tang and Goel (1989) reported findings from a full-scale six-storey steel test structure constructed in the Large Size Structures Laboratory of the Building Research Institute (BRI) in Tsukuba, Japan as part of the US-Japan Joint Research Programme. The building was designed as a six-storey structure with a general floor plan shown in Figure 2.14(a). It was 15m square in plan with two 7.5m bays in each direction. The height of the structure was 22.38m from the test floor to the top of the roof girders. The structure consisted of three frames (A, B, and C) parallel to the direction of loading and three frames (1, 2, and 3) perpendicular to the loading direction, as shown in Figure 2.14 (b, c and d).

The building was tested by four different approaches in four phases. One of these phases involved testing the building with concentrically braced frames as the lateral resisting system. The test frame was subjected to scaled versions of the N-S component of the 1978 Miyagi-ken-Oki earthquake record through servo-controlled actuators attached to a huge reaction wall and to each floor level. Elastic, moderate and major size earthquakes were conducted by scaling the peak acceleration of the earthquake record to different levels.

For the elastic test, a small earthquake was used. Approximations to the design level forces in the building members were generated. All of the members remained elastic as expected with a maximum roof displacement of 4.0cm. In the second step, a moderate-sized earthquake was applied. The objective of this test was to generate a large enough response that brace buckling would be initiated at some locations. Limited brace buckling and plastic deformation was noted on some floor levels, but the structure appeared to be

in good condition. A failure occurred at a brace-beam connection detail, illustrating the importance of design details for satisfactory seismic performance. When applying the major earthquake, severe brace buckling was observed on many braces during the first few seconds of the acceleration record because of the high energy input of the Miyagi-ken-Oki acceleration record and because of the imperfections induced by previous testing. The braces were cold-formed carbon steel with square hollow sections. Effective slenderness ratios, KL/i , of the braces varied from 51 to 79. In-plane and out-of-plane brace buckling occurred. Local tears occurred at the corners because of high concentration of strains induced by plastic hinging of the brace and due to the reduced ductility from the forming process. Slabs consisted of reinforced lightweight concrete on formed metal deck. In several stories, slab cracks were observed. Several beams and columns suffered from yielding, which illustrates the importance of capacity design. In the storeys that suffered from severe brace buckling and fracture, the maximum storey drift was 1.9%. However, all other storeys had a drift of less than 1%. At 11.37 sec into the seismic record, a brace was ruptured completely causing a soft storey with considerably reduced strength. Hence, the test was stopped at this point. This illustrates that this type of premature fracture of braces must be avoided in seismic resistance systems.

In the early stages of the earthquake, most of the energy dissipated (about 80%) was achieved by the braces and the rest were carried out by moment resisting frames. However, after the severe buckling and initiation of fracture in the braces, the moment resisting frames carried about 60% of the lateral load. The building may have been at serious risk after the fracture of the braces without the moment resisting frames as a secondary lateral resisting system.

Lee and Lu (1989) carried out quasi-static cyclic tests on a 0.305 scaled model of a six-storey prototype steel building. The testing was carried out with different lateral load-resisting schemes; one of them was a dual system of a moment resisting frame with chevron concentric braces. They found that the buckling of braces caused a marked reduction of the stiffness of the test structure, but its load-carrying capacity did not

reduce too rapidly until one of the braces in a storey ruptured. They found that when fractures initiated in each of the compact square hollow section braces, the maximum drifts corresponded to an average of 1.8% drift.

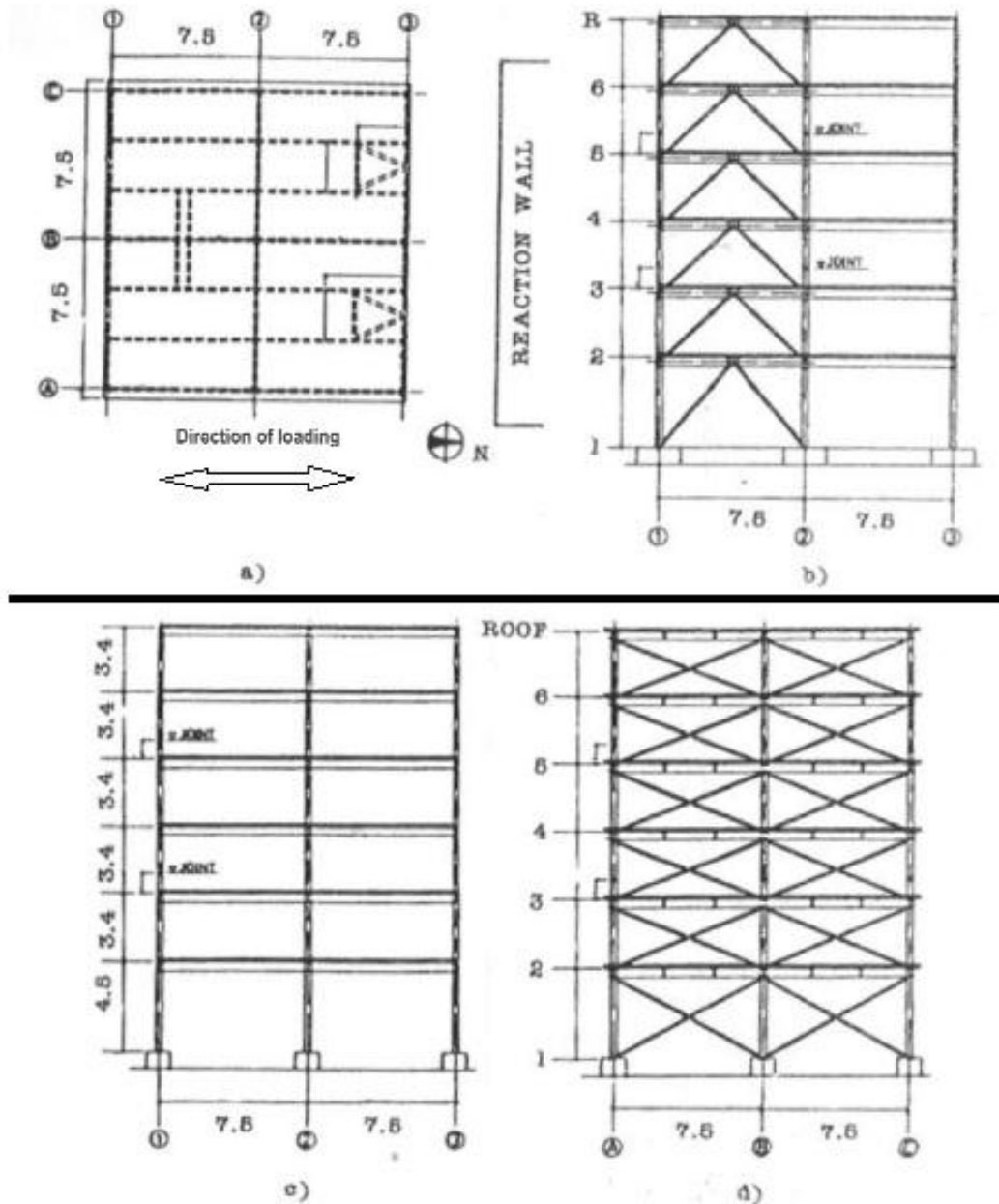


Figure 2.14: Typical plan and elevation of US-Japan Joint Research Programme full-scale test frame: (a) Typical floor plan, (b) Frame B elevation, (c) Frame A and C elevation, and (d) Frame 1 and 3 elevation (Foutch et al. 1987).

Fukuta et al. (1989) carried out quasi-static cyclic tests on 3-storey 2-bay chevron braced frames. Braces were fabricated from rectangular hollow sections with slenderness ratio ranging from 70 to 120. Many of the braces in test frames had three plastic hinges after their flexural buckling; one was formed at the mid-span and the other two were at their ends. After a few cycles of loading, fracture occurred at plastic hinge locations, especially at mid-span of the braces. They found that the brace buckling load can be predicted correctly by assuming the effective length factor of the brace to be equal to unity while using a pinned connection.

Tremblay et al. (2003) carried out 24 cyclic quasi static tests on concentrically braced frames in both single bracing and X-bracing configurations. All braces were cold-formed rectangular hollow sections (RHS) with normalised slenderness ratios, $\bar{\lambda}$, ranged from 0.83 to 2.10, which is approximately equivalent to effective slenderness ratio, KL/i , ranged from 63 to 160. They noticed that compression load measured in braces at first occurrence of buckling, C_r , were more than those predicted using code equations. They also observed that energy dissipation decreases nearly linearly with the increase of brace slenderness for the both bracing configurations and that the local buckling and fracture of the RHS braces occurred at a lower ductility level in X-bracing systems than in the single braces systems due to a higher curvature demand imposed in the X-bracing configuration. Furthermore, the linear relationship between the sum of ductility levels reached in tension and compression before fracture, μ_f , and the slenderness ratio, $\bar{\lambda}$, shown in Equation [2.2] predicted the fracture of the single bracing members relatively well, but was unconservative for the X-bracing specimens.

Celik et al. (2004) carried out quasi static cyclic tests on a half-scale single storey X-braced frame using cold formed carbon steel square hollow sections and solid rectangular bars to demonstrate the effect of using channels installed on both sides of the bracing system (in the plane of the braced bay) to restrain out-of-plane buckling of the members. These cold formed channels permitted second mode buckling of members when they were installed. However, the increased plastic rotation in the hollow members led to premature fracturing of the braces during earlier cycles when compared to the non-

restrained members. The cold formed channels were sized to restrain the hollow sections from buckling, and as a result, substantially strengthened and stiffened the assembly. Typical failure mechanisms for the braces involved plastic hinges, eventually leading to local buckling and fracture at the local buckle. The hollow unconstrained brace fractured at a drift of 2.8%, whereas the constrained brace fractured at a drift of 1.9%.

Elghazouli et al. (2005) performed shake table tests on eight one-storey-one-bay CBFs. For each test, two cold formed carbon steel hollow brace specimens were rigidly connected at their top ends to the bottom flange of the transverse beams and at their lower ends to the table platform. Non-dimensional slenderness ratios, $\bar{\lambda}$, for the braces ranged from 1.4 to 3.0, which is equivalent to effective slenderness ratio, KL/i , ranged from 131 to 281. The two braces were not connected at mid-length and were separated in plan by a spacing of 200 mm to avoid contact during out-of-plane buckling. Five of the shake table tests were subjected to a scaled acceleration history from the El Centro earthquake, one was subjected to an artificial earthquake and another two were subjected to sine ramp for comparison purposes. Drifts found during these shake table tests ranged from 1.4% to 5.1%. These shake table tests will be discussed in more detail in the following chapters and will be used to validate a robust numerical model for single storey CBFs and to develop a direct displacement based design methodology for single storey CBFs.

2.5 Response analysis procedures

In seismic design, linear static and dynamic procedures are widely used. For complex structures and evaluation studies non-linear static and dynamic analysis are used. Each of these analysis types will be discussed briefly in the following sub-sections.

2.5.1 Linear static analysis

Linear static analysis is used with the equivalent lateral force procedure for seismic design specified in EC8 (CEN 2004). The effect of earthquake horizontal ground motion is represented by distributing forces to the lateral resisting elements in the building, typically defined by a seismic design response spectrum. These static lateral forces are applied on an appropriate structural model and are used for design and analysis of the

building. The buildings are assumed to respond in their fundamental mode. By calculating the natural period of the structure, the response is read from a design response spectrum. A force reduction factor is used to reduce the forces obtained from the linear analysis, in order to account for the non-linear response of a structure. This reduction factor is associated with the material, the structural system and the design procedures.

2.5.2 Linear dynamic analysis

A linear dynamic analysis can be classified into a response spectrum analysis or a time history analysis. EC8 (CEN 2004) recommends the use of the response spectrum analysis to determine the distribution of lateral forces in buildings that have irregularity in the distribution of mass or stiffness; for example, buildings with vertical or horizontal setbacks. The response of a structure can be described as a combination of different modes. Its intention is to determine the structural response directly from an earthquake design spectrum for each mode, based on the modal frequency and the modal mass, and these are then combined to provide an estimate of the total response of the structure.

In linear dynamic time history analysis, the response of each mode to specific ground acceleration is computed by numerical integration and the resulting modal responses are superimposed by suitable modal combination rules.

The consideration of the higher modes on the linear dynamic procedures is the main advantage with respect to linear static procedures. On the other hand, linear dynamic procedures are based on linear elastic response and, hence, the applicability decreases with increasing nonlinear behaviour, which is approximated by global force reduction factors. In cases where structures are either too irregular, too tall or of significance to a community in disaster response, linear dynamic analysis is no longer appropriate, and more complex analysis is often required, such as non-linear static or dynamic analysis.

2.5.3 Non-linear static (pushover) analysis

Non-linear static or pushover analysis is an incremental nonlinear analysis wherein the structure is loaded with a lateral force profile. The structure is pushed laterally by the forces of this load pattern until the level of deformation expected in the design earthquake

is attained. Nonlinear static procedures use equivalent SDOF structural models and represents seismic ground motion with response spectra. Storey drifts and component actions are related subsequently to the global demand parameter by the pushover or capacity curves that are the basis of the non-linear static procedures. The following information may be obtained from such an analysis: estimates of the strength and deformation demands on the structural elements, effect of deterioration of individual components on the behaviour of the structure, overload of brittle elements and identification of possible weak links in the lateral load path.

Pushover analysis cannot account for the effect of higher modes. Neither can it account for changes in dynamic response and inertial load distributions that occur as the structure degrades in stiffness. However, it is superior to linear analysis methods as it considers the actual strength of the structural elements.

To improve the accuracy of pushover analysis in predicting the seismic-induced demands of structures, an adaptive pushover method was developed (Antoniou and Pinho 2004). This was achieved by proposing a modification to the regular pushover analysis in a way that the lateral load pattern would be determined using the structure's first mode shape and its effective modal mass. This was followed by another approach to change the lateral load pattern during an analysis as the plastic hinges are formed in the structure (Rofoeia et al. 2007). The adaptive pushover analysis method automates the pushover analysis and improves its performance in predicting the system's demand parameters (Rofoeia et al. 2007).

2.5.4 Non-linear dynamic analysis

Nonlinear time history analysis (NLTHA) is the most accurate procedure in the seismic response analysis. Ground motion records are subjected in NLTHA on a detailed structural model producing estimates of component deformations for each degree of freedom in the model. It employs numerical integration in the time domain and explicitly accounts for nonlinear stiffness and strength characteristics of the structural elements. It also accounts for the effect of higher modes and shifts in inertial load patterns as structural softening takes place.

In NLTHA, the calculated response can be very sensitive to the characteristics of the individual ground motion used as seismic input and, therefore, several appropriate selected accelerograms should be used in the analyses to achieve a meaningful and reliable estimation of the of structural response. Furthermore, Goggins and Sullivan (2009) advised that care should be taken with developing NLTHA models (e.g. selection of material, numerical model type, connection parameters, etc.), as otherwise they may not correctly predict the real behaviour of the structural system. In addition, Goggins and Sullivan (2009) noted that NLTHA techniques should be developed further to better predict the displacement response of CBF systems.

2.6 Design procedure in Eurocode 8 (EC8)

2.6.1 Ground conditions

EC8 (CEN 2004) suggests that ground conditions should be identified by appropriate investigations. It should be ensured that the construction site and the nature of the supporting ground is free from risks of ground rupture, slope instability and permanent settlements caused by liquefaction or densification in the event of an earthquake. EC8 (CEN 2004) specifies five soil class types A, B, C, D, and E, described by the stratigraphic profiles and parameters such as average shear wave velocity, $v_{s,30}$, standard penetration test blow count, $NSPT_{(blows/30cm)}$, and the undrained shear strength of the soil, c_u , as shown in Table 2.3. Ground types depend mainly on the value of the average shear wave velocity, $v_{s,30}$. If the value of the average shear wave velocity is not available, then standard penetration test blow count can be used. There are two special ground types, S1 or S2, as defined in Table 2.3, which requires special attention taking into account the possibility of soil failure under the seismic action.

2.6.2 Seismic zones

According to EC8 (CEN 2004), National Authorities should divide national territories into seismic zones, depending on the local hazard, where the hazard within each zone is assumed to be constant (see for example, Figure 2.15 for Italy). For most of the applications, the hazard is described in terms of a single parameter, i.e. the value of the

Table 2.3: Ground types according to EC8 (CEN 2004).

Ground type	Description of stratigraphic profile	Parameters		
		$v_{s,30}$ (m/s)	NSPT (blows/30cm)	c_u (kPa)
A	Rock or other rock-like geological formation, including at most 5 m of weaker material at the surface.	> 800		
B	Deposits of very dense sand, gravel, or very stiff clay, at least several tens of metres in thickness, characterised by a gradual increase of mechanical properties with depth.	360 – 800	> 50	> 250
C	Deep deposits of dense or medium-dense sand, gravel or stiff clay with thickness from several tens to many hundreds of metres.	180 – 360	15 - 50	70 - 250
D	Deposits of loose-to-medium cohesion-less soil (with or without some soft cohesive layers), or of predominantly soft-to-firm cohesive soil.	< 180	< 15	< 70
E	A soil profile consisting of a surface alluvium layer with v_s values of type C or D and thickness varying between about 5 m and 20 m, underlain by stiffer material with $v_s > 800$ m/s.			
S1	Deposits consisting, or containing a layer at least 10 m thick, of soft clays/silts with a high plasticity index ($PI > 40$) and high water content	< 100 (indicative)		10 - 20
S2	Deposits of liquefiable soils, of sensitive clays, or any other soil profile not included in types A – E or S1			

reference peak ground acceleration on type A ground, a_{gR} . The design ground acceleration on type A ground, a_g , is equal to a_{gR} times the importance factor γ_I (i.e. $a_g = \gamma_I \cdot a_{gR}$). The effect of the site-specific stratigraphic profile on the ground acceleration is taken into account in EC8 (CEN 2004) by altering the amplitude and corner periods of the response spectrum. This will be discussed further in Section 2.6.3.

Seismic zones with design ground acceleration on type A ground, a_g , not greater than $0.08g$ (where g is the acceleration due to gravity = 9.81m/s^2) are considered as low

seismicity zones, where simplified seismic design procedure can be applied for certain types of structures. However, if the design ground acceleration on type A ground, a_g , is less than $0.04g$ the provisions of EC8 (CEN 2004) need not to be observed.

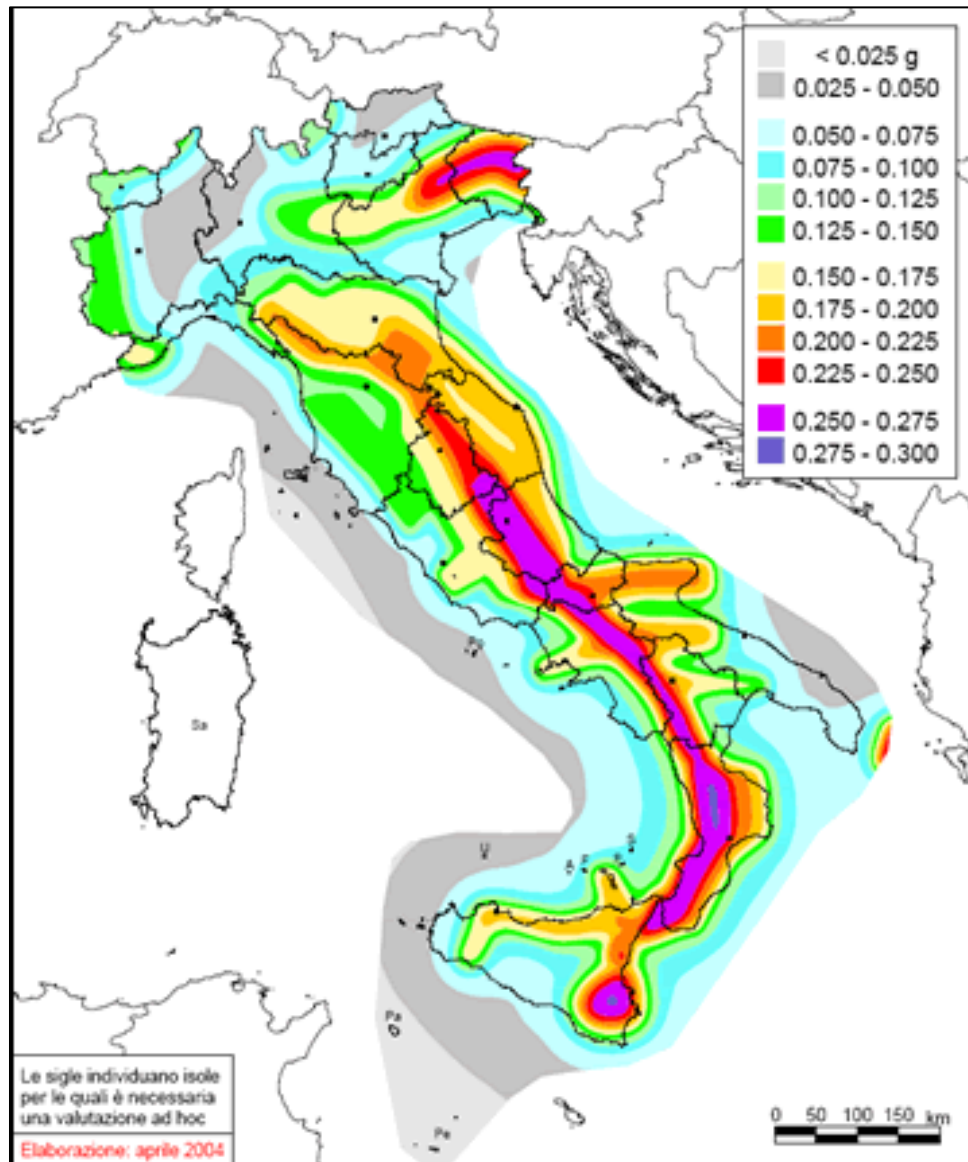


Figure 2.15: Seismic zone map for Italy, showing the peak ground accelerations that have a 10% probability of exceedance in 50 years (return period of 475 years) (INGV 2004).

2.6.3 Basic representation of the seismic action

The earthquake motion at a given point on the surface is represented by an elastic response spectrum. The shape of the elastic response spectrum is taken as being the same for the no-collapse requirement (ultimate limit state, design seismic action) and for the damage limitation requirement. The horizontal seismic action is described by two orthogonal components assumed to be independent.

2.6.3.1 Horizontal elastic response spectrum

The elastic response spectrum $S_e(T)$ for the horizontal components of the seismic action is shown in Figure 2.16 and defined by the following expressions:

$$0 \leq T \leq T_B : S_e(T) = a_g * S * \left[1 + \frac{T}{T_B} * (\eta * 2.5 - 1) \right] \quad [2.9]$$

$$T_B \leq T \leq T_C : S_e(T) = a_g * S * \eta * 2.5 \quad [2.10]$$

$$T_C \leq T \leq T_D : S_e(T) = a_g * S * \eta * 2.5 * \left[\frac{T_C}{T} \right] \quad [2.11]$$

$$T_D \leq T \leq 4s : S_e(T) = a_g * S * \eta * 2.5 * \left[\frac{T_C T_D}{T^2} \right] \quad [2.12]$$

where T is the vibration period of a linear single-degree-of-freedom system, a_g is the design ground acceleration on type A ground ($a_g = \gamma_I \cdot a_{gR}$), T_B is the lower limit of the period of the constant spectral acceleration branch, T_C is the upper limit of the period of the constant spectral acceleration branch, T_D is the value defining the beginning of the constant displacement response range of the spectrum, S is the soil factor, and η is the damping correction factor ($\eta = \sqrt{10/(5 + \xi)}$) with a reference value of $\eta = 1$ for 5% viscous damping, ξ .

EC8 (CEN 2004) recommends two types (shapes) of spectra. Type 1 is adopted if earthquakes that contribute most to the seismic hazard defined for a site for the purpose of probabilistic seismic hazard assessment have a surface-wave magnitude, M_s , of more than 5.5. A Type 2 spectrum is adopted if $M_s \leq 5.5$. The values of the periods T_B , T_C and T_D and of the soil factor S describing the shape of the elastic response spectrum depend upon the ground type and are given for both spectra types in Table 2.4 and Table 2.5. For

ground types S1 and S2, special studies should provide the corresponding values of S , T_B , T_C and T_D .

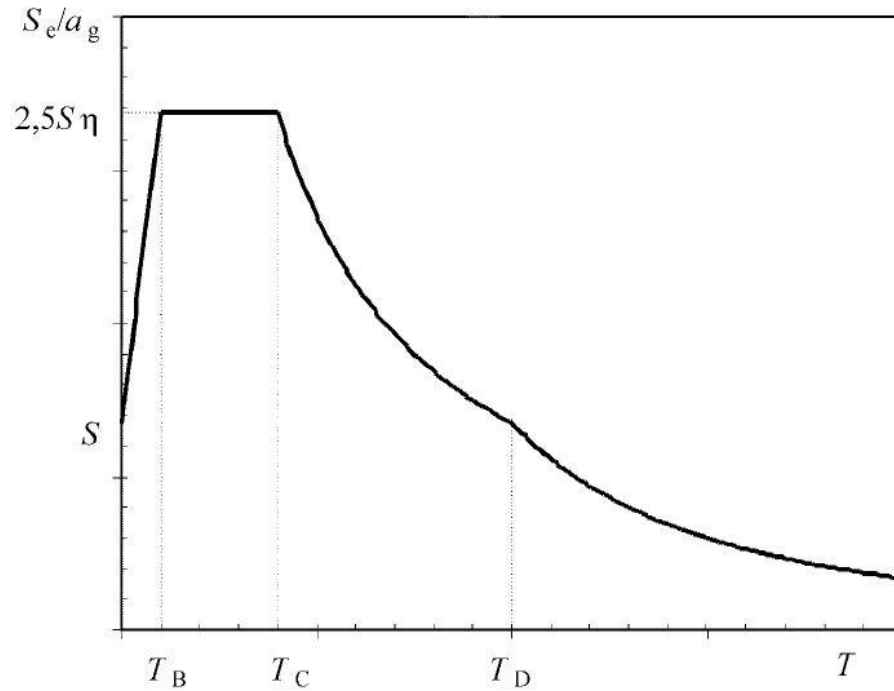


Figure 2.16: Shape of the elastic response spectrum from EC8 (CEN 2004).

Table 2.4: Values of the parameters describing the recommended Type 1 elastic response spectra EC8 (CEN 2004).

Ground Type	S	T_B	T_C	T_D
A	1.0	0.15	0.4	2.0
B	1.2	0.15	0.5	2.0
C	1.15	0.20	0.6	2.0
D	1.35	0.20	0.8	2.0
E	1.4	0.15	0.5	2.0

Table 2.5: Values of the parameters describing the recommended Type 2 elastic response spectra EC8 (CEN 2004).

Ground Type	S	T _B	T _C	T _D
A	1.0	0.05	0.25	1.2
B	1.35	0.05	0.25	1.2
C	1.5	0.1	0.25	1.2
D	1.8	0.1	0.3	1.2
E	1.6	0.05	0.25	1.2

2.6.3.2 Design spectrum for elastic analysis

The design of structural systems resisting seismic actions generally permits their capacity in the non-linear range to be smaller than those corresponding to a linear elastic response. To do this, a behaviour factor, q , is introduced, which is an approximation of the ratio of the seismic forces that the structure would experience if its response was completely elastic with 5% viscous damping to the seismic forces that may be used in the design, with a conventional elastic analysis model, still ensuring a satisfactory response of the structure. This behaviour factor is used to reduce the elastic response spectrum developing a design spectrum that can be used to take into account the capacity of the structure to dissipate energy, mainly through the ductile behaviour of its elements and/or other mechanisms. The values of the behaviour factor q , which also account for the influence of the viscous damping being different from 5%, are given in the code for various materials and structural systems according to the relevant ductility classes (CEN 2004).

The design spectrum, $S_d(T)$, can be defined for the horizontal components of the seismic action by the following expressions

$$0 \leq T \leq T_B : S_d(T) = a_g * S * \left[\frac{2}{3} + \frac{T}{T_B} * \left(\frac{2.5}{q} - \frac{2}{3} \right) \right] \quad [2.13]$$

$$T_B \leq T \leq T_C : S_d(T) = a_g * S * \frac{2.5}{q} \quad [2.14]$$

$$T_C \leq T \leq T_D : S_d(T) = a_g * S * \frac{2.5}{q} * \left[\frac{T_C}{T} \right] \quad [2.15]$$

$$S_d(T) \geq \beta * a_g$$

$$T_D \leq T : S_d(T) = a_g * S * \eta * \frac{2.5}{q} * \left[\frac{T_C T_D}{T^2} \right] \quad [2.16]$$

$$S_d(T) \geq \beta * a_g$$

where β is the lower bound factor for the horizontal design spectrum with a recommended value of 0.2.

2.6.4 Design procedure for CBFs in Eurocode 8

EC8 (CEN 2004) defines concentrically braced frames as those frames in which the horizontal forces are mainly resisted by members subjected to axial forces. It suggests that the dissipative zones should be mainly located in the diagonals and divides the bracings into one of the two categories: (a) active tension diagonal bracings, in which the horizontal forces can be resisted by the tension diagonals only, neglecting the compression diagonals, (b) V bracings, in which the horizontal forces can be resisted by taking into account both tension and compression diagonals, where the intersection point of these diagonals lies on a horizontal member which shall be continuous. EC8 (CEN 2004) does not allow the use of the K bracings, in which the intersection of the diagonals lies on a column.

Lateral loads must be resisted by the bracings. EC8 (CEN 2004) assumes that the brace members do not carry any gravitational loads and only resist the seismic forces. The seismic base shear, F_b , can be found by the following

$$F_b = S_d(T_1) \cdot m \cdot \lambda \quad [2.17]$$

where $S_d(T_1)$ is the ordinate of the design spectrum at period T_1 which is the fundamental period of vibration of the building for lateral motion in the direction considered. A

behaviour factor, q , is used to obtain the design spectrum to allow for the ductility expected for the structural system. For diagonal CBFs, q is taken as 4. The total mass of the building, above the foundation or above the top of a rigid basement, is m , computed as the addition of the gravity dead load and 0.3 of the gravity live load. λ is the correction factor, the value of which is equal to 0.85 if $T_1 < 2T_c$ and the building has more than two storeys where T_c is the upper limit of the period of the constant spectral acceleration branch, or $\lambda = 1.0$ otherwise.

The base shear, F_b , can be distributed to all floor levels in proportion to the product of mass and displacements and the horizontal forces, F_i , which can be given as the following

$$F_i = F_b \frac{m_i s_i}{\sum m_j s_j} \quad [2.18]$$

where s_i and s_j are the displacements of the masses m_i and m_j of storey i and j respectively, in the fundamental mode shape.

When the fundamental mode shape is approximated by horizontal displacements increasing linearly along the height, the horizontal forces, F_i , can be given at each storey i as follows:

$$F_i = F_b \frac{m_i z_i}{\sum m_j z_j} \quad [2.19]$$

where z_i , z_j are the heights of the masses m_i , m_j above the level of application of the seismic action.

As discussed earlier, brace members are the main elements to resist these seismic forces and are designed to dissipate energy through yielding in tension or buckling in compression. When a compression force is applied to the brace, global buckling occurs after which there is usually a reduced post-buckling compressive resistance. When the load is reversed the brace reverts to its previous position and the basis of dissipating the energy is the yielding of the brace member in tension provided the brace did not fail due to fracture induced by local buckling, low cyclic fatigue or connection fracture. In order to prevent or delay local buckling, which is affected mainly by width-to-thickness ratio of

the cross section and overall member slenderness, EC8 (CEN 2004) suggests to use Class 1 cross-section classification described in EC3 (CEN 2005). In frames with X diagonal bracings, non-dimensional slenderness ratio of a member, $\bar{\lambda}$, is limited in EC8 to $1.3 < \bar{\lambda} < 2.0$, which is equivalent to an effective slenderness ratio between 122 and 188. The 1.3 limit is defined to avoid overloading columns in the pre-buckling stage (when both compression and tension diagonals are active) beyond the action effects obtained from an analysis at the ultimate stage where only the tension diagonal is taken as active. In frames with diagonal bracings in which the diagonals are not positioned as X-diagonal bracings, the non-dimensional slenderness, $\bar{\lambda}$, should be less than or equal to 2.0 (effective slenderness ratio of 188).

EC8 (CEN 2004) requires that the diagonal elements of bracings shall be placed in such a way that the structure exhibits similar load deflection characteristics at each storey in opposite senses of the same braced direction under load reversals. To avoid significant asymmetric response effect, the following rule should be met at every storey

$$\frac{|A^+ - A^-|}{A^+ + A^-} \leq 0.05 \quad [2.20]$$

where A^+ and A^- are the areas of the horizontal projections of the cross-sections of the tension diagonals, when the horizontal seismic actions have a positive or negative direction respectively as shown in Figure 2.17.

In order to satisfy a homogeneous dissipative behaviour of the diagonals, EC8 (CEN 2004) specifies a brace overstrength factor, Ω , as the following

$$\Omega_i = \frac{N_{pl,Rd,i}}{N_{Ed,i}} \quad [2.21]$$

where $N_{pl,Rd,i}$ is the design resistance of diagonal i and $N_{Ed,i}$ is the design value of the axial force in the same diagonal i in the seismic design situation. EC8 (CEN 2004) requires that the maximum brace overstrength should not differ from the minimum value by more than 25%.

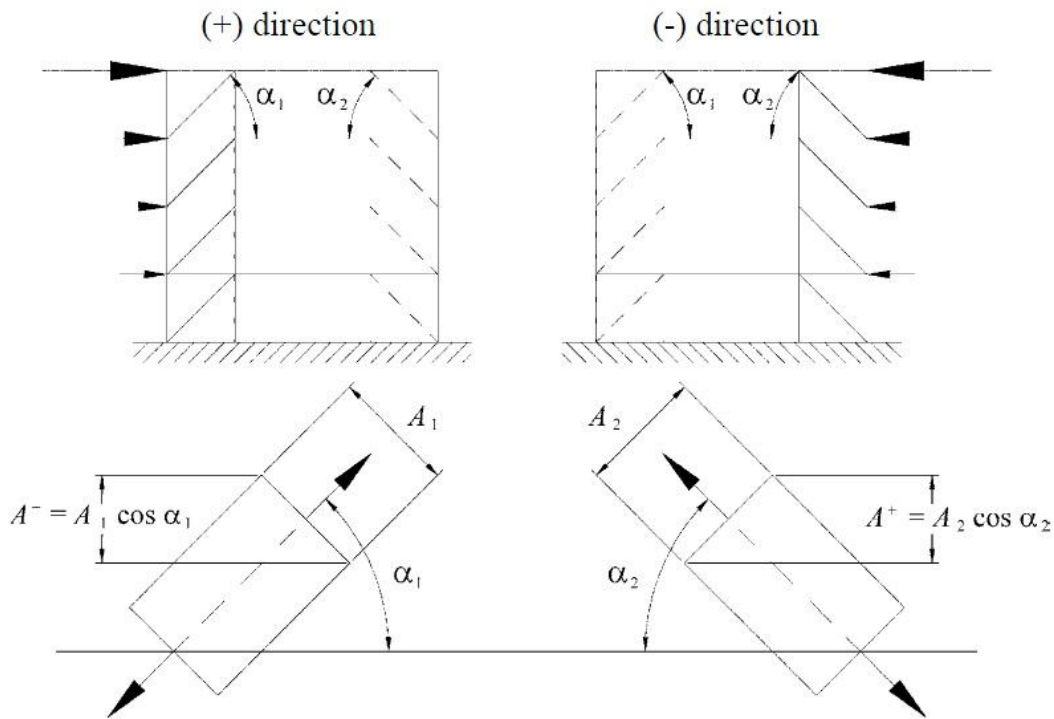


Figure 2.17: Lateral resistance of CBF where the symmetry should be satisfied (CEN 2004).

In EC8 (CEN 2004) concentrically braced frames shall be designed so that yielding of the diagonals in tension will take place before failure of the connections and before yielding or buckling of the beams or columns. Thus, beams and columns with axial forces should meet the following minimum resistance requirement:

$$N_{pl,Rd}(M_{Ed}) \geq N_{Ed,G} + 1.1\gamma_{ov}\Omega N_{Ed,E} \quad [2.22]$$

where $N_{pl,Rd}(M_{Ed})$ is the design buckling resistance of the beam or the column taking into account the interaction of the buckling resistance with the bending moment M_{Ed} , defined as its design value in the seismic design situation; $N_{Ed,G}$ is the axial force in the beam or in the column due to the non-seismic actions included in the combination of actions for the seismic design situation; $N_{Ed,E}$ is the axial force in the beam or in the column due to the design seismic action; γ_{ov} is the material overstrength factor; Ω is the minimum value of Ω_i over all the diagonals of the braced frame system.

2.7 Direct displacement based design (DDBD) procedure for CBFs

Calvi and Sullivan (2009) published a design code for DDBD methodology. The provisions in this DDBD code have been well developed for reinforced concrete structures. However, further research and developments are required for steel structures and in particular for CBFs.

Della Corte and Mazzolani (2008) and Della Corte et al. (2010) proposed a direct displacement based design (DDBD) methodology for chevron concentrically braced frames. They proposed formulae for the calculation of inter-storey drift angles and associated displacements, considering the brace buckling distribution up the building height. Some disadvantages of this procedure are the complexity of the formulae and the lack of an equivalent viscous damping model developed specifically for concentrically braced frames.

Goggins and Sullivan (2009) investigated a trial direct displacement based design (DDBD) procedure for concentrically braced frames. They found that their methodology is conservative and overestimates the required brace cross-sectional size. They emphasised the need to develop an equivalent viscous damping (EVD) model specifically for CBF systems.

Wijesundara (2009) proposed an equivalent viscous damping, ξ , model for concentrically braced frames as a function of non-dimensional slenderness ratio, $\bar{\lambda}$, and the ductility, μ , as shown in the following equations

$$\xi = 0.03 + \left(0.23 - \frac{\bar{\lambda}}{15}\right)(\mu - 1) \quad \mu \leq 2 \quad [2.23]$$

$$\xi = 0.03 + \left(0.23 - \frac{\bar{\lambda}}{15}\right) \quad \mu \geq 2 \quad [2.24]$$

This model was developed based on cyclic displacement pushover simulations of fifteen SDOF CBF systems with different brace configurations. The area based approach proposed by Jacobsen (1960) was used to estimate the EVD value from the hysteretic loops. Furthermore, the model was correlated to the results of twelve single-storey braced

frames obtained from an experimental programme conducted by Archambault (1995) on brace members subjected to displacement histories to replicate the behaviour of single storey CBFs. Wijesundara (2009) carried out NLHTA using seven real earthquakes scaled to an appropriate displacement spectrum for each frame to validate the EVD values obtained from the area based approach. Wijesundara (2009) recommended that if the brace normalised slenderness ratio was either below 0.4 or above 1.6, then these limits should be used in place of the actual normalised slenderness ratio in Equations [2.23] and [2.24].

Wijesundara (2009) proposed a DDBD procedure for MDOF CBFs with a linear displacement shape and damping model shown in Equations [2.23] and [2.24] as outlined in the flowchart in Figure 2.18.

A limitation to the validation of the DDBD carried out by Wijesundara (2009) include that numerical models used to validate the method could not capture fracture due to low cyclic fatigue and were not calibrated using physical full scale structural systems subjected to real earthquake loadings. This limitation will be overcome in the current study.

2.8 Summary

Concentrically braced frames (CBFs) are one of the most effective structural systems to resist lateral loads during earthquakes. Energy dissipated during the seismic action is mainly resisted by the inelastic action of the brace members.

From the study of the behaviour of CBFs during previous earthquakes, the main reasons for failure were fracture of the braces at their ends or mid-length due to low cyclic fatigue and local buckling, failure of connections between braces and other structural members, and failure of beams and columns. Hence, Class 1 steel cross-section (CEN 2006) should be employed to avoid local buckling and yielding of brace members. Moreover, capacity design for beams and columns should be applied.

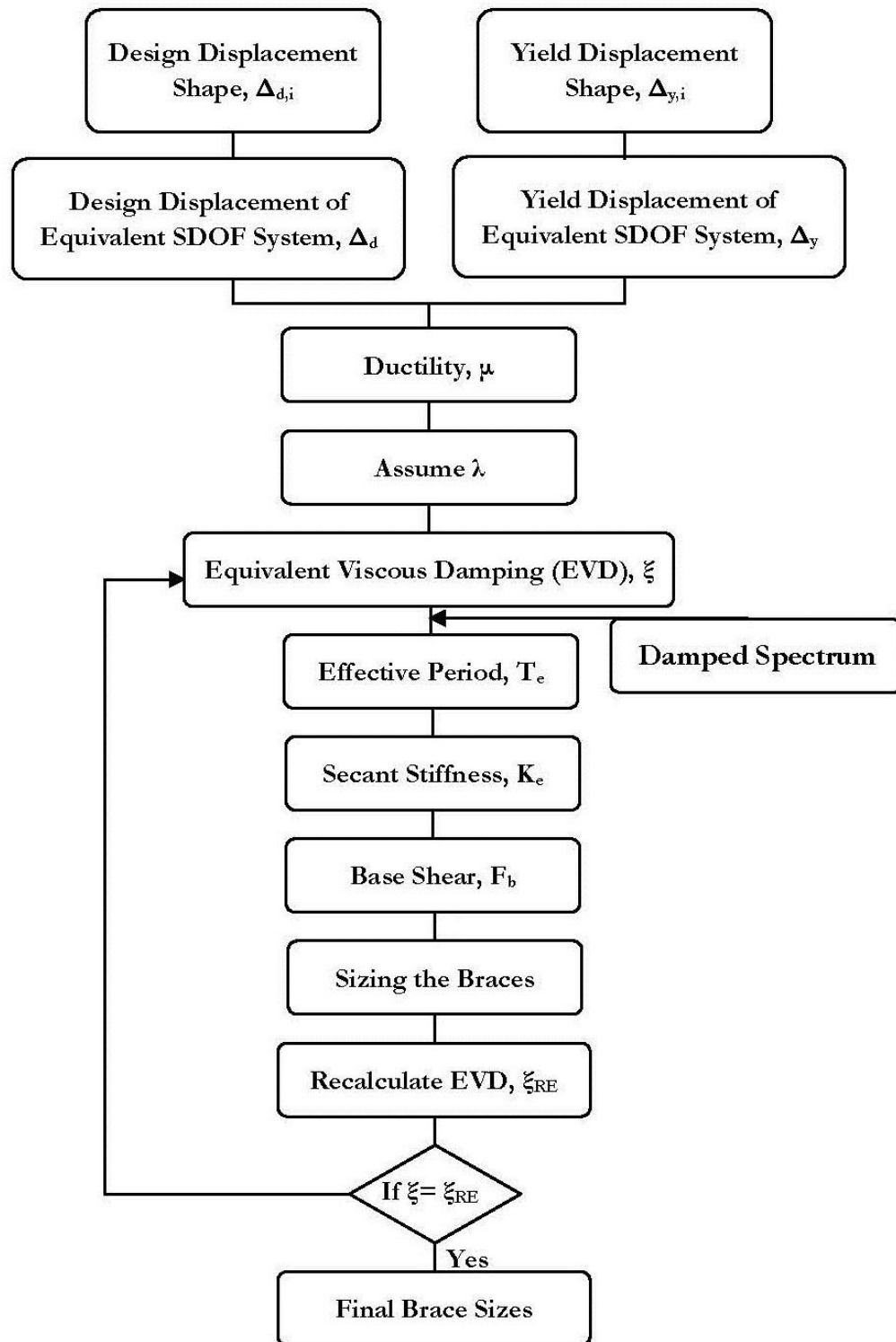


Figure 2.18: Flow chart of the DDBD procedure for CBFs adapted from (Wijesundara 2009).

Physical tests on CBFs showed that the effective member slenderness ratio is the most important parameter influencing the inelastic behaviour of the specimens tested. They clearly indicated that local buckling and fracture are the main limitations of energy dissipation and that fracture life of square hollow section braces is affected by the width to thickness ratio of the section brace walls.

Numerical models to predict the behaviour of concentrically braced frames were discussed and the need for an efficient numerical model validated using physical tests taking into account low cyclic fatigue was highlighted. This new numerical model can be used to develop and validate new design methodologies for CBFs.

Chapter 3

Numerical model for steel brace members incorporating a fatigue model

3.1 Introduction

The brace element is the main element in concentrically braced frame (CBF) systems that undergoes inelastic deformations to dissipate energy during seismic actions. It is destined to carry reversed axial forces in which it may experience yield in tension, buckle in compression or may fracture due to the demand cycles that it is expected to endure during seismic actions. Structural hollow sections (square, rectangular, circular and oval shaped) are commonly used as braced elements. Furthermore, increased interest has been shown in studying the performance of hollow structural steel sections (Kahn and Hanson 1976; Popov et al. 1979; Black et al. 1980; Jain et al. 1980; Popov and Black 1981; Ballio and Perotti 1987; Archambault 1995; Mamaghani et al. 1996; Tremblay 2002; Zhao et al. 2002; Elchalakani et al. 2003; Shaback and Brown 2003; Tremblay et al. 2003; Broderick et al. 2005; Elghazouli et al. 2005; Goggins et al. 2005; Goggins et al. 2006; Broderick et al. 2008; Nip et al. 2010) in order to model their inelastic behaviour.

In this chapter, the hysteretic behaviours of cold-formed square and rectangular hollow steel sections (SHS and RHS) subjected to inelastic cyclic loading carried out by Goggins (2004) will be studied. A robust numerical model for cold-formed carbon steel square and rectangular structural hollow sections will be developed. Then, the model will be validated by comparing its predictions to findings by Nip et al (2010) for cold-formed

carbon steel hollow sections. Its applicability to cold-formed stainless steel and hot rolled carbon steel square and rectangular structural hollow sections will also be investigated. This numerical model will be advanced in the next chapters and then employed in non-linear time history analysis (NLTHA) modelling to assess the behaviour of CBF systems.

3.2 Cyclic tests of steel brace specimens

Goggins (2004) carried out many cyclic tests on cold-formed square and rectangular hollow steel sections in order to obtain experimental data to validate numerical models. In particular, the performance of fifteen specimens fabricated from 20x20x2.0SHS, 40x40x2.5SHS and 50x25x2.5RHS sections with normalised slenderness ratios, $\bar{\lambda}$, defined in Eurocode 3 (CEN 2005), of between 0.4 to 3.2 subjected to cyclic tests were investigated. Two different lengths of specimens (1100 and 3300mm) were used to obtain the broad range of slenderness ratios. The tests carried out by Goggins (2004) on intermediate and long length brace specimens were subjected to increasing amplitude cyclic displacements. For these cyclic tests, the loading was applied according to the provisions of the ECCS (1986). The recommended complete testing procedure was followed, for which the axial deformation history is shown in Figure 3.1. This implies using one cycle at each level of 0.25, 0.5, 0.75 and 1.0 e_y , followed by three cycles at each level of 2, 4, 6 e_y , etc., where e_y represents the estimated axial yield displacement. Yield displacements evaluated from the monotonic tensile tests on short specimens were used to determine the amplitudes of the cycles (Goggins et al. 2005).

Nip et. al. (2010) carried out sixteen cyclic tests on square and rectangular hollow steel section in order to study the cyclic response of tubular bracing members of three structural materials: hot-rolled carbon steel, cold-formed carbon steel and cold-formed stainless steel. These specimens were fabricated from 40x40x3.0SHS, 40x40x4.0SHS, 50x50x3.0SHS, 60x60x3.0SHS and 60x40x3.0RHS sections with normalised slenderness ratios between 0.34 to 1.4. They were subjected to increasing amplitude cyclic displacements, similar to the loading regime used by Goggins (2004). Three different lengths of specimens (1250mm, 2050mm and 2850mm) were used. In this chapter, the physical tests carried out by Goggins (2004) are used to calibrate a numerical model that

can capture fracture of the specimens. The numerical model will then be validated by comparing its performance to the results from the physical tests by Nip et al. (2010).

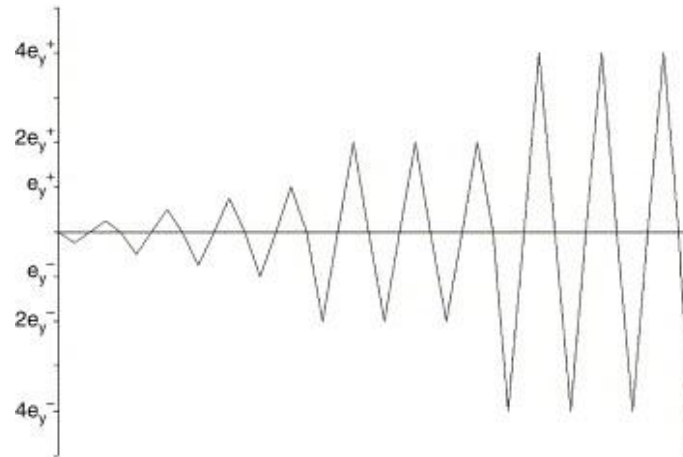


Figure 3.1: Cyclic displacement waveform for ECCS procedure.

Throughout this chapter, test ID's are identified by member size (depth X width X thickness X length), material (either carbon steel, CS, or stainless steel, SS), forming process (either hot-rolled, HR, or cold-formed, CF); tests carried out by Goggins (2004) are followed by the letter G with the specimen number and tests carried out by Nip et al (2010) are followed by the letter N with the specimen number. Test ID's are given in Table 3.1, together with normalised slenderness ratios of the brace about the minor axis (λ_{y-y}), yield strength, f_y , number of cycles needed to fracture the specimen, maximum tensile force, F_{max} , initial buckling load, F_c , the total energy dissipated by the specimens, W_{tot} , and the energy dissipated by the specimens at the first cycle of ductility of 4, $W_{\mu=4}$.

In order to study the behaviour of concentrically braced members, a brief discussion of the hysteretic response (axial load-axial displacement response) of the brace 40X40X2.5X1100-CS-CF-G1 tested by Goggins (2004) is presented here. Figure 3.2 shows the 40X40X2.5X1100-CS-CF-G1 bracing test specimen with the results from the test showing the hysteretic behaviour of the specimen, which is described by the hysteretic response of axial force plotted against resulting axial displacements (Goggins 2004). Compression loads are negative and tension loads are positive. The area under the hysteretic curves represents the hysteretic energy dissipated by the brace.

Table 3.1: Parameters and results for the specimens used to calibrate the numerical model.

Specimen ID	λ_{y-y}	f_y (MPa)	No. of cycles to fracture	F_{max} (KN)	F_c (KN)	W_{tot} (KN.m)	$W_{u=4}$ (KN.m)
40X40X2.5X1100-CS-CF-G1 ^a	0.40	285	16	113	-104	147.90	2.18
40X40X2.5X1100-CS-CF-G2 ^a	0.40	285	15	112	-107	143.40	2.20
20X20X2.0X1100-CS-CF-G3 ^a	0.90	304	26	45	-27	561.00	0.49
20X20X2.0X1100-CS-CF-G4 ^a	0.90	304	17	46	-32	299.50	0.51
50X25X2.5X1100-CS-CF-G5 ^a	0.60	304	16	111	-82	225.20	1.53
50X25X2.5X1100-CS-CF-G6 ^a	0.60	304	16	112	-91	186.60	1.59
40X40X2.5X3300-CS-CF-G7 ^b	1.30	344	-	144	-53	98.80	3.97
40X40X2.5X3300-CS-CF-G8 ^b	1.30	350	-	144	-53	83.40	3.89
40X40X2.5X3300-CS-CF-G9 ^b	1.30	332	-	142	-50	68.80	3.74
20X20X2.0X3300-CS-CF-G10 ^a	3.20	443	7	71	-5	4.90	0.58
20X20X2.0X3300-CS-CF-G11 ^a	3.00	399	7	70	-5	3.90	0.55
20X20X2.0X3300-CS-CF-G12 ^a	3.00	399	7	72	-6	6.12	0.62
50X25X2.5X3300-CS-CF-G13 ^b	1.90	312	-	113	-24	61.20	2.22
50X25X2.5X3300-CS-CF-G14 ^b	2.20	428	-	181	-24	28.00	1.57
50X25X2.5X3300-CS-CF-G15 ^b	2.20	428	-	183	-22	28.70	1.65
60X60X3.0X2050-CS-HR-N16 ^a	0.57	458	10	366	-320	31.20	7.79
40X40X3.0X2050-CS-HR-N17 ^a	0.89	478	19	220	-160	54.06	4.21
40X40X3.0X1250-CS-HR-N18 ^a	0.50	478	14	220	-203	28.27	3.97
60X60X3.0X2050-CS-CF-N19 ^a	0.53	361	10	220	-205	24.27	5.70
40X40X4.0X2050-CS-CF-N20 ^{a, c}	0.89	410	13	230	-150	28.16	4.26
40X40X3.0X2050-CS-CF-N21 ^{a, c}	0.90	451	10	200	-125	18.07	4.47
40X40X3.0X1250-CS-CF-N22 ^a	0.50	451	10	200	-185	18.86	4.51
60X60X3.0X2850-SS-CF-N23 ^a	0.89	483	9	395	-197	33.51	10.68
50X50X3.0X2850-SS-CF-N24 ^a	1.16	552	13	330	-160	58.58	9.36
60X40X3.0X2850-SS-CF-N25 ^{a, c}	1.40	538	10	370	-105	31.41	8.44
60X60X3.0X2050-SS-CF-N26 ^a	0.62	483	10	390	-280	37.63	10.10
50X50X3.0X2050-SS-CF-N27 ^a	0.80	552	10	375	-205	30.39	8.61
60X40X3.0X2050-SS-CF-N28 ^a	0.97	538	10	370	-178	28.25	7.69
60X60X3.0X1250-SS-CF-N29 ^a	0.34	483	10	390	-350	30.53	8.28
50X50X3.0X1250-SS-CF-N30 ^a	0.45	552	10	360	-290	25.57	7.54
60X40X3.0X1250-SS-CF-N31 ^a	0.54	538	9	360	-280	21.59	6.61
^a Tested to failure							
^b Tested to maximum displacement ductility demand of between 5.6 and 9.5 without specimen failure							
^c Failed at end condition during physical test							

As shown in the hysteretic response in Figure 3.2b, the loading was applied according to the provisions of the ECCS (1986) discussed earlier. After the occurrence of the first buckling in compression at Point 1, the compressive strength decreased as a plastic hinge formed at the mid-height of the brace and next to the connection with the stiffener. The compressive strength continued to degrade significantly due to the Baushinger effect (an increase in tensile yield strength causes decrease of the compressive yield strength) and to residual deformations from previous cycles. After yielding, at every cycle of increased displacement amplitude, the brace accumulated permanent elongation. For stockier members, the local imposed deformation at hinge location is increased at each cycle and the amount of inelastic rotation imposed to the hinge is increased. As the brace is stocky with slenderness ratio, $\bar{\lambda}$, of 0.4, local buckling of the cross section developed at the hinge location at mid-height and close to the end stiffeners, which induced high localised strains in the steel material and contributed to reduce the brace compressive strength further. The maximum tension force obtained is shown at Point 2 in Figure 3.2(b). Fracture took place at the hinges at Point 3 when the brace was stretched in tension after local buckling has occurred, and the ultimate failure occurred at Point 4. The described failure of the specimen above is shown in Figure 3.3. It should be noted that the above sequence of behaviour was observed for the stockier members only (e.g. those specimens with normalised slenderness less than 1.3). For more slender specimens (e.g. those specimens with normalised slenderness greater than 1.3), little or no local buckling was observed during the tests. However, premature fracture occurred for specimens with high slenderness ratios (i.e. specimens with slenderness ratio of 3.2). Eurocode 8 (CEN 2004) specifies limits to the normalised slenderness ratio between 1.3 and 2.0 for concentrically braced frames with X diagonal bracing and suggests to use low width to thickness ratio and Class 1 cross-section defined in Eurocode 3 (CEN 2005). Further details on specimens and physical test set-up, as well as specimen performance in low cyclic fatigue loading are given in Goggins et al. (2005).

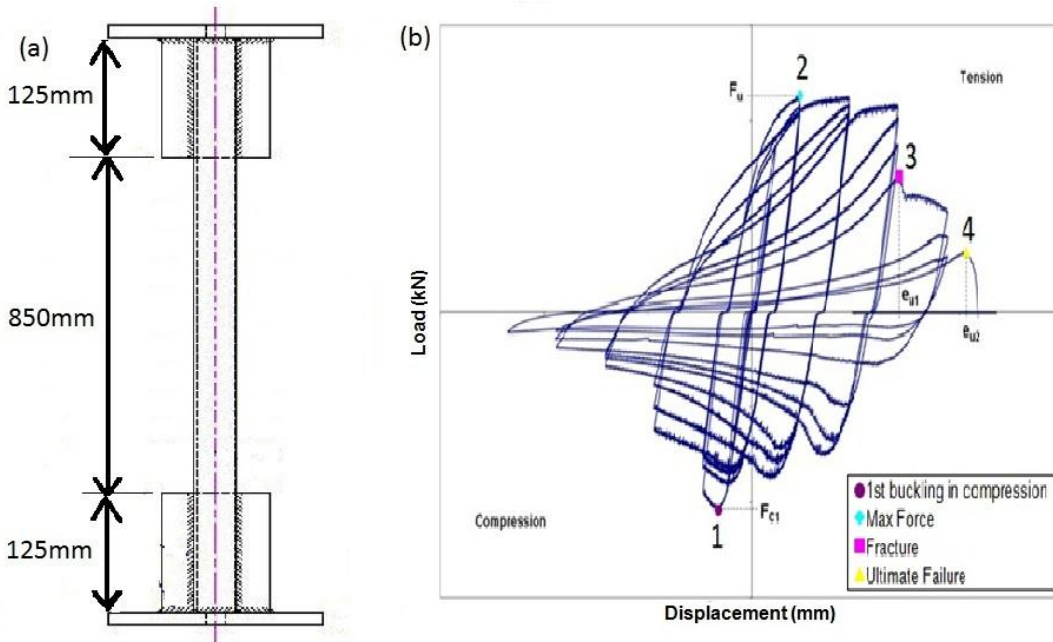


Figure 3.2: (a) Specimen diagram and (b) experimental load-displacement response of the Specimen 40X40X.2.5X1100-CS-CF-G1 (Goggins 2004).

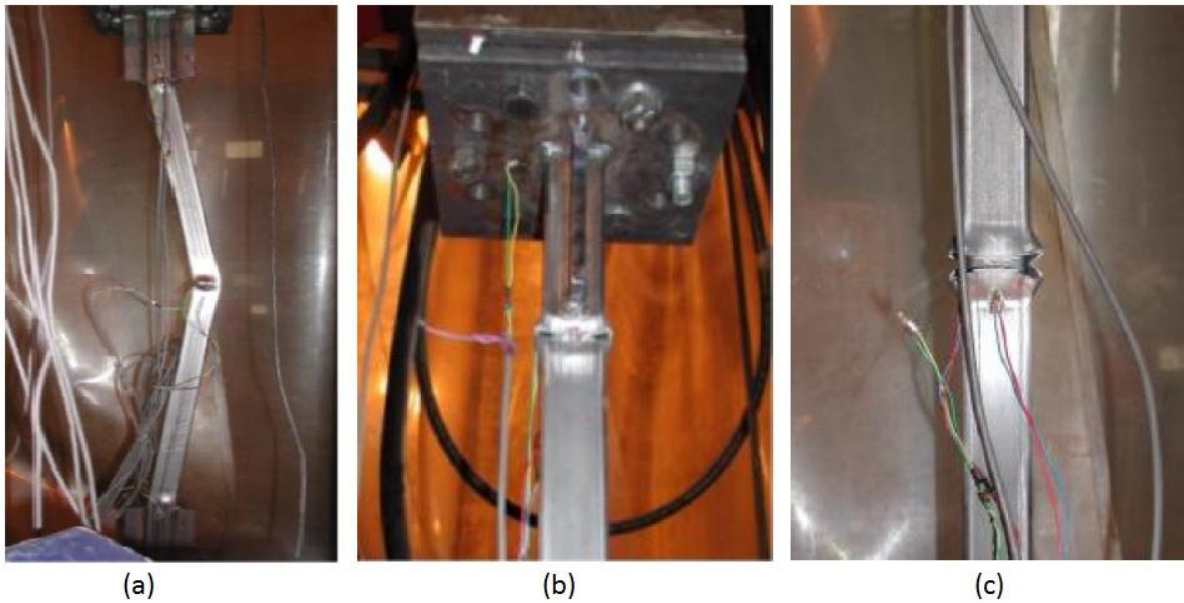


Figure 3.3: Failure of specimen 40X40X.2.5X1100-CS-CF-G1. (a) Lateral and local buckling. (b) Fracture across local buckled area near top stiffener. (c) Fracture across local buckled area at mid-height of the specimen (Goggins 2004).

3.3 Numerical modelling of steel brace elements

The computational framework Open System for Earthquake Engineering Simulation (OpenSees) (McKenna et al. 2000) is used in this study to develop numerical models of structural steel hollow section brace elements that capture the salient features of the response of these elements to low-cycle tension-compression loading. OpenSees uses the physical-theory models to represent the braces. Two ways to represent the physical theory models are found in Opensees. The first is distributed plasticity, which considers the spread of plasticity along the element and is used for this work. The second is concentrated plasticity (also known as lumped plasticity), where the interior of the element behaves elastically with plasticity considered to be concentrated over specified hinge lengths at the element ends. Lotfollahi and Alinia (2009) used two different nonlinear finite element programmes to study the behaviour of braces. They have studied three different tension braces, one is designed according to AISC seismic provisions (2005), the second is weaker and the third is stronger brace element in three typical sets of single storey braced moment resisting frames. They used lumped plasticity models in the software package RAM-Perform 3D (RAM-Perform 3D 2003), and distributed plasticity models in the software package ABAQUS (2006). They found that the maximum difference between the two approaches in the linear stage is 4.1% and in the nonlinear stage 5.8%, as shown in Figure 3.4. This shows that using either lumped plasticity approach or distributed plasticity approach will be satisfactory as the results are close. The material model used is Uniaxial Giuffre-Menegotto-Pinto steel material model with isotropic strain hardening and monotonic envelop with Young modulus equal to 200GPa. The displacement history was applied according to the provisions of the ECCS (1986) which is identical to the history used in the tests. An example of the OpenSees numerical model is shown in Appendix C1.

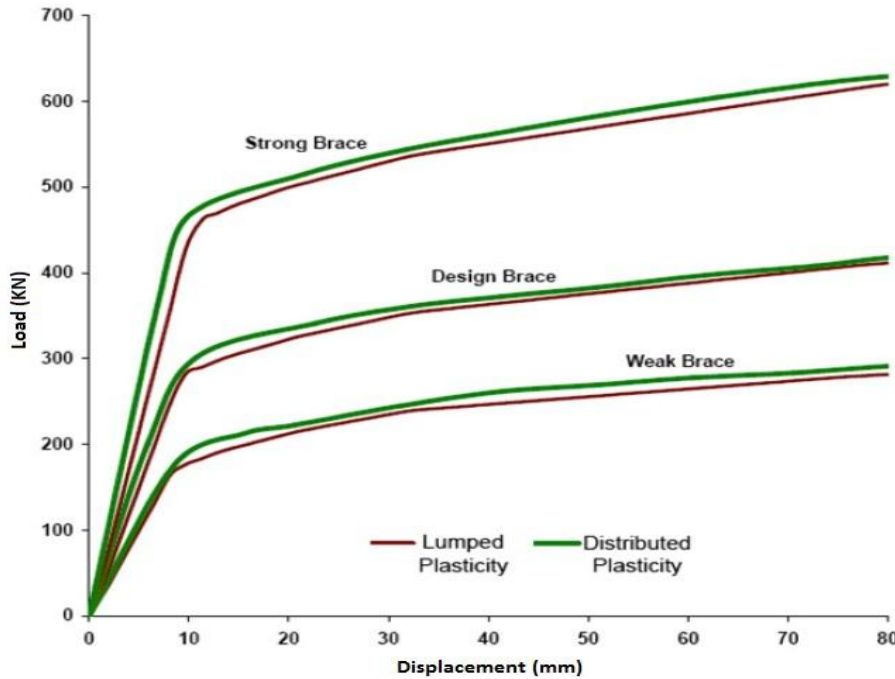


Figure 3.4: Pushover curves of braced moment resisting frame while using lumped and distributed plasticity, adapted from Lotfollahi and Alinia (2009).

The main limitation in the physical theory model used in OpenSees is that plane sections are assumed to remain plane and it does not account for the section distortion and the local buckling, so the accuracy of the model is degraded after the occurrence of the local buckling. This limitation can be minimised by calibrating the parameters of the numerical model to represent test models.

Many commercial software packages available to represent the brace behaviour use finite element models that can overcome the limitations in the physical theory models (for example ANSYS (2002), RAM-Perform 3D (2003), and ABAQUS(2006)). These programmes can be used efficiently for individual elements. However, for the purpose of this work, where the brace element model is studied to be extended to be used for multi-storey structure investigations, the finite element models are not recommended because of the complexity of the models, difficulties in preparing input files and the computational expenses to run them, especially for whole building structures.

A numerical model to be used in OpenSees for brace members was proposed by Uriz (2005), which is able to model the effect of global buckling. Uriz (2005) also calibrated a material model that can be incorporated in the numerical model to account for the effects of low cyclic fatigue, which will be discussed and implemented in Section 3.4.

Many parameters affect the behaviour of the numerical brace model, such as initial camber, number of integration points and number of elements. These will be studied in the following paragraphs in order to obtain a robust numerical model that can be validated using data from physical member tests. A graph of the numerical model setup is shown in Figure 3.5. This model matches the general characteristic of the physical test specimen, including the specimen length, end conditions and material properties for each individual cyclic test specimen used. End stiffeners were also modelled. Fixed end conditions were provided except for the axial displacement at the loaded end (Point 5 at Figure 3.5). The numerical model will first be developed using fifteen cyclic tests carried out by Goggins (2004) and then be validated using sixteen cyclic tests carried out by Nip et. al. (2010).

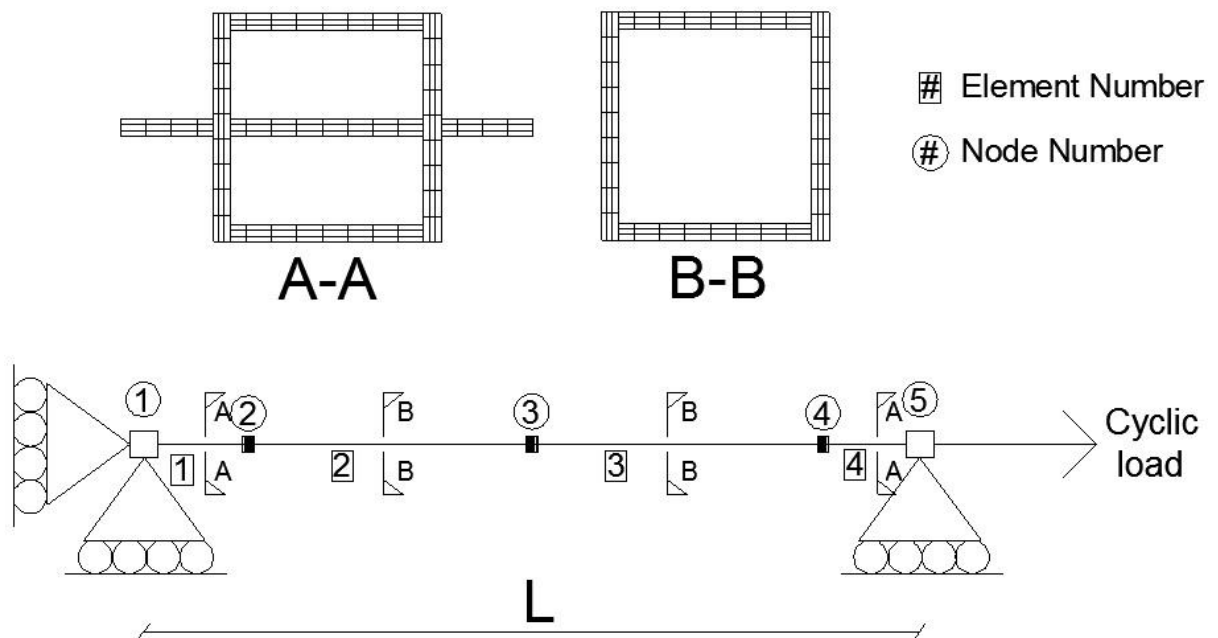


Figure 3.5: Setup and loading direction of the numerical model used in OpenSees.

The uniaxial Giuffre-Menegotto-Pinto steel material model with isotropic strain hardening and the monotonic envelop shown in Figure 3.6 is used in this study. However, a low value of strain hardening (<0.008) was used in this study.

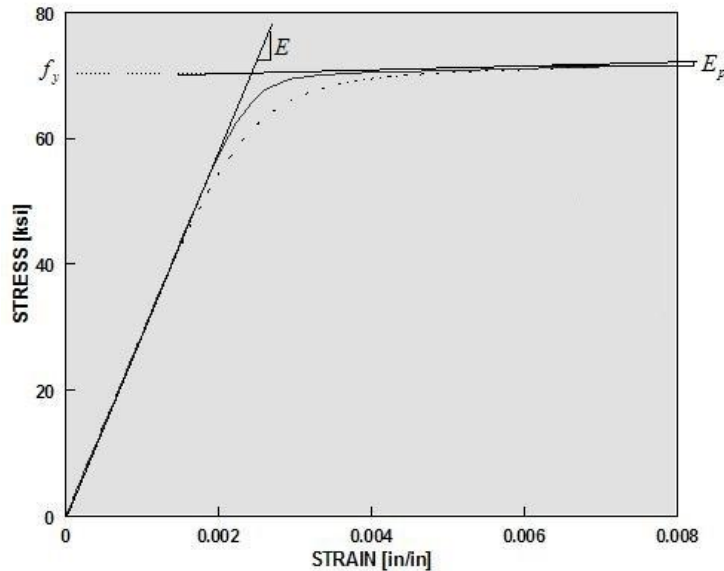


Figure 3.6: Monotonic envelop for uniaxial Giuffre-Menegotto-Pinto steel material (McKenna et al. 2000).

A nonlinear fibre beam-column element model based on the force formulation proposed by Spacone et al. (1996) is used. This model considers the spread of plasticity along the element through integration of material response over the cross section and subsequent integration of section response along the element. The inelastic beam-column element is derived by small deformation theory, which is used for computation of local stresses and strains along the element. In accordance to the corotational theory described by Filippou and Fenves (2004), nonlinear geometry under large displacements is accounted for during transformation of the element forces and deformations to the global reference system. By using the corotational theory the moderate to large deformation effects of inelastic buckling of the concentric brace can be presented (small strains and large displacements). Using this approach, the brace needs to be subdivided into at least two inelastic beam-column elements. However, it may be necessary to divide the brace into more elements to represent accurately local deformations and steel strains at the critical sections.

In order to get accurate buckling loads and hysteretic behaviour, Opensees represents elements by fibres. Uriz (2005) noted that when there are fewer fibres representing the cross section, sensitivity to the interaction between moment and axial loads increased and a loss of stiffness when Opensees numerically integrates to determine the area moment of inertia is found. When there are fewer fibres representing the same area, lower centroid for the fibres will be achieved and the equivalent moment of inertia will be smaller than the cross section with more fibres. This calculation is more sensitive to the number of fibres across the thickness than the number of fibres around the perimeter.

To check the effect of changing number of fibres across the thickness, a comparison of the response of the numerical model was carried out using 1, 3, and 5 fibres across the thickness and $2(h+b)/3$ fibres around the perimeter of the cross section where b and h are the width and the height of the cross section in mm. The results of the comparison are shown in Figure 3.7. It is found that there is a difference in the behaviour when using 1 fibre compared to using 3 fibres across the thickness with a maximum difference of 12%. However, almost identical results were found when using 3 and 5 fibres across the thickness with a maximum difference of less than 1%. For that, a recommendation of using a minimum of 3 fibres across the thickness is made in this study.

To check the effect of changing number of fibres along the perimeter of the cross section, a comparison of the response of the numerical model was carried out using a number of fibres of $2(h + b)/5$, $2(h + b)/3$, $2(h + b)/1$ respectively around the perimeter as shown in Figure 3.8. Three fibres across the thickness are used. It is found that there is a difference in the behaviour when using a number of fibres around the perimeter of $2(h + b)/5$ and $2(h + b)/3$ fibres with a maximum difference of 4%. However, nearly identical results were found when using $2(h + b)/3$ and $2(h + b)/1$ fibres along the perimeter with a maximum difference of 0.4%. For that, a recommendation of using a minimum of $2(h + b)/3$ fibres along the perimeter is made in this study.

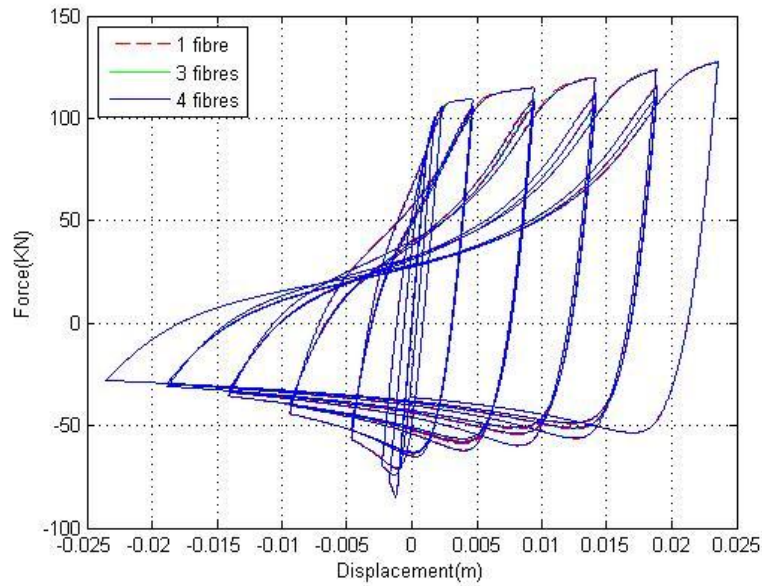


Figure 3.7: Effect on the force displacement response of changing the number of fibres across the thickness of the cross section of the brace in the numerical model.

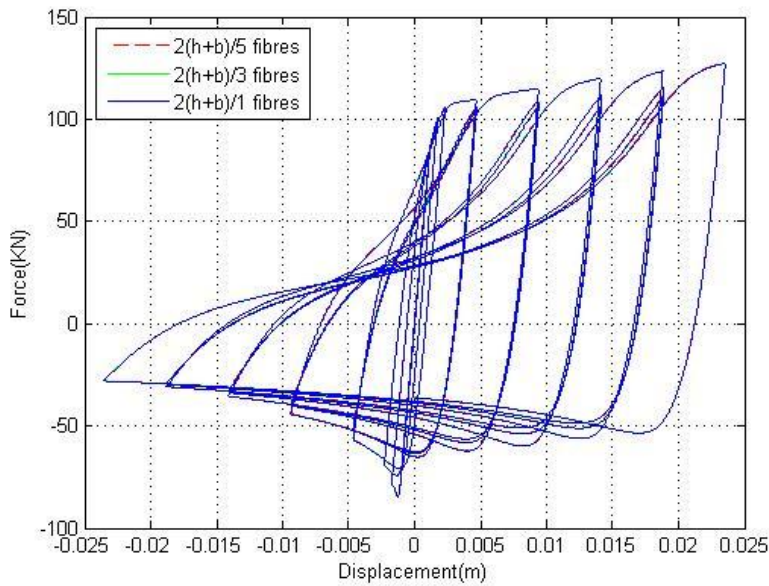


Figure 3.8: Effect on the force displacement response of changing the number of fibres along the perimeter of the cross section of the brace in the numerical model.

In OpenSees, in order to consider buckling in an axially loaded brace, it is essential to include an imperfection either to the geometry of the brace in the form of initial camber

or to the properties of the member in the form of a residual stress distribution over the cross section. In this model, initial camber is used to consider buckling. Uriz (2005) proposed to use an initial camber displacement at mid-length of the brace with a magnitude varied between 0.05 to 0.1% of the brace length, whereas Wijesundara (2009) recommends to use the initial camber displacement at mid-length of 0.5% of the brace length.

Small initial cambers between 0.05 and 0.1% were found to be suitable for stocky members. However, when using these values for intermediate and slender members, it is found that the buckling is delayed and the buckling force is overestimated in comparison to measured values from physical tests, as shown in Figure 3.9. On the other hand, incorporating initial cambers of 0.5%, as recommended by Wijesundara (2009), was not representing the observed response for all members. For this study, initial camber between 0.1 and 1.0% is found to give satisfactory results, where the lower bound is used for stockier specimens and larger initial camber values are used for more slender specimens, as will be shown in Section 3.5. It is also noted that for a brace member with specified material and section properties, the initial camber is the main parameter that plays the major role for determining the first buckling load in the numerical model, but does not affect the general behaviour of the hysteretic response.

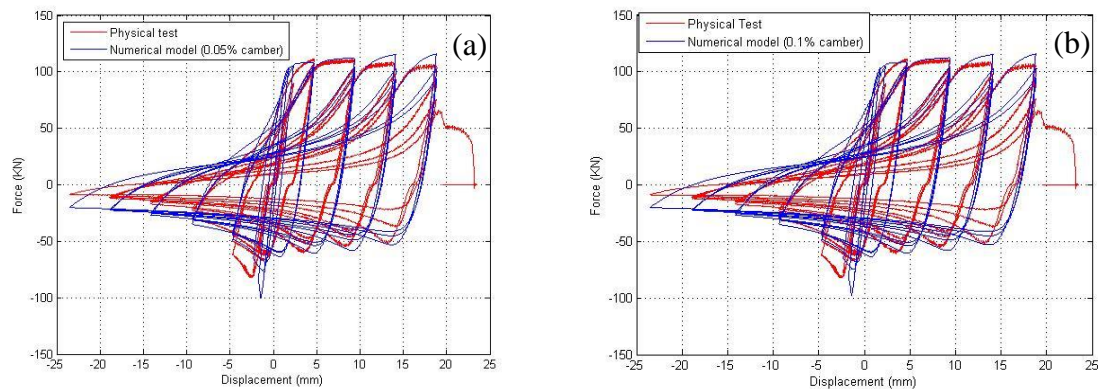


Figure 3.9: Experimental force-displacement response of specimen 50X25X2.5X1100-CS-CF-G5 compared to the hysteretic model found from OpenSees with (a) 0.05% initial camber and (b) 0.1% initial camber.

Figure 3.10 shows the effect of changing the number of non-linear beam column elements for the unstiffened length of the brace in the numerical model for the force displacement response using 3 integration points per element and constant initial camber of 0.5% of the length of the brace. By changing the number of non-linear beam column elements, the first buckling strength is nearly identical and relatively insensitive to the number of sub-elements, but depends upon initial camber value used. However, the brace modelled with two elements resists less force than a brace modelled with four elements in the post buckling range with a maximum difference of 18.7% (Figure 3.10). Similarly, a brace modelled with eight elements resists slightly less force in the post buckling range than the brace modelled with four elements with a maximum difference of 5.8% (Figure 3.10).

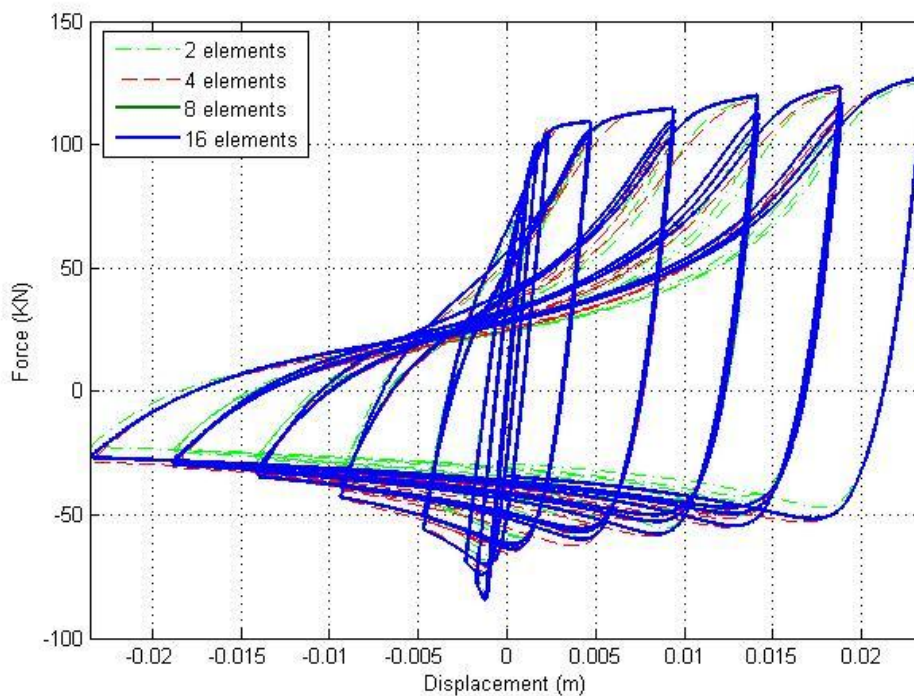


Figure 3.10: Effect on the force displacement response of changing the number of non-linear beam column elements to represent the unstiffened length for the brace in the numerical model using 3 integration points per element.

The brace modelled with sixteen elements has nearly identical behaviour in the post buckling range and the internal curvature with the brace modelled with eight elements (Figure 3.10). However, there was a maximum difference of 1% in the post buckling range at the second loop, but it was nearly identical for other loops. As expected, the internal curvature and the post buckling range are more accurately represented when more elements are used with three integration points per element. From the above, it is noted that a minimum number of elements of eight should be used while using three integration points. On the other hand, it is expected that less elements can be used in the brace when more integration points are assigned, in order to minimise the time needed for modelling and computational efforts.

The integration along the element is based on Gauss-Lobatto quadrature (integration) rule (two integration points at the element ends) (McKenna et al. 2000). This numerical quadrature rule interpolates polynomial displacements of order $2n-3$ exactly, where n is the number of integration points. However, due to nonlinear material properties, these polynomial interpolants may not be physically accurate, which may result in distributions of deformations that are not adequately described by polynomials (Uriz 2005). Uriz (2005) observed that the specimen with only two integration points exhibits a slightly more dramatic loss of compressive strength in the post-buckling range. This can also be seen in Figure 3.11. This is due to an under integration of the element. Under-integration of element response is not recommended and the minimum number of integration points recommended for every inelastic beam-column element is three (Uriz 2005). In Figure 3.11, the brace was divided into eight elements and different integration points were used for every element. While using two integration points, lower compression resistance in the post buckling range is observed as compared to models containing three, five and seven integration points with a maximum difference of 18%. However, identical results in hysteretic response were found in models containing three, five, and seven integration points as observed in Figure 3.11.

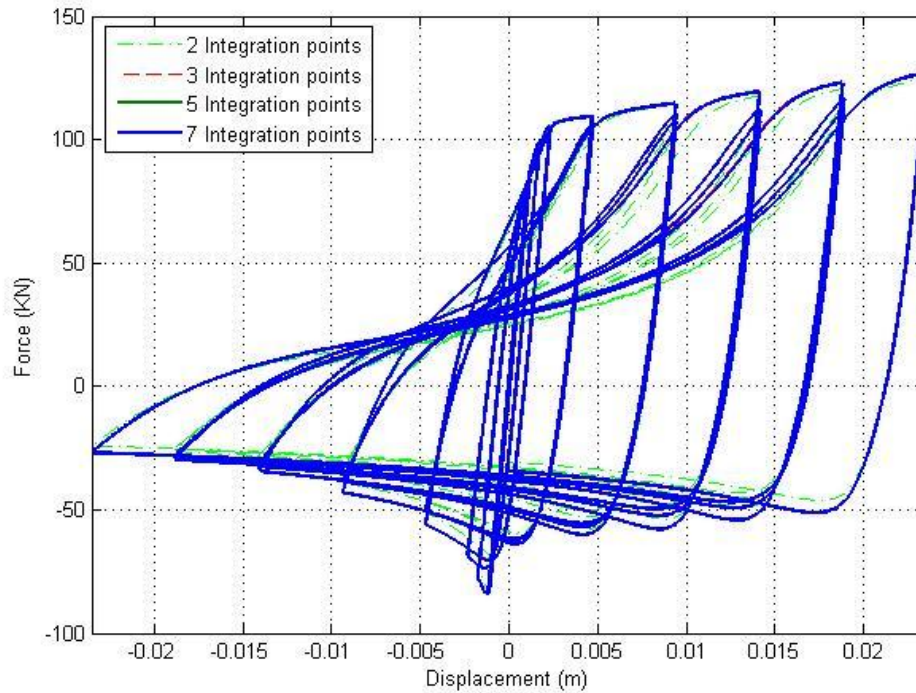


Figure 3.11: Effect on the force displacement response of changing the number of integration points for the brace in the numerical model using eight non-linear beam-column elements per brace over the unstiffened length.

To check the interaction between the number of elements of the brace and the number of integration points per element, a comparison of the response of the numerical models was conducted by changing the number of elements and the number of integration points per element as follows: eight elements with three integration points per element, six elements with four integration points per element, four elements with six integration points per element and two elements with ten integration points per element, which is the maximum integration points that can be used for an element in OpenSees. Figure 3.12 shows that when a finer subdivision is used by dividing the brace into a number of elements or dividing the sub-element into number of integration points the results are nearly identical with a maximum difference of 9% between the hysteretic curves. Thus, two elements with 10 integration points per element for the buckling brace could be a suitable choice.

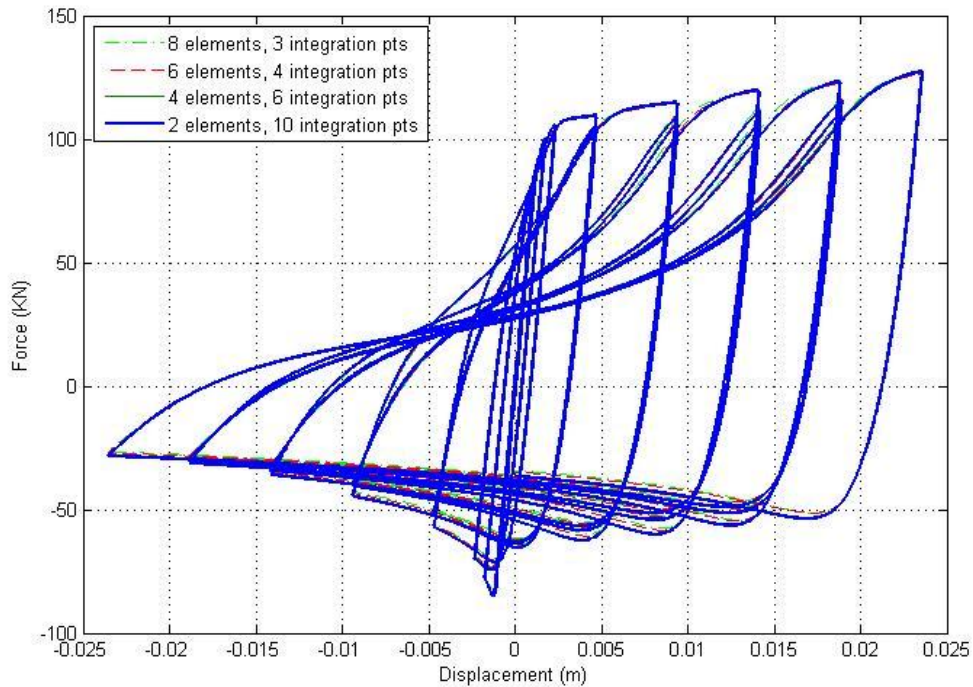


Figure 3.12: Effect on the force displacement response of changing both the number of elements and integration points for the unstiffened brace in the numerical model.

A sensitivity analysis on the predicted behaviour of the model containing two elements and various numbers of integration points (three, four, five, six, eight and ten) was conducted (see Figure 3.13). It is concluded that two elements and three integration points cannot accurately represent the real hysteretic response of brace members with a maximum difference of 32% when compared to the results obtained from the numerical model while using two elements and ten integration points per element. Furthermore, there is a difference as well in the behaviour when using four, five and six integration points with a maximum difference of 23%, 19% and 13% respectively when compared to the results obtained from the numerical model while using two elements and ten integration points per element. However, close results were found when using eight and ten integration points per element with a maximum difference of 8%. In this study, a minimum number of ten integration points per element is recommended while using 2 elements per brace.

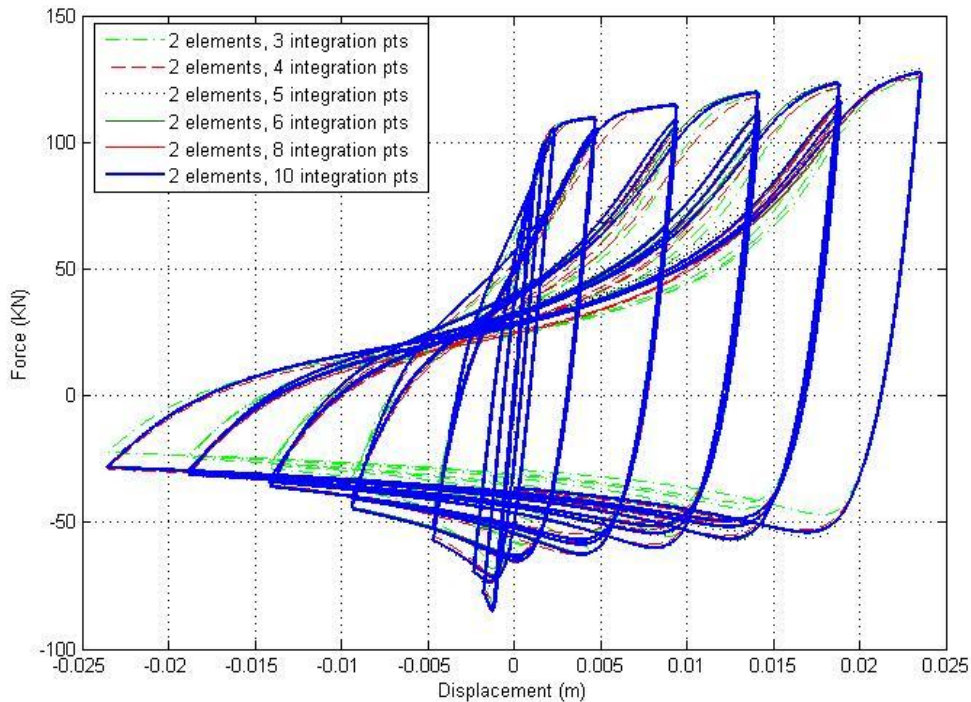


Figure 3.13: Effect on the force displacement response of changing the number of integration points for the brace in the numerical model using two non-linear beam-column elements per brace over the unstiffened length.

To assure the validity of the numerical model, a comparison between the performance of the model to cyclic and monotonic loading is carried out in OpenSees for the same brace element as shown in Figure 3.14. Acceptable results are found, specifically for the first and post buckling loads. However, maximum tensile forces in the brace member during the first cycle at each new displacement demand were higher than those predicted in monotonic tests in post yield range. An explanation for this difference may be the numerical rounding, especially with the massive number of numerical operations required. On the other hand, the maximum tensile force experienced in second and third cycles at a given displacement amplitude were reduced due to Baushinger effect.

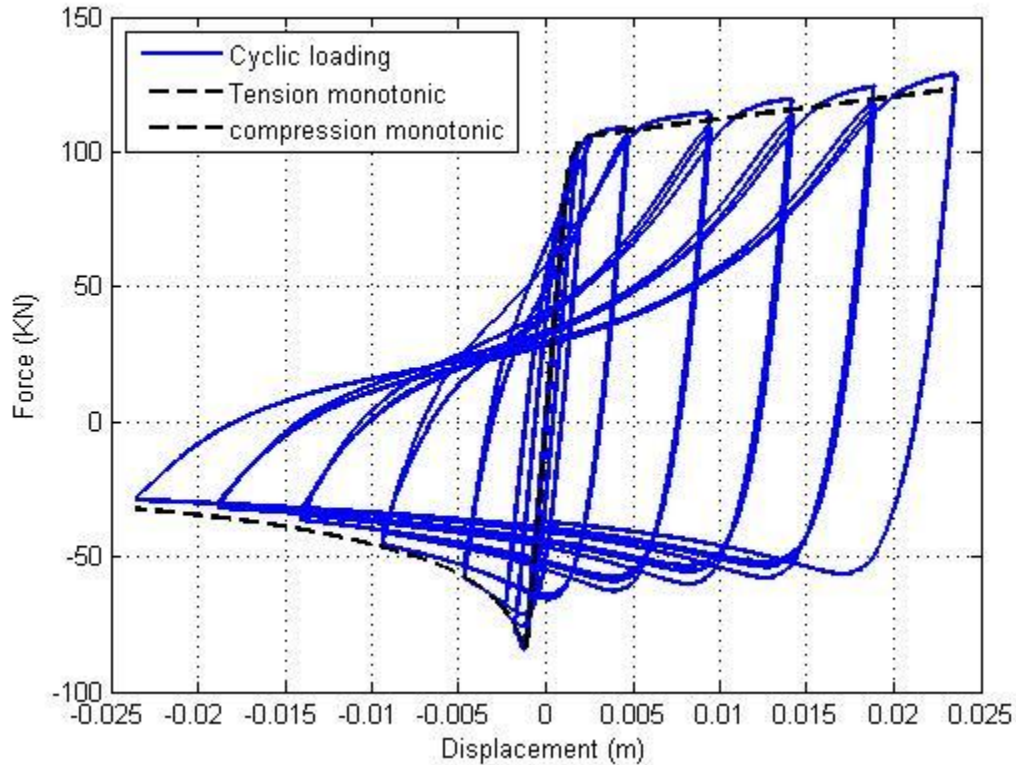


Figure 3.14: Comparison of response of numerical model to monotonic and cyclic loading.

3.4 Low cyclic fatigue modelling

Brace steel members subjected to inelastic cyclic loading suffer stages of buckling and yielding. After the occurrence of buckling, rotational plastic hinges can form. They experience large rotational demands undergoing large strain deformation histories causing fracture due to low cyclic fatigue. Fatigue process consists of three stages: initial crack nucleation, progressive crack growth across the section and finally a sudden fracture of the remaining cross section. The fatigue strength of a material is determined experimentally. This is achieved by subjecting test specimens to repeated loads or strains of specified amplitude or ranges, and determining the number of cycles required to produce failure (Duggan and Byrne 1977). ASTM (2005) defines fatigue life, N_f , as the number of cycles of stress or strain of a specified character that a given specimen sustains before failure of a specified nature occurs.

Occurrence of local buckling within the plastic hinge increases strain demands, causing faster fracture initiation. When local buckling occurs, and the braces deform in compression, cracks will form after the braces are loaded in tension (Gugerli 1982; Lee and Goel 1987; Shermann 1996; Tremblay 2002; Goggins 2004). From the cyclic tests carried out by Goggins (2004) and discussed earlier, it is found that slender braces can exhibit better fracture life performance than braces with low member slenderness ratio. A possible reason of that is the occurrence of local buckling within the plastic hinge for stockier members, which increases strain demands and reduce fatigue life.

To quantify the damage in braces, a discrete form of damage accumulation rule called Palmgren–Miner’s rule can be used. This rule describes the damage in the low cycle fatigue with constant plastic strain amplitude and associated with the relative reduction of deformability to quantify the damage for cyclic loading, DI, as in Equation [3.1] (Xue 2008).

$$DI = \frac{4n\Delta\varepsilon_p}{4N_f\Delta\varepsilon_p} \quad [3.1]$$

where $\Delta\varepsilon_p$ is the plastic strain amplitude, n is the current number of cycles and N_f is the number of life cycles. In Equation [3.1], the numerator $4n\Delta\varepsilon_p$ denotes the current plastic strain and the denominator $4N_f\Delta\varepsilon_p$ denotes the total plastic deformability, which varies depending on the given plastic strain amplitude. However, during earthquakes the amplitude of the cycles is not constant. As such, the amplitude of each cyclic excursion in deformation history and the number of cycles at each amplitude identified can be computed using a rainflow cycle counting method (Fisher et al. 1997; ASTM 2003; Uriz 2005). Damage for each amplitude of cycling is estimated by

$$DI_i = \frac{n_i}{N_{fi}} \quad [3.2]$$

where n_i is the number of cycles at an amplitude and N_{fi} is the number of constant amplitude cycles of that amplitude necessary to cause failure. Manson (1953) and Coffin (1954) working independently in fatigue problems, proposed a characterisation of fatigue life based on the plastic strain amplitude. They noted that when the logarithm of the

plastic strain amplitude experienced in each cycle, ε_i , was plotted against the logarithm of the number of cycles to failure, N_f , a linear relationship resulted for metallic materials as shown in Equation [3.3] (Stephens et al. 2001).

$$\varepsilon_i = \varepsilon_0(N_f)^m \quad [3.3]$$

where ε_0 is the fatigue ductility coefficient which is the material parameter that roughly indicates the strain amplitude at which one complete cycle on a virgin material will cause failure, and m is the fatigue ductility exponent which is the material parameter which describes the sensitivity of the log of the total strain amplitude to the log of the number of cycles to failure.

Overall damage due to low cycle fatigue is estimated by linearly summing the damage for all of the amplitudes of deformation cycles considered (ε_i) (Uriz 2005). During cycling, to get N_{fi} for current amplitude, constant coefficients ε_0 and m for Equation [3.3] should be known and Equation [3.2] can be written as

$$DI_i = \frac{n_i}{10^{\left(\frac{\log\left(\frac{\varepsilon_i}{\varepsilon_0}\right)}{m}\right)}} \quad [3.4]$$

Uriz (2005) developed and calibrated a low cycle fatigue model to be used with the Opensees fibre-based nonlinear beam-column model for simulating the large displacement and the inelastic buckling behaviour of steel struts. As described in OpenSees command language manual (McKenna et al. 2000), in order to account for the effects of low cycle fatigue, a modified rainflow cycle counter has been implemented to track strain amplitudes. Rainflow cycle counting necessitate examination of the entire time strain history for each fibre at each time step, since the strain history changes as each increment of strain occurs. Thus, rainflow cycle counting analyses strain histories after the termination of loading to determine the number and the amplitude of the imposed cycles. Because of the computational effort involved in this procedure, a modified method is proposed by Uriz (2005) that utilizes the traditional rainflow cycle counting method to accumulate damage, but does so by analyzing only a relatively short moving window of recent strain history. This cycle counter is used in Miner's Rule

shown in Equation [3.4] as the linear strain accumulation model based on Coffin-Manson log-log relationships describing low cycle fatigue failure. This material wraps around the parent material and does not influence the force-deformation relationship of the original material. Once the fatigue material model reaches a damage level of one, the resistance of the parent material becomes zero. More precisely, in practice the material stress of the parent material is reduced to 1.0×10^{-8} MPa. If failure is triggered in compression, the material stress is dropped at the next zero-force crossing where compression force never drops to zero. The fatigue material assumes that each point is the last point of the history, and tracks damage with this assumption. If failure is not triggered, this pseudo-peak is discarded. The material also has the ability to trigger failure based on a maximum or minimum strain.

In summary, damage during each cycle is found based upon Palmgren–Miner’s using coffin-Manson relationship where constant coefficient ϵ_0 and m should be calibrated. Accumulated damage is found by using Palmgren–Miner’s rule assuming the damage accumulated linearly using a modified rainflow cycle counting technique as in the following Equation:

$$DI_{i+1} = DI_i + \frac{n}{10^{\left(\frac{\log\left(\frac{\epsilon}{\epsilon_0}\right)}{m}\right)}} \quad [3.5]$$

If in any point the damage index at time step $i+1$ (DI_{i+1}) becomes one or more, then the corresponding fibre in the cross section is removed from the cross section by reducing its stress and stiffness to zero.

Uriz (2005) calibrated OpenSees low cyclic fatigue models for four different sections and found the constant coefficient for each of them as follows: wide flange sections ($\epsilon_0 = 0.191$, $m = -0.458$), hollow structural section (HSS) members ($\epsilon_0 = 0.095$, $m = -0.5$), buckling restrained brace (BRB) members ($\epsilon_0 = 0.12$, $m = -0.458$) and reinforcing bars ($\epsilon_0 = 0.081$, $m = -0.43$). It is evident that most of the material models have a very similar value for the parameter, m , but the value of ϵ_0 varies significantly between section types. For the HSS, the fatigue parameters were calibrated for 6”X6”X3/8” HSS members only.

In this chapter, new parameters representing different brace sections are proposed. It is important to know that the model does not account for the local buckling effect and the computed strains do not represent the actual strains in the member, but parameters used in the model can be calibrated to compensate for this fact.

To check a consistent model for the minimum number of elements that can be used for the brace using the fatigue model and the number of integration points per element, numerical models are tested using different number of elements and constant number of integration points. It is found that using six integration points per element with four elements or more gives consistent results as shown in Figure 3.15. On the other hand, using 10 integration points per element with two elements for the numerical model is satisfactory and gives the same results as dividing the brace into more elements, as shown in Figure 3.16. This is a similar finding to the sensitivity study presented in Section 3.3, which investigated a similar numerical model without the fatigue model.

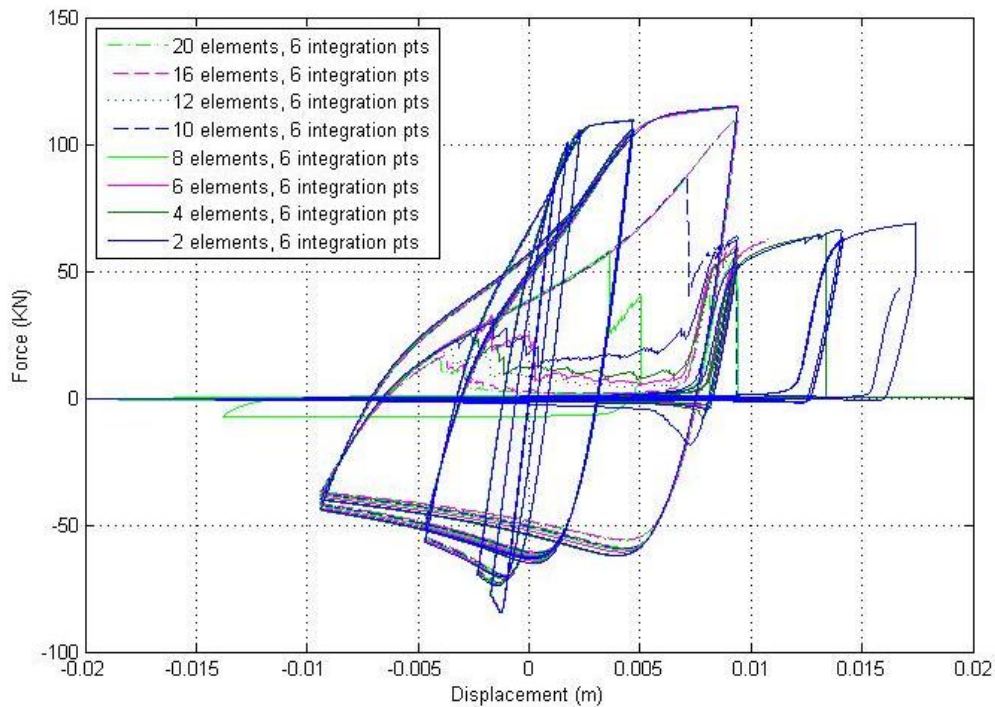


Figure 3.15: Effect on the force displacement response of changing the number of non-linear beam column elements for the brace in the numerical model while using the fatigue model and 6 integration points per element.

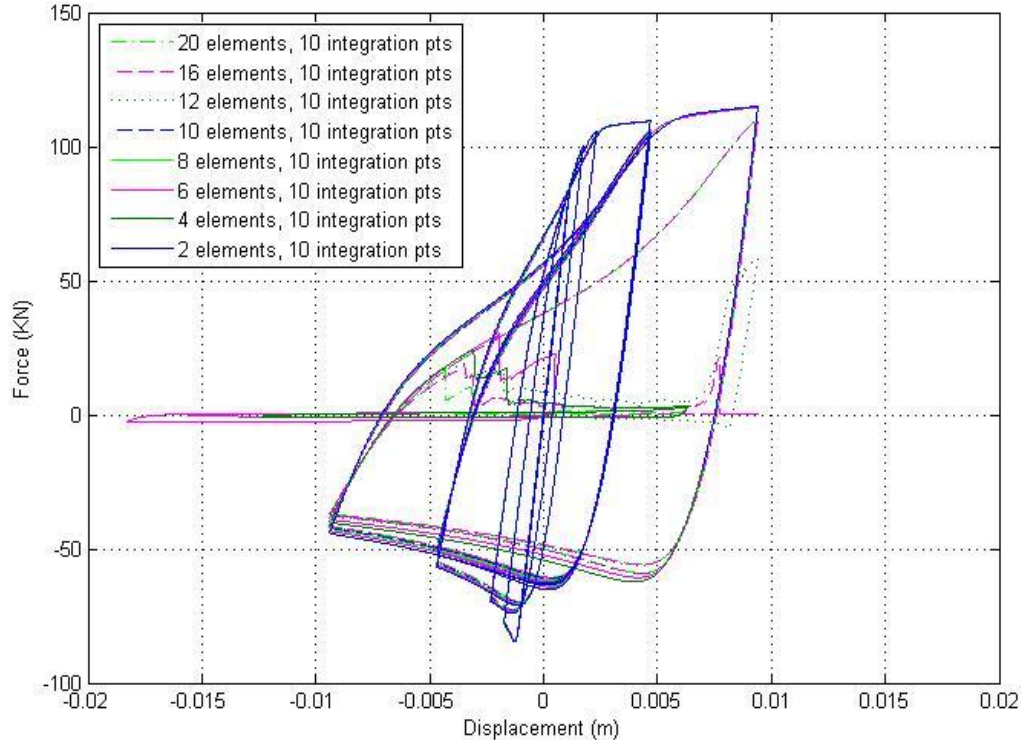


Figure 3.16: Effect on the force displacement response of changing the number of non-linear beam-column elements for the brace in the numerical model while using the fatigue model and 10 integration points per element.

The numerical models incorporating the fatigue model with the parameters suggested by Uriz (2005) did not represent the real behaviour of the physical specimens tested by Goggins (2004) during the cyclic loading, where the numerical model force decreases faster than the real behaviour of the specimen, as shown for example in Figure 3.17. This may be due to the fact that Uriz (2005) only used one section size (6"X6"X3/8" HSS) to calibrate his model. He suggested performing further refinement of input parameters for other sizes, width-to-thickness ratios or shapes. Thus, the model was re-calibrated using new parameters that can represent the behaviour of the specimens with a range of normalised slenderness ratios from 0.4 to 3.2. After many trials, it was found that by calibrating the fatigue parameters in the numerical model to $\varepsilon_0 = 0.19$ and $m = -0.5$, better results are achieved, at least for the sections tested by Goggins (2004), as will be shown

in the next section. Further, independent tests by Nip et al (2010) are used to validate this numerical model.

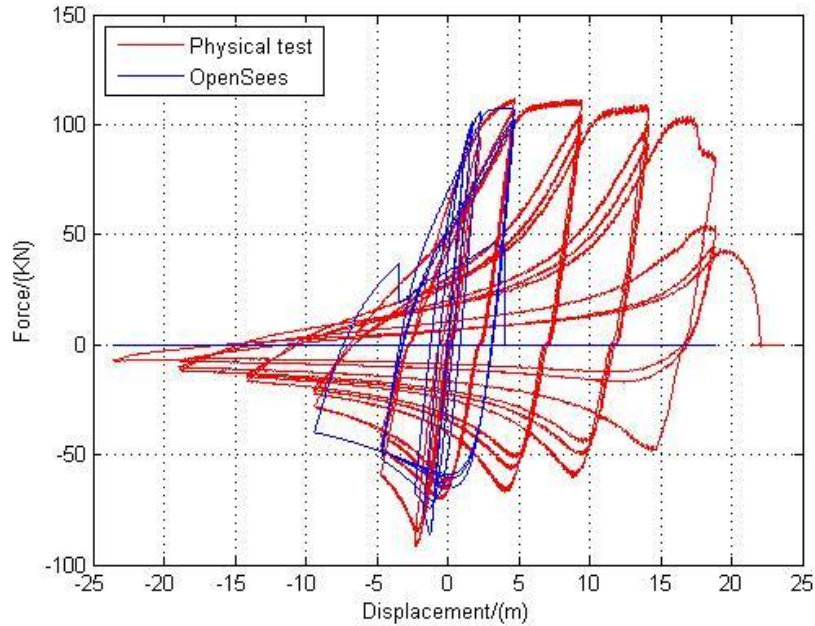


Figure 3.17: Experimental force-displacement response of the specimen 50X25X2.5X1100-CS-CF-G6 compared to the hysteretic model in OpenSees using parameters suggested by Uriz (2005).

3.5 Verification of the numerical model

OpenSees numerical models were studied for fifteen cyclic test specimens carried out by Goggins (2004) and sixteen cyclic test specimens carried out by Nip et. al. (2010). Cyclic tests were having different dimensions, lengths, normalised slenderness ratios, and material properties, as shown in Table 3.2 and Table 3.3.

Most of the parameters for the numerical models were taken the same as the ones found in the physical tests. Strain hardening in the numerical model was ignored in many cases. However, in some models it was necessary to include a low value of strain hardening (<0.008) to improve stability of the analysis. Full fixity is assumed for end conditions. Yield strengths used in the numerical model for the cold form carbon steel specimens carried out by Goggins (2004) are taken as the increased average yield strength, f_{ya} , of the

cross-section due to cold working as specified in Eurocode 3 (CEN 2006) without using the upper limit value:

$$f_{ya} = f_{yb} + \frac{knt^2}{A_g} (f_u - f_{yb}) \quad [3.6]$$

where f_{yb} is the basic yield strength value of sheet obtained from coupon tests, A_g is the gross cross sectional area (mm^2), t is the design core thickness of the steel material before cold forming (mm), n is the number of 90° bends in the cross-section with an internal radius $r \leq 5t$ (fractions of 90° bends are counted as fractions of n), k is a numerical coefficient that depends on the type of forming ($k = 7$ for cold rolling and $k = 5$ for other methods of forming) and f_u is the basic ultimate tensile strength of sheet taken from coupon test. For the tests of Nip et al (2010), the yield strengths are taken as the offset yield strengths with a value set at 0.2% of the strain. This offset yield point is used normally for high strength steel, which does not exhibit a yield point.

A comparison between the hysteretic axial force-axial displacement response for the tests and the numerical model is carried out and shown from Figure 3.18 to Figure 3.48.

Table 3.2 and Table 3.3 give section properties of the specimens, normalised slenderness about the Y-Y axis as defined in Eurocode 3 (CEN 2005), λ_{y-y} , where the effective length is assumed to be $0.5L$, yield strength, f_y , initial camber used in the numerical model, number of cycles needed to fracture for both physical tests and numerical model.

Furthermore, ratios of the maximum tensile force (F_{\max}), initial buckling load (F_c), the total energy dissipated by the specimens (W_{tot}) and the energy dissipated by the specimens at the first cycle of ductility of 4 ($W_{\mu=4}$) found from the numerical models and those measured from the physical tests are given in Table 3.2 and Table 3.3.

Table 3.2: Parameters and results for the specimens used to calibrate the numerical model.

Specimen ID	λ_{v-y}	f_y (MPa)	Initial camber (%)	No. of cycles to fracture		Numerical model/ physical tests			
				physical tests	numerical model	F_{max}	F_c	W_{tot}	$W_{n=4}$
40X40X2.5X1100-CS-CF-G1 ^a	0.40	285	0.10	16	14	1.06	0.99	1.15	1.13
40X40X2.5X1100-CS-CF-G2 ^a	0.40	285	0.10	15	14	1.07	1.02	1.19	1.12
20X20X2.0X1100-CS-CF-G3 ^a	0.90	304	0.50	26	16	0.99	0.87	0.72	1.16
20X20X2.0X1100-CS-CF-G4 ^a	0.90	304	0.50	17	16	0.98	1.03	1.31	1.14
50X25X2.5X1100-CS-CF-G5 ^a	0.60	304	0.30	16	14	1.05	0.90	1.06	1.22
50X25X2.5X1100-CS-CF-G6 ^a	0.60	304	0.30	16	14	1.04	1.00	1.27	1.18
40X40X2.5X3300-CS-CF-G7 ^b	1.30	344	0.50	-	-	0.91	1.03	1.07	0.88
40X40X2.5X3300-CS-CF-G8 ^b	1.30	350	0.50	-	-	0.93	1.02	1.09	0.89
40X40X2.5X3300-CS-CF-G9 ^b	1.30	332	0.50	-	-	0.89	0.99	1.06	0.78
20X20X2.0X3300-CS-CF-G10 ^a	3.20	443	1.00	7	4	0.81	0.82	-	-
20X20X2.0X3300-CS-CF-G11 ^a	3.00	399	1.00	7	4	0.79	0.79	-	-
20X20X2.0X3300-CS-CF-G12 ^a	3.00	399	1.00	7	4	0.76	0.92	-	-
50X25X2.5X3300-CS-CF-G13 ^b	1.90	312	1.00	-	-	1.00	1.00	1.22	0.85
50X25X2.5X3300-CS-CF-G14 ^b	2.20	428	1.00	-	-	0.85	1.00	1.16	0.74
50X25X2.5X3300-CS-CF-G15 ^b	2.20	428	1.00	-	-	0.84	0.92	1.14	0.70
Mean						0.93	0.95	1.12	0.98
C_v						0.11	0.08	0.13	0.20

^a Tested to failure

^b Tested to maximum displacement ductility demand of between 5.6 and 9.5 without specimen failure

Table 3.3: Parameters and results for the specimens used to validate the numerical model.

Specimen ID	λ_{y-y}	f_y (MPa)	Initial camber (%)	No. of cycles to fracture		Numerical model/ physical tests			
				physical tests	numerical model	F_{max}	F_c	W_{tot}	$W_{\mu=4}$
60X60X3.0X2050-CS-HR-N16 ^a	0.57	458	0.20	10	11	1.14	1.14	1.67	1.25
40X40X3.0X2050-CS-HR-N17 ^a	0.89	478	0.50	19	14	1.01	1.19	0.80	1.25
40X40X3.0X1250-CS-HR-N18 ^a	0.50	478	0.20	14	9	1.01	1.05	0.89	1.40
60X60X3.0X2050-CS-CF-N19 ^a	0.53	361	0.20	10	11	0.88	0.92	1.92	1.49
40X40X4.0X2050-CS-CF-N20 ^{a,c}	0.89	410	0.50	13	15	0.95	1.00	1.89	1.27
40X40X3.0X2050-CS-CF-N21 ^{a,c}	0.90	451	0.50	10	13	0.98	0.98	2.30	1.28
40X40X3.0X1250-CS-CF-N22 ^a	0.50	451	0.20	10	9	0.97	1.01	1.05	1.24
60X60X3.0X2850-SS-CF-N23 ^a	0.89	483	0.50	9	13	1.17	0.92	2.63	1.18
50X50X3.0X2850-SS-CF-N24 ^a	1.16	552	0.50	13	14	1.03	1.00	1.45	1.13
60X40X3.0X2850-SS-CF-N25 ^{a,c}	1.40	538	0.50	10	16	1.17	0.85	2.74	1.14
60X60X3.0X2050-SS-CF-N26 ^a	0.62	483	0.30	10	10	1.15	1.00	1.38	1.20
50X50X3.0X2050-SS-CF-N27 ^a	0.80	552	0.50	10	10	1.18	0.93	1.44	1.21
60X40X3.0X2050-SS-CF-N28 ^a	0.97	538	0.50	10	12	1.18	0.95	1.96	1.19
60X60X3.0X1250-SS-CF-N29 ^a	0.34	483	0.10	10	10	1.15	1.08	1.45	1.20
50X50X3.0X1250-SS-CF-N30 ^a	0.45	552	0.10	10	8	1.13	0.96	0.99	1.25
60X40X3.0X1250-SS-CF-N31 ^a	0.54	538	0.20	9	9	1.16	1.01	1.34	1.29
Mean						1.08	1.00	1.62	1.25
C_v						0.09	0.09	0.36	0.07

^a Tested to failure

^c Failed at end condition during physical test

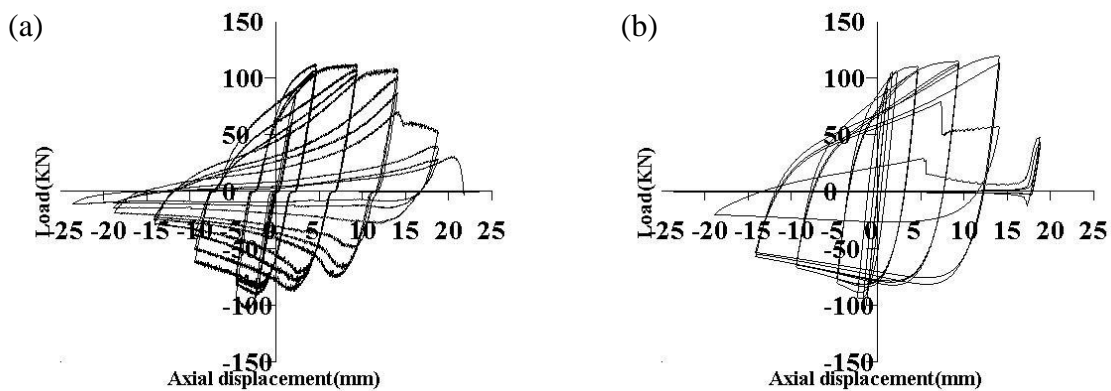


Figure 3.18: (a) Physical test and (b) numerical model load displacement hysteretic loops for Specimen 40X40X2.5X1100-CS-CF-G1.

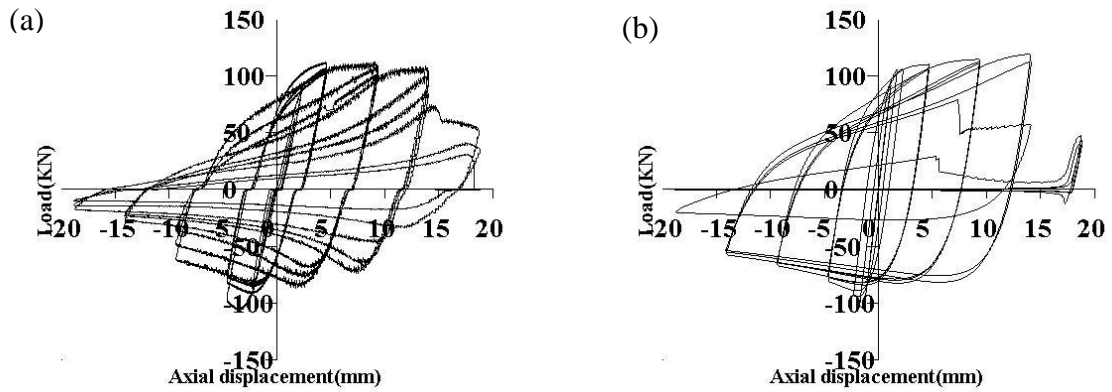


Figure 3.19: (a) Physical test and (b) numerical model load displacement hysteretic loops for Specimen 40X40X2.5X1100-CS-CF-G2.

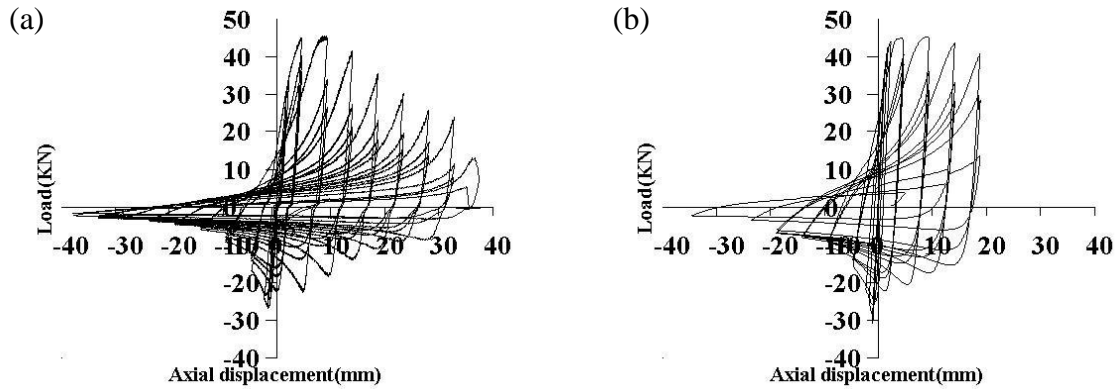


Figure 3.20: (a) Physical test and (b) numerical model load displacement hysteretic loops for Specimen 20X20X2.0X1100-CS-CF-G3.

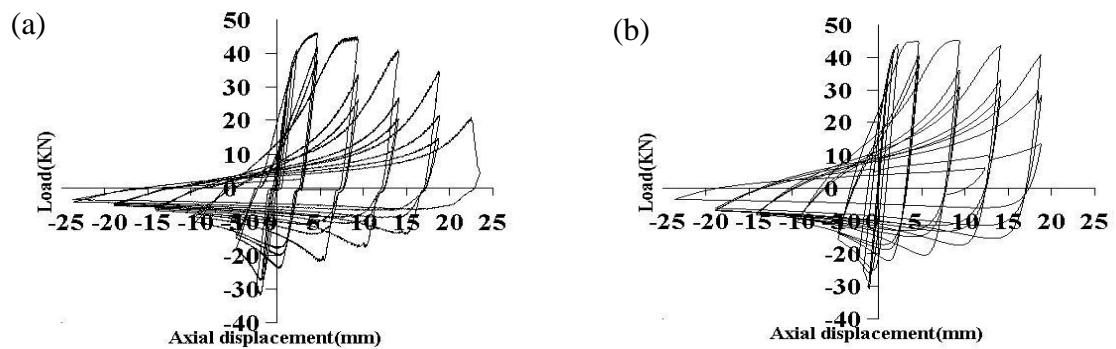


Figure 3.21: (a) Physical test and (b) numerical model load displacement hysteretic loops for Specimen 20X20X2.0X1100-CS-CF-G4.

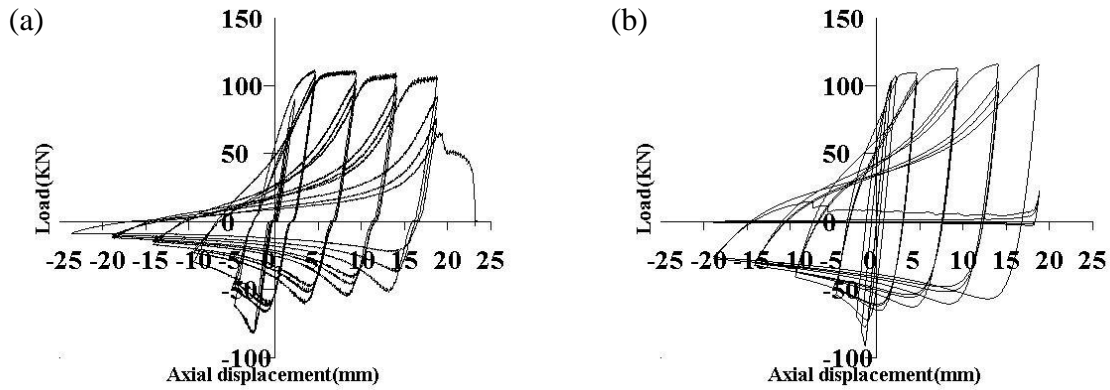


Figure 3.22: (a) Physical test and (b) numerical model load displacement hysteretic loops for Specimen 50X25X2.5X1100-CS-CF-G5.

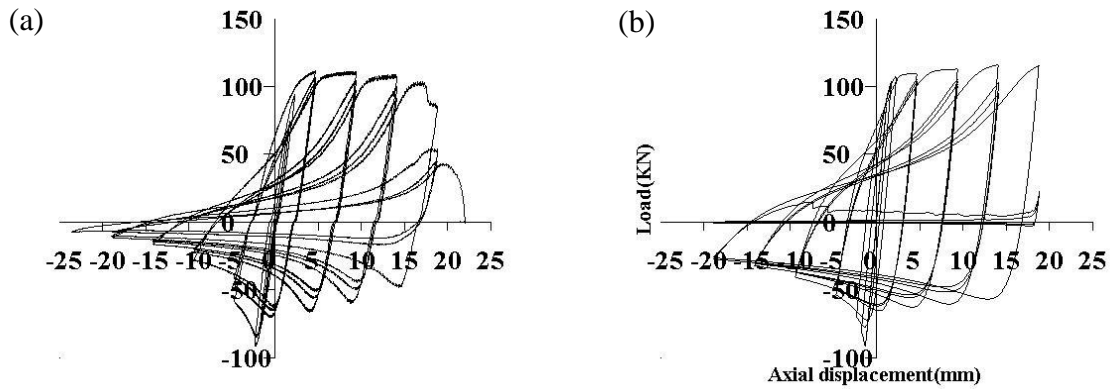


Figure 3.23: (a) Physical test and (b) numerical model load displacement hysteretic loops for Specimen 50X25X2.5X1100-CS-CF-G6.

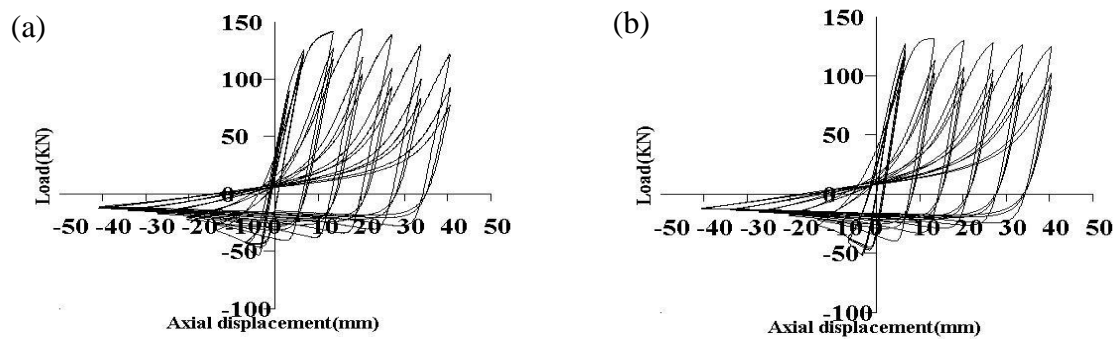


Figure 3.24: (a) Physical test and (b) numerical model load displacement hysteretic loops for Specimen 40X40X2.5X3300-CS-CF-G7.

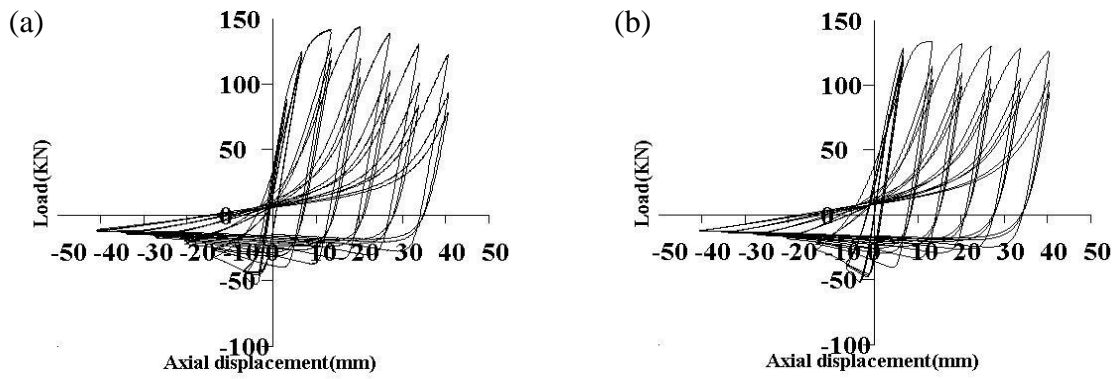


Figure 3.25: (a) Physical test and (b) numerical model load displacement hysteretic loops for Specimen 40X40X2.5X3300-CS-CF-G8.

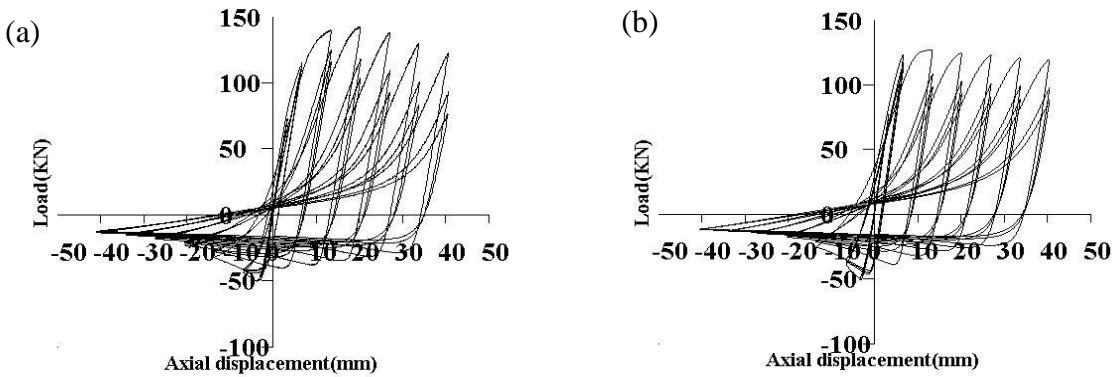


Figure 3.26: (a) Physical test and (b) numerical model load displacement hysteretic loops for Specimen 40X40X2.5X3300-CS-CF-G9.

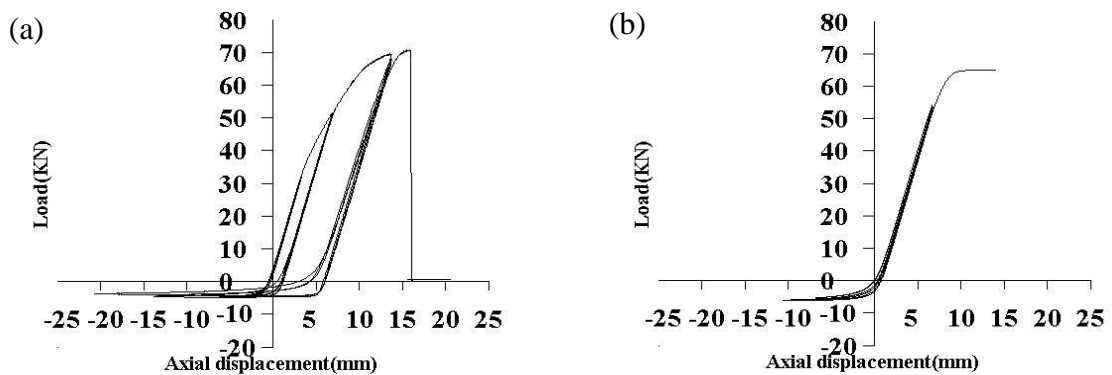


Figure 3.27: (a) Physical test and (b) numerical model load displacement hysteretic loops for Specimen 20X20X2.0X3300-CS-CF-G10.

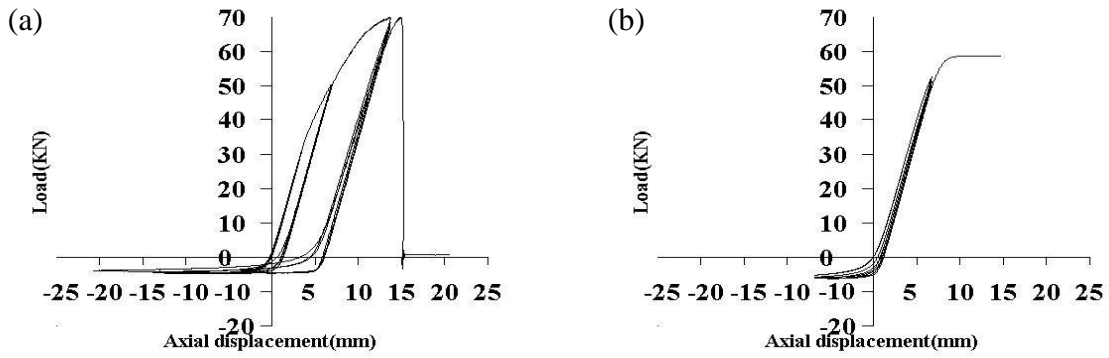


Figure 3.28: (a) Physical test and (b) numerical model load displacement hysteretic loops for Specimen 20X20X2.0X3300-CS-CF-G11.

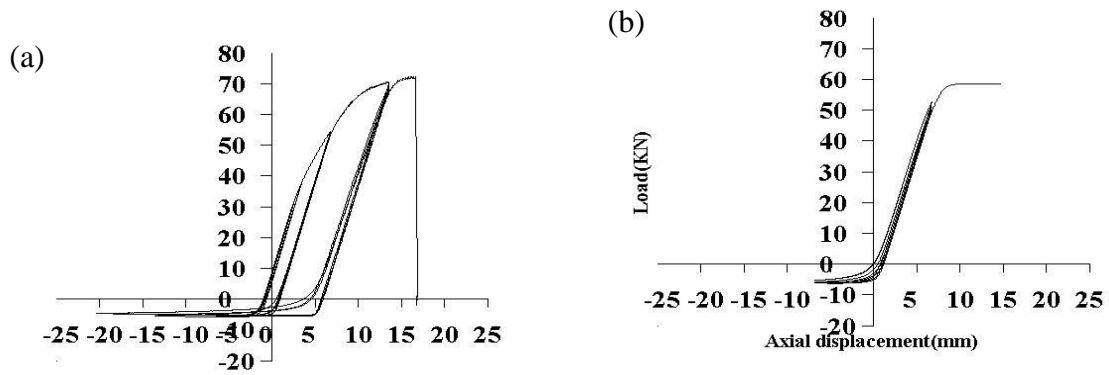


Figure 3.29: (a) Physical test and (b) numerical model load displacement hysteretic loops for Specimen 20X20X2.0X3300-CS-CF-G12.

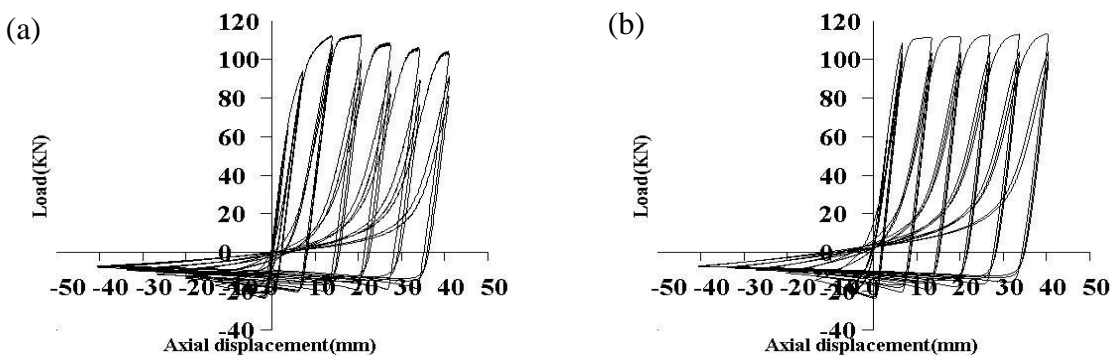


Figure 3.30: (a) Physical test and (b) numerical model load displacement hysteretic loops for Specimen 50X25X2.5X3300-CS-CF-G13.

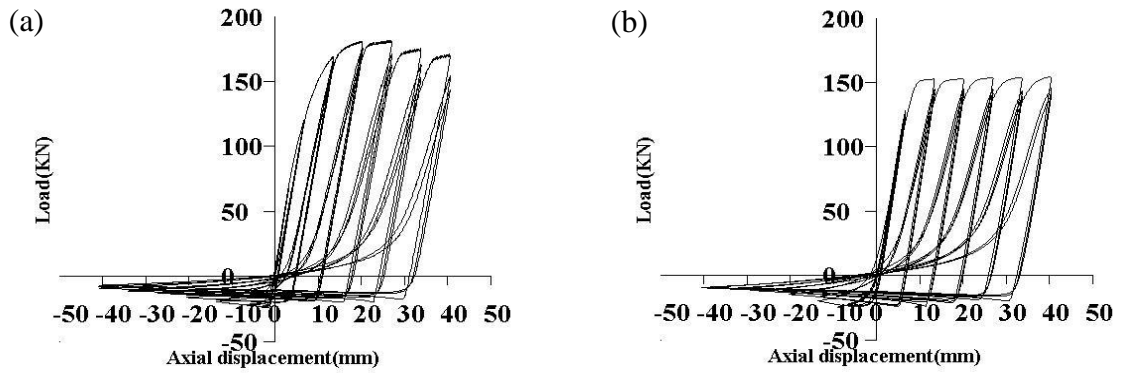


Figure 3.31: (a) Physical test and (b) numerical model load displacement hysteretic loops for Specimen 50X25X2.5X3300-CS-CF-G14.

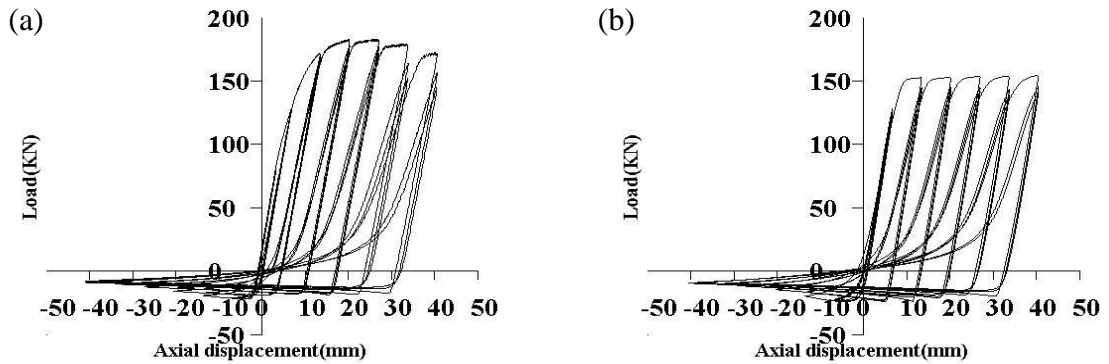


Figure 3.32: (a) Physical test and (b) numerical model load displacement hysteretic loops for Specimen 50X25X2.5X3300-CS-CF-G15.

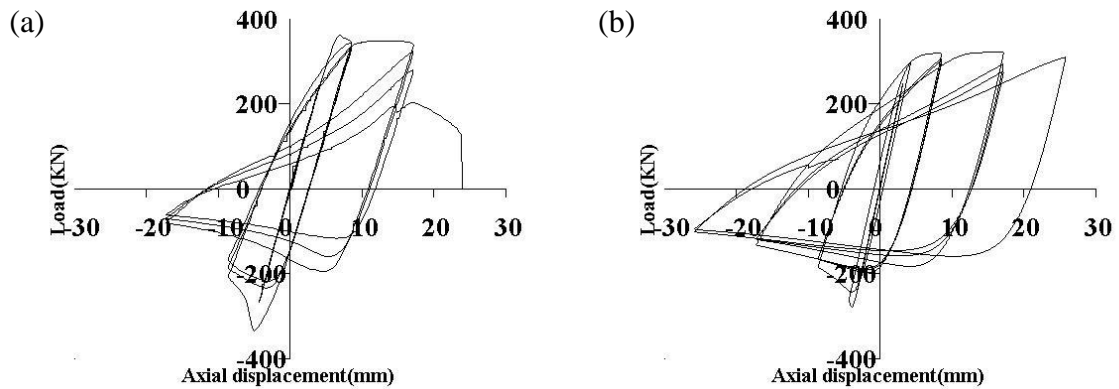


Figure 3.33: (a) Physical test and (b) numerical model load displacement hysteretic loops for Specimen 60X60X3X2050-CS-HR-N16.

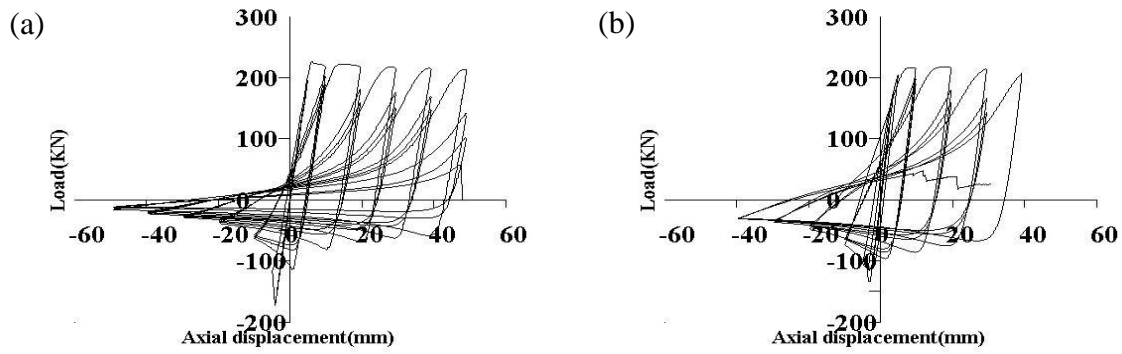


Figure 3.34: (a) Physical test and (b) numerical model load displacement hysteretic loops for Specimen 40X40X3X2050-CS-HR-N17.

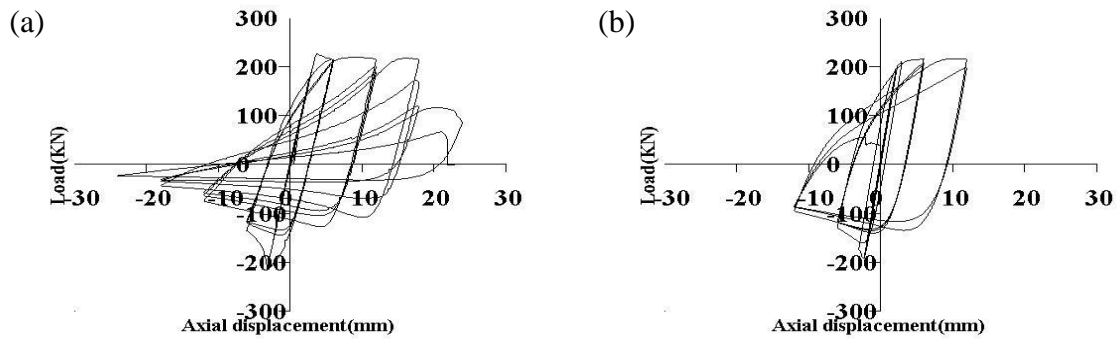


Figure 3.35: (a) Physical test and (b) numerical model load displacement hysteretic loops for Specimen 40X40X3X1250-CS-HR-N18.

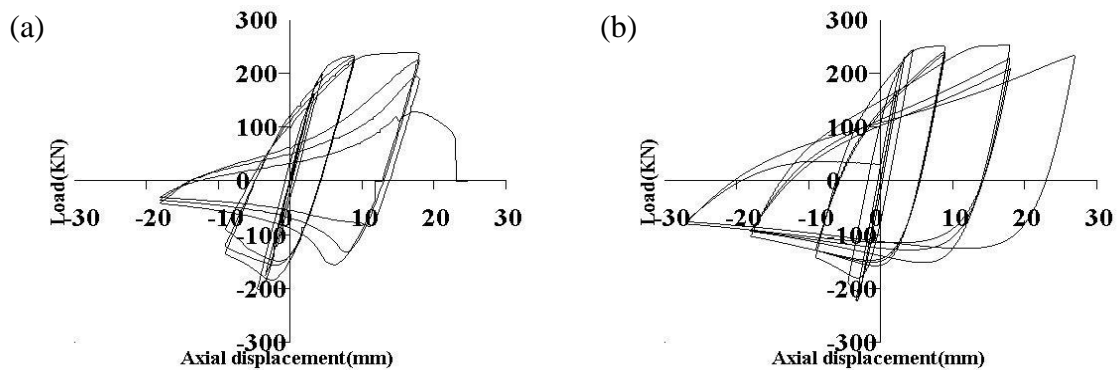


Figure 3.36: (a) Physical test and (b) numerical model load displacement hysteretic loops for Specimen 60X60X3X2050-CS-CF-N19.

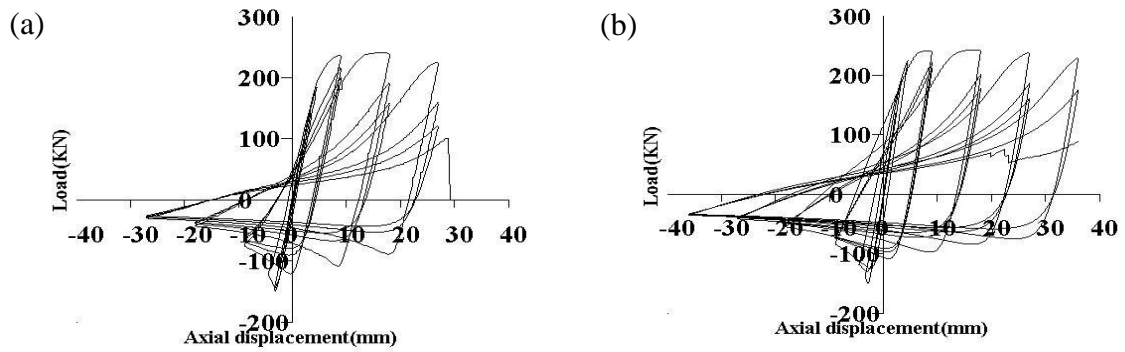


Figure 3.37: (a) Physical test and (b) numerical model load displacement hysteretic loops for Specimen 40X40X4X2050-CS-CF-N20.

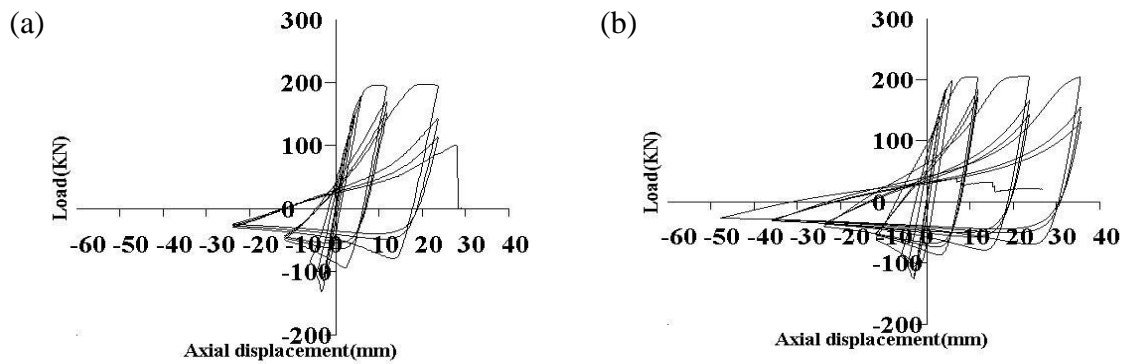


Figure 3.38: (a) Physical test and (b) numerical model load displacement hysteretic loops for Specimen 40X40X3X2050-CS-CF-N21. Specimen failed at end connection.

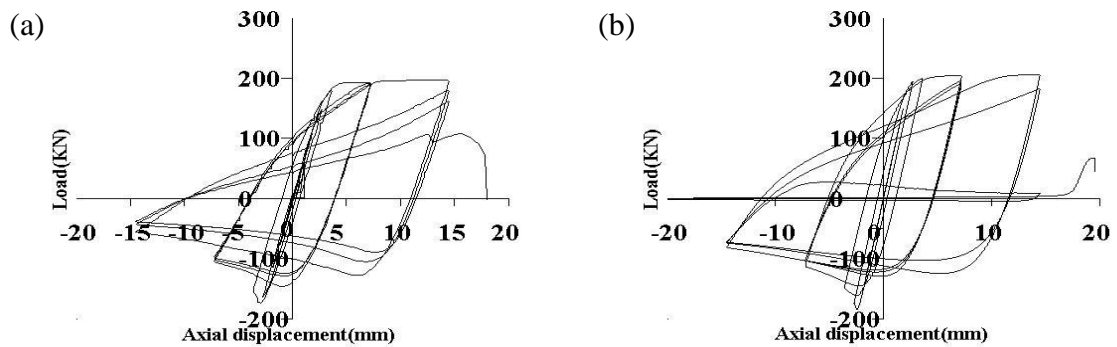


Figure 3.39: (a) Physical test and (b) numerical model load displacement hysteretic loops for Specimen 40X40X3X1250-CS-CF-N22.

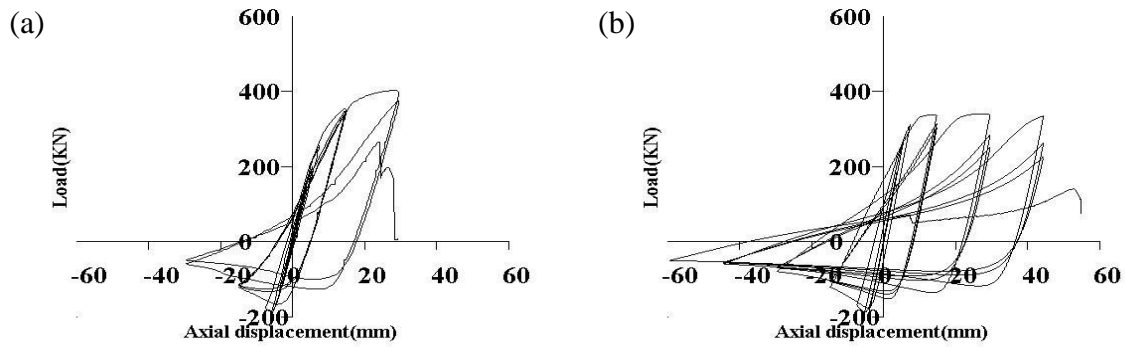


Figure 3.40: (a) Physical test and (b) numerical model load displacement hysteretic loops for Specimen 60X60X3X2850-SS-CF-N23.

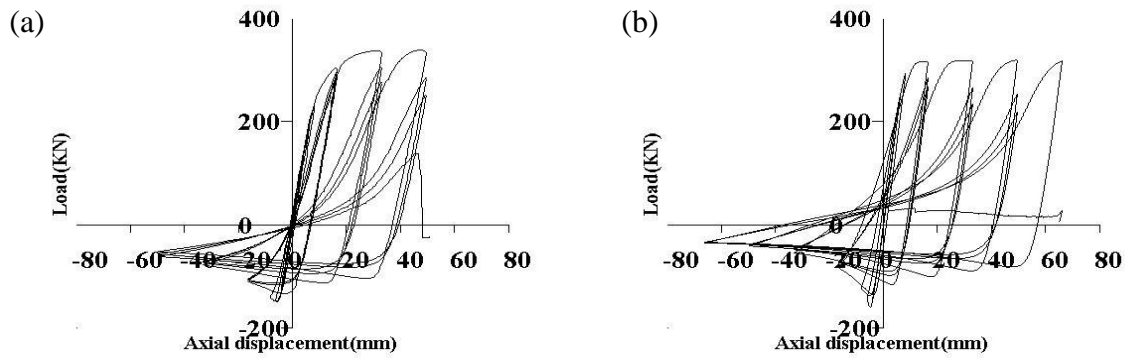


Figure 3.41: (a) Physical test and (b) numerical model load displacement hysteretic loops for Specimen 50X50X3X2850-SS-CF-N24.

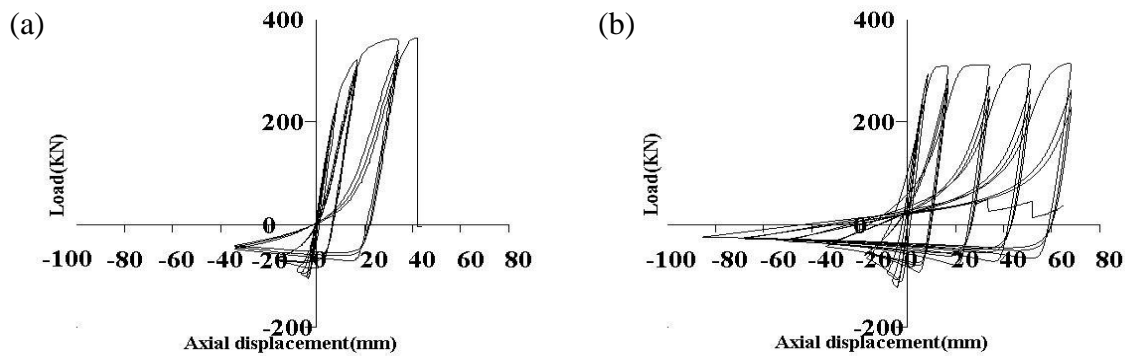


Figure 3.42: (a) Physical test and (b) numerical model load displacement hysteretic loops for Specimen 60X40X3X2850-SS-CF-N25. Specimen failed at end connection.

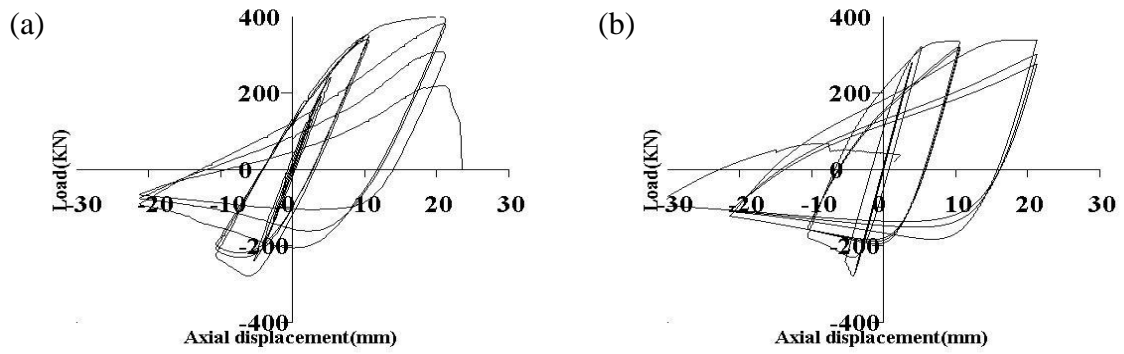


Figure 3.43: (a) Physical test and (b) numerical model load displacement hysteretic loops for Specimen 60X60X3X2050-SS-CF-N26.

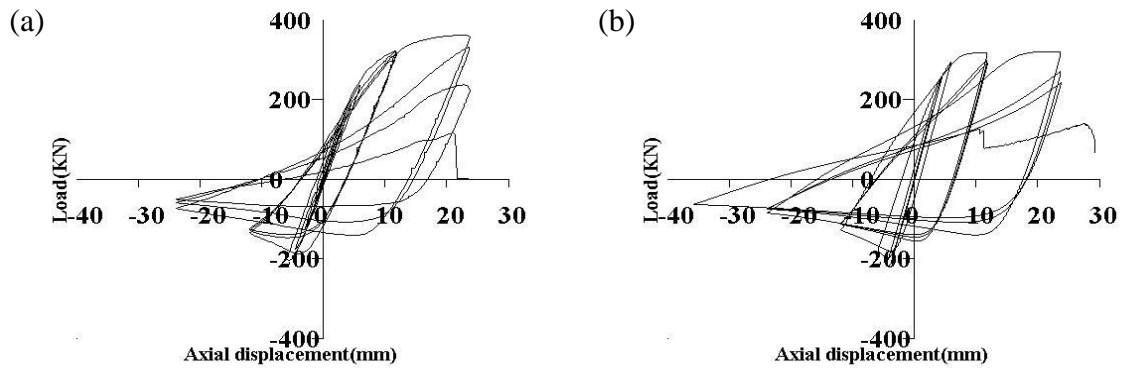


Figure 3.44: (a) Physical test and (b) numerical model load displacement hysteretic loops for Specimen 50X50X3X2050-SS-CF-N27.

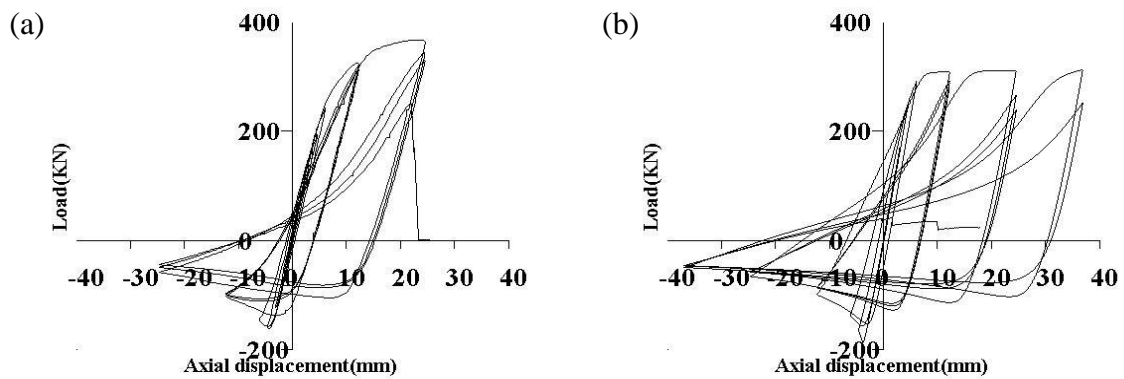


Figure 3.45: (a) Physical test and (b) numerical model load displacement hysteretic loops for Specimen 60X40X3X2050-SS-CF-N28.

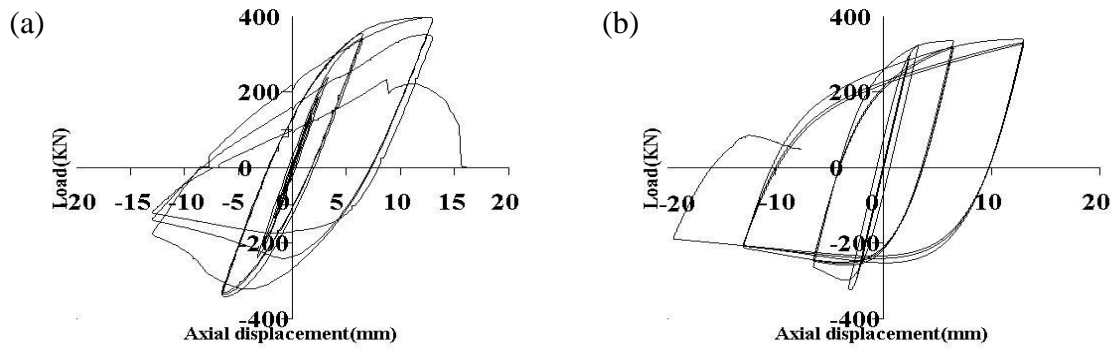


Figure 3.46: (a) Physical test and (b) numerical model load displacement hysteretic loops for Specimen 60X60X3X1250-SS-CF-N29.

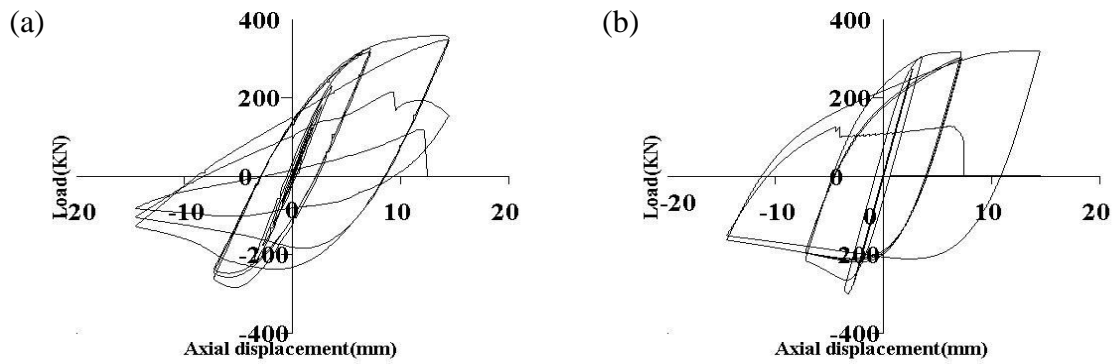


Figure 3.47: (a) Physical test and (b) numerical model load displacement hysteretic loops for Specimen 50X50X3X1250-SS-CF-N30.

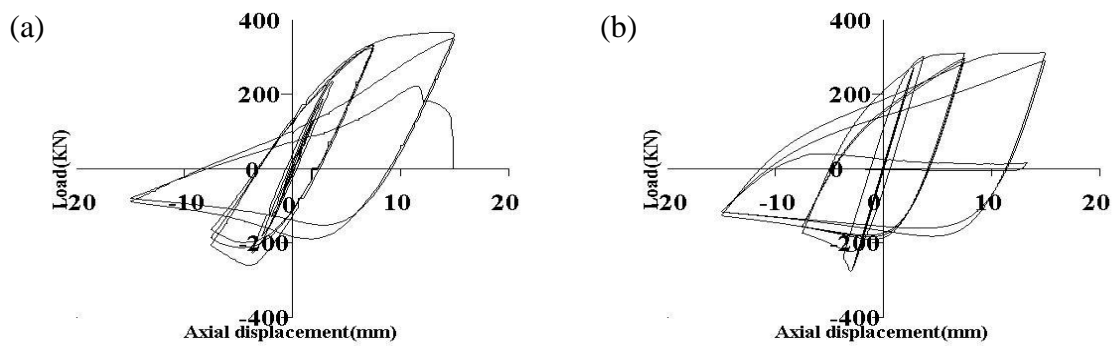


Figure 3.48: (a) Physical test and (b) numerical model load displacement hysteretic loops for Specimen 60X40X3X1250-SS-CF-N31.

3.5.1 Buckling and tensile loads

From Table 3.2 and Table 3.3, it is evident that there is relatively good agreement between the numerical model and physical tests results of the maximum tensile forces (F_{\max}) and initial buckling loads (F_c) for most of the specimens investigated. Moreover, the calibrated models had average ratios of numerical model to physical test model values for F_{\max} and F_c of 0.93 and 0.95, respectively, with corresponding coefficients of variation (C_V) of 0.11 and 0.08, respectively (Table 3.2). The models were validated for cold-formed carbon steel, hot-rolled carbon steel, and cold-formed stainless steel by comparing predictions from the numerical model to findings from experimental physical tests carried out by Nip et al (2010), where average ratios of numerical model to physical test model values for F_{\max} and F_c was 1.08 and 1.00, respectively, with corresponding C_V values of 0.09 and 0.09, respectively (Table 3.3). Thus, the equivalent mean values for F_{\max} and F_c for the total 31 specimens studied were 1.01 and 0.98, respectively, with corresponding C_V values of 0.12 and 0.09, respectively.

Initial buckling loads obtained from the numerical model were found to be affected by initial camber provided at the middle of the specimens, which increases for slender braces with low initial buckling force. It is noticed that some post buckling cycles obtained from the numerical models are fatter having more post buckling capacity than the cycles obtained from the physical tests. One possible explanation would be the limitation of the model that plane sections are assumed to remain plane, which will not capture the local buckling at the plastic hinge locations on the specimen. Local buckling phenomenon can be mitigated in practise by using low width to thickness ratio and Class 1 cross-section suggested in Eurocode 3 (CEN 2005), which can form a plastic hinge with the rotation capacity required from plastic analysis without reduction in resistance that may be caused by local buckling.

While comparing the force-displacement response of the experimental and numerical model for 50X25X2.5X3300-CS-CF-G14 and 50X25X2.5X3300-CS-CF-G15, it is found that the yield capacity of the braces in the numerical model is lower than the yield capacity on the physical experiments (see Figure 3.31 and Figure 3.32). A possible

explanation of that is the specific feature of the cold formed elements of increasing locally their yield strength due to cold forming. Even though the average yield strength defined in Eurocode 3 (CEN 2006) that takes into account the effect of cold forming is used, the yield displacement for experimental results is found to have higher values than the numerical model for these two tests, but was satisfactory for all other tests.

3.5.2 Fracture

For many tests, plastic hinges formed in the brace specimens after they experienced very large rotational demands and large strains, which caused fracture due to low cyclic fatigue. The numerical model incorporating a fatigue model could predict fracture after a number of cycles close to the ones obtained in the physical tests for the specimens tested until fracture occurred (see Table 3.2 and Table 3.3). However, some of the physical test specimens suffered from early fracture at end connections, where the weld itself or the heat affected zone adjacent to the stiffener fractured during the physical tests, which is not accounted for in the numerical model. For this reason it is found that numerical model for 40X40X4.0X2050-CS-CF-N20, 40X40X3.0X2050-CS-CF-N21 and 60X40X3.0X2850-SS-CF-N25 had more cycles before capturing fracture as it is developed to have the fracture at the middle of the brace element not at the end connections. Specimens 40X40X2.5X3300-CS-CF-G7, 40X40X2.5X3300-CS-CF-G8, 40X40X2.5X3300-CS-CF-G9, 50X25X2.5X3300-CS-CF-G13, 50X25X2.5X3300-CS-CF-G14 and 50X25X2.5X3300-CS-CF-G15 were not tested to failure, and all of them survived displacement ductility demands between 5.6 and 9.5.

Tremblay (2002) proposed a simple approach to find the total ductility reached at fracture, μ_f . This approach is related only to the normalised slenderness parameter, $\bar{\lambda}$, as shown in Equation [2.2]. Moreover, Goggins et al. (2006) used their test data to develop new relationships expressing the displacement ductility, μ_f , in terms of global slenderness, $\bar{\lambda}$, and width to thickness ratio (b/t) as shown in Equations [2.4] and [2.5]. However, Nip et al. (2010) proposed new predictive expressions for the displacement ductility in terms of global slenderness ratio, $\bar{\lambda}$, and width to thickness ratio (b/t) for hot-rolled carbon steel, cold-formed carbon steel and cold-formed stainless steel as shown

from Equation [2.6] to [2.8]. Figure 3.49 compares predicted displacement ductility values obtained from the numerical model to those obtained from the expressions established by Nip et al. (2010). It is found that Nip et al. (2010) expressions for predicting displacement ductility gives close results to the values obtained from the numerical model. However, these relationships overestimated the displacement ductility for very slender specimens with slenderness ratio more than three as shown in Figure 3.49.

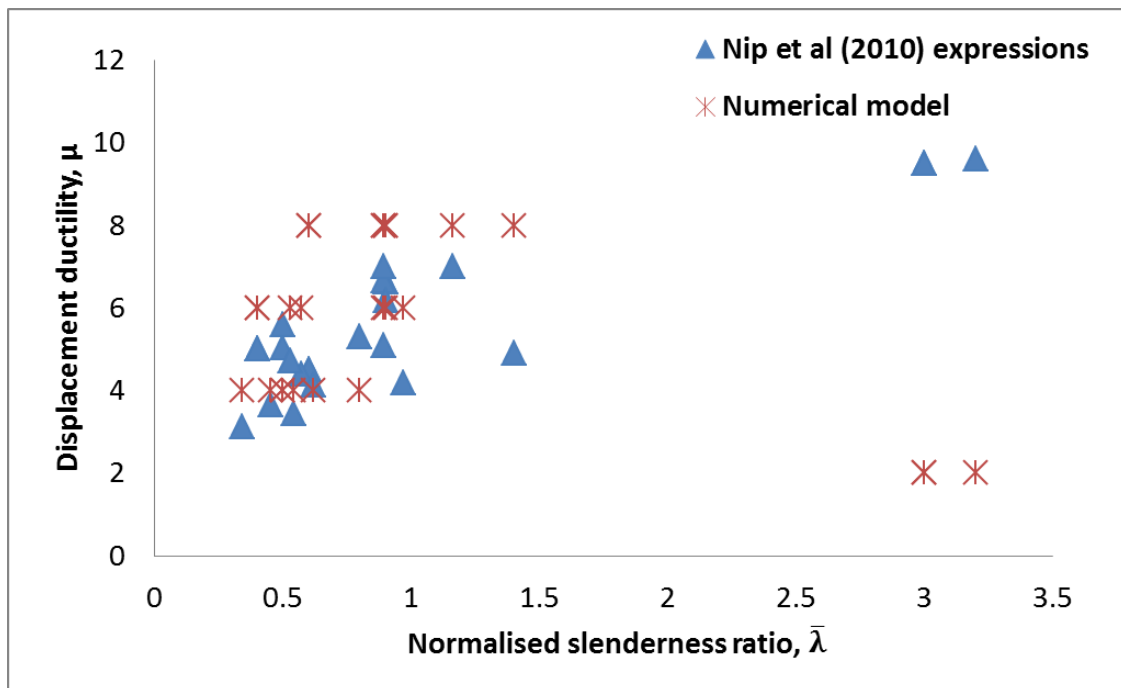


Figure 3.49: Comparison of displacement ductility, μ , values obtained from the expressions established by Nip et al. (2010) to the numerical model results.

3.5.3 Energy dissipated

As shown in Table 3.2, Table 3.3, and Figure 3.50, the numerical model gave good predictions of the total energy dissipated, W_{tot} , and energy dissipated at the first cycle of ductility of 4, $W_{\mu=4}$, when compared to the results obtained from the physical tests during cyclic loading. However, some cycles obtained from the numerical models were found to be fatter than the cycles obtained from the tests, specifically for stockier specimens as the numerical model could not capture the local buckling. This is the reason why the energy

dissipated results predicted from numerical model was slightly more than the energy dissipated results obtained from physical tests. Total energy dissipated for specimens 40X40X4.0X2050-CS-CF-N20, 40X40X3.0X2050-CS-CF-N21 and 60X40X3.0X2850-SS-CF-N25, which suffered from early fracture at end connection, was less than the total energy dissipated predicted from the numerical models which have more hysteretic cycles. However, for the specimens survived 10 or more cycles, close results of energy dissipated were found when comparing the energy dissipated up to the 10th cycle (see Figure 3.50).

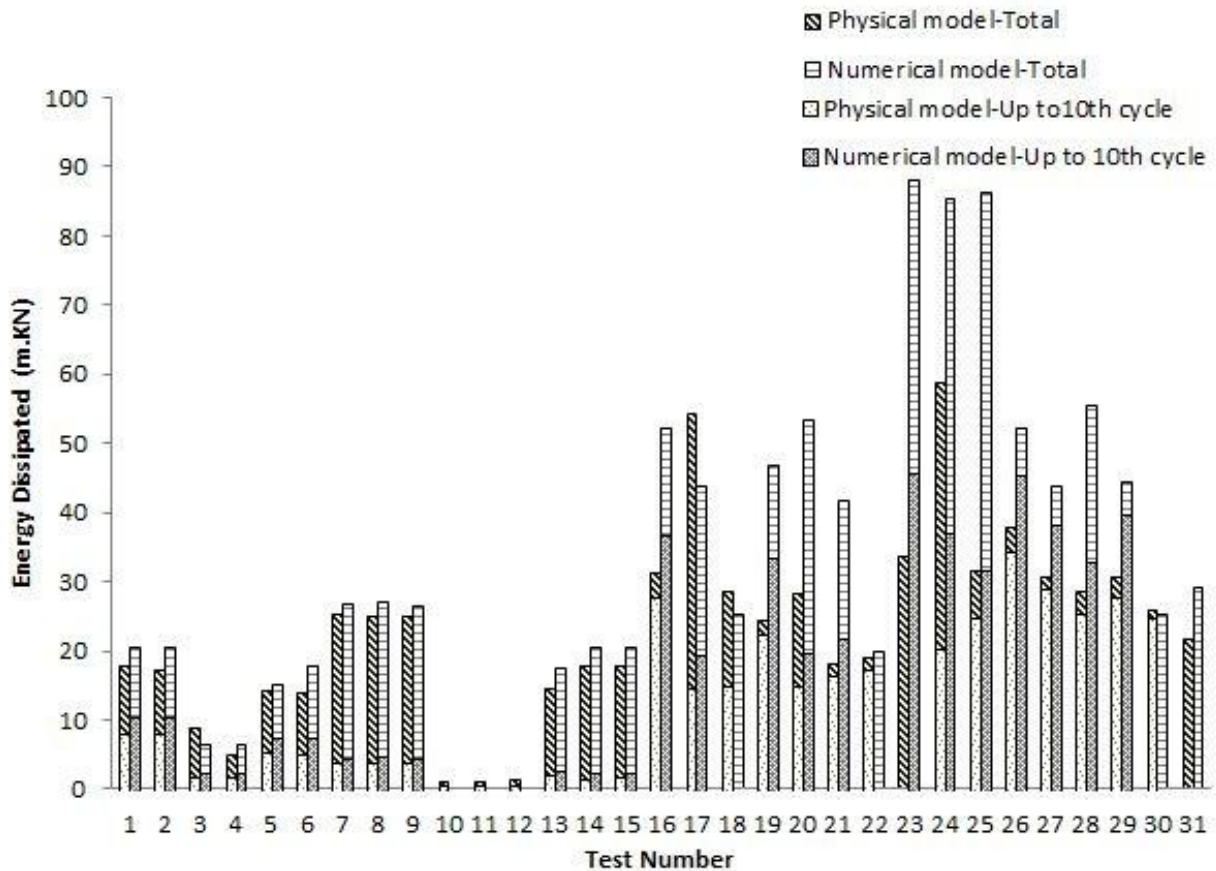


Figure 3.50: Energy dissipated by specimens in physical tests (Goggins et al. 2005; Nip et al. 2010) and the numerical models.

Similar to the observations in the measured hysteretic loops of the physical test specimens, the stockier specimens dissipated more energy due to their larger cross-sectional areas and the significant yield plateaus they exhibited. Figure 3.51 shows the

energy index (the area under the load–axial deflection curve in both tension and compression regions during the first cycle at a ductility level of 4 normalised to the elastic energy of the strut) plotted against the normalised slenderness ratio. This shows how the energy dissipated is reduced with brace slenderness. As can be seen from Figure 3.51, the numerical model gives good average prediction of the energy index of the first cycle at ductility of four for specimens over a large range of slenderness.

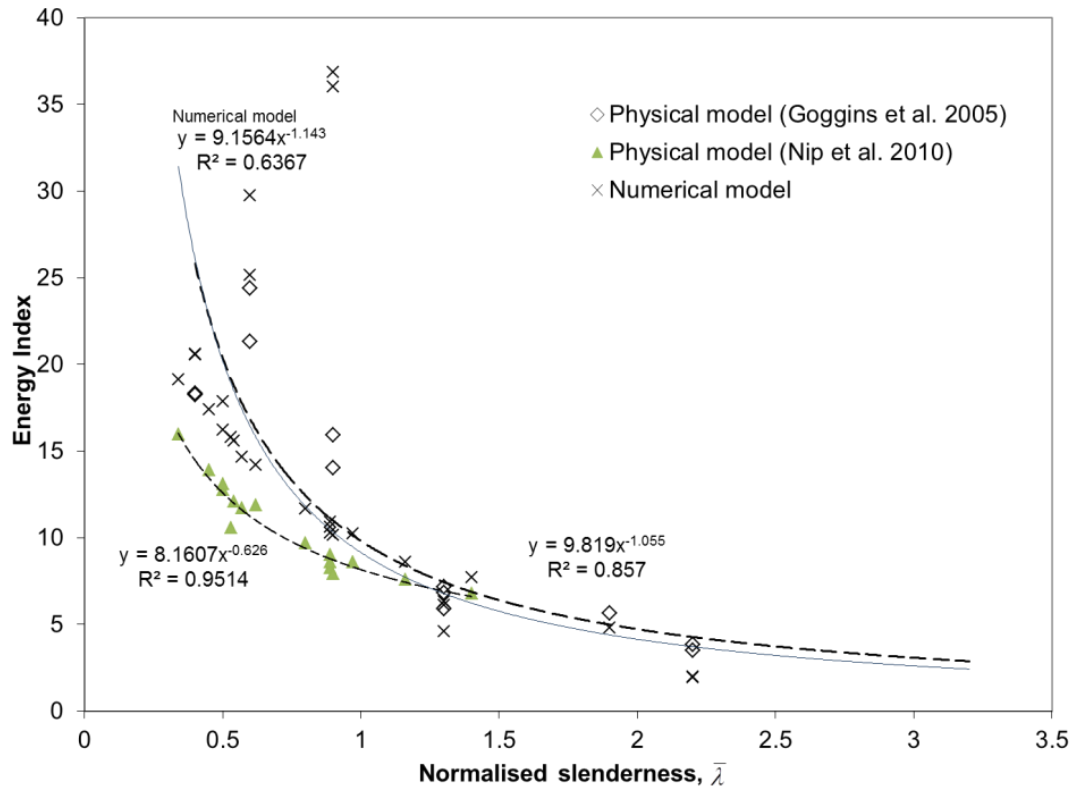


Figure 3.51: Energy index versus slenderness for the first cycle at a ductility of 4 measured in physical tests (Goggins et al. 2005; Nip et al. 2010) and obtained from numerical models.

3.6 Summary and conclusion

In this chapter, a study of the behaviour of braces, which are the main elements to dissipate energy in concentrically braced frames, is carried out. A numerical model is developed and found to be capable to simulate the hysteretic behaviour of braces. A nonlinear beam-column element with distributed plasticity is used where the cross section of the brace is divided into fibres along the perimeter and across the thickness. In this

model, the brace is suggested to be divided into a minimum of two elements using ten integration points per element. An initial camber to the middle of the brace is used to account for the overall buckling and a value between 0.1 and 1% of the length of the brace is found to give the best results for the first buckling load. A low cyclic fatigue model with new parameters is proposed and used to wrap the fibre based nonlinear beam-column model in order to capture fracture in the braces. It has been shown in this study that this model can accurately predict the maximum displacement ductility demand of the brace members when fracture occurs.

In general, good agreement was found between the main response parameters of the numerical and physical tests, including the maximum tensile force (F_{\max}), initial buckling load (F_c), number of cycles to fracture, the total energy dissipated by the specimens (W_{tot}) and the energy dissipated by the specimens at the first cycle of ductility of 4 ($W_{\mu=4}$). However, there was a difference in the response between the numerical model and some tests in the post buckling range and, in general, the hysteretic loops were fatter in the numerical model. One possible reason is that the model does not account for local buckling which should be taken into account in future research.

Chapter 4

Ground motions

4.1 Introduction

Non-linear time history analysis (NLTHA) is increasingly used in verifying the performance of inelastic behaviour of structures to develop and obtain important design parameters. Furthermore, it can be used as an accurate method for seismic evaluation of existing structures and design of new complex structures.

Current design codes specify using a number of accelerograms (recording of ground acceleration) for NLTHA. If at least seven accelerograms are used, current design codes such as EC8 (CEN 2004) and ASCE (2006) permit using the average value of the response parameters (i.e. member forces, displacements, and drifts) from all the accelerograms. However, if less than seven accelerograms are used, the maximum response parameter resulted from the analysis of the accelerograms should be used. The minimum number of accelerograms to be used in NLTHA as specified in EC8 (CEN 2004) is three.

This chapter presents two sets of eight accelerograms, which will be scaled to have displacement spectra matching different design displacement spectra to be used to verify non-linear time history analysis of concentrically braced frames (CBFs) in the case of shaking table tests or to verify the direct displacement based design (DDBD) procedure for CBFs.

4.2 Ground motion parameters

Ground motion parameters for the use of earthquake engineering purposes can be taken from time histories (accelerograms) or response spectra. The most common ground motion parameters obtained from time histories are peak ground acceleration, PGA, peak ground velocity, PGV, and peak ground displacement, PGD, which can be experienced by a particle in the ground.

Response spectra describes the maximum response of single degree of freedom (SDOF) structures to a particular time history as a function of natural period and damping ratio of these structures.

Three ranges of structural periods within which the response is dependent on the values of ground motion acceleration, velocity or displacement is identified (Elnashai and Sarno 2008). For structure with periods less than 0.5 seconds, the response of the structure is found to be sensitive to the peak ground acceleration, while structures with periods between 0.5 to 2.0 seconds are found to be sensitive to peak ground velocity. Moreover, structures with periods longer than 2 seconds are found to be more dependent on displacement.

4.3 Choice of accelerograms for NLTHA

Accelerograms to be used in the NLTHA should be spectrum compatible. For the purpose of this work, NLTHA is used to validate design procedure using a displacement response spectrum. Because of that, the accelerograms should have spectra compatible with the response spectrum used in the design.

EC8 (CEN 2004) allow using artificial accelerograms matching the response spectrum, as well as recorded or simulated accelerograms scaled to response spectrum. According to EC8 (CEN 2004) design should be carried out using acceleration spectrum and the suite of accelerogram used should satisfy the following. The zero period spectral response acceleration value (calculated from the individual time histories) should not be smaller than the value of $a_g \cdot S$, where a_g is the peak ground acceleration (PGA) and S describes the shape of the elastic response spectrum which is dependent upon the ground type. No

value of the mean 5% damping elastic spectrum, calculated from all accelerograms, should be less than 90% of the corresponding value of the 5% damping elastic response spectrum for periods between $0.2T$ and $2.0T$, where T is the fundamental period of the structure in the direction where the accelerogram will be applied.

Scaling the accelerograms to a PGA value before applying them to NLTHA has advantages, as it is simple to apply and agrees with the methods used by design codes in defining seismic loads. On the other hand, peak ground velocity and peak ground displacement values also play a significant role in determining the severity of seismic response.

For the purpose of this work, in order to verify the performance of the DDBD methodology for the concentrically braced frames (CBFs), non-linear time-history analyses will be carried out by applying different accelerograms that are scaled to be compatible with the design displacement spectrum of every case study. The displacement response spectrum is used because the purpose of this study is to validate a direct displacement based design (DDBD) approach, which uses the displacement spectrum to define the maximum displacements the structure will undergo during earthquakes.

However, firstly the NLTHA models need to be validated using data from shake table tests of full scale single storey CBFs (refer to Chapter 5). Thus, a number of records and artificially adjusted accelerograms will be scaled to match the ground motion spectrums used for the shake table tests to check its sensitivity to different earthquakes.

Furthermore, NLTHA will be used to verify the numerical model representing the SDOF CBFs. For Chapter 6, NLTHA will be used to verify DDBD methodology for SDOF structures. For Chapter 7, accelerograms will be scaled to match the Eurocode 8 (CEN 2004) spectrum, which will be used to design the case studies. Two sets of earthquakes will be used; the first set consists of eight artificially adjusted earthquakes and the second consists of real earthquakes.

4.3.1 Artificially adjusted earthquakes

Eight accelerograms from four different earthquakes (2 components in orthogonal direction for each earthquake) were taken from Pennucci et al. (2009). The records were selected by using a computer programme that first filters the whole PEER record database (PEER 2008) on user-defined selection criteria, then calculates an optimum linear scaling factor for all filtered records to best fit the target spectrum across a period range of interest, and finally ranks these records in order of root-mean-square error (ARUP 2007; Grant et al. 2008). For this study the following earthquakes were selected: the Northridge earthquake, January 17, 1994, with two components (EQ3a and EQ3b); the Imperial Valley earthquake October 15, 1979, with two components (EQ4a and EQ4b); Hector earthquake, October 16, 1999, with two components (EQ5a and EQ5b); and Landers earthquake, June 28, 1992, with two components (EQ6a and EQ6b). The earthquakes used are shown in Table 4.1, which gives the PEER ID, the magnitude, M , and the epicentre distance, r . The accelerograms for these records are shown from Figure 4.1 to Figure 4.8.

Table 4.1: Properties of the first set ground motions.

Earthquake	ID used	Date	PEER ID	Magnitude, M	Distance, r (km)
Northridge	EQ3a, EQ3b	Jan. 17, 1994	959	6.7	5
Imperial Valley	EQ4a, EQ4b	Oct. 15, 1979	169	6.5	34
Hector	EQ5a, EQ5b	Oct. 16, 1999	1762	7.13	48
Landers	EQ6a, EQ6b	Jun. 28, 1992	900	7.28	86

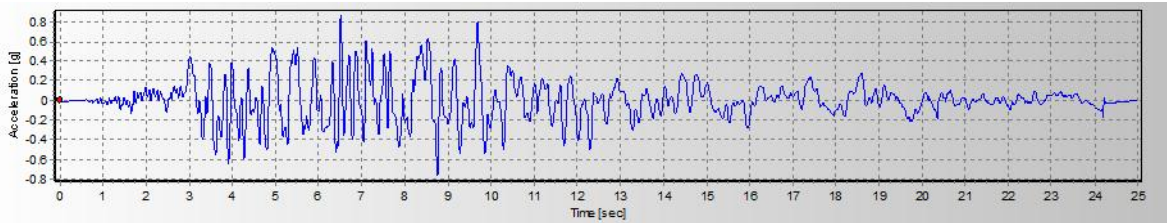


Figure 4.1: Northridge earthquake, January 17, 1994, EQ3a.

Ground motions

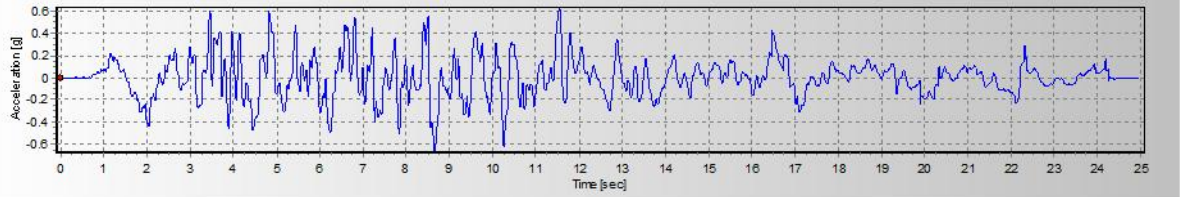


Figure 4.2: Northridge earthquake, January 17, 1994, EQ3b

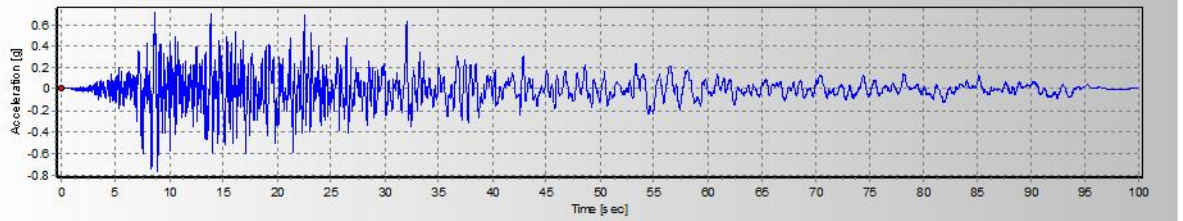


Figure 4.3: Imperial Valley earthquake, October 15, 1979, EQ4a.

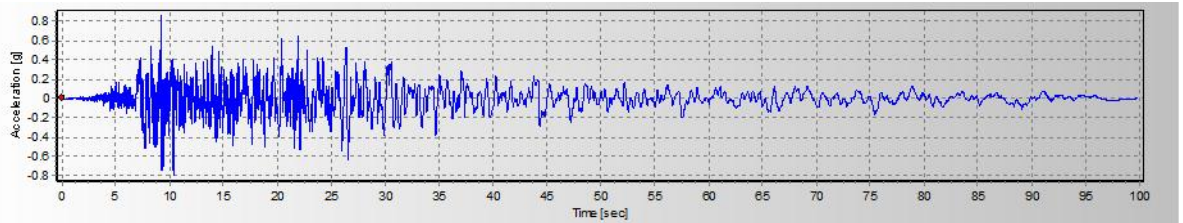


Figure 4.4: Imperial Valley earthquake, October 15, 1979, EQ4b.

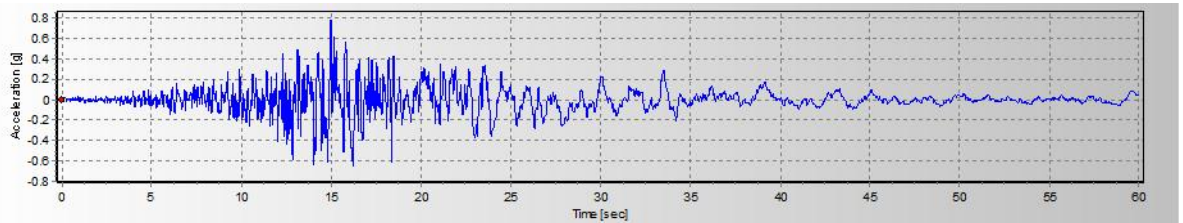


Figure 4.5: Hector earthquake, October 16, 1999, EQ5a.

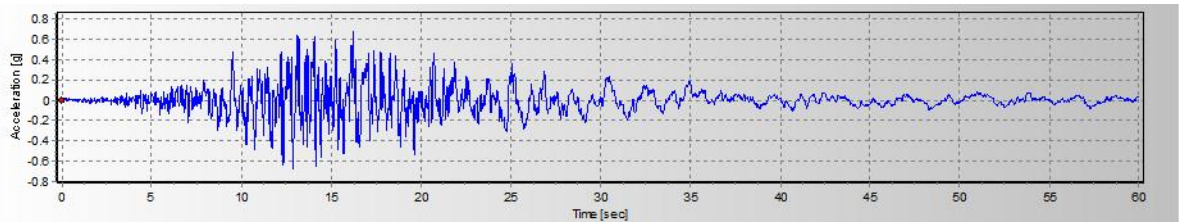


Figure 4.6: Hector earthquake, October 16, 1999, EQ5b.

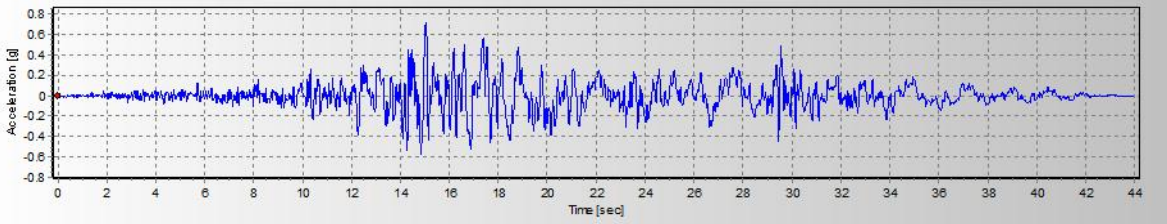


Figure 4.7: Landers earthquake, June 28, 1992, EQ6a.

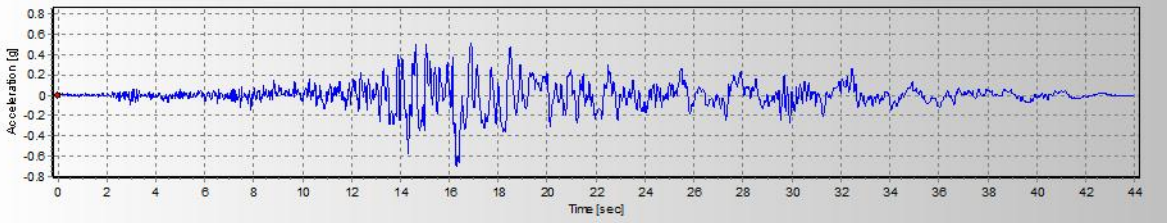


Figure 4.8: Landers earthquake, June 28, 1992, EQ6b.

4.3.1.1 Artificially adjusted accelerograms with spectra scaled to match shake table tests accelerograms spectra.

Time history accelerograms are scaled to get a displacement response spectrum that matches the shake table tests response spectrum. Response spectra for the scaled accelerograms were found using the programme SeismoSignal (SeismoSoft 2007) for test frames ST2-50H, ST5-20H, ST5-20HB and ST8-40H. These are shown from Figure 4.9 to Figure 4.12, respectively.

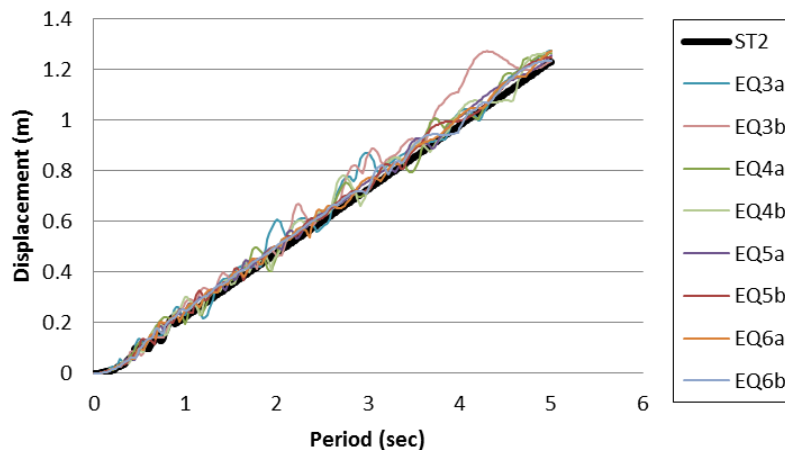


Figure 4.9: Displacement response spectrum for eight different earthquakes scaled to be compatible with the displacement spectrum for the earthquake used in ST2 test.

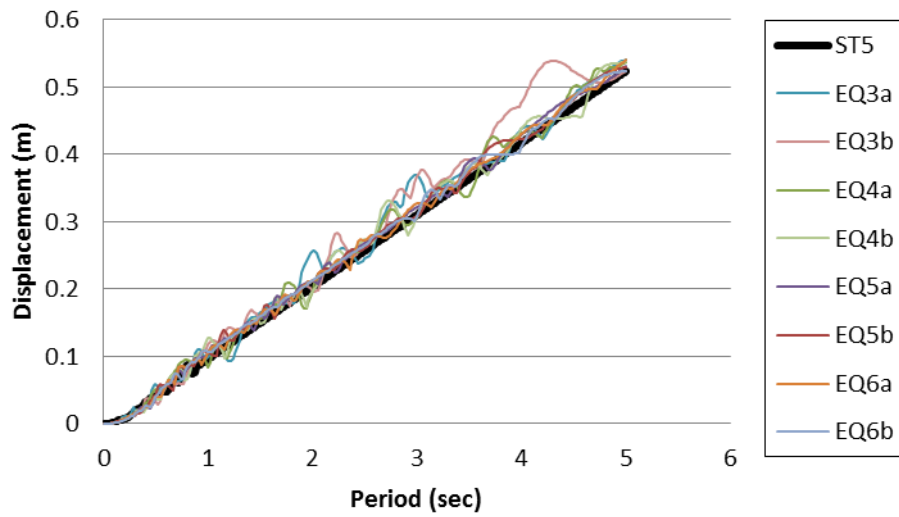


Figure 4.10: Displacement response spectrum for eight different earthquakes scaled to be compatible with the displacement spectrum for the earthquake used in ST5-20H test.

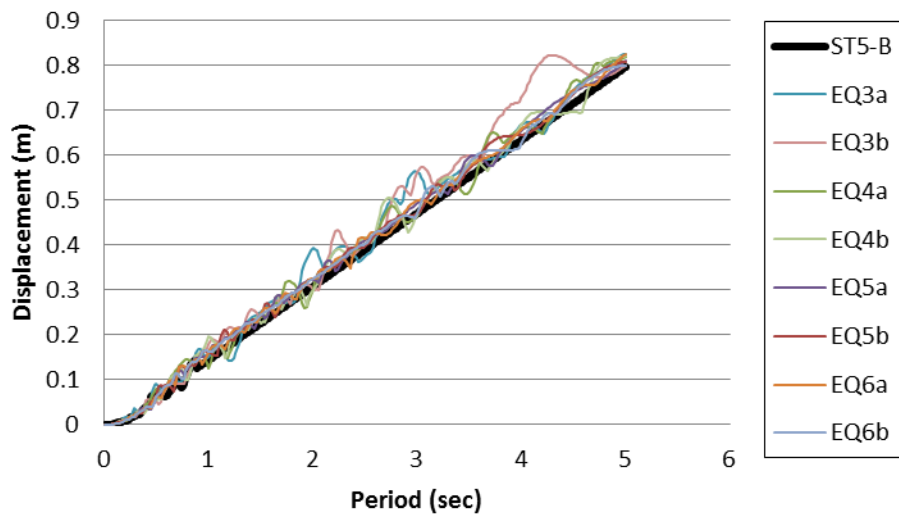


Figure 4.11: Displacement response spectrum for eight different earthquakes scaled to be compatible with the displacement spectrum for the earthquake used in ST5-20HB test.

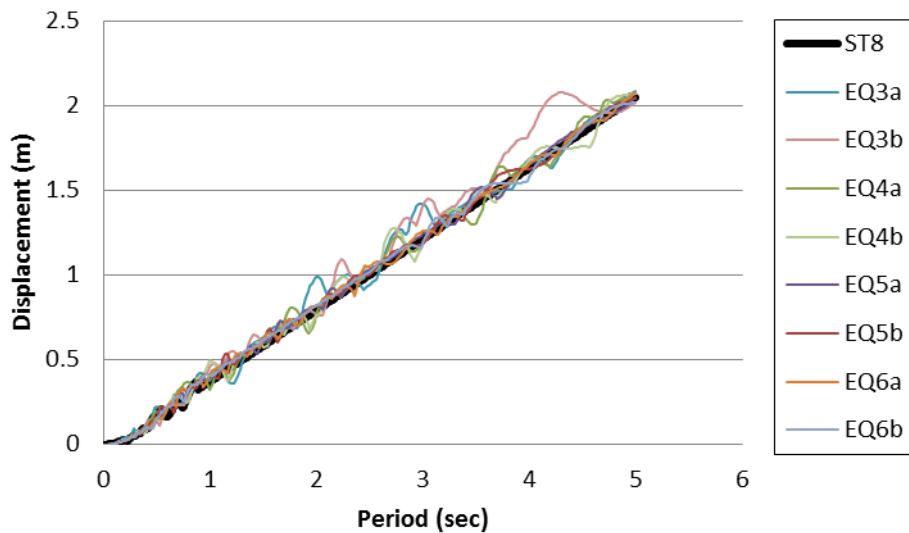


Figure 4.12: Displacement response spectrum for eight different earthquakes scaled to be compatible with the displacement spectrum for the earthquake used in ST8 test.

4.3.1.2 Artificially adjusted accelerograms with spectra scaled to match EC8 type 1 spectrum, soil type C.

All the above time histories are also scaled with the proportions that make the response spectra of these time histories match the soil type C design displacement spectrum with 5% damping from EC8 (CEN 2004), which used in the DDBD methodology for the multi-storey CBF structures case studies. Response spectra for the scaled accelerograms were found using the programme SeismoSignal (SeismoSoft 2007) with 5% damping value and showed a good match with the design spectrum, as shown in Figure 4.13.

Figure 4.14 shows the average of the entire earthquakes response spectra and compares it with the design response spectrum. It is found that the average of the earthquakes response spectra perfectly matches the design response spectrum.

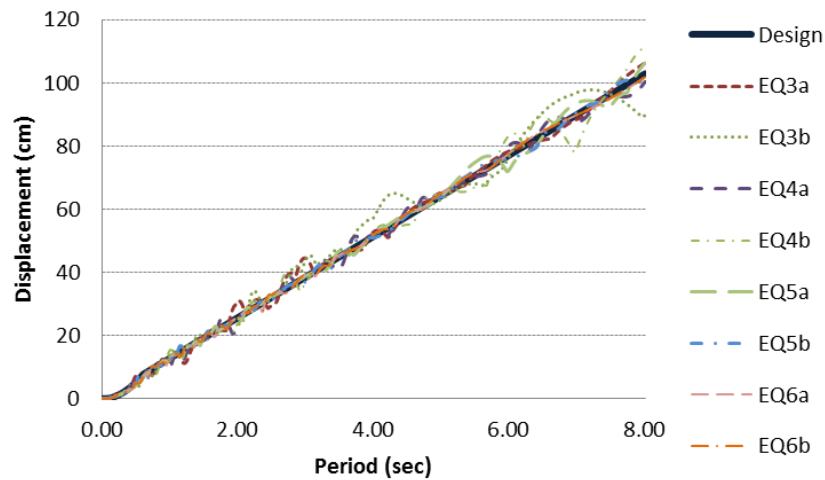


Figure 4.13: 5% design spectrum compared to the scaled displacement spectra for eight accelerograms used to verify the design procedure using NLTHA.

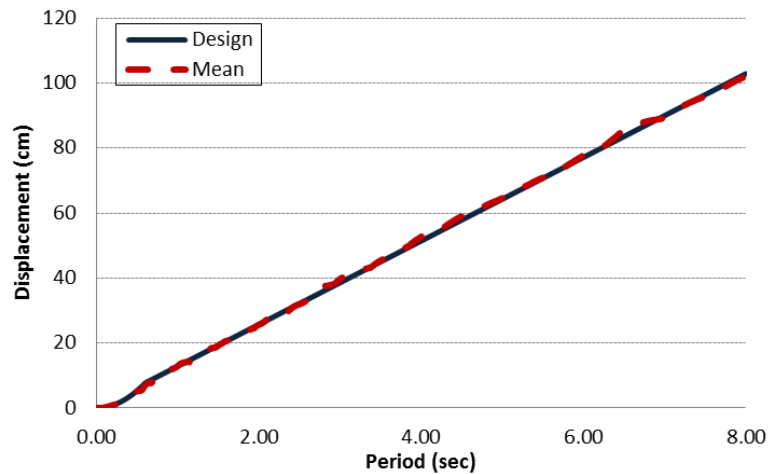


Figure 4.14: 5% design spectrum compared to the scaled displacement spectra for the average of eight accelerograms used to verify the design procedure using NLTHA.

4.3.2 Real earthquakes

In the second set of earthquakes, accelerograms were chosen without any artificial adjustment. Eight different earthquakes from Maley et al. (2012) were selected. These were: Denali earthquake, Nov. 3, 2002, LA1; Chi-Chi earthquake Sep. 9, 1999, from three locations, LA2, LA3, LA4; Darfield earthquake, Sep. 4, 2010, LA5; Loma Prieta earthquake, Oct. 17, 1989, from two locations LA6, LA7; and Irpinia earthquake, Nov.

23, 1980, LA8. The earthquakes used are shown in Table 4.2, which gives the ID used for the study, Date of the earthquake, PEER ID, the magnitude, M and the epicentre distance, r. The corresponding accelerograms are shown from Figure 4.15 to Figure 4.22.

Table 4.2: Second set of ground motions used in the study.

Earthquake	ID used	Date	PEER ID	Magnitude, M	Distance, r (km)
Denali, Alaska	LA1	Nov. 3, 2002	2111	7.9	62
Chi-Chi, Taiwan	LA2	Sep. 9, 1999	1518	7.62	107
Chi-Chi, Taiwan	LA3	Sep. 9, 1999	1440	7.62	173
Chi-Chi, Taiwan	LA4	Sep. 9, 1999	1352	7.62	148
Darfield, NZ	LA5	Sep. 4, 2010	-	7.1	-
Loma Prieta	LA6	Oct. 17, 1989	804	6.93	84
Loma Prieta	LA7	Oct. 17, 1989	804	6.93	84
Irpinia, Italy-01	LA8	Nov. 23, 1980	284	6.9	33

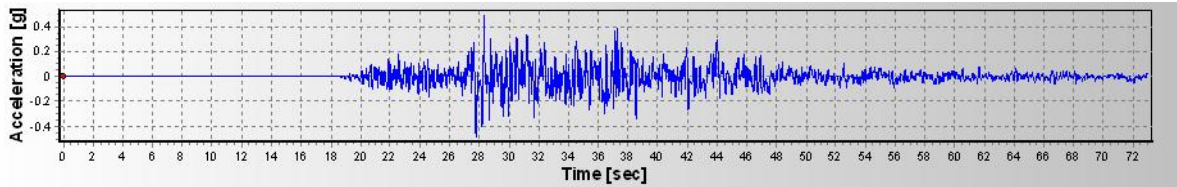


Figure 4.15: Denali earthquake, Nov. 3, 2002, LA1.

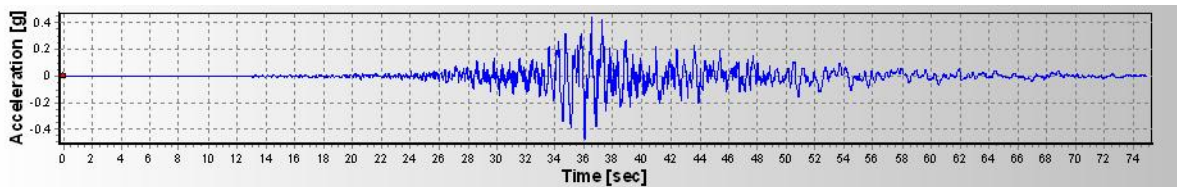


Figure 4.16: Chi-Chi earthquake, Sep. 9, 1999, LA2.

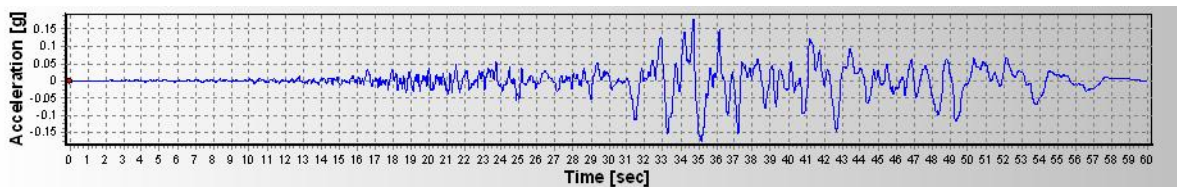


Figure 4.17: Chi-Chi earthquake, Sep. 9, 1999, LA3.

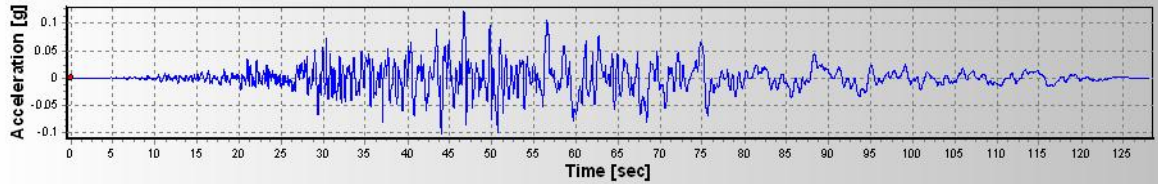


Figure 4.18: Chi-Chi earthquake, Sep. 9, 1999, LA4.

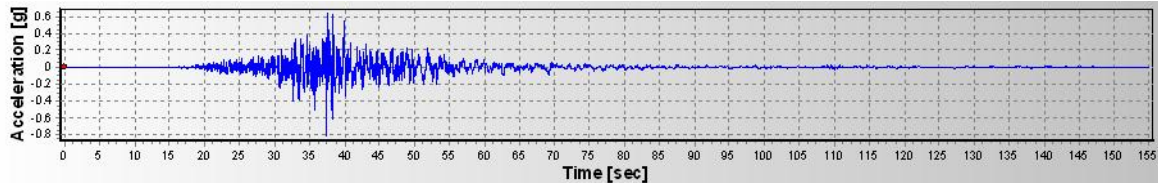


Figure 4.19: Darfield earthquake, Sep. 4, 2010, LA5.

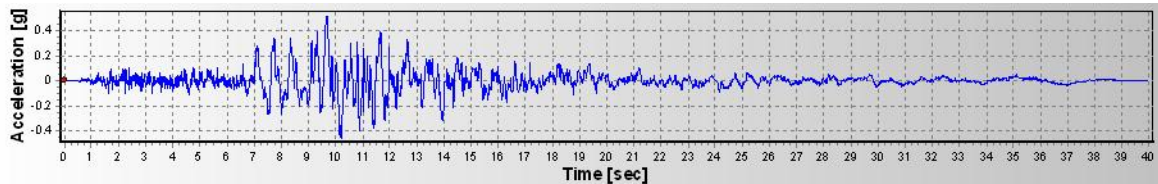


Figure 4.20: Loma Prieta earthquake, Oct. 17, 1989, LA6.

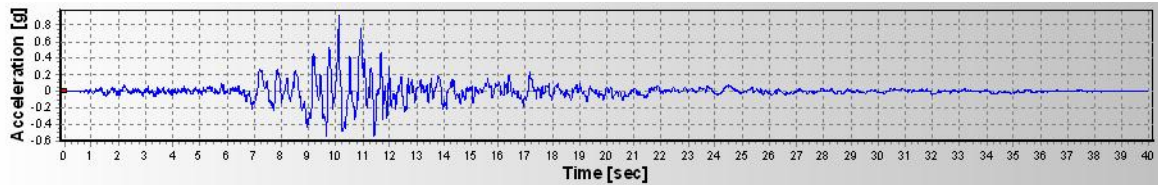


Figure 4.21: Loma Prieta earthquake, Oct. 17, 1989, LA7.

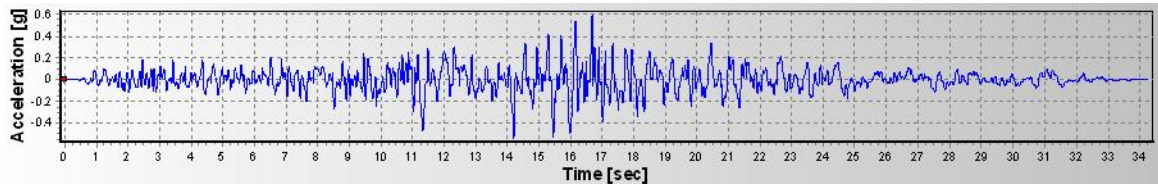


Figure 4.22: Irpinia, Nov. 23, 1980, LA8.

Similar to the artificially adjusted records presented in Section 4.3.1, the time history accelerograms for the second set of earthquakes are scaled to get a displacement response spectrum that matches the soil type C design displacement spectrum with 5% damping from EC8 (CEN 2004), which is used to verify the DDBD for the case studies presented

in Chapter 7. Response spectra for the scaled accelerograms are found using the programme SeismoSignal (SeismoSoft 2007) for the elastic response spectra with 5% damping. These are shown in Figure 4.23 and Figure 4.24. They showed quite good spectrum-compatibility with EC8 type 1 spectrum, soil type C, at the period range of interest in this study (i.e. $T_e \leq 7s$).

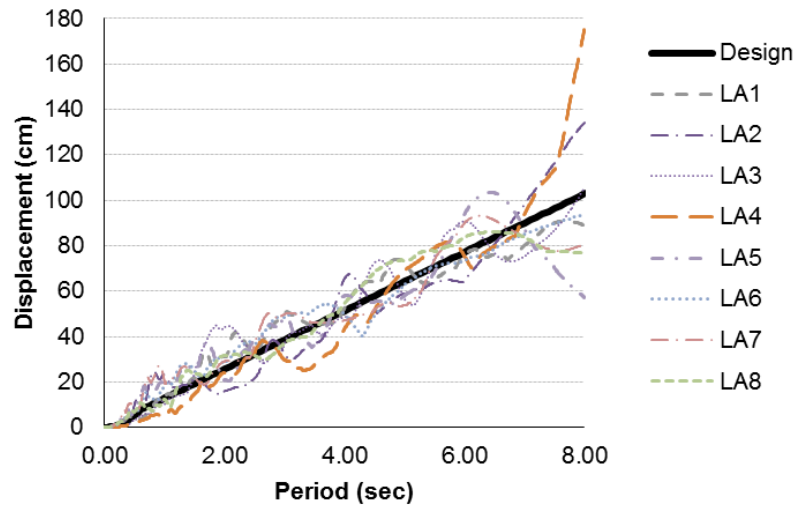


Figure 4.23: 5% design spectrum compared to the scaled displacement spectra for real eight accelerograms used to verify the design procedure using NLTHA.

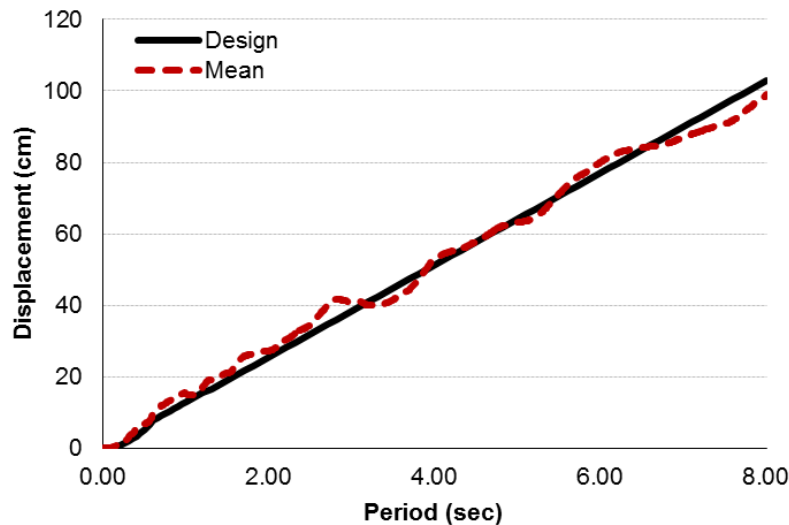


Figure 4.24: 5% design spectrum compared with the average of scaled displacement spectra for real eight accelerograms used to verify the design procedure using NLTHA.

4.4 Generation of inelastic displacement spectra

The DDBD procedure requires a modification of the elastic displacement response spectrum to account for ductile response, where the influence of ductility is represented by equivalent viscous damping. Seismologists have derived formulas for a damping modifier, R_ξ , to be applied to the elastic displacement spectrum for different levels of damping ξ . The expression used for the reduction factor in the current study is taken from the 1998 edition of EC8 (CEN 1998) and is shown in the following equation:

$$R_\xi = \left(\frac{0.07}{(0.02 + \xi)} \right)^{0.5} \quad [4.1]$$

The expression for R_ξ used in this study was defined in the 1998 edition of EC8 (CEN 1998) and it is different from the one that specified in the 2004 edition of EC8 (CEN 2004). The reason for using the 1998 expression is that the DDBD methodology was developed using this damping modifier.

To assure the compatibility between the modified displacement spectrum at the required level of damping and the response spectra generated by the accelerograms at the same level of damping, the damping levels of 16.4% and 18.54% for a 4-storey and 12-storey buildings, respectively, which will be used as case studies for validating the DDBD for multi-storey CBFs in Chapter 7 are chosen. The damping modifiers, R_ξ , are found and applied to the elastic displacement spectrum and design displacement spectrum is found. In parallel to this, the displacement response spectra for the two sets of accelerograms (artificially adjusted and real accelerograms) are found using SeismoSignal (SeismoSoft 2007) with 16.4% and 18.54% damping values and the spectra were then compared to the design displacement spectrum, as shown from Figure 4.25 to Figure 4.28. In addition, the average of the entire earthquakes response spectra for every set of earthquakes at 16.4% and 18.54% damping were compared with the modified design spectrum, in Figure 4.29 to Figure 4.32. It is apparent that the match can be considered as acceptable for the period range of interest in this study (i.e. $T_e \leq 7$ secs)

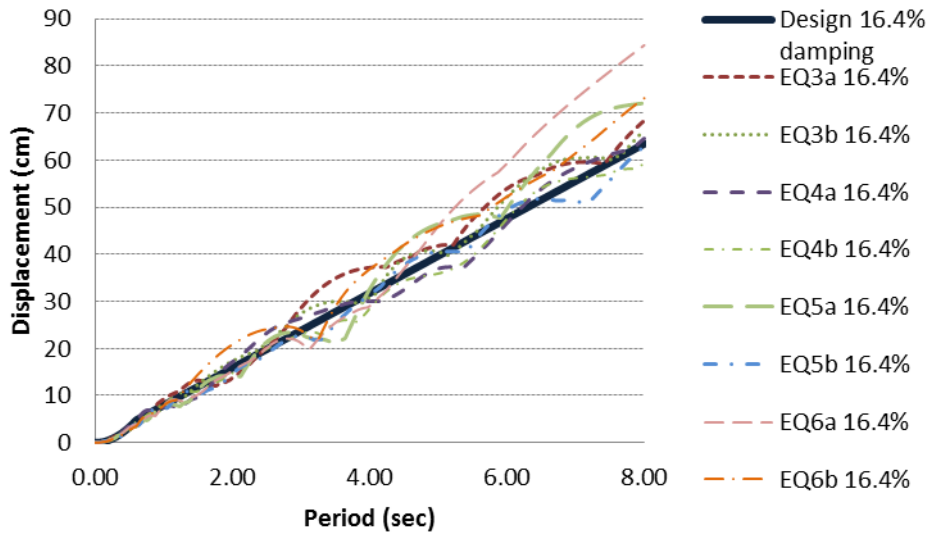


Figure 4.25: Design displacement response spectrum of 16.4% damping compared with the displacement spectra for the artificially adjusted accelerograms of 16.4% damping.

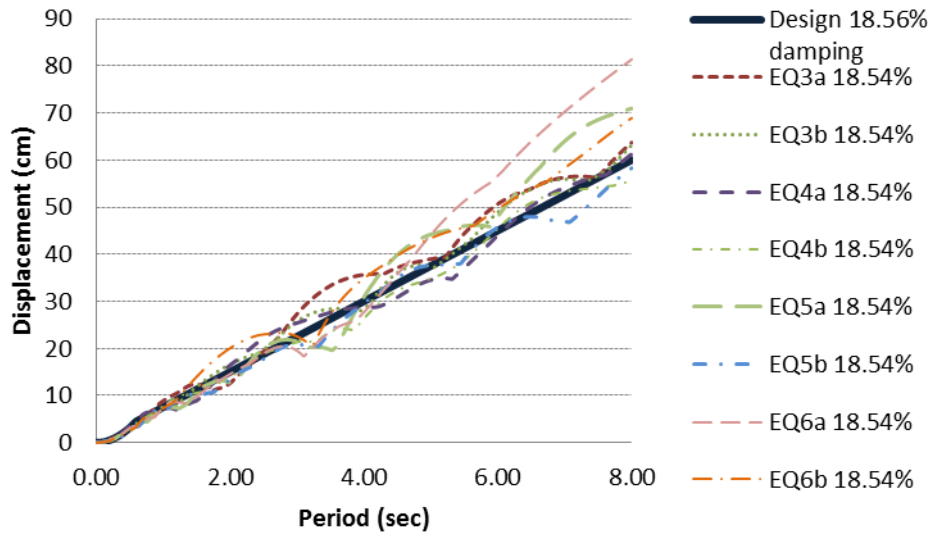


Figure 4.26: Design displacement response spectrum of 18.54% damping compared with the displacement spectra for the artificially adjusted accelerograms of 18.54% damping.

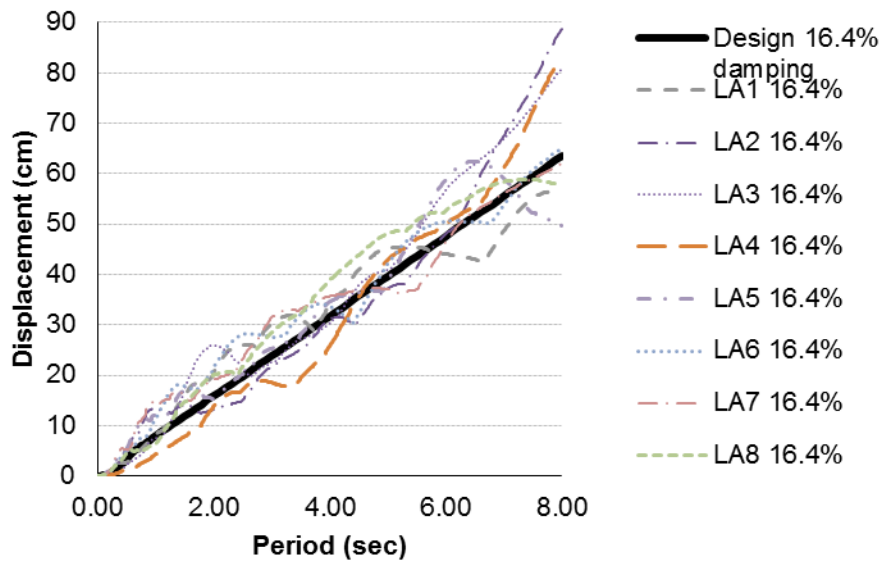


Figure 4.27: Design displacement response spectrum of 16.4% damping compared with the displacement spectra for the real accelerograms of 16.4% damping.

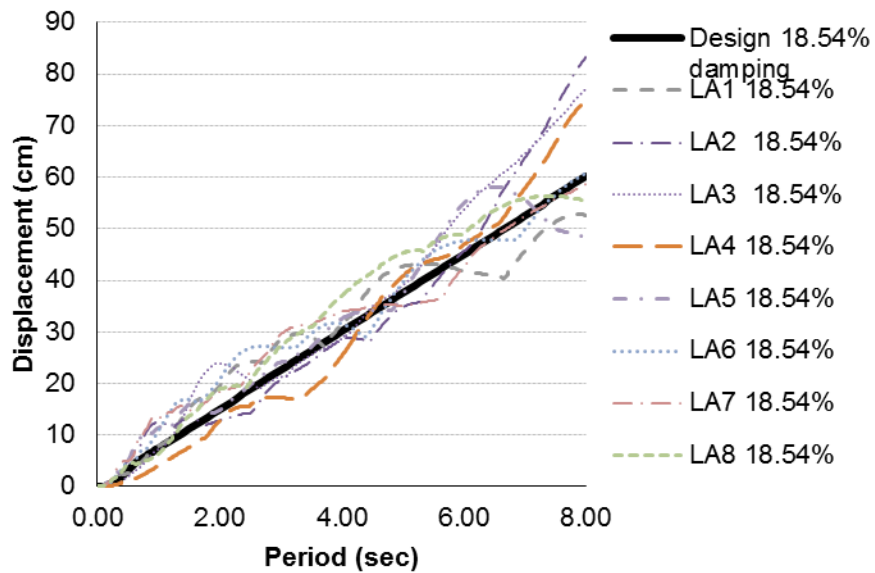


Figure 4.28: Design displacement response spectrum of 18.54% damping compared with the displacement spectra for the real accelerograms of 18.54% damping.

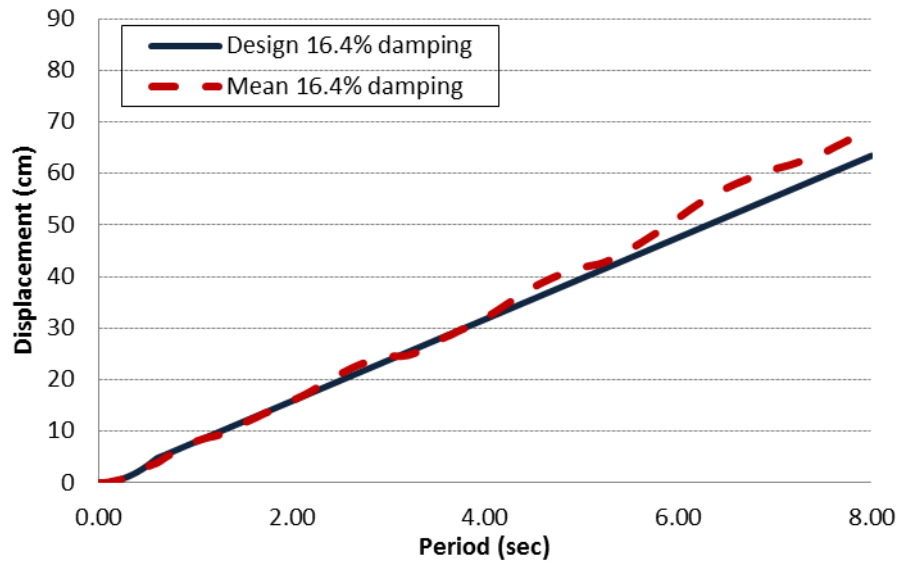


Figure 4.29: Design displacement response spectrum of 16.4% damping compared with the mean of displacement spectra for the artificially adjusted accelerograms of 16.4% damping.

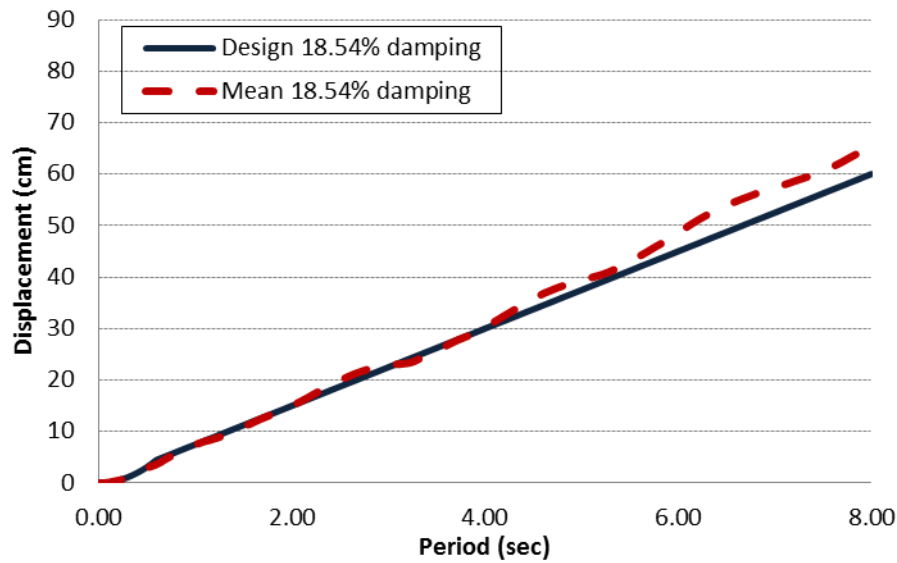


Figure 4.30: Design displacement response spectrum of 18.54% damping compared with the mean of displacement spectra for the artificially adjusted accelerograms of 18.54% damping.

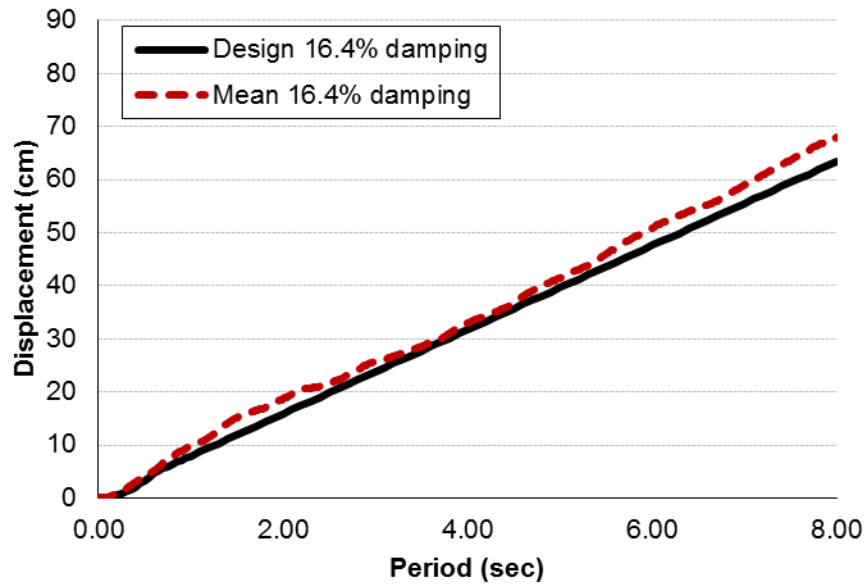


Figure 4.31: Design displacement response spectrum of 16.4% damping compared with the mean of displacement spectra for the real accelerograms of 16.4% damping.

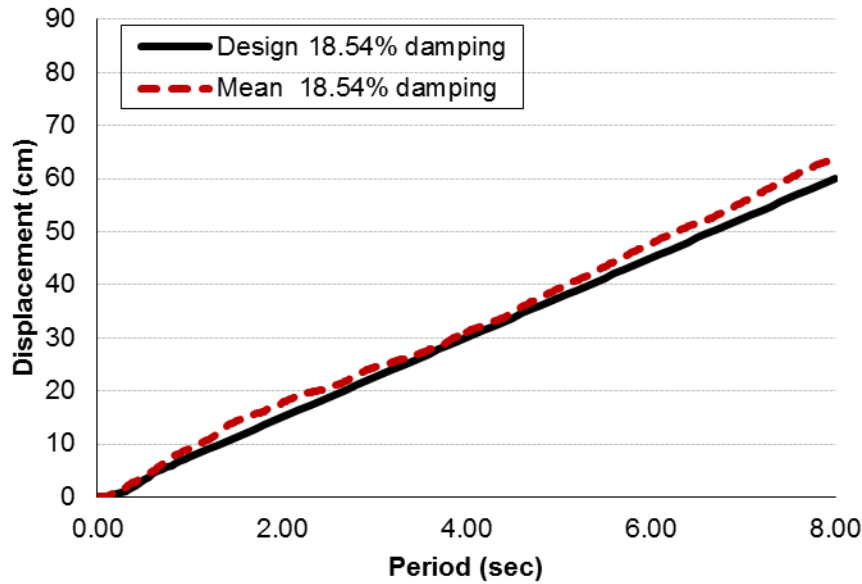


Figure 4.32: Design displacement response spectrum of 18.54% damping compared with the mean of displacement spectra for the real accelerograms of 18.54% damping.

4.5 Summary and conclusion

In this chapter, two sets of earthquakes were presented to be used in NLTHA. Each set of accelerograms is scaled to match the ground motion spectra used for design. The first set consists of artificially adjusted accelerograms and is scaled to match the displacement spectra for the accelerograms used for the shake table tests. Furthermore, it is scaled to have a displacement spectra matching EC8 type 1, soil type C spectrum, which will be used to design case studies for multi-storey concentrically braced frames. NLTHA will be used to verify the design procedure using these scaled accelerograms. To check the sensitivity of the case studies to different earthquakes, another set of real earthquakes presented in this chapter with displacement spectra matching the design displacement spectra will be used.

Chapter 5

Validation of non-linear time history analysis models for single storey concentrically braced frames using full scale shake table tests

5.1 Introduction

It is imperative that accurate, reliable and robust numerical models are available to represent the behaviour of structural systems during earthquakes, as these are often used to verify and refine designs carried out using more conventional code-based methods. Moreover, nonlinear time history analysis is often used to develop and validate important design parameters in direct displacement based design procedures. For example, this is the approach taken by Wijesundara (2009) when developing a direct displacement based design methodology for concentrically braced frames (CBFs) with rectangular hollow sections (RHS) as brace members. The objective of this chapter is to validate a numerical model for brace members in CBFs that can be used in nonlinear time history analysis to determine the performance of the structural system when excited by an earthquake.

The computational framework Open System for Earthquake Engineering Simulation (OpenSees) (McKenna et al. 2000) is used for numerical modelling in this study. In Chapter 3, a nonlinear beam column element model for steel structural hollow sections based on fibre elements incorporating a fatigue model that detects fracture was calibrated, and subsequently validated, using pseudo-static cyclic tests on brace members. A good agreement between the main response parameters of the numerical models and physical

pseudo-static cyclic tests, including the maximum tensile capacity, initial buckling capacity, number of cycles to fracture, and the energy dissipated by the specimens was found. In this chapter, the model developed for the structural steel hollow section brace element in Chapter 3 will be incorporated into a two-dimensional numerical model of concentrically braced frames and validated using real-time shake table tests that utilise real earthquake records that have been scaled to impart significant ductility demand on the structural systems. Each test model represents an idealisation of a single storey within a typical form of concentrically braced frame, in which the load-sharing between the tension and compression braces is accounted for. Non-linear time history analysis (NLTHA) will be performed on the test model with applied base excitation. Results will be compared with measured data from shake table tests to prove its validity. Furthermore, the sensitivity of the model to earthquake inputs is investigated.

5.2 Shake table tests

5.2.1 Test set-up

Elghazouli et al. (2005) carried out shaking table tests at the Laboratory for Earthquake Engineering of the National Technical University of Athens (NTUA) on full scale structures that represented an idealisation of a single storey within a typical form of concentrically braced frame, in which the load-sharing between the tension and compression braces is accounted for. The earthquake simulator consists of a rigid steel 4m x 4m platform with a system for controlling the motion of the table and recording the response of the specimen tested on it. The table capacity specified a maximum acceleration of 1.5g in each horizontal direction (g is the acceleration due to gravity and equal 9.81m/s^2), but for experimental design, a maximum acceleration of 1.0g was assumed. A maximum mass of 10,000kg was permitted, if the centre of gravity is at 2m above the simulator's platform. The operating frequencies of the shake table (for each degree of freedom) are 0.1 to 50 Hz.

Considering the table limits and characteristics, together with ease of specimen handling and turnover, the test frame had an overall height of 2.89m and plan dimensions of 2.70m x 2.47m, as shown in Figure 5.1. The one-storey-one-bay frames tested were supporting a

mass of approximately 10,000kg. Columns and beams were designed to behave elastically with pinned end connections in the direction of the earthquake. For each test, two hollow brace specimens were rigidly connected at their top ends to the bottom flange of the transverse beams, and at their lower ends to the table platform. The two braces are not connected at mid-length, and are separated in plan by an appropriate spacing to avoid contact during out-of-plane buckling. A view of the test frame is shown Figure 5.2.

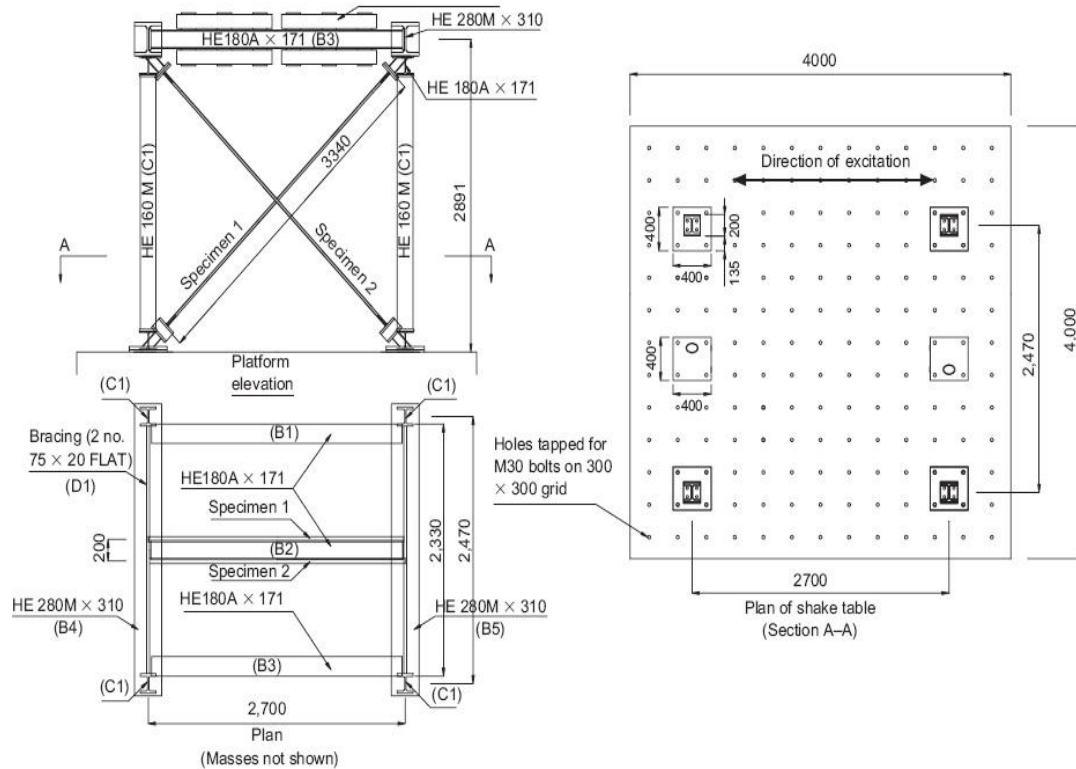


**Figure 5.1: Diagram of the experimental set-up for the shake table test (all dimensions are in mm)
(Elghazouli et al. 2005).**

5.2.2 Specimen properties

The constraints on the capacity of the shaking table limited the cross-sectional size of the bracing members that could be tested under strong earthquake loading. To enable adequate examination of the parameters under consideration, rectangular and square hollow sections manufactured from cold-formed steel S235JRH, with nominal minimum yield strength of 235MPa and an ultimate strength of between 360MPa and 510MPa (CEN 1997) were utilised. Braces with three different cold-formed square and rectangular

hollow cross-section sizes were examined ($20 \times 20 \times 2.0$, $50 \times 25 \times 2.5$ and $40 \times 40 \times 2.5$). These sizes were selected to provide a range of section and member slenderness within the capacity of the shake table. When using the RHS $50 \times 25 \times 2.5$ as the braces for the shake table tests, the brace specimens were oriented to have the weaker axis in-plane in order to obtain in-plane buckling.



Figure 5.2: Photo of the experimental set-up for the shake table test (Goggins 2004).

Seven test frames are studied in this chapter. Shake table and specimen parameters are shown in Table 5.1, which includes the test IDs, brace section sizes, yield force, F_y , slenderness ratio, $\bar{\lambda}$, the wave form of the table (ground) excitation and the peak ground acceleration, PGA, applied to the table. Test ID's assigned to describe the tests were the same used by Goggins (2004) for ease of referencing. The first two letters 'ST' are abbreviation of shake table followed by the test number, letter 'R' represents Sine Ramp, letter 'E' represents the earthquake (El Centro or synthetic) followed by a number which represent the nominal depth of the hollow steel section represented by 'H'. Tests ST2-E50H, ST5-E20H-B, ST7-E40H and ST8-E40H were subjected to a scaled acceleration history from the Imperial Valley record of the El Centro earthquake. The original record, with a peak ground acceleration of about 0.34g was appropriately scaled for each frame

depending on the expected strength. The estimate of the scaling factor for each frame size was based on the following relationship: [(maximum expected base shear X behaviour factor)/(mass X dynamic magnification factor X peak ground acceleration)]. A behaviour factor of 3.0 was assumed as a representative value for CBFs. Tests ST1-R50H, ST4-R20H and ST7-R40H were subjected to sine ramp. Test ST5-E20H was subjected to a synthetic record representing the range of dominant frequencies in an idealized Eurocode 8 spectrum.

Detailed discussions of the results and observations from the shake table tests are found in Goggins (2004), Elghazouli et al. (2005) and Broderick et al. (2008). Global displacement ductility demands, calculated as the ultimate lateral frame deformation normalised by the estimated lateral displacement at yield with reference to the average yield strength measured from monotonic static tensile tests on specimens cut from the steel length, as high as 13 were experienced during the shake table tests (Elghazouli et al. 2005). Many of the test frames experienced ductility demands greater than 6 without failure, with ultimate brace failure only occurring with ductility demands of the order of 14 or more.

The ultimate failure mode of the hollow bracing members was observable in tests ST7-E40H and ST8-E40H. Following brace global buckling, local buckling occurred at mid-length and close to the fixed brace ends, causing high strains to develop in the corner regions of the cross-section, where the steel exhibits a reduced fracture strain due to cold-working. Cracks eventually formed in these regions, and gradually propagated through the cross-section under repeated cyclic loading.

Only slight local buckling at mid-length and brace ends was evident in the 50x25x2.5 brace members. No significant local buckling was observed for the 20x20x2.5 members. The initiation of local buckling and fracture is influenced by the width-to-thickness ratio of the elements of the cross-section, as well as the applied loading history. There is also a strong dependence on brace slenderness, since for a given level of lateral deformation, higher curvature arises in plastic hinges that form in members with relatively low slenderness (Goggins et al. 2005). The brace failure in tests ST7-E40H and ST8-E40H

can therefore be attributed to a combination of relatively low member slenderness and high width-to-thickness ratio, coupled with a significant ductility demand. Thus, the slenderness of a brace appears to be the most important factor in determining the hysteretic behaviour and their ductility is reduced significantly due to local buckling in the sections. This was also observed by Jain et al. (1977; 1978; 1980), Black et al. (1980), Popov and Black (1981), Gugerli and Goel (1982), Astaneh-Asl and Goel (1984), Astaneh-Asl et al. (1985), Tang and Goel (1989), Walpole (1995), Tremblay (2002) and Goggins et al. (2006).

Table 5.1: Shake table and specimen parameters.

Table test ID	Section size	F _y (MPa)	$\bar{\lambda}$	Table input characteristics	
				Wave form	PGA (m/s ²)
ST1-R50H	50X25X2.5RHS	328	2.21	Sine Ramp	8.5
ST2-E50H	50X25X2.5RHS	315	2.23	El-Centro	7.9
ST4-R20H	20X20X2.0SHS	300	2.78	Sine Ramp	10
ST5-E20H	20X20X2.0SHS	400 (300) ^a	2.87	Synthetic	5.1
ST5-E20H-B	20X20X2.0SHS	435	2.87	El-Centro	5.0
ST7-E40H ^b	40X40X2.5SHS	358	1.49	El-Centro	19.6
ST8-E40H ^b	40X40X2.5SHS	396	1.58	El-Centro	19.7
^a The braces had different yield strength					
^b Full fracture of brace specimen observed in physical test causing frame to collapse					

5.3 Non-linear time-history analysis (NLTHA)

Understanding the real behaviour of structures is important for reliable seismic design. For example, target maximum displacements (also known as design displacements) are used as the starting point in direct displacement based design. In force based design, a check is carried out in the latter stages of the design process to ensure maximum displacement design limits are not exceeded. Neither of these common design methodologies explicitly takes into account the displacement time history of the structure during the earthquake. For example, the direct displacement based design technique uses equivalent viscous damping models, developed specifically for various structural systems

at different ductility levels, to account for the transient hysteretic behaviour of the system during earthquakes. Non-linear time-history analysis (NLTHA) gives the response of a structure over time during and after the application of a load. However, Goggins and Sullivan (2009) noted that non-linear time-history analysis techniques and models should be developed further to better predict the displacement response of CBF systems. A numerical model for CBF systems employed in nonlinear time history analysis, in which the load-sharing between the tension and compression structural steel hollow section braces is accounted for, will be validated in this chapter. This will be achieved by comparing the predictions of the numerical model to real-time shake table tests that utilise real earthquake records that have been scaled to impart significant ductility demand on the structural system.

The computational framework Open System for Earthquake Engineering Simulation (OpenSees) (McKenna et al. 2000) is used for numerical modelling of CBF systems in this study. As discussed in Chapter 3, OpenSees uses the physical-theory models to represent the structural elements. To represent the shake table tests, two-dimensional numerical models are carried out. In the numerical model, two columns and a beam are modelled to behave elastically with pinned end conditions. Two hollow brace specimens are modelled with fixed connections with the beam at their top ends and fixed to the ground at their lower ends, as shown in Figure 5.3.

The columns and beams are modelled as elastic beam-column elements. The nonlinear beam-column element presented in Chapter 3 is employed to represent the brace member. As a consequence of the study presented in Chapter 3, every brace consists of two nonlinear beam-column elements with ten integration points per element and an initial camber added to the middle of the braces to allow the braces to buckle. The initial camber was taken as approximately 1% of the length of the brace. The initial camber used was in the in-plane direction to have in-plane buckling, which is the weaker direction due to the orientation of the brace and end connection detail (see Figure 5.1 and Figure 5.2). Young modulus of the material, E , was taken as 200GPa. Yield strength values for every model were varied according to the material coupon tests as recorded in

the experimental study (Goggins 2004). A strain hardening ratio of 0.008 is used. A solution algorithm of type KrylovNewton is used. This solution algorithm tests convergence on the norm of the displacement increment vector with a tolerance of $1e-12$ and a maximum number of iterations of 1000. A Newmark acceleration time integration method with gamma and beta of 0.5 and 0.25 respectively is used. Rayleigh damping model proportional to mass and stiffness is used. Elastic damping of 3% was specified which was found from the physical tests. The equations are formed using UmfPack system and numbered using an RCM (reverse Cuthill-McKee) numberer (McKenna et al. 2000). The constraints are enforced with a transformation constraint handler.

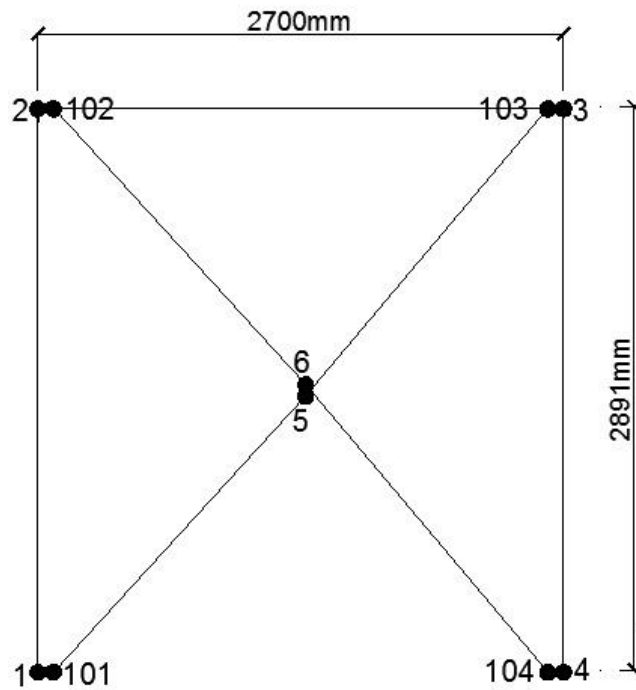


Figure 5.3: Shake table model used in OpenSees.

5.4 Comparison between shake table tests and NLTHA

Non-linear time history analysis (NLTHA) was performed on the test models detailed in Section 5.2 using OpenSees. The brace material properties, brace dimensions, frame dimensions, mass and table (ground) input excitation properties used in the NLTHA were as measured in physical tests. Results from the NLTHA are compared with those from

shake table tests in Table 5.2. In particular, the maximum relative lateral frame displacement, Δ_{\max} , maximum base shear, F_b , total energy dissipated, W_{tot} , and equivalent viscous damping, ξ_{eq} , observed in the physical tests and the numerical models are given in terms of ratios of data obtained from the numerical models to that obtained from the physical tests. It was found that, in general, the numerical model gives a good prediction of the maximum measured displacements and base shear forces with the mean values being 0.87 and 1.11 of those measured in the physical tests, respectively. The corresponding coefficients of variation (C_V) were 0.17 and 0.09, respectively.

Comparisons of the energy dissipated and equivalent viscous damping between the physical tests and the numerical models were carried out. The procedure used to calculate the energy for both the physical test and the numerical model was based on equating the total energy absorbed by the frame during its response to specific accelerogram.

The work done, W_D , or energy dissipated, by a viscous dashpot in a linear SDOF system for a total time T , is given by

$$W_D = \int_0^T c \dot{u}(t) \cdot \delta u = c \int_0^T \dot{u}(t)^2 \cdot dt = c \sum_{i=1}^N \frac{(\Delta u_i)^2}{\Delta t_i} \quad [5.1]$$

where c is the damping coefficient, Δu_i is the change in relative displacement measured over a time step $\Delta t_i = t_{i+1} - t_i$. The actual energy dissipated, E_{nc} , by the concentrically braced frames during the test (non-viscous damping mechanisms) can be given by

$$E_{\text{nc}} = \int_0^T Q(t) \cdot du = \sum_{i=1}^N Q_i \Delta u_i \quad [5.2]$$

where $Q(t)$ is the restoring force which is comprised of a conservative force ($F = ku(t)$, where k is the stiffness of the system and $u(t)$ is the relative displacement) and non-conservative force. Assuming that the energy due to the conservative load is zero when summing a whole cycle, the energy dissipated in an equivalent linear SDOF system can be equated to that dissipated during the inelastic shake table tests and resulting in:

$$c_{eq} = \frac{\sum_{i=1}^N Q_i \Delta u_i}{\sum_{i=1}^N \frac{(\Delta u_i)^2}{\Delta t_i}} \quad [5.3]$$

And the equivalent viscous damping factor is

$$\xi_{eq} = \frac{c_{eq}}{2\omega_n m} \quad [5.4]$$

where c_{eq} is the equivalent viscous damping coefficient, m is the mass and ω_n is the natural circular frequency.

For some cases, the numerical model underestimated the total energy dissipated and the equivalent viscous damping, as shown in Table 5.2. On the other hand, as observed in Chapter 3, numerical models of the brace members only subjected to cyclic axial loading generally slightly overestimated the energy dissipated estimated from physical tests due to fatter hysteretic loops in the numerical models, especially for stockier elements where local buckling could not be captured. In CBFs subjected to earthquake loadings presented in this chapter, the idealisation in the numerical model of the connections between columns and beams as being perfectly pinned, which does not dissipate any energy, may be not the case for the actual physical shake table tests. This and other sources of energy dissipation in the actual physical tests, such as potential slip between the masses and the beams, led to the simple numerical model underestimating the total energy dissipated for most of the test frames.

As discussed earlier, some common design methodologies, such as direct displacement based design (DDBD) and force based design (FBD), do not explicitly take into account the displacement time history of the structure during the earthquake. Moreover, non-linear time history analysis (NLTHA) is used as a tool in the development of more simplified design methodologies. For example, NLTHA has been used to determine equivalent viscous damping models for various structural systems at different ductility levels to account for the transient behaviour of the system during earthquakes, which in turn have been employed in a direct displacement based design (DDBD) methodology. Furthermore, understanding the real behaviour of structures is important for reliable

seismic design. Thus, the following sub-sections will investigate the transient displacement and forces observed in the CBF systems, as well as the estimated equivalent viscous damping values.

Table 5.2: Comparison of the results between the physical shake table tests and the numerical models in OpenSees.

Test ID	Physical test results				Numerical model/ Physical test			
	Δ_{\max} (mm)	F_b (KN)	W_{tot} (Nm)	ξ_{eq} (%)	Δ_{\max}	F_b	W_{tot}	ξ_{eq}
ST1-R50H	18.8	84.9	31474	7.22	1.15	1.20	0.58	0.59
ST2-E50H	61.5	96.0	41496	7.72	0.93	1.03	0.72	0.83
ST4-R20H	32.0	38.8	8769	3.58	0.92	1.28	0.56	0.81
ST5-E20H	59.9	53.2	6759	7.34	0.69	1.09	1.05	0.82
ST5-E20H-B	83.5	54.1	15962	4.06	0.74	1.12	0.74	0.97
ST7-E40H	128.0	113.3	66395	5.35	0.87	1.00	0.74	0.87
ST8-E40H	131.0	122.0	73384	6.37	0.83	1.08	0.99	0.96
Mean					0.87	1.11	0.77	0.84
C_v					0.17	0.09	0.24	0.15

5.4.1 Displacement and axial force time history response

Knowing displacements induced during earthquakes will help to understand the behaviour of structures, which normally are designed to achieve or not exceed a design limit displacement, depending on the design methodology used. For example, Figure 5.4 shows a good agreement between the transient relative lateral displacement of the test frame ST2-E50H measured in physical tests and that obtained from the numerical model, reflecting the ability of the numerical model to accurately predict the transient displacement response of the test frame. For test ST8-E40H, a failure of a brace occurred through accumulation of damage by local buckling and tensile yielding, as shown in Figure 5.5. The numerical model did not detect damage to the brace members (Figure 5.5). This is probably due to the inability of the numerical model to explicitly account for the accumulative damage to the brace member by local buckling of the structural hollow section. However, as will be discussed in Section 5.5, the same numerical model for frame ST8-E40H did detect damage and full fracture of the brace when subjected to other earthquakes that had similar displacement demand spectra to that

employed in the shake table test. The fatigue material model used in the brace element was calibrated using cyclic tests on brace members as shown in Chapter 3. There was a difference in the response between the numerical model and some tests containing stockier members in the post buckling range and the hysteretic loops were fatter. However, this model could accurately predict the maximum displacement ductility demand of the brace members when fracture occurs as was verified in Chapter 3 and by many of the NLTHA carried out in this chapter (see Appendix A for full set of transient displacement and load graphs).

Furthermore, the transient brace axial force response obtained from the NLTHA gave a very good representation of the real behaviour of the brace and showed that the fatigue model predicted damage to parts of the braces. The comparison between the brace axial force time history response of the shake table tests and the analytical model for test frames ST2-E50H and ST8-E40H are shown from Figure 5.6 to Figure 5.9. In addition, the numerical model captures the salient features of the hysteretic loops in the base shear-lateral displacement response, as well as the axial force-axial displacement brace member response, as shown for test frames ST2-E50H and ST8-E40H in Figure 5.10 to Figure 5.13.

For all the shake table tests subjected to earthquakes, the numerical model could predict the axial force behaviour of the physical tests relatively well and the displacement history results between the tests and the numerical models were relatively close (see Appendix A). However, for the shake table tests ST1-R50H and ST4-R20H, which were subjected to a sine ramp excitation, there was a significant difference between the displacement and force response in the physical tests and numerical models over the initial loading duration (see, for example, Figure 5.14 and Figure 5.15). The difference in amplification of the response was due to the natural frequencies of the actual physical test frame being slightly different from the idealised numerical model due to, for example, lack of fit connection details, slight difference in masses and the idealisation of beam-column connections as perfectly pinned in the numerical model. Due to the nature of excitation, which was a sine ramp with a period set at 0.8 times the expected fundamental period of

the physical test, slight differences between the fundamental period of the numerical and physical models lead to significant differences in force and displacements amplitude values during the initial period excitation. However, in latter stages after some yielding and buckling of brace members occurred, the numerical model closely predicts the response of the actual physical model, as the fundamental periods of the numerical and physical models are then similar (see, for example, Figure 5.14 and Figure 5.15).

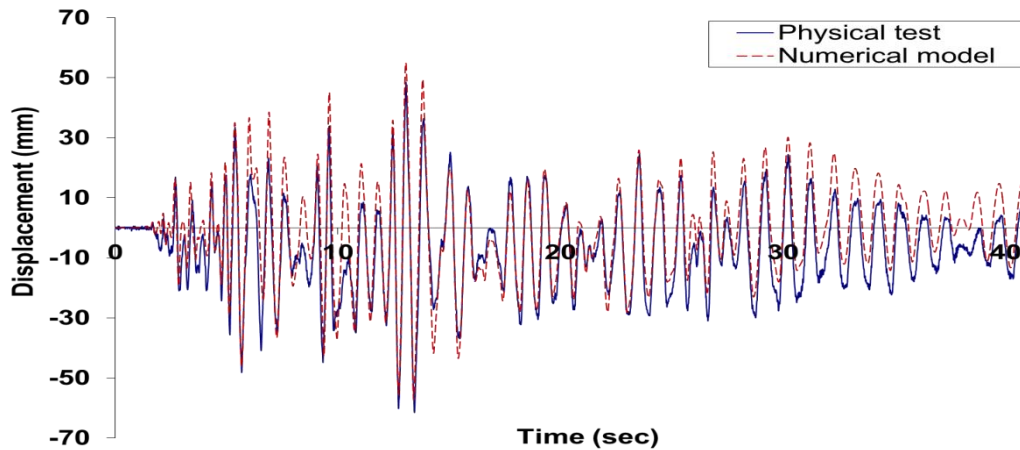


Figure 5.4: Comparison for the displacement time-history response of test ST2-E50H and the numerical model in OpenSees.

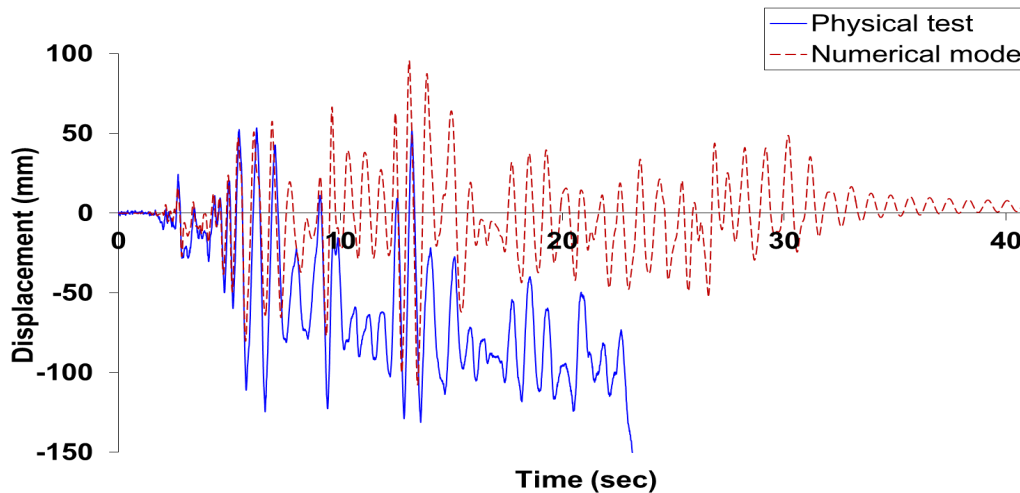


Figure 5.5: Comparison for the displacement time-history response of test ST8-E40H and the numerical model in OpenSees.

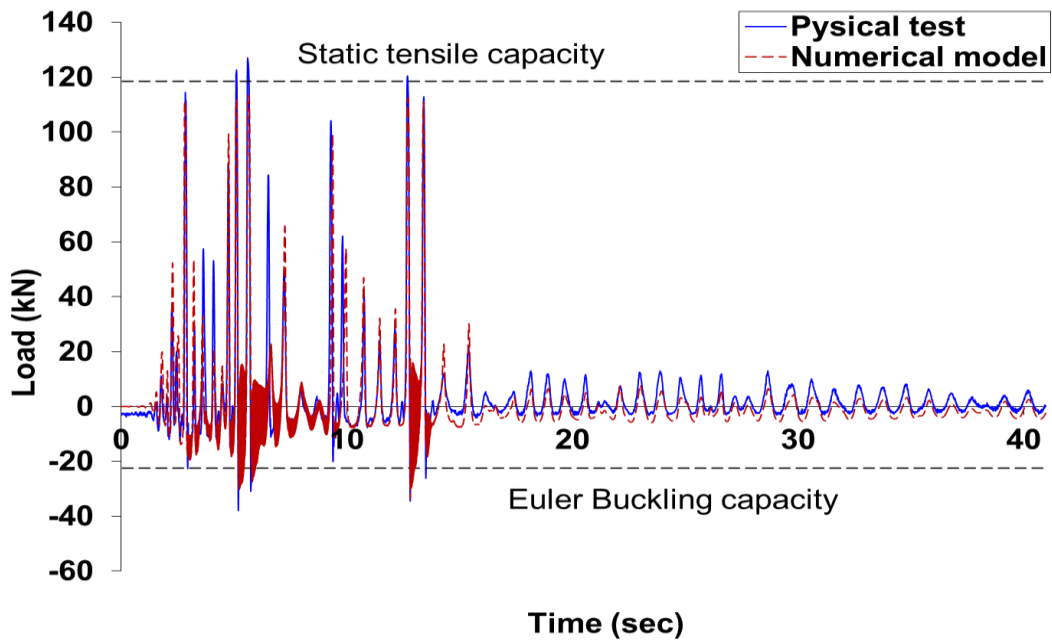


Figure 5.6: Comparison for the axial load time-history response of the first brace specimen of test ST2-E50H and the numerical model in OpenSees.

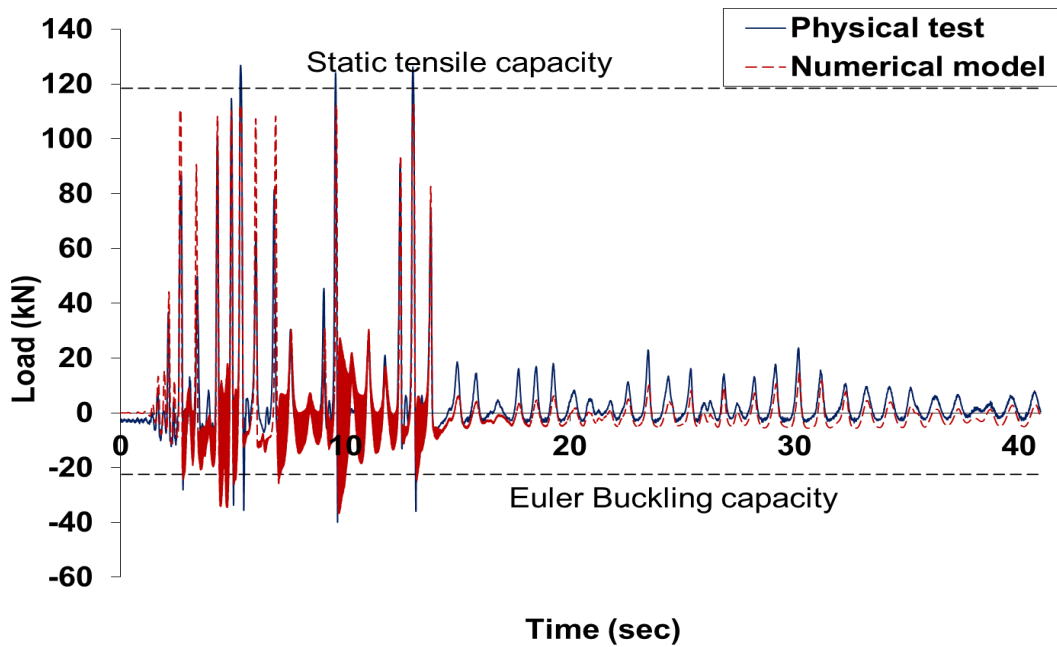


Figure 5.7: Comparison for the axial load time-history response of the second brace specimen of test ST2-E50H and the numerical model in OpenSees.

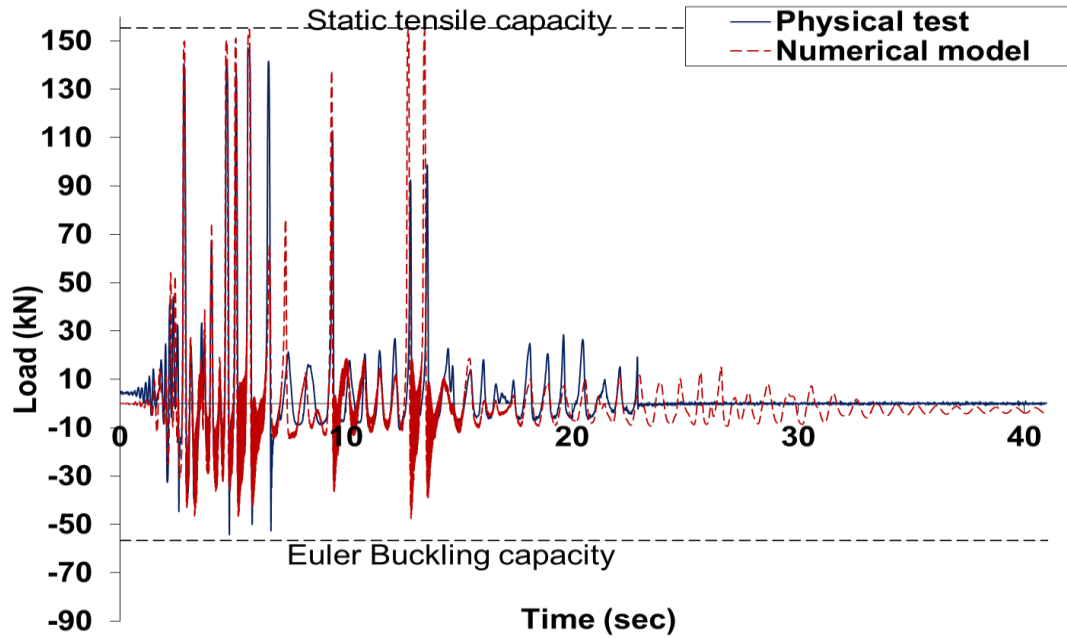


Figure 5.8: Comparison for the axial load time-history response of the first brace specimen of test ST8-E40H and the numerical model in OpenSees.

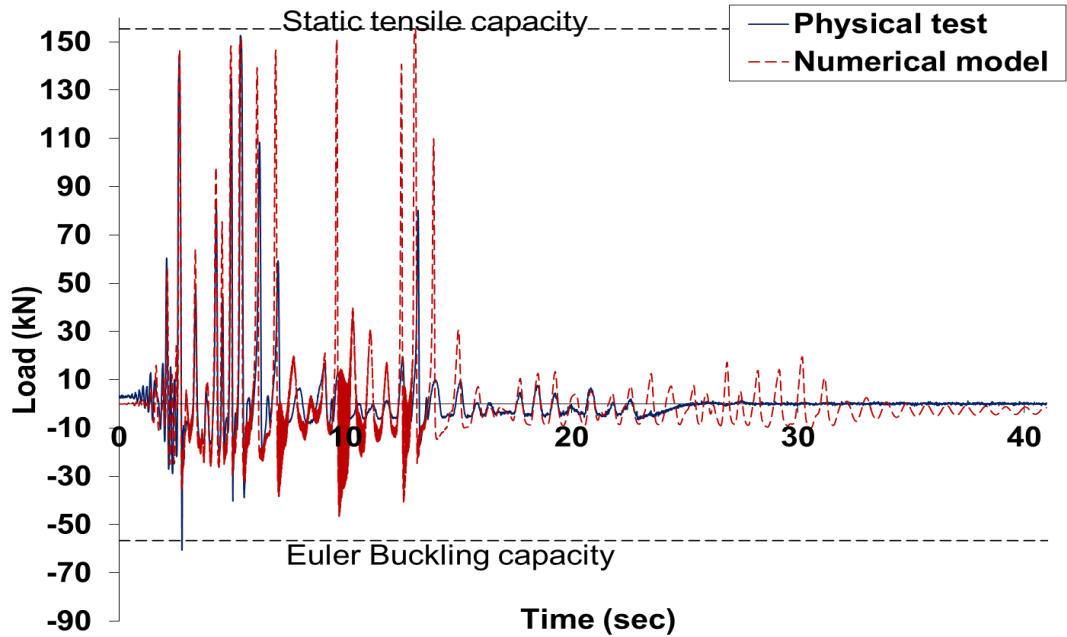


Figure 5.9: Comparison for the axial load time-history response of the second brace specimen of test ST8-E40H and the numerical model in OpenSees.

Validation of non-linear time history analysis models for single storey concentrically braced frames using full scale shake table tests

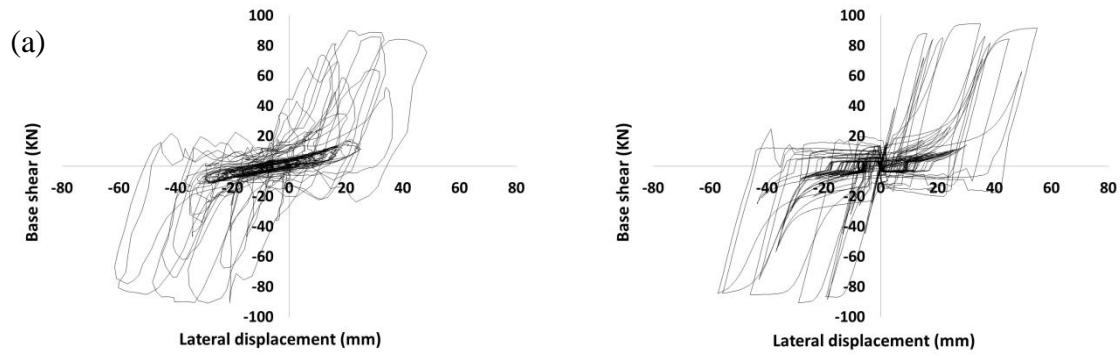


Figure 5.10: (a) Physical test and (b) numerical model base shear-lateral displacement hysteretic response of test ST2-E50H

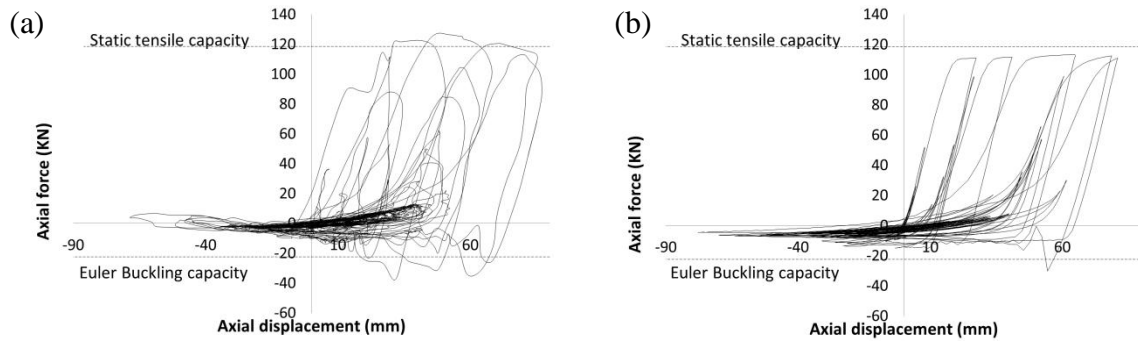


Figure 5.11: (a) Physical test and (b) numerical model axial force-axial displacement response of a brace element from test ST2-E50H.

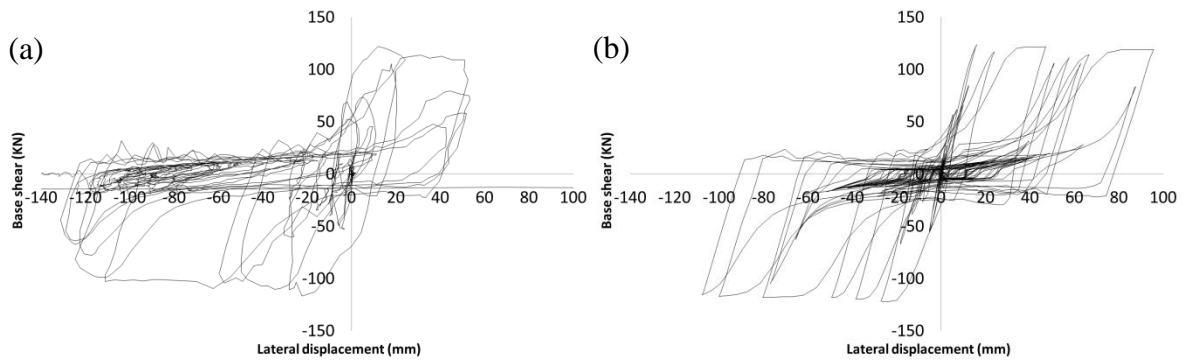


Figure 5.12: (a) Physical test and (b) numerical model base shear-lateral displacement hysteretic response of test ST8-E40H.

Validation of non-linear time history analysis models for single storey concentrically braced frames using full scale shake table tests

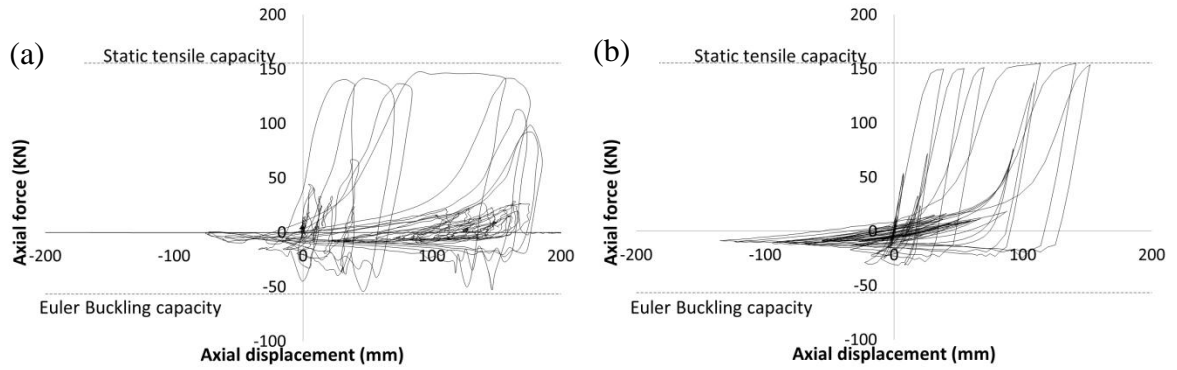


Figure 5.13: (a) Physical test and (b) numerical model axial force- axial displacement response of a brace element from test ST8-E40H.

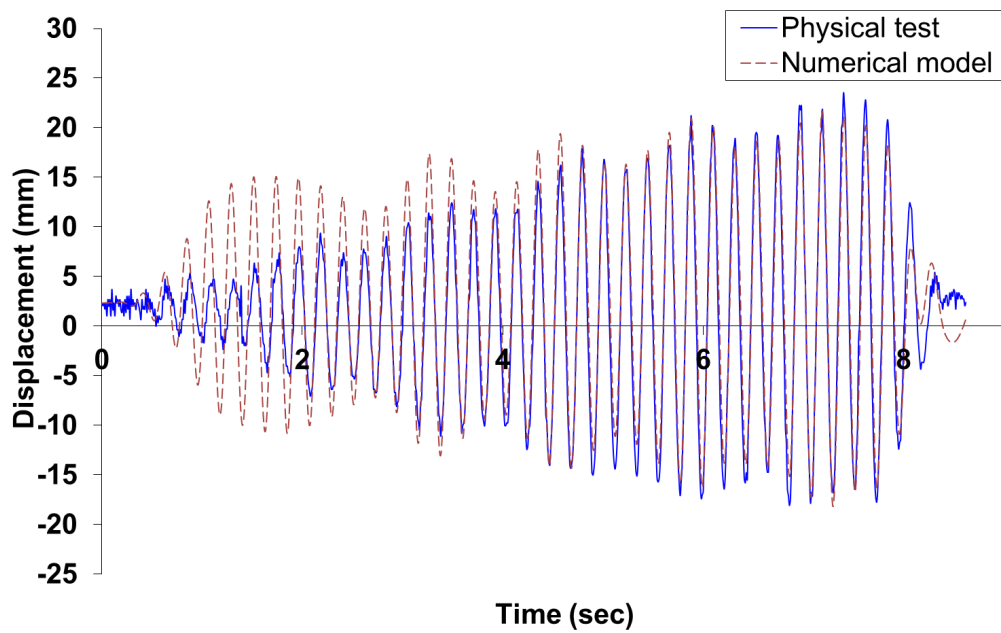


Figure 5.14: Comparison for the displacement time-history response of test ST1-R50H and the numerical model in OpenSees.

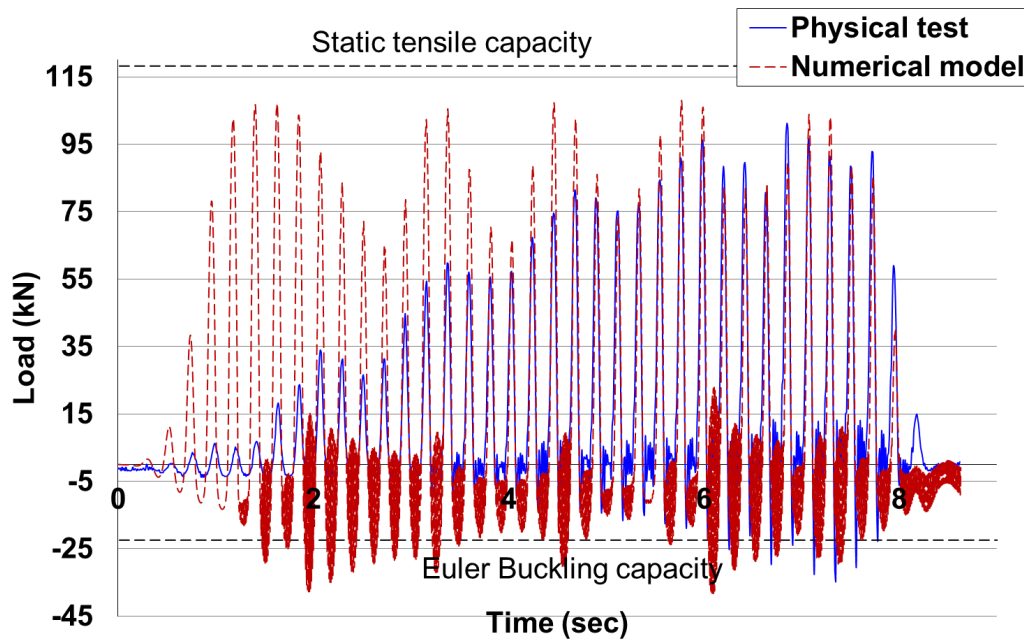


Figure 5.15: Comparison for the axial load time-history response of the first brace specimen of test ST1-R50H and the numerical model in OpenSees.

5.4.2 Equivalent viscous damping

The equivalent viscous damping (EVD), ξ_{eq} , is the sum of the elastic, ξ_o , and the hysteretic, ξ_{hyst} , damping and can be given by

$$\xi_{eq} = \xi_o + \xi_{hyst} \quad [5.5]$$

The elastic damping ratio is commonly taken as 0.03 for steel structures and the hysteresis damping depends on the hysteresis rule appropriate for the structure being designed. Hysteretic damping accounts for the effect of energy dissipated through nonlinear inelastic response.

A comparison is given in Figure 5.16 of equivalent viscous damping values from the shaking table tests, NLTHA and many different models, such as Wijesundara (2009) given in Equations [5.6] and [5.7], Kwan and Billington (2003) given in Equation [5.8], flag-shaped model given in Equation [5.9] (Priestley et al. 2007), thin Takeda model given in Equation [5.10] (Kowalsky 1994), and Ramberg-Osgood model given in Equation [5.11] (Priestley et al. 2007).

$$\xi_{eq} = 0.03 + \left(0.23 - \frac{\lambda}{15}\right) (\mu - 1) \quad \mu \leq 2 \quad [5.6]$$

$$\xi_{eq} = 0.03 + \left(0.23 - \frac{\lambda}{15}\right) \quad \mu \geq 2 \quad [5.7]$$

$$\xi_{eq} = 0.228 \left(\frac{\mu - 1}{\mu}\right) + 0.352\mu\xi_o \quad [5.8]$$

$$\xi_{eq} = \xi_o + 0.186 \left(\frac{\mu - 1}{\mu\pi}\right) \quad [5.9]$$

$$\xi_{eq} = \xi_o + \frac{1}{\pi} \left(1 - \frac{1-r}{\mu^{0.5}} - r\mu^{0.5}\right) \quad [5.10]$$

$$\xi_{eq} = \xi_o + 150 \left(\frac{\mu - 1}{\mu\pi}\right) \quad [5.11]$$

where ξ_{eq} is the equivalent viscous damping, μ is the ductility, ξ_o is the elastic damping and r is the second slope stiffness ratio.

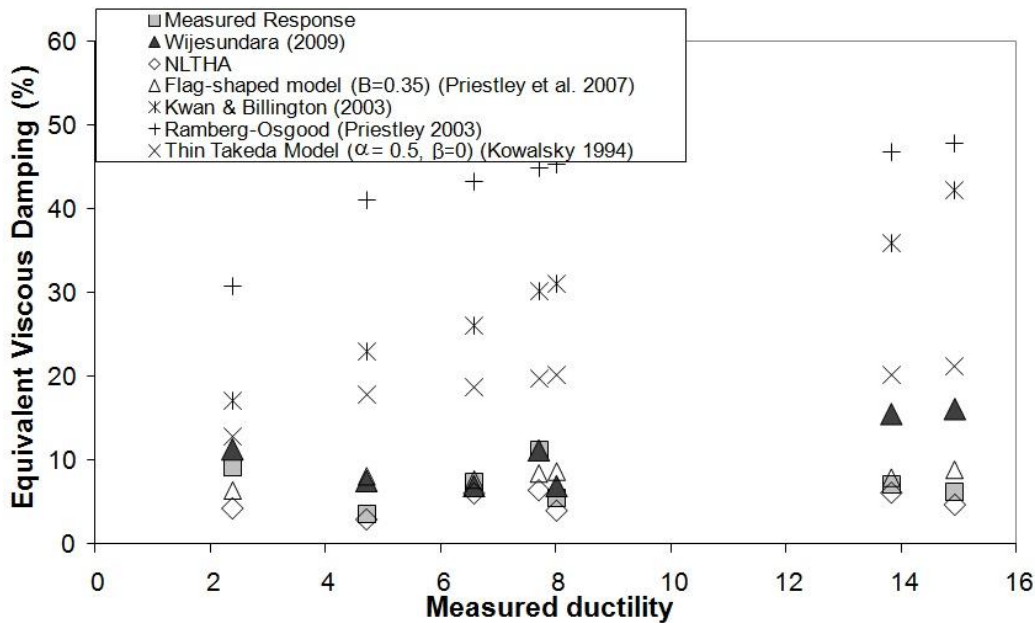


Figure 5.16: Comparison of equivalent viscous damping values.

Figure 5.16 shows that the NLTHA numerical model gives a reasonable prediction of the equivalent viscous damping when compared to the values obtained from the shake table

tests. However, in general the values from the NLTHA are lower than those estimated from the shake table tests. The equations which best represent the equivalent viscous damping values observed in the shake table tests values are those developed by Wijesundara (2009). It is, therefore, recommended that these values are used in the direct displacement based design (DDBD) methodology for single storey CBFs.

The expressions of Wijesundara (2009) were initially developed based on cyclic displacement pushover simulations of fifteen SDOF CBF systems with different brace configurations – five frames with X-bracing having braces connected at mid-length and ten frames containing diagonal bracing. The simulations were carried out using OpenSees (McKenna et al. 2000). The area based approach proposed by Jacobsen (1960) was used to estimate the EVD value from the hysteretic loops. The normalised slenderness ratio of brace members ranged from 0.44 to 1.6. All brace members had compact class 1 cross sections. The model was correlated to the results of twelve single storey braced frames (seven containing X-bracing having braces connected at mid-length and five containing diagonal bracing), which were obtained from an experimental programme conducted by Archambault (Archambault 1995) on brace members subjected to displacement histories to replicate the behaviour of single storey CBFs. The brace member slenderness ratios ranged from 0.8 to 1.57.

Gulkan and Sozen (1974) extended Jacobsen’s approach based of a limited experimental results and introduced substitute viscous damping $\xi_{\text{substitute}}$. They obtained $\xi_{\text{substitute}}$ as the following:

$$\xi_{\text{substitute}} = \frac{T_{\text{substitute}} \int_0^T \ddot{u}_g \cdot \dot{u} dt}{4\pi \int_0^T \dot{u}^2 dt} \quad [5.12]$$

where u is the structure displacement, T is total time of the accelerogram, \ddot{u}_g is the ground acceleration, \dot{u} is the ground velocity and $T_{\text{substitute}}$ is the effective period corresponding to the secant stiffness to maximum response. (Judi et al. 2000) found significant differences between Jacobsen (1960) equivalent viscous damping factor and Gulkan and Sozen (1974) substitute damping factor.

Chopra and Goel (2001) found that the area-based formulations for equivalent viscous damping proposed by Jacobsen (1960) are not able to successfully predict the response of certain hysteretic types as it assumes complete loops of the hysteretic models under sinusoidal excitation. Blandon and Priestley (2005) recommended to correct the viscous damping factor developed using this approach, for different types of earthquakes, ductility levels and structural systems.

Because of that, Wijesundara (2009) validated the EVD values obtained from the area based approach for each target relative lateral frame displacement by carrying out NLHTA using seven real earthquakes scaled to an appropriate displacement spectrum for each frame. If the target relative lateral frame displacement used in the DDBD method differed by more than 5% from the average maximum relative lateral displacement of the frame obtained from the NLTHA, then the EVD value was corrected and subsequent set of NLTHA simulations were performed to real earthquakes scaled to the appropriate displacement spectrum taking account of the new corrected EVD value. An appropriate EVD value for each frame at prescribed target lateral relative frame displacements were deemed to be achieved when the lateral relative frame displacements used in the DDBD method differed by no more than 5% from the average maximum lateral relative displacement of the frame obtained from the NLTHA.

Wijesundara (2009) recommended that if the brace normalised slenderness ratio was either below 0.4 or above 1.6, then these limits should be used in place of the actual normalised slenderness ratio in Equations [5.6] and [5.7]. In the current study, for which brace normalised slenderness ratios ranged from 1.5 to 2.9, no such limits were imposed.

5.5 Sensitivity of frame response to different earthquake excitation

To check the sensitivity of the shake table test frames to different earthquake input excitation, a NLTHA is carried out for ST2-50H, ST5-20H, ST5-20HB and ST8-40H using eight different earthquakes, which are scaled to have displacement response spectrums compatible with the displacement spectrums used in the physical shake table tests as described in Chapter 4 (see Figure 5.17 for example). The earthquakes used are listed in Table 5.3, which gives the name of the earthquake, the ID's used for the two

components in orthogonal direction for each earthquake, the date of the earthquake, the PEER ID (PEER 2011), the magnitude, M , the epicentre distance, r , and the peak ground acceleration, PGA, when scaled to every shake table test spectrum. Table 5.4 to Table 5.7 present the results from the numerical models of frames ST2-E50H, ST5-E20H, ST5-E20H-B and ST8-E40H, each of which were subjected to eight compatible earthquake accelerogram records that have been filtered. Comparisons between the mean values obtained from the numerical model and those measured in the physical tests are also given for each test frame in the aforementioned tables.

Figure 5.18 and Figure 5.19 show the relative frame displacement time history and brace axial force time history results, respectively, for frame ST2-E50H subjected to EQ3b accelerogram whose displacement spectrum was scaled to match that of the actual excitation record used in the physical test of frame ST2-E50H. Similar plots are shown for frame ST8-E40H in Figure 5.20 and Figure 5.21, respectively.

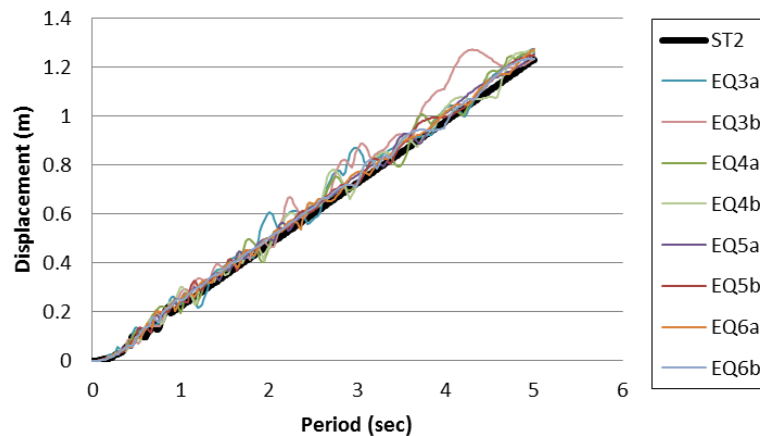


Figure 5.17: Displacement response spectrum for eight different earthquakes scaled to be compatible with the displacement spectrum for the table excitation employed in test ST2-E50H.

As expected, it is found that the average of the maximum displacements obtained from the time history analysis are close to the values obtained from the shake table tests (See Table 5.4 to Table 5.7). Furthermore, the maximum base shear values recorded for each of the test frames was similar for all input earthquake excitations and the average values of the maximum base shear of the frames subjected to the eight accelerograms are close to the base shear values obtained from the physical tests (See Table 5.4 to Table 5.7).

Table 5.3: Properties of ground motions used.

Earthquake	ID	Date	PEER ID	M	r (km)	PGA (g) (ST2)	PGA (g) (ST5)	PGA (g) (ST5-B)	PGA (g) (ST8)
Northridge	EQ3a	Jan. 17, 1994	959	6.7	5	0.75	0.32	0.49	1.23
	EQ3b					0.59	0.25	0.38	0.96
Imperial Valley	EQ4a	Oct. 15, 1979	169	6.5	34	0.67	0.28	0.43	1.09
	EQ4b					0.74	0.32	0.48	1.22
Hector	EQ5a	Oct. 16, 1999	1762	7.13	48	0.67	0.29	0.44	1.1
	EQ5b					0.59	0.25	0.38	0.96
Landers	EQ6a	Jun. 28, 1992	900	7.28	86	0.62	0.26	0.4	1.01
	EQ6b					0.61	0.26	0.39	0.99

When subjecting the eight compatible earthquake records to the test frames, NLTHA predicted a full fracture of the brace member causing collapse of test frames ST2-E50H and ST5-E20H-B when subjected to two of the eight compatible earthquake records. On the other hand, NLTHA predicted full fracture of a brace member in tests ST5-E20H and ST8-E40H with one earthquake, whereas, partial fracture of brace members was observed several times for the rest of the earthquakes. However, full fracture of the brace member occurred in test frame ST8-E40H in the physical test, causing collapse of the test frame. Whereas, full frame collapse did not occur in test frames ST2-E50H, ST5-E20H or ST5-E20H-B during the physical tests. This highlights the sensitivity of the response of the frame to the earthquake inputs, even when they have similar displacement response spectra. The numerical models give reasonable predictions of the energy dissipated, W_{tot} , during the physical shake table tests, as seen in Table 5.4 to Table 5.7. Furthermore, the numerical model could predict relatively well the equivalent viscous damping, ξ_{eq} , obtained from the shake table tests ST2-E50H, ST5-E20H-B and ST8-E40H, but significantly underestimates the equivalent viscous damping obtained from ST5-E20H physical test as shown in Table 5.4 to Table 5.7.

Table 5.4: Numerical model results using eight different accelerograms compatible to displacement spectrum for ST2-E50H test and comparison with the results from physical test.

Earthquake ID	PGA (g)	Δ_{\max} (mm)	F_b (kN)	W_{tot} (Nm)	ξ_{eq} (%)
EQ3a	0.75	91.4	104.6	40164	7.13
EQ3b	0.59	65.3	108.2	31904	7.51
EQ4a*	0.67	96.9	101.3	9105	8.03
EQ4b	0.74	75.3	96.6	80380	5.84
EQ5a	0.69	45.7	102.9	30258	7.25
EQ5b	0.59	36.6	113.3	27005	7.07
EQ6a	0.62	34.7	105.3	18271	6.83
EQ6b*	0.61	60.0	87.5	2109	5.87
Mean	0.66	63.2	102.5	29899	6.94
C_v	0.10	0.37	0.08	0.80	0.11
Physical test	0.81	61.5	96.0	41496	7.72
Physical test/ Mean	1.22	0.97	0.94	1.39	1.11

* Full fracture of a brace member causing collapse of the frame

Table 5.5: Numerical model results using eight different accelerograms compatible to displacement spectrum for ST5-E20H test and comparison with the results from physical test.

Earthquake ID	PGA (g)	Δ_{\max} (mm)	F_b (kN)	W_{tot} (Nm)	ξ_{eq} (%)
EQ3a	0.32	35.9	60.0	6531	5.85
EQ3b	0.25	22.4	59.8	2958	3.98
EQ4a	0.28	43.5	58.2	14897	4.00
EQ4b	0.32	28.3	62.8	9447	3.61
EQ5a	0.29	16.9	59.6	2119	3.07
EQ5b*	0.25	51.9	62.1	2923	5.94
EQ6a	0.26	32.1	56.6	3644	4.32
EQ6b	0.26	112.7	61.9	6987	5.03
Mean	0.28	43.0	60.1	6188	4.48
C_v	0.10	0.71	0.04	0.70	0.23
Physical test	0.52	41.70	53.20	6759	7.34
Physical test/ Mean	1.87	0.97	0.88	1.09	1.64

* Full fracture of a brace member causing collapse of the frame

Table 5.6: Numerical model results using eight different accelerograms compatible to displacement spectrum for ST5-E20H-B test and comparison with the results from physical test.

Earthquake ID	PGA (g)	Δ_{\max} (mm)	F_b (kN)	W_{tot} (Nm)	ξ_{seq} (%)
EQ3a	0.49	138.0	64.3	15175	3.68
EQ3b	0.38	76.7	62.8	15904	4.71
EQ4a	0.43	85.4	66.4	38224	3.02
EQ4b	0.48	83.4	65.8	40861	3.39
EQ5a	0.44	65.7	68.6	22279	4.27
EQ5b*	0.38	99.2	52.3	3508	6.30
EQ6a*	0.40	89.7	46.3	1834	3.20
EQ6b	0.39	45.5	72.6	7901	3.39
Mean	0.42	85.5	62.4	18211	3.99
C_v	0.10	0.31	0.14	0.81	0.27
Physical test	0.51	83.5	54.07	15962	4.06
Physical test/ Mean	1.20	0.98	0.87	0.88	1.02

* Full fracture of a brace member causing collapse of the frame

Table 5.7: Numerical model results using eight different accelerograms compatible to displacement spectrum for ST8-E40H test and comparison with the results from physical test.

Earthquake ID	PGA (g)	Δ_{\max} (mm)	F_b (kN)	W_{tot} (Nm)	ξ_{seq} (%)
EQ3a	1.23	222	125.2	113974	4.66
EQ3b	0.96	125	131.9	76827	6.06
EQ4a*	1.09	190	132.8	129589	5.34
EQ4b	1.22	161	138.0	134901	5.37
EQ5a	1.1	177	128.4	115585	5.55
EQ5b	0.96	53.3	124.1	65564	7.06
EQ6a	1.01	111.1	125.7	78734	6.29
EQ6b	0.99	89.1	131.0	58002	6.82
Mean	1.07	141.1	129.6	96647	5.89
C_v	0.10	0.40	0.04	0.31	0.14
Physical test	2	131.0	122.0	73384	6.37
Physical test/ Mean	1.87	0.93	0.94	0.76	1.08

* Full fracture of a brace member causing collapse of the frame

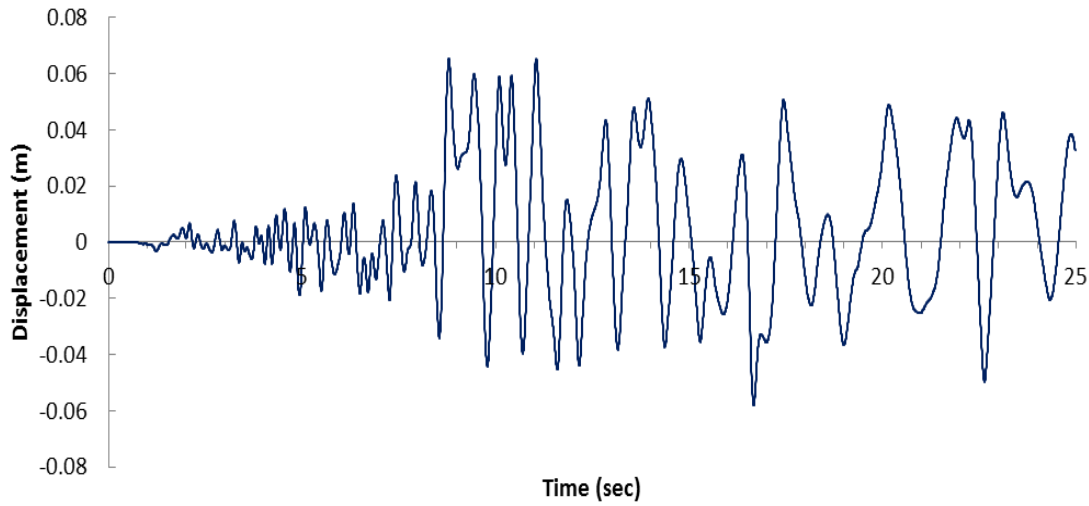


Figure 5.18: Lateral frame displacement-time history response of ST2-E50H frame using EQ3b earthquake.

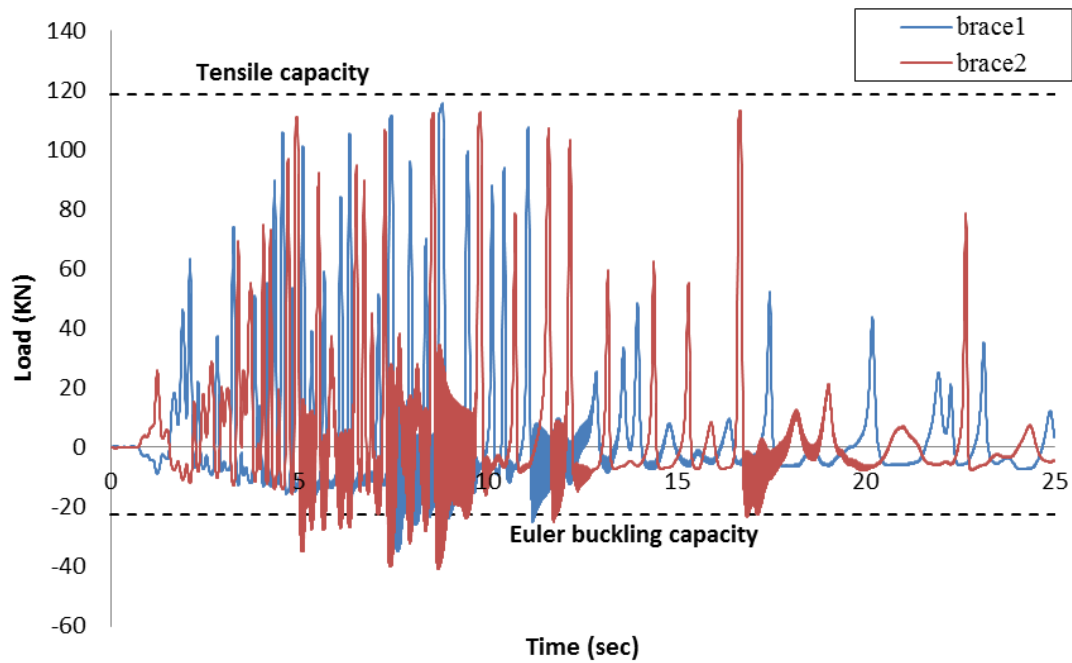


Figure 5.19: Axial load-time history response of braces for frame ST2-E50H using EQ3b.

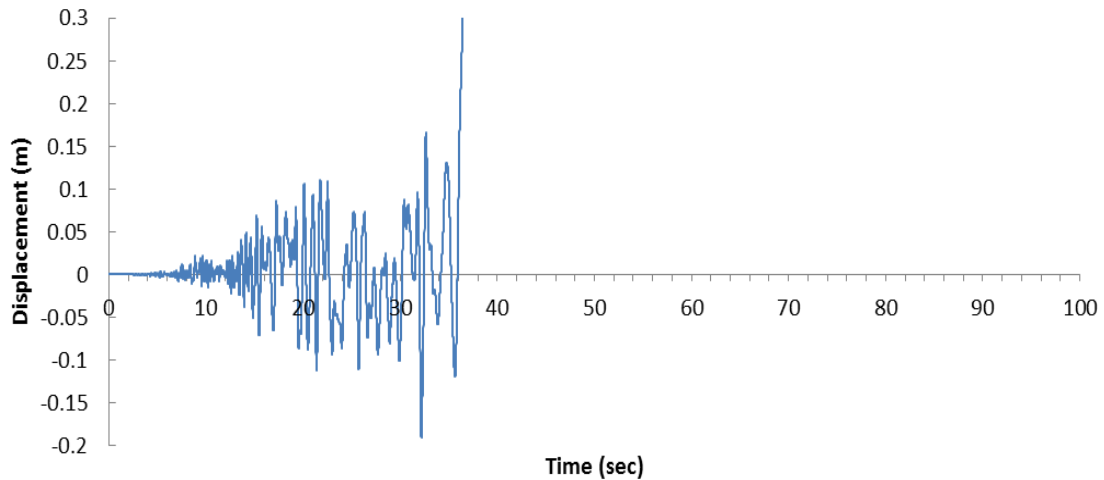


Figure 5.20: Displacement-time history response of ST8-E40H frame using EQ4a earthquake.

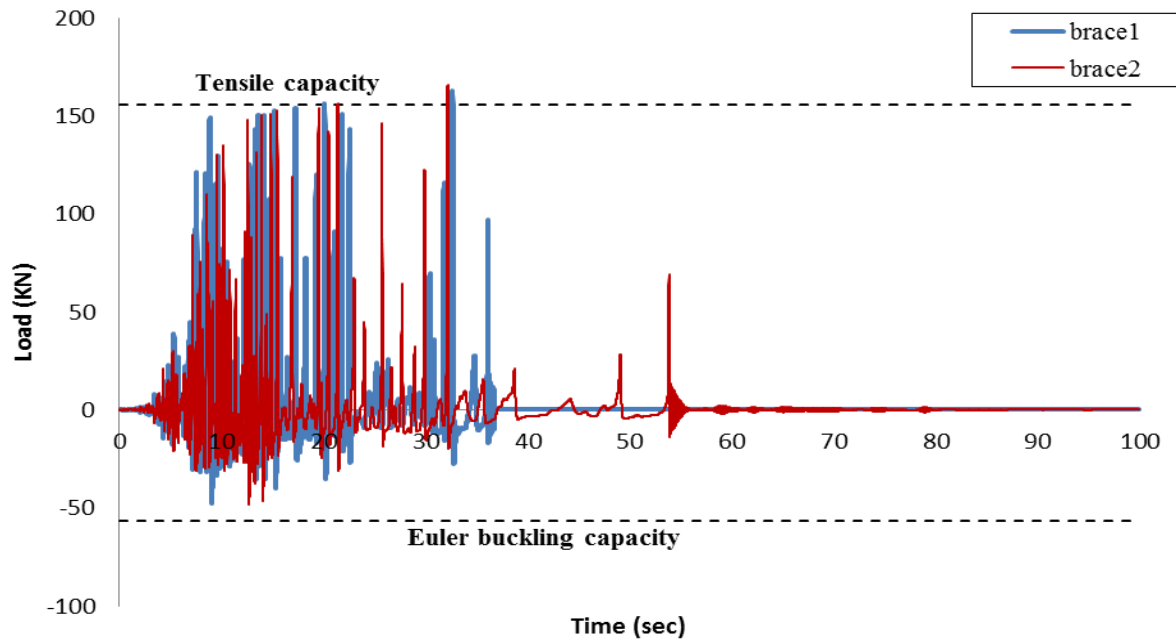


Figure 5.21: Axial load-time history response of braces for frame ST8-E40H using EQ4a earthquake.

5.6 Summary and conclusion

The response of concentrically-braced frames to significant earthquake loading depends strongly on the asymmetric axial resistance of the bracing members. The prediction of this response requires accurate modelling of the cyclic inelastic response of the members, including buckling capacity, post-buckling resistance, tensile yielding and strain-hardening. The experimental response of single-storey braced frames measured in shake

table tests was compared with the results of nonlinear time history analysis. The test frames considered a range of brace slenderness. Furthermore, in the NLTHA four of the test frames were subjected to eight earthquake records that had been scaled to the record used in the shake table tests.

The comparison of experimental and numerical results shows that the use of inelastic fibre elements with a bilinear material relationship to represent the behaviour of bracing members leads to accurate modelling of the response of brace elements to earthquake excitations. The model captured the displacement response, the axial forces, energy dissipated and the equivalent viscous damping relatively well.

The prediction of structural collapse using earthquake analysis relies upon an accurate assessment of structural displacements, leading to a quantification of the ductility demand experienced by dissipative elements such as bracing members. This study has highlighted the sensitivity of the response of braced frame to the earthquake input motion, even when the accelerograms are scaled to have compatible displacement response spectrums.

It is important that numerical models used to develop seismic design methodologies are validated through full scale experimental testing. The results of this study suggest that the equivalent viscous damping values developed by Wijesundara (2009) can be used in the direct displacement based design of single storey CBFs.

There is a strong role to be played by nonlinear analysis in providing parametric studies for examining the likely response of different structural configurations to a variety of ground motions. The comparative assessments presented in this chapter indicate that numerical tools which incorporate material and geometric nonlinearities can largely capture the salient features related to the seismic behaviour of concentrically-braced frames. Particular attention should however be placed on interpreting the inter-storey drift results in time-history analysis by careful consideration of material idealisation and characteristics of the selected seismic excitations.

Chapter 6

Direct displacement based seismic design for single storey CBFs

6.1 Introduction

A draft model code for seismic design using a new performance based design methodology known as direct displacement based design (DDBD) has been published by Calvi and Sullivan (2009). This new displacement based design approach was developed as a result of the shortcoming of the force based design approach identified by Priestley (1993; 2003), which led to Priestley et al. (2007) publishing a book on displacement based seismic design of structures. The provisions in this DDBD code have been well developed for reinforced concrete structures. However, the recommendation for steel concentrically braced frame (CBF) structures are limited in the draft model code (Calvi and Sullivan 2009) and had not been well verified. Thus, the aim of this chapter is to develop a robust approach for the DDBD procedure for single degree of freedom (SDOF) concentrically braced frames (CBFs).

Eurocode 8 (CEN 2004) prescribes the force based design methodology for the seismic design of structures. In this approach, preliminary estimates of geometry and section sizes are carried out. Seismic forces are achieved from an elastic response spectrum. To dissipate energy, these forces are reduced by a reduction factor dependent upon the type of the building. These seismic forces are then used to analyse the structure and find the

structural displacements limit which are checked against the code displacement limits. If the presented limits are exceeded, redesign is required.

On the other hand, the direct displacement based design (DDBD) procedure (Priestley et al. 2007) starts by considering a design displacement depending upon the drift limit chosen, then the strength required to achieve this displacement is calculated.

In this chapter, the DDBD procedure will be developed for one-storey CBFs and compared with a series of full scale shake table tests and large range of non-linear time history analysis (NLTHA) to assure its validity. Full details of the shake table tests, including observations and findings from these tests are presented in Chapter 5 and in more details elsewhere (Goggins 2004; Elghazouli et al. 2005; Broderick et al. 2008). Special attention is paid to the choice of the equivalent viscous damping model for use in the DDBD of CBFs.

6.2 Direct displacement based design (DDBD)

Some researchers (Goggins and Sullivan 2009; Wijesundara 2009; Della Corte et al. 2010) developed a new methodology for the DDBD of CBFs based on limited data from tests and numerical models. In this chapter, a robust DDBD procedure is validated using both shake table tests and a robust NLTHA which was calibrated using shake table tests, as explained in Chapter 5. Complete design and assessment approaches for DDBD of single degree of freedom (SDOF) structures are outlined in the following subsections. The latter sections will check the validity of the method using shake table tests and NLTHA.

6.2.1 Design displacement

For a SDOF structure, the lateral design displacement of the frame can be taken as the maximum lateral frame displacement that occurs based on the design drift limit chosen, where the maximum lateral frame displacement can be found by:

$$\Delta_D = \theta_C * h \quad [6.1]$$

where θ_C is the design drift limit and h is the height of the storey.

6.2.2 Yield displacement

The yield displacement of the CBF, Δ_y , is required to find the displacement ductility of the frame, μ , in order to calculate the equivalent viscous damping, ξ_{eq} . The yield displacement of CBFs is governed by the conditions to cause yielding of the bracing elements. Goggins et al (2006b) showed that the resistance of the tension brace only, for a CBF with X-braced members, represents a good estimation of the overall resistance and stiffness of the braced frame. This is in agreement with the provisions of EC8 (CEN 2004). Therefore, assuming the tension diagonals only participates in the lateral resistance of the structure and that strains in the beams and columns are negligible with respect to strains in the brace for a single storey structure, then from geometry shown in Figure 6.1 the yield displacement can be found as the following using Pythagoras' theorem:

$$(L_b + \varepsilon_y L_b)^2 = h^2 + (B + \Delta_y)^2 \quad [6.2]$$

$$L_b^2 + 2\varepsilon_y L_b^2 + (\varepsilon_y L_b)^2 = h^2 + B^2 + 2B\Delta_y + \Delta_y^2 \quad [6.3]$$

where L_b is the brace length, B is the bay width, h is the storey height, ε_y is the yield strain of the brace and Δ_y is the yield displacement of the frame. Neglecting $(\varepsilon_y L_b)^2$ and $(\Delta_y)^2$ because they are very small compared to other terms, and knowing that $L_b^2 = h^2 + B^2$, the equation can be rearranged as

$$\Delta_y = \frac{\varepsilon_y L_b^2}{B} \quad [6.4]$$

However, $\cos\alpha = B/L_b$, $\sin\alpha = h/L_b$ and $(\sin 2\alpha = 2 \cos\alpha \sin\alpha)$, where α is the brace angle with the horizontal. Thus, Equation [6.4] can be written as

$$\Delta_y = \frac{2\varepsilon_y h}{\sin 2\alpha} \quad [6.5]$$

From Equation [6.5] it is noticed that the yield drift is dependent upon the material strength and the geometry, but is independent of the cross section or strength of the members.

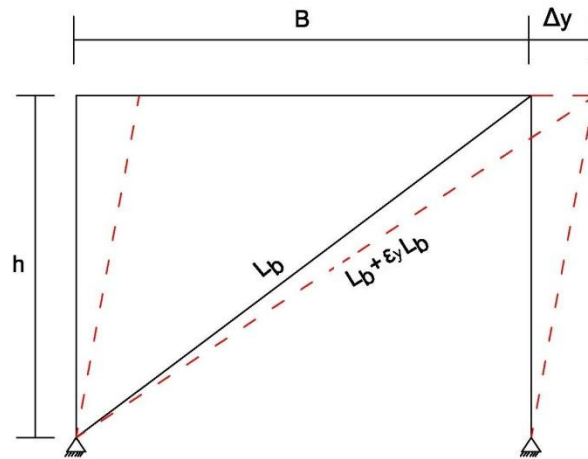


Figure 6.1: Yield deformation of the CBF due to brace elongation.

6.2.3 Design displacement ductility

The design displacement ductility factor of the frame, μ , is found by dividing the design displacement, Δ_D , over the yield displacement, Δ_y , as shown in Equation [6.6]:

$$\mu = \frac{\Delta_D}{\Delta_y} \quad [6.6]$$

6.2.4 Equivalent viscous damping

The equivalent viscous damping (EVD), ξ_{eq} , is the sum of the elastic and the hysteretic damping. The elastic damping ratio is commonly taken as 0.03 for steel structures and the hysteresis damping depends on the hysteresis rule appropriate for the structure being designed. Hysteretic damping accounts for the effect of energy dissipated through nonlinear inelastic response.

The energy dissipated and, therefore, the equivalent viscous damping values for CBF systems with slender braces is relatively low compared to other structures because inelastic axial deformations in the braces are not recovered and the hysteretic behaviour is significantly pinched (Goggins and Sullivan 2009). Goggins and Sullivan (2009) trialled several EVD models referred to in the literature (for example, models presented in (Kowalsky 1994; Kwan and Billington 2003; Priestley et al. 2007), and compared with equivalent viscous damping values computed from measured hysteretic loops obtained

from shake table tests using Jacobsen's approach (Jacobsen 1960). They noted that, at the time, there was no equivalent viscous damping model developed specifically for use in the DDBD of CBFs. Equivalent viscous damping expression given by Priestley et al. (2007) for the flag-shaped hysteretic rule with $\beta = 0.35$ was selected by Goggins and Sullivan (2009) for use within the DDBD approach, as this gave the closest estimates to the EVD values obtained from shake table tests. However, Goggins and Sullivan (2009) emphasised that this model was not developed for steel CBF structures and a new relationship should be developed as part of future work. A study carried out by Wijesundara (2009) proposed EVD equations for CBFs based on bilinear approximation, as discussed in Section 5.4.2 and given by Equations [5.6] and [5.7].

As noted in Section 5.4.2, Wijesundara (2009) recommended that if the brace normalised slenderness ratio was either below 0.4 or above 1.6, then these limits should be used in replace of the actual normalised slenderness ratio in Equations [5.6] and [5.7]. In the current study, for which brace normalised slenderness ratios ranged from 1.5 to 2.9, no such limits were imposed.

Figure 6.2 compares various EVD models with equivalent viscous damping values computed from measured hysteretic loops obtained from shake table tests conducted by Elghazouli et al. (2005) using Jacobsen's approach (Jacobsen 1960). In particular, EVD values for a given measured ductility are obtained using the EVD expression given by Priestley et al. (2007) for the flag-shaped hysteretic rule with $\beta = 0.35$ (Equation [5.9]), EVD equations for CBFs proposed by Wijesundara (2009) and given in Equations [5.6] and [5.7] without any limits of normalised slenderness ratio, and EVD values estimated from NLTHA simulations of the frames tested in the shake table tests. It is evident from Figure 6.2 that both the values obtained from the NLTHA and Equations [5.6] and [5.7] (Wijesundara 2009) give reasonable predictions of the measured equivalent viscous damping values. It is recommended to use the expressions in Equations [5.6] and [5.7] proposed by Wijesundara (2009), but without imposing upper limits on the normalised slenderness ratio, as these have been independently developed specifically for CBFs and

match relatively well with values computed from shake table tests carried out by Elghazouli et al. (2005).

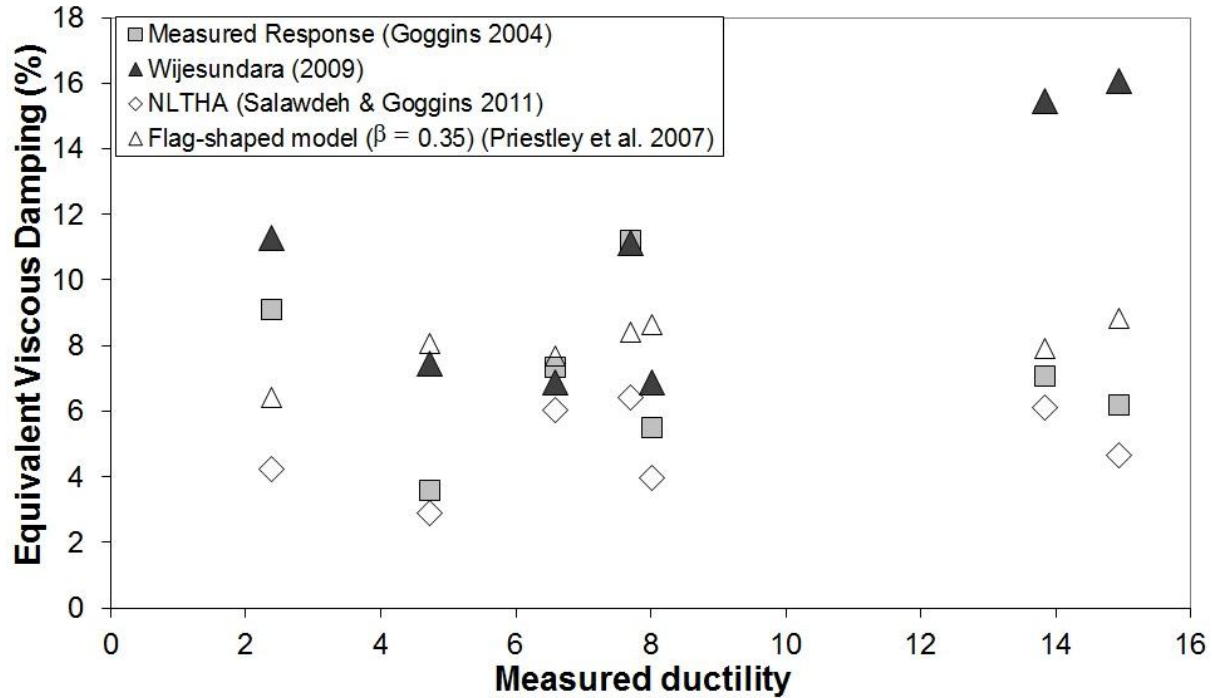


Figure 6.2: Comparison of equivalent viscous damping values.

6.2.5 Effective period of the structure

To find the effective period, the design displacement spectrum should be developed at the design level of damping. This can be achieved by applying a damping modifier, R_{ξ} , to the elastic displacement spectrum. In this work, the damping modifier expression used in 1998 edition of EC8 [18] has been adopted, as the DDBD methodology was carried out using this expression:

$$R_{\xi} = \left(\frac{0.07}{(0.02 + \xi)} \right)^{0.5} \quad [6.7]$$

The relative lateral frame design displacement, Δ_D , given for example in Figure 6.3 for test frame ST2-50H which will be explained in Section 6.3, is then used to read off (or interpolate between known points) the required effective period, T_e , from the displacement spectrum developed at the design level of damping.

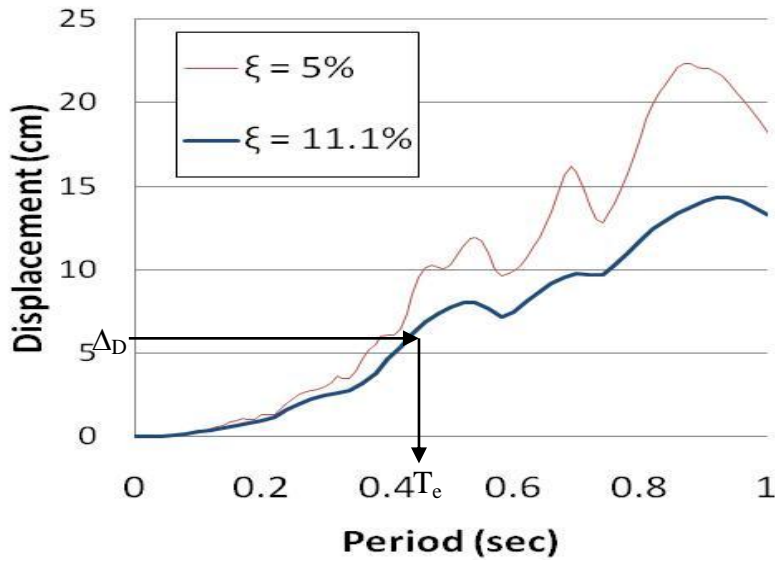


Figure 6.3: Displacement spectrum for design of frame ST2-50H.

6.2.6 Effective stiffness of substitute structure

With the effective period, T_e , established, the effective stiffness, K_e , is determined as:

$$K_e = \frac{4\pi^2 m_e}{T_e^2} \quad [6.8]$$

where m_e is the mass and T_e is the effective period.

6.2.7 Design base shear force

In the DDBD approach, the design base shear required to limit the response to the target relative lateral frame displacement is obtained by multiplying the required effective stiffness, K_e , (Equation [6.8]) by the design displacement, Δ_D , as shown:

$$F_b = K_e \Delta_D \quad [6.9]$$

In the DDBD approach, it is recommended that the design base shear be increased to account for the reduction in effective lateral stiffness due to P- Δ effects (Priestley et al. 2007). The increase in the lateral force required to account for P- Δ effects in steel structures can be estimated as:

$$F_{P-\Delta} = \frac{mg}{H_e} \Delta_D \quad [6.10]$$

where g is acceleration due to gravity and H_e is the effective height of the SDOF system.

Thus, the new base shear can be found by

$$F_b = \left(K_e + \frac{m_e g}{H_e} \right) \Delta_D \quad [6.11]$$

6.2.8 Brace cross-section size

EC8 (CEN 2004) suggested for frames with concentric bracings that tension diagonal bracings should be designed to resist the shear and no contribution in resistance is assumed by compression braces. In contrast, during the real-time shake table tests (Elghazouli et al. 2005), a percentage of the shear was found to be resisted by the compression member. Goggins and Sullivan (2009) studied the shake table tests and estimated that the cross-section of the brace members, A_b , can be found by:

$$A_b = \frac{F_b}{C f_y \cos \alpha} \quad [6.12]$$

where f_y is the actual yield stress obtained from monotonic tensile tests on the sections, α is the slope of the brace members to the horizontal, and C is an overstrength ratio which accounts for the expected maximum brace resistance being higher than the yield stress due to strain hardening and strain rate. Goggins and Sullivan (2009) suggested to take C as 1.24 and mentioned that this factor can be modified to take into account the contribution of the compression brace to the lateral resistance of the structure. The factor C from the different sources of overstrengths and the contribution of the compression members was found from the tests to range from 1.18 to 1.47 with an average value of 1.28.

For the frames tested in this chapter and by assigning a percentage of the shear to be resisted by the compression member, full fracture of brace members occurred and caused collapse of the frame in physical tests ST7-E40H and ST8-E40H (See Section 5.2) and in many frames during NLTHA while checking the sensitivity of the shake table tests to different earthquakes as discussed in Section 5.5. For comparison reasons in this chapter,

the factor C for the design methodology will be taken similar to the value found in the physical tests even though collapse of the test frame occurred during shake table tests. However, in Chapter 7, which discusses the DDBD methodology for multi-storey structures, the factor C will be taken as unity, which means designing the tension diagonal bracings to resist the shear assuming no contribution in resistance by compression braces, as suggested by EC8 (CEN 2004) in order to be conservative, but more so to prevent any failure of the structure, which is the primary design objective of EC8 (CEN 2004).

6.3 Comparison of DDBD with shake table tests

Shake table tests described in Section 5.2 and carried out by Elghazouli et al. (2005) at the laboratory for earthquake engineering of the National Technical University of Athens (NTUA) are used to validate the DDBD for a single storey CBF system. These real-time full scale tests represent an idealisation of a single storey within a typical form of concentrically braced frame, in which the load-sharing between the tension and compression braces is accounted for.

The DDBD methodology is performed for the shake table tests by taking the target displacement, Δ_d , as the maximum lateral relative frame displacement obtained during the tests. For every test, a design displacement spectrum is developed for the design level of damping, as shown for example in Figure 6.3 for ST2-E50H test. From this spectrum, the effective period corresponding to the design displacement can be obtained. Then, the effective stiffness and the base shear can be calculated. The results and a comparison between the base shear, F_b , and brace cross-sectional areas A_b obtained from the DDBD and the physical experiments are given in Table 6.1, where F_b and A_b were obtained using Equations [6.11] and [6.12]. As can be seen from Table 6.1, the trial DDBD methodology proposed here gives very good estimates of the required base shear strength, F_b , and, hence, the required cross-sectional area, A_b . In fact, the mean and coefficient of variation (C_V) for the ratio of base shear (F_b) and the required brace cross sectional areas (A_b) estimated from the DDBD to the measured values in shake table tests are 1.09 and 0.12, respectively.

Table 6.1: Results from DDBD and comparison to physical experimental results

Test ID	f_y (N/mm ²)	Δ_y (mm)	$\bar{\lambda}$	Δ_d (mm)	μ	ξ_{seq} (%)	Estimated		Measured		Estimated/ Measured	
							F_b (kN)	A_b (mm ²)	F_b (kN)	A_b (mm ²)	F_b	A_b
ST2-50H	333	7.56	2.23	61.5	8.14	11.1	123	430	96	334	1.29	1.29
ST3-50F	333	7.55	2.33	47.6	6.30	10.5	109	389	94	334	1.16	1.16
ST5-20H	377	8.56	2.87	59.9	7.00	6.9	52	133	53	135	0.99	0.99
ST5-20HB	435	9.87	2.87	83.5	8.46	6.9	59	151	54	138	1.09	1.09
ST6-20F	292	6.62	2.92	90.5	13.7	6.5	50	169	40	136	1.24	1.24
ST7-40H	358	8.14	1.49	128	15.8	16.1	109	338	113	351	0.96	0.96
ST8-40H	396	8.99	1.58	131	14.6	15.5	115	335	122	357	0.94	0.94
ST9-40F	507	11.5	1.83	33.9	2.94	13.8	156	369	151	357	1.04	1.04
Mean											1.09	1.09
C_v											0.12	0.12

6.4 Verification of DDBD methodology using NLTHA

Another method to verify the DDBD methodology is the NLTHA. It is chosen here because it is the most accurate numerical method to represent the inelastic performance of structures. The software used is the computational framework Open System for Earthquake Engineering Simulation (OpenSees) (McKenna et al. 2000). To assure that the numerical model is representing the real behaviour of CBFs, it was validated using physical tests as described in Chapter 3 and 5. First, a study of the behaviour of brace members using pseudo-static cyclic tests was carried out to get a robust nonlinear beam column element model for steel structural rectangular hollow sections representing the cyclic behaviour of the brace elements (see Chapter 3). This model is based on fibre elements incorporating a fatigue model that detect fracture due to low cyclic fatigue.

This model was advanced to get a robust numerical model for concentrically braced frames representing the shake table tests, as outlined in Chapter 5. Two-dimensional

numerical models are carried out, in which columns and beams are modelled to behave elastically with a pinned end conditions. The hollow brace specimens are modelled as nonlinear beam column elements with fixed connections with the beam at their top ends, and to the ground at their lower ends. This model is found to represent very well the behaviour of the shake table tests as shown in Chapter 5. Figure 6.4 and Figure 6.5 show an example of the comparison between displacement and axial force time history response of the physical test ST2-E50H and the numerical model results. These results assure that the NLTHA model can be used for different CBFs with different earthquakes with confidence.

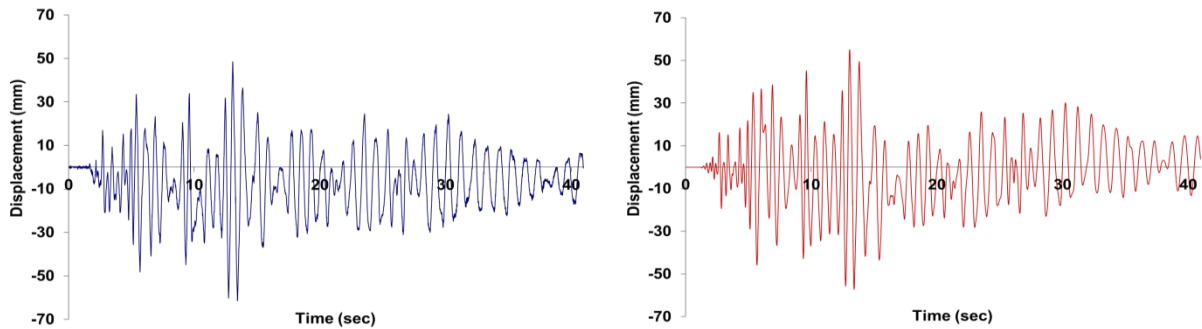


Figure 6.4: Measured displacement time-history response of test ST2-E50H in (a) physical test and (b) numerical model.

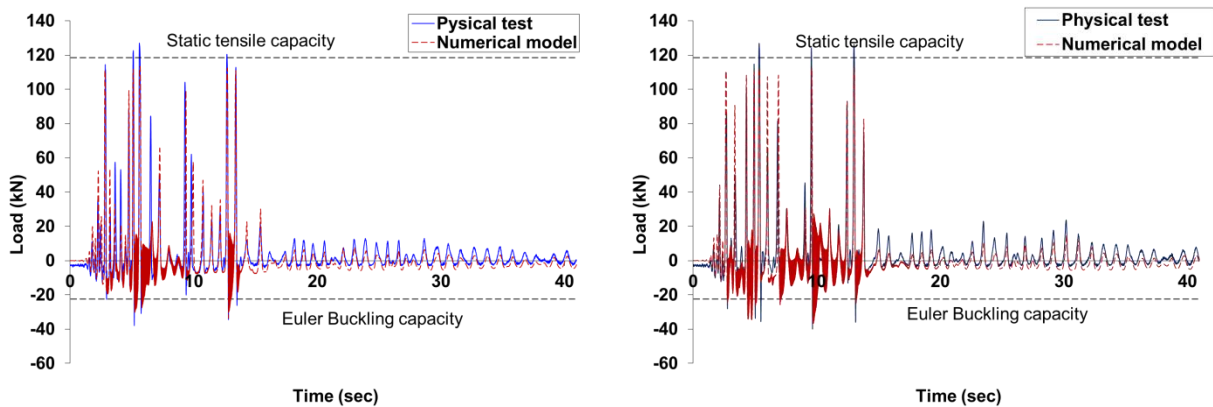


Figure 6.5: Comparison for the axial load time-history between the physical test ST2-E50H and the numerical model for (a) first brace and (b) second brace.

For this study, frames ST2-50H, ST5-20H, ST5-20HB and ST8-40H designed using DDBD procedure above are subjected to different earthquakes scaled to have

displacement response spectrums compatible with the displacement spectrums used for the shake table tests, as described in Chapter 4 (see for example the displacement spectrums used for ST2-50H shown in Figure 4.9). Eight accelerograms from four different earthquakes (2 components in orthogonal direction for each earthquake) are used, which are the Northridge earthquake, January 17, 1994, with two components (EQ3a and EQ3b), the Imperial Valley earthquake October 15, 1979, with two components (EQ4a and EQ4b), Hector earthquake, October 16, 1999, with two components (EQ5a and EQ5b) and Landers earthquake, June 28, 1992, with two components (EQ6a and EQ6b).

After carrying out the NLTHA for the frames, it is found that the average of the maximum displacements obtained from the time history analyses are very close to the values obtained from DDBD, as seen in Table 6.2. Furthermore, the maximum base shear values recorded for each of the test frames was similar for all input earthquake excitations (see Table 5.4 to Table 5.7) and the average values of the maximum base shear of the frames, F_b , subjected to the eight accelerograms are close to the base shear values obtained from DDBD (see Table 6.2). Table 6.2 shows that, the mean and coefficient of variation (C_v) for the ratio of base shear (F_b) estimated from the DDBD to the values obtained from NLTHA are 1.04 and 0.14, respectively. Furthermore, Table 6.2 shows that, the average of the maximum relative lateral displacement, Δ_{max} , for each test frame subjected to eight accelerograms in NLTHA are close to the values employed in the DDBD methodology. The mean and coefficient of variation (C_v) for the ratio of the maximum displacement (Δ_{max}) estimated from the DDBD to values obtained from NLTHA are 1.06 and 0.03, respectively.

Residual drifts were not accounted for in the design procedure used here. Significant residual drifts can occur in CBFs, as observed in full scale physical shake table tests (Goggins 2004). In fact, it is evident that Frame ST8-40H did not recover to its original vertical position after the large amplitude cycles and oscillated about an inclined position after the first strong motion period (see Figure 6.6). This is due to the permanent elongation of the brace members. As residual deformations could be an important

performance parameter, it is clear that residual drifts should be accounted for in the seismic design methodology. However, this is outside the scope of the current project, but forms part of another research project in the earthquake Engineering Research Group (EERG) at NUIG.

Table 6.2: Comparison of displacements and base shear obtained from NLTHA and DDBD.

Test ID	Average value from NLTHA for 8 different earthquakes		DDBD		NLTHA/DDBD	
	Δ_{max} (mm)	F_b (KN)	Δ_{max} (mm)	F_b (KN)	Δ_{max}	F_b
ST2-50H	66.8	102.5	61.5	123	1.09	0.83
ST5-20H	43.5	60.1	41.7	52	1.04	1.16
ST5-20H-B	85.5	62.4	83.5	59	1.02	1.06
ST8-40H	140.9	129.6	131.0	116	1.08	1.12
Mean					1.06	1.04
C_v					0.03	0.14

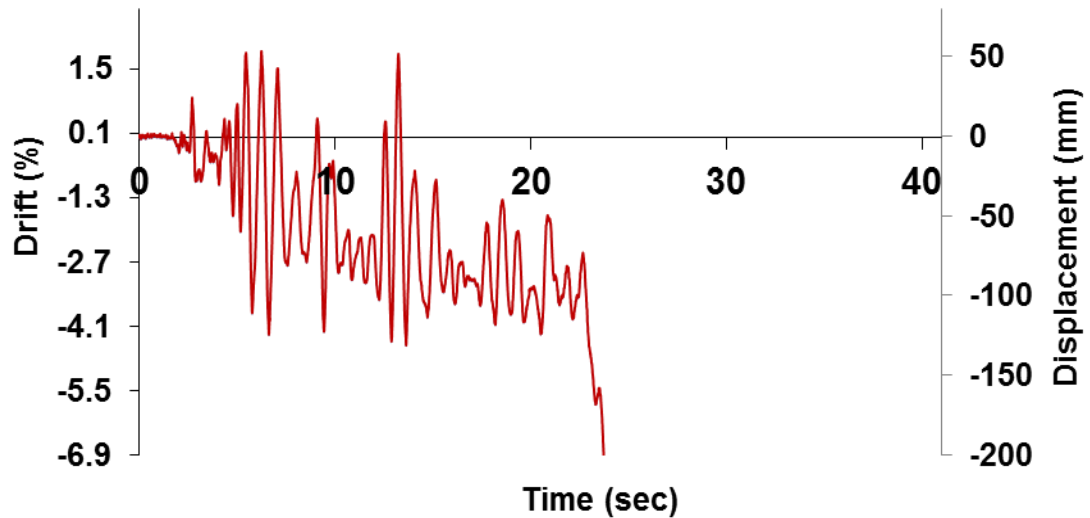


Figure 6.6: Measured displacement time-history response of test frame ST8-E40H in shake table test.

6.5 Summary and conclusion

A direct displacement based design (DDBD) procedure for single-storey concentrically braced frames (CBFs) was presented. An equivalent viscous damping model developed specifically for CBFs by Wijesundara (2009) was validated using full scale shake table tests.

DDBD was validated using shake table tests and NLTHA. DDBD was performed for all the shake table tests with a target displacement equal to the maximum displacement from the shake table tests. It was found that estimated base shear forces and required brace cross sectional sizes predicted by the DDBD methodology match very closely to the actual values obtained from shake table tests.

NLTHA is used to verify the DDBD methodology using eight different accelerograms scaled to have displacement spectrum equal to displacement spectrums used for the DDBD. It was found that the average of the displacements and base shear obtained from NLTHA and the ones obtained from DDBD are very similar.

Thus, the DDBD methodology presented in this chapter has been shown to give accurate and reliable results, which was proved by using real-time physical full scale shake table tests and a large range of NLTHA.

Chapter 7

DDBD for multi-storey CBFs

7.1 Introduction

In Chapter 6, a DDBD methodology was validated for single storey concentrically braced frame (CBF) structures using shake table tests and non-linear time history analysis (NLTHA). The numerical model for the NLTHA was validated in two stages. In the first stage, a robust numerical model taking into account fatigue for brace element, which is the main element in CBF systems to dissipate energy during seismic actions through its inelastic behaviour of yielding in tension and buckling in compression, was developed using pseudo static cyclic tests as was discussed in Chapter 3. This numerical model was advanced in Chapter 5 to represent a single storey CBF structures by comparing it to shake table tests and a large range of NLTHA.

In this chapter, this reliable numerical model will be extended to be used to check the validity of direct displacement based design (DDBD) procedure for multi-degree of freedom (MDOF) structures. The validity of the method will be assessed by designing 4-storey and 12-storey CBF buildings, in which the performance is checked by using the non-linear time history analysis (NLTHA) model employing different accelerograms with displacement spectra matching the design displacement spectrum. In this procedure, the inelastic behaviour is permitted for brace elements in order to dissipate energy induced from seismic actions, ensuring that beams and columns will remain elastic. Fundamentals

of DDBD procedure for frames are taken from Priestley et al. (2007) and an equivalent viscous damping model developed specifically for CBF by Wijesundara (2009) is used.

This chapter will be divided into several parts, as follows:

- A brief explanation of the DDBD procedure for multi-storey CBF will be carried out.
- Two case studies with four and twelve storeys will be designed using DDBD procedure.
- The validity of the design procedure will be checked using NLTHA, employing two sets of real earthquakes with displacement spectra matching the design displacement spectrum.
- The first set of earthquakes consists of eight different accelerograms, which were adjusted artificially then scaled to have spectra matching the design displacement spectrum (see Section 4.3.1).
- The second set of earthquakes consists of eight different accelerograms scaled to have spectra matching the design displacement spectrum without any artificial adjustment (see Section 4.3.2).

7.2 DDBD procedure for multi-storey CBFs

The design process starts by representing the MDOF system in the form of equivalent SDOF system with an effective mass at an effective height. Furthermore, DDBD characterises the structure by a secant stiffness at the maximum displacement with a level of equivalent viscous damping, and then the base shear can be found and distributed to the floors, as will be explained in the next sub-sections.

7.2.1 Design storey displacements

As discussed in Chapter 6, the main concept of the DDBD procedure is to design the structure for a specified target displacement. Della Corte and Mazzolani (2008) proposed a drift shape for MDOF chevron CBFs taking into account axial deformations of columns

and braces, as well as beam flexural deformations due to the unbalanced vertical force transmitted by the tension and compression braces, as follows:

$$\theta_{i,d} = \frac{v_{i,d}^r - v_{i,d}^l}{L} + \frac{2\varepsilon_{i,d}^{\text{tension}}}{\sin 2\alpha} + \frac{v_{b,i,d}}{h_i} \tan \alpha + \frac{\varepsilon_{c,i,d}^r - \varepsilon_{c,i,d}^l}{2} \tan \alpha \quad [7.1]$$

where $\theta_{i,d}$ is the design drift, $v_{i,d}^r$ and $v_{i,d}^l$ are vertical displacements at the base of the i^{th} storey right and left column due to elongation or shortening of columns from the first to the $(i-1)^{\text{th}}$ storey; L is the braced bay length; α is the angle of the brace on the horizontal axis; $\varepsilon_{i,d}^{\text{tension}}$ is the tension brace axial strain at the i^{th} storey; $v_{b,i,d}$ is the beam mid-span vertical deflection at the i^{th} storey; h_i is the i^{th} storey height; $\varepsilon_{c,i,d}^r$ and $\varepsilon_{c,i,d}^l$ are the right and left column axial strains at the i^{th} storey. As shown in Equation [7.1], which represents chevron CBFs drifts which is not considered in this study, this equation is complicated and has many different variables. A simpler equation which can represent the displacement shape of CBFs suggested by Priestley et al. (2007), and from the results of several researchers (Medhekar and Kennedy 2000; Medhekar and Kennedy 2000; Moghaddam and Hajirasouliha 2006; Wijesundara 2009) on the dynamic analysis of CBFs, is used for this study. The design storey displacements of the CBF, Δ_{Di} , can be obtained from a linear displacement pattern, which depends upon the normalised inelastic mode shape, δ_i , and the displacement of the critical storey, Δ_1 . Thus, the design storey displacements, Δ_{Di} , can be obtained from the following equation

$$\Delta_{Di} = \delta_i \left(\frac{\Delta_1}{\delta_1} \right) \quad [7.2]$$

where Δ_1 is the displacement of the critical storey and δ_1 is the normalised inelastic mode shape of the critical storey. The critical storey is normally the first storey level.

The inelastic mode shape can be found by the following equations (Priestley et al. 2007)

$$\text{For } n \leq 4: \quad \delta_i = \frac{H_i}{H_n} \quad [7.3]$$

$$\text{For } n > 4: \quad \delta_i = \frac{4}{3} \left(\frac{H_i}{H_n} \right) \left(1 - \frac{H_i}{4H_n} \right) \quad [7.4]$$

where n is the total number of storeys, i is the storey number, H_i is the storey height of the i^{th} level and H_n is the roof height. Priestley et al. (2007) suggested to use Equation [7.3] only for CBFs regardless of the number of storeys in the frame. However, using Equation [7.3] for structures with less than 4 storeys and Equation [7.4] for structures with more than 4 storeys gave satisfactory results, as will be discussed in the validation part of this chapter. Calvi and Sullivan (2009) proposed an approach to include an allowance for higher mode amplification of drift, reducing the design floor displacements in Equations [7.3] and [7.4] by a drift reduction factor, ω_θ , as the following:

$$\omega_\theta = 1.15 - 0.0034H_n \leq 1 \quad [7.5]$$

However, this approach is not used for this study. In order to account for the higher mode effects, 10% of the base shear force is allocated for to the roof level and the remaining 90% of the base shear force is distributed to all floor levels including the roof in proportion to the product of mass and displacement as shown in Equation [7.19].

7.2.2 Equivalent SDOF system characteristics

With the knowledge of the displacement profile, it is possible to obtain various equivalent SDOF properties of the structure (Priestley et al. 2007). The equivalent SDOF design displacement, Δ_D , which is related to the storey displacements, is given by

$$\Delta_D = \frac{\sum m_i \Delta_{Di}^2}{\sum m_i \Delta_{Di}} \quad [7.6]$$

where m_i is the mass at , H_i , associated with displacement, Δ_i . The effective mass, m_e , can be found by

$$m_e = \frac{\sum m_i \Delta_{Di}}{\Delta_D} \quad [7.7]$$

and the effective height, H_e , of the SDOF structure is given by

$$H_e = \frac{\sum m_i \Delta_{Di} H_i}{\sum m_i \Delta_{Di}} \quad [7.8]$$

7.2.3 Design displacement ductility

The design displacement ductility, μ , is found by dividing the design displacement, Δ_D , by the yield displacement, Δ_y , as the following

$$\mu = \frac{\Delta_D}{\Delta_y} \quad [7.9]$$

where the equivalent SDOF yield displacement, Δ_y , related to the storey yield displacements can be found by

$$\Delta_y = \frac{\sum m_i \Delta_{yi}^2}{\sum m_i \Delta_{yi}} \quad [7.10]$$

where Δ_{yi} is the yield displacement at the i^{th} floor. This displacement is the lateral drift from yielding of the brace combined with column deformation, which can be obtained from

$$\Delta_{yi} = \sum_{j=1}^i \left(\frac{\varepsilon_{br,y}}{\sin \alpha \cos \alpha} h_j + \beta_j \varepsilon_{col,y} h_j \tan \alpha \right) \quad [7.11]$$

where $\varepsilon_{br,y}$ is the brace axial yield strain, α is angle of the brace with the horizontal axis, h_j is the storey height, β_j is the ratio of the design force to the yielding force of the column section at the j^{th} floor and $\varepsilon_{col,y}$ is the column axial yield strain. The derivation of Equation [7.11] can be found in Della Corte and Mazzolani (2008) and Wijesundara (2009).

In order to limit the damage to the structural elements, the design ductility values should be less than the ductility values obtained from the expressions established by Nip et al. (2010) for hot-rolled and cold-formed steel shown in Equations [2.6] and [2.7].

7.2.4 Equivalent viscous damping

Wijesundara (2009) determined equivalent viscous damping for concentrically braced frames as a function of non-dimensional slenderness ratio, $\bar{\lambda}$, and the ductility, μ , as shown in the following equations

$$\xi = 0.03 + \left(0.23 - \frac{\bar{\lambda}}{15}\right)(\mu - 1) \quad \mu \leq 2 \quad [7.12]$$

$$\xi = 0.03 + \left(0.23 - \frac{\bar{\lambda}}{15}\right) \quad \mu \geq 2 \quad [7.13]$$

This EVD model was verified using shake table tests and large range of NLTHA on single storey CBFs, as outlined in Chapter 5. This was validated for use in the DDBD of single storey CBF systems in Chapter 6.

7.2.5 Effective period

The effective period at the design displacement, T_e , can be read from the displacement spectrum which is multiplied by a displacement reduction factor to give the spectrum at the design damping level, as shown in Figure 7.1.

Pennucci et al. (2011) studied displacement reduction factors for the design of medium and long-period structures. They suggested that if an existing EVD expression is used for design, it is important that it is used together with the damping reduction relationship that was used to develop the EVD expression itself from specific records. This is the reason that Priestley et al. (2007) have been advocating the use of the old EC8 (1998) damping reduction expression for DDBD for quite some time, even though it was known that the current EC8 (2004) damping reduction expressions can better represent the effects of elastic damping on real ground motion spectra.

The reduction factor used in this work is the one used in 1998 edition of EC8 (CEN 1998), as the DDBD methodology was carried out using this expression and it was used to develop the EVD models by Wijesundara (2009), as shown in Equation [7.14].

$$R_{\xi} = \left(\frac{0.07}{(0.02 + \xi)}\right)^{0.5} \quad [7.14]$$

where ξ is the equivalent viscous damping obtained from Equation [7.12] or [7.13].

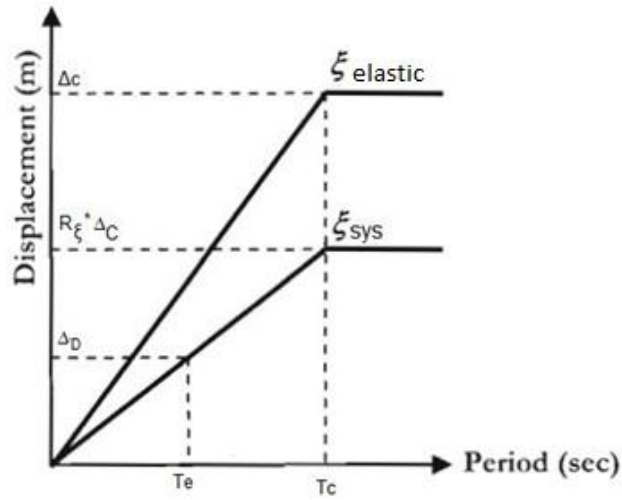


Figure 7.1: Displacement response spectrum.

7.2.6 Effective stiffness of substitute structure

With the effective period established, the effective stiffness, K_e , is determined as:

$$K_e = \frac{4\pi^2 m_e}{T_e^2} \quad [7.15]$$

where m_e is the mass calculated in Equation [7.7] and T_e is the effective period.

7.2.7 Design base shear force

The base shear, F_b , is then obtained by multiplying the effective stiffness, K_e , by the design displacement, Δ_D , as the following equation

$$F_b = K_e \Delta_D \quad [7.16]$$

As discussed in Chapter 6, in the DDBD approach, it is recommended that the design base shear be increased to account for the reduction in effective lateral stiffness due to P- Δ effects (Priestley et al. 2007). The increase in the lateral force required to account for P- Δ effects in steel structures can be estimated as:

$$F_{P-\Delta} = \frac{m_e g}{H_e} \Delta_D \quad [7.17]$$

where g is acceleration due to gravity and H_e is the effective height of the SDOF system. Thus, the new base shear can be found by

$$F_b = \left(K_e + \frac{m_e g}{H_e} \right) \Delta_D \quad [7.18]$$

As suggested by Priestley et al. (2007) and in order to take into account the higher modes effect, 10% of the base shear force is allocated for to the roof level and the remaining 90% of the base shear force is distributed to all floor levels including the roof in proportion to the product of mass and displacement as the following equation

$$F_i = F_t + 0.9F_b \frac{m_i \Delta_i}{\sum m_i \Delta_i} \quad [7.19]$$

where $F_t = 0.1F_b$ at roof level and $F_t = 0$ at all other levels, m_i and Δ_i are the mass and design displacement of the i^{th} floor.

For this work the recommendation of EC8 (CEN 2004), that only tension diagonal bracings should be designed to resist the shear forces, is used. The brace area can found by dividing the axial force in the brace, $N_{Ed,i}$, by the yield strength, f_y . The axial force in the brace, $N_{Ed,i}$, can be found by dividing the amount of floor shear assigned to this brace by cosine of the angle of the brace with the horizontal, α . All columns and beams should be capacity designed to ensure that dissipative behaviour is provided primarily by the braces as suggested by EC8 (CEN 2004) (see Section 7.3.2).

7.3 Case studies for DDBD for CBFs

Two case studies of 4-storey and 12-storey buildings are designed to investigate the DDBD for CBFs. The buildings dimension is 32m by 32m in plan consisting of two CBFs in each direction as the lateral resisting frames, as shown in Figure 7.3. These buildings are symmetric in plan and elevation with a uniform storey height of 3m. For simplicity, stiffness and strength contributions of the interior partitions and the exterior cladding are ignored and the accidental torsion is neglected. Plan view and elevation for the 4-storey structure are shown in Figure 7.3 and Figure 7.4, respectively. Columns are assumed to be continuous along the height and pinned at the base. The connections

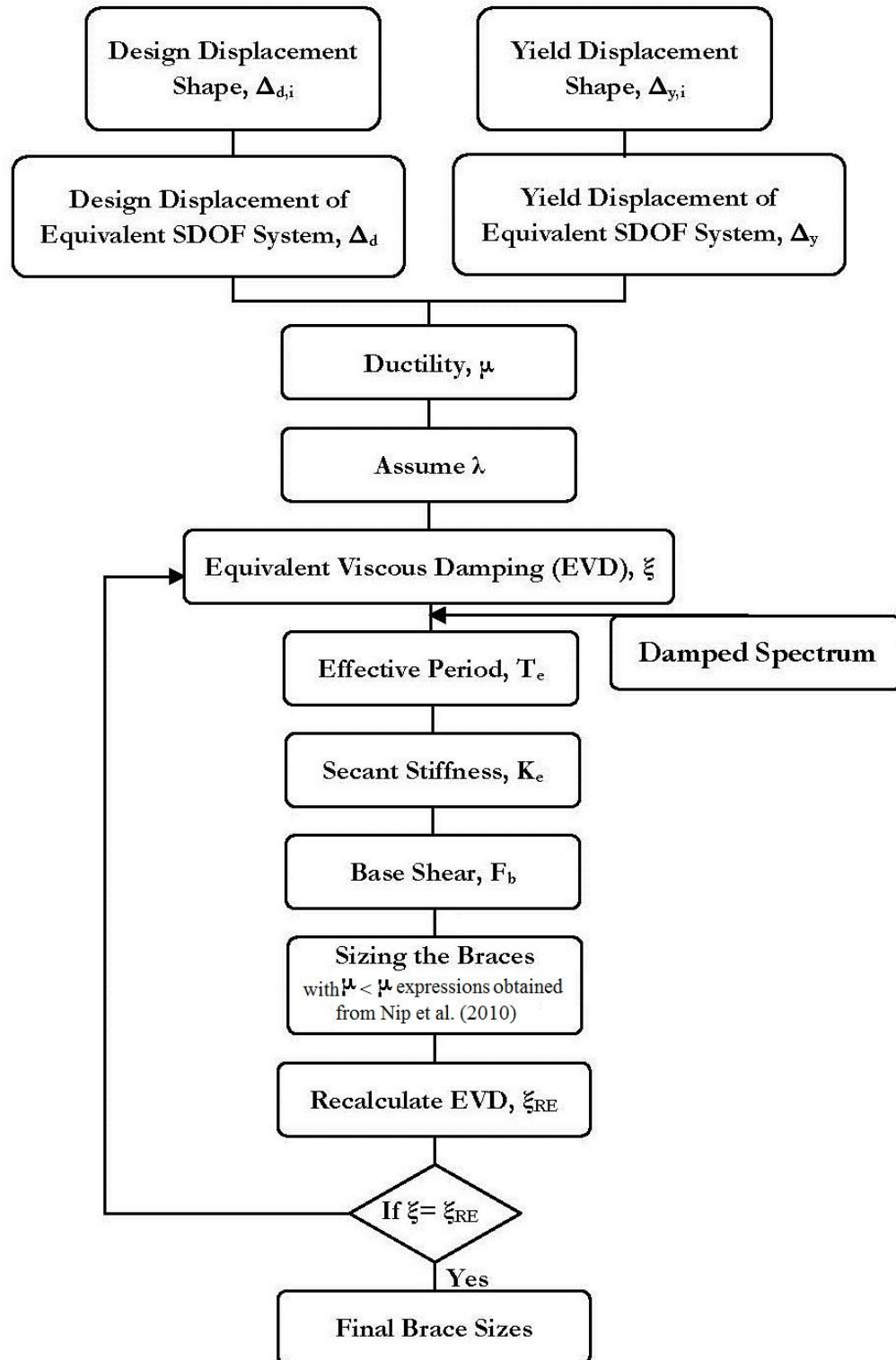


Figure 7.2: Flow chart of the DDBD procedure for CBFs adapted from (Wijesundara 2009).

between columns and beams are assumed to be pinned and the lateral forces are assumed to be resisted by the braces on the 4m bays represented by the dashed line. Bracing end conditions are considered to be pinned in both ends. Characteristic dead and imposed loads of 8.1KPa and 3KPa, respectively, were selected using provisions of EC1 (CEN 2004). Seismic loads were taken as the summation of the unfactored dead load and a reduced live load (seismic load = $G_k + 0.3 \cdot Q_k = 8.1 + 0.3 \cdot 3 = 9$ KPa, where G_k is the characteristic dead load and Q_k is the characteristic imposed load). Grade S355 steel with nominal yield strength of 355N/mm^2 was chosen for all elements. Eurocode 8 (CEN 2004) type 1 elastic response spectrum for soil type C and peak ground acceleration (PGA) of 0.3g was chosen. Design storey drifts of 2.5% were selected to control damage of non-structural elements.

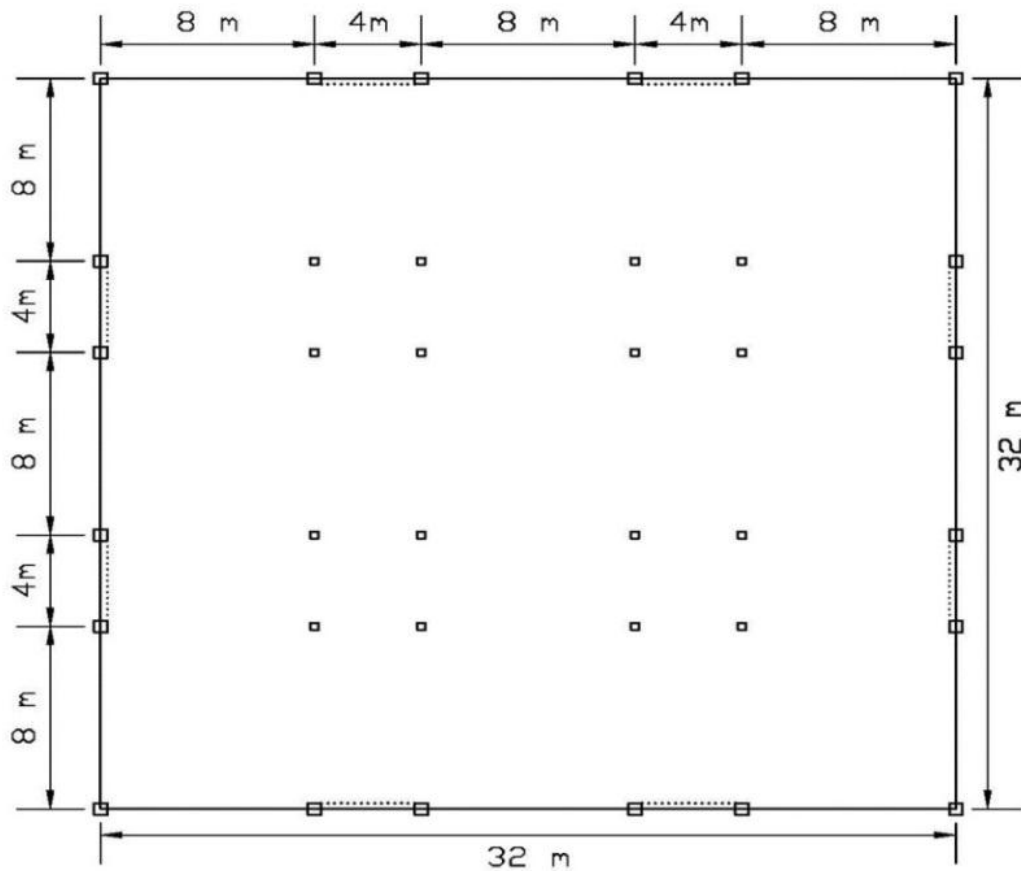


Figure 7.3: Plan view of the four storey CBF case study.

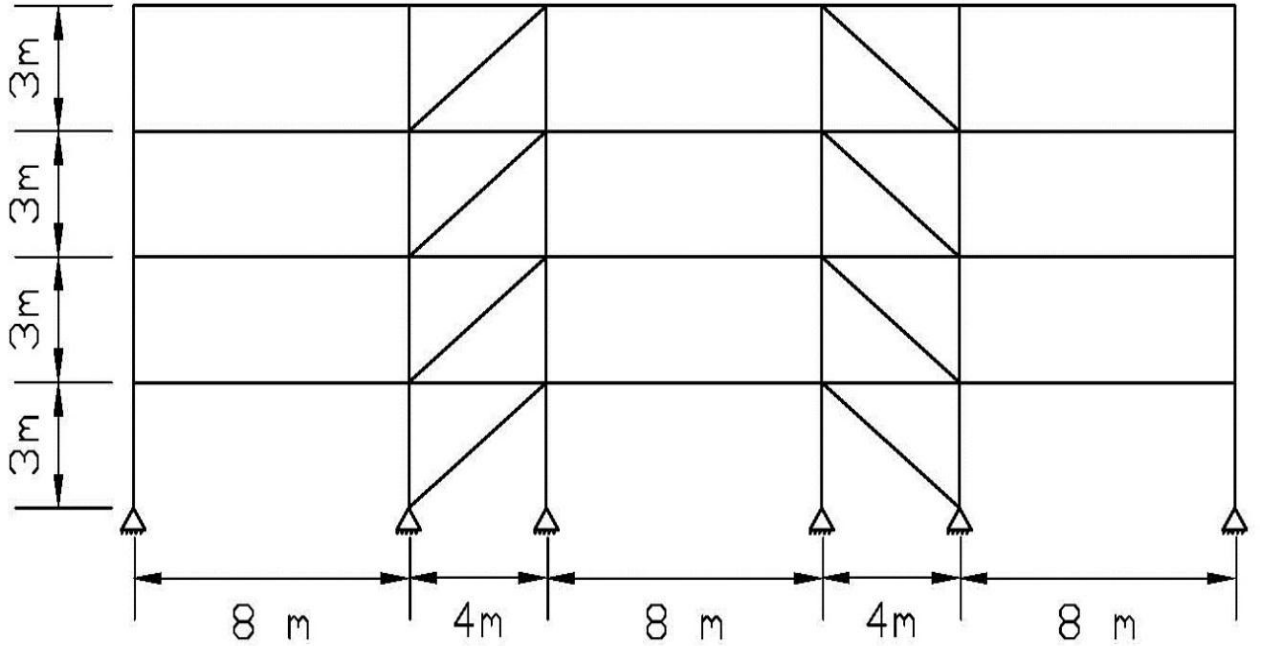


Figure 7.4: Elevation of the 4-storey CBF case study.

To design the building, first the substitute structure displacement, Δ_D , effective height, H_e , effective mass, m_e , and ductility, μ , are found. The necessary calculations are summarised in Table 7.1 and the following equations.

$$\Delta_D = \frac{\sum m_i \Delta_{Di}^2}{\sum m_i \Delta_{Di}} = \frac{77.76}{345.60} = 0.225\text{m} \quad [7.20]$$

$$\Delta_y = \frac{\sum m_i \Delta_{yi}^2}{\sum m_i \Delta_{yi}} = \frac{2.85}{66.21} = 0.043\text{m} \quad [7.21]$$

$$\mu = \frac{\Delta_D}{\Delta_y} = \frac{0.225}{0.043\text{m}} = 5.22 \quad [7.22]$$

$$H_e = \frac{\sum m_i \Delta_{Di} H_i}{\sum m_i \Delta_{Di}} = \frac{3110.4}{345.60} = 9\text{m} \quad [7.23]$$

$$m_e = \frac{\sum m_i \Delta_{Di}}{\Delta_D} = \frac{345.6}{0.225} = 1536 \text{ tons} \quad [7.24]$$

Table 7.1: Calculations for design displacements, effective height and yield displacement.

1	2	3	4	5	6	7	8	9	10	11
Level	Height (m)	Mass, m_i (ton)/fr	δ_i	Δ_{id}	$m_i\Delta_{id}$	$m_i\Delta_{id}^2$	$m_i\Delta_{id}H_i$	Δ_{iy}	$m_i\Delta_{iy}$	$m_i\Delta_{iy}^2$
4	12	460.8	1.00	0.30	138.24	41.47	1658.88	0.06	26.49	1.52
3	9	460.8	0.75	0.23	103.68	23.33	933.12	0.04	19.86	0.86
2	6	460.8	0.50	0.15	69.12	10.37	414.72	0.03	13.24	0.38
1	3	460.8	0.25	0.08	34.56	2.59	103.68	0.01	6.62	0.10
Sum		1843.2			345.60	77.76	3110.40		66.21	2.85

To get the damping level, the equivalent viscous damping (EVD) equations suggested by Wijesundara (2009), which is a function of ductility, μ , and non-dimensional slenderness ratio, $\bar{\lambda}$, as shown in Equations [7.12] and [7.13] are used. Because the slenderness ratio is unknown at this stage of design, an initial assumption of slenderness ratio is assumed to obtain a value for the EVD. Then, the initial design of braces is carried out. A number of trials should be performed in which new shear forces and brace member sizes are found. These trials stop when the same brace sizes are found to be adequate for the two consecutive trial designs, as will be explained in the following. A slenderness ratio, $\bar{\lambda}$, is first assumed as 1.3 giving a damping ratio of 17.33% by employing the EVD equation of Wijesundara (2009) as follows:

$$\xi = 0.03 + \left(0.23 - \frac{1.3}{15}\right) = 0.1733 \quad [7.25]$$

Following the EC8 (CEN 1998) recommendation for relationship between damping and displacement reduction, the reduction factor to be applied to the 5% displacement spectrum to get the 17.33% displacement spectrum is given by

$$R_{\xi} = \left(\frac{0.07}{(0.02 + 0.1733)} \right)^{0.5} = 0.602 \quad [7.26]$$

The displacement spectra for the design example are shown in Figure 7.5 from which the effective period, T_e , corresponds to the design displacement, Δ_D , can be read and is found to be 2.908 seconds.

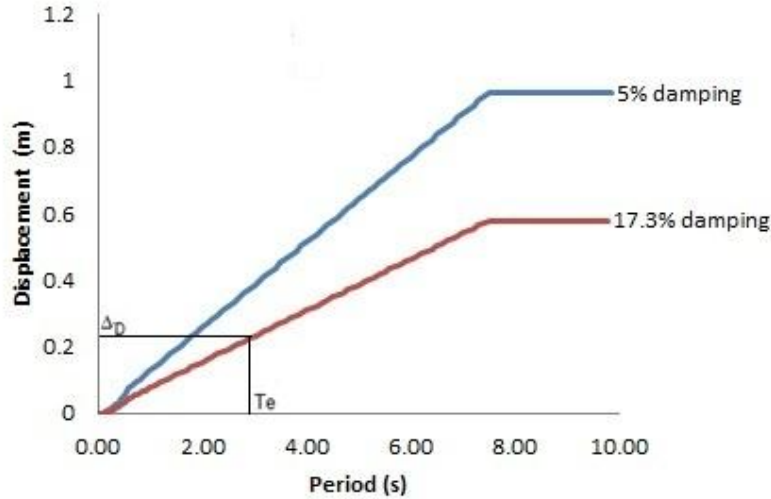


Figure 7.5: Displacement response spectra for the 5% and 17.3% damping.

By knowing the effective mass, m_e , and the effective period, T_e , the effective stiffness can be found by

$$K_e = \frac{4\pi^2 m_e}{T_e^2} = \frac{4\pi^2 * 1536}{(2.908)^2} = 7171 \text{ KN/m} \quad [7.27]$$

Then the base shear, F_b , can be found by

$$F_b = \left(K_e + \frac{m_e g}{H_e} \right) \Delta_D = 1990 \text{ KN} \quad [7.28]$$

7.3.1 Braces design

The base shear is distributed to the floor levels using Equation [7.19] as shown in Table 7.2 for the initial calculations (i.e. iteration step $n = 1$). Storey shear forces, $V_{i,n}$ are found by summing the floor forces above the storey considered. Assuming only tension diagonal bracings resisting the shear as suggested by EC8 (CEN 2004), the axial force in

the brace, $N_{Ed,i,n}$, is found by dividing the amount of floor shear assigned to this brace by cosine of the angle of the brace with the horizontal, α . The brace area is found by dividing the axial force in the brace, $N_{Ed,i,n}$, by the yield strength, f_y . All braces are chosen to be Class 1 with a slenderness ratio $\bar{\lambda} \leq 2$, as suggested by EC8 (CEN 2004), where slenderness ratio, $\bar{\lambda}$, is found by

$$\bar{\lambda} = \frac{L_{cr}}{i} \frac{1}{\lambda_1} \quad [7.29]$$

where L_{cr} is the length of the brace, i is radius of gyration and $\lambda_1 = 93.9\varepsilon$, where $\varepsilon = \sqrt{235/f_y}$. Note that Class 1 sections are defined as those that adhere to the limit $c/t \leq 33\varepsilon$, where c is width or depth of a part of the cross section ($c = h$ (or b) $- 2t - 2r$, where h is the height of the brace section, b is the width of the brace section, t is the thickness of the brace wall and r is the radius of root fillet) as described in EC3 (CEN 2005).

Table 7.2: Initial calculation of forces, shear and the design of brace elements (n = 1).

1	2	3	4	5	6	7	8	9	10
level	$F_{i,n}$ (kN)	$V_{i,n}$ (kN)	$N_{Ed,i,n}$ (kN)	proposed area, $A_{b,n}$ (cm ²)	section size	c/t	class	i (cm)	$\bar{\lambda}_n$
4	916	916	1144	32.24	100X100X10	7	1	3.64	1.80
3	537	1453	1816	51.16	120X120X12.5	6.6	1	4.34	1.51
2	358	1811	2264	63.77	150X150X12.5	9	1	5.57	1.17
1	179	1990	2488	70.08	160X160X12.5	9.8	1	5.98	1.09
Sum	1990								

A check for the brace overstrength, Ω , is carried out at each iteration step, n , as the following

$$\Omega_{i,n} = \frac{N_{pl,Rd,i,n}}{N_{Ed,i,n}} \quad [7.30]$$

where $N_{pl,Rd,i,n}$ is the design resistance of diagonal i and $N_{Ed,i,n}$ is the design value of the axial force in the same diagonal i in the seismic design situation. This check is carried out assuring that it satisfies the EC8 (CEN 2004) requirements that the maximum brace

overstrength does not differ from the minimum value by more than 25% in order to satisfy the homogeneous dissipative behaviour of the diagonals as shown in Table 7.3.

At this stage of design, the slenderness ratio and ductility are found for all the braces. So, the equivalent viscous damping can be found for every floor level using Equation [7.13] as the real slenderness ratio values are found and the ductility, μ , is more than two. The new calculated equivalent viscous damping values, $\xi_{i,n+1}$, for every floor from iteration step n , are shown in Table 7.3. The system equivalent viscous damping in iteration step n can be found by using the following equation

$$\xi_{sys} = \frac{\sum V_{i,n} \Delta_{D,i} \xi_{i,n+1}}{\sum V_{i,n} \Delta_{D,i}} = \frac{167.90}{1022.52} = 0.1642 \quad [7.31]$$

Table 7.3: Calculation of overstrength factor and the new equivalent viscous damping (n = 1)

1	2	3	4	5	6	7
Level	Real $A_{b,n}$ (cm^2)	$N_{pl,i,n}$ (kN)	$\Omega_{i,n}$	$\xi_{i,n+1}$	$V_{i,n} * \Delta_{D,i}$	$V_{i,n} * \Delta_{D,i} * \xi_{i,n+1}$
4	34.9	1239	1.08	0.14	274.66	38.49
3	52.1	1850	1.02	0.16	326.91	52.13
2	67.1	2382	1.05	0.18	271.68	49.36
1	72.1	2559	1.03	0.19	149.27	27.92
Sum					1022.52	167.90

This revised equivalent viscous damping is 5.4% less than the trial one found by using the assumed slenderness ratio. Thus, the above procedure is carried out again using the new equivalent viscous damping and finding adequate braces. The trials are finished when the same brace sizes are found to be adequate in two sequential trials.

The braces were chosen in this example after the second trial (i.e. $n = 2$) as shown in Table 7.4. All braces satisfied the EC8 (CEN 2004) requirements to be Class 1 with a

slenderness ratio $\bar{\lambda} \leq 2$. Brace members were chosen carefully to represent the design values as close as possible, as the purpose of this design is to verify the design methodology, where the maximum brace overstrength factor, $\Omega_{i,n}$, was 7% as shown in Table 7.4.

Table 7.4: Final trial results of designing the braces (n = 2)

1	2	3	4	5	6	7	8	9	10
Level	$F_{i,n}$ (kN)	$V_{i,n}$ (kN)	$N_{Ed,i,n}$ (kN)	Proposed $A_{b,n}$ (cm ²)	section size	Real $A_{b,n}$ (cm ²)	$N_{pl,i,n}$ (kN)	$\Omega_{i,n}$	$\bar{\lambda}_{i,n}$
4	922	922	1153	32.48	100X100X10	34.9	1239	1.07	1.80
3	541	1464	1830	51.54	150X150X10	54.9	1949	1.07	1.15
2	361	1825	2281	64.25	150X150X12.5	67.1	2382	1.04	1.17
1	180	2005	2507	70.61	160X160X12.5	72.1	2560	1.02	1.09
Sum	2005								

7.3.2 Columns and beams capacity design

Columns and beams are capacity designed to behave elastically ensuring that dissipative behaviour is provided primarily by the braces by the following combination from EC8 (CEN 2004). Thus the following equations are employed in the design of columns and beams from EC8 (CEN 2004).

$$N_{pl,Rd} \geq N_{Ed,G} + 1.1\gamma_{ov}\Omega N_{Ed,E} \quad [7.32]$$

$$M_{pl,Rd} \geq M_{Ed,G} + 1.1\gamma_{ov}\Omega M_{Ed,E} \quad [7.33]$$

$$V_{pl,Rd} \geq V_{Ed,G} + 1.1\gamma_{ov}\Omega V_{Ed,E} \quad [7.34]$$

where

- $N_{pl,Rd}$, $M_{pl,Rd}$ is the design buckling resistance, and shear resistance respectively of the beam or the column in accordance with EC3 (CEN 2006), taking into account the interaction of the buckling resistance with the bending moment.
- $V_{pl,Rd}$
- $N_{Ed,G}$, $M_{Ed,G}$ is the axial force, bending moment and shear respectively in the beam or in the column due to the non-seismic actions included in the combination of actions for the seismic design situation.
- $V_{Ed,G}$
- $N_{Ed,E}$, $M_{Ed,E}$ is the axial force, bending moment and shear respectively in the beam or in the column due to the design seismic action
- $V_{Ed,E}$
- γ_{ov} is the overstrength factor taken as 1.25.
- Ω The brace overstrength taken as the minimum of Ω_i found in Equation [7.30].

The selected beams and columns for the 4-storey building under consideration are shown in Table 7.5.

Table 7.5: Column and Beam designed sections from capacity design principles.

Level	Columns	Beams
4	HD 320X127	HE 320 B
3	HD 320X158	HE320 M
2	HD 400X187	HE 340 M
1	HD 400X237	HE 400 M

The DDBD procedure outlined in this chapter was also applied to a similar 12-storey building. Full details of the calculations are given in Appendix B, while a summary of the estimated final structure element sizes are given in Table 7.6.

Table 7.6: Structural member sizes for 12-storey building estimated using DDBD.

Level	Braces			Columns	Beams
	section size	Ab (cm ²)	$\bar{\lambda}$	Section size	Section size
12	120X120X6.3	28.2	1.42	HD 320X198	HE 400 M
11	120X120X10	42.9	1.47	HD 320X198	HE 400 M
10	120X120X12.5	52.1	1.51	HD 320X198	HE 400 M
9	140X140X12.5	62.1	1.27	HD 400X314	HE 400 M
8	160X160X12.5	72.1	1.09	HD 400X314	HE 550 M
7	180X180X12.5	82.1	0.96	HD 400X314	HE 550 M
6	180X180X14.2	92	0.97	HD 400X421	HE 550 M
5	180X180X16	102	0.99	HD 400X421	HE 550 M
4	180X180X16	102	0.99	HD 400X421	HE650X340
3	200X200X16	115	0.88	HD 400X509	HE650X341
2	200X200X16	115	0.88	HD 400X509	HE650X342
1	200X200X16	115	0.88	HD 400X509	HE650X343

7.4 Verification of the DDBD procedure

In order to verify the performance of the DDBD method used to design the CBF case studies, non-linear time history analyses (NLTHA) are carried out with time histories having displacement spectra that match the design displacement spectrum used in the DDBD application. The computer programme used for the verification is OPENSEES (McKenna et al. 2000).

7.4.1 Numerical model

Two-dimensional numerical models are employed, in which columns and beams are modelled to behave elastically. The connections between columns and beams, as well as between beams and braces, are assigned as pinned connections. Columns are assumed to be continuous along the height and pinned at the base. Braces are modelled as nonlinear beam-column element with distributed plasticity, where the cross section of the brace is divided into fibres along the perimeter and across the thickness. In this model, the brace is suggested to be divided into a minimum of two elements using ten integration points per element, as per the recommendations developed in Chapter 3. An initial camber of 1% of the length of the brace is applied to the middle of the brace to account for the overall buckling. This camber is applied in in-plane direction to have in-plane buckling. A low cyclic fatigue model with parameters calibrated in Chapter 3 is used to wrap the fibre based nonlinear beam column model in order to capture fracture in the braces. Uniaxial Giuffre-Menegotto-Pinto steel material model with isotropic strain hardening and monotonic envelop is used in this study with a value of strain hardening equal to 0.008. More information about the model of the brace element can be found in Chapter 3. The numerical integration method used to evaluate the dynamic response of the structure is Hilber-Hughes-Taylor (HHT) method, which is an extension to the Newmark method with constant Gamma equal to 0.5. Rayleigh damping model is used which assumes that the damping matrix is proportional to the mass and stiffness matrices. Elastic damping of 3% was specified. Similar value was found from the physical tests and used in DDBD methodology. The numerical model was verified using cyclic tests in braces and shake table tests for single storey CBF structures, as explained in Chapter 3 and Chapter 5.

7.4.2 Ground motions used in the study

Two sets of earthquakes are employed in the NLTHA models to validate the DDBD procedure.

In the first set, eight artificially adjusted accelerograms from four different earthquakes (2 components in orthogonal direction for each earthquake) taken from Pennucci et al. (2009) are used in the NLTHA, as outlined in Section 4.3.1.

Time history accelerograms are scaled to get a displacement response spectrum that matches the soil type C design displacement spectrum with 5% damping from EC8 (CEN 2004), which was used in the DDBD for the case studies. Response spectra for the scaled accelerograms are found using the programme SeismoSignal (SeismoSoft 2007) for the elastic response spectra with 5% damping, as shown in Figure 4.13 and Figure 4.14.

In the second set of earthquakes, eight different accelerograms were chosen without any artificial adjusting, as outlined in Section 4.3.2.

Similar to the first set, time history accelerograms for the second set of earthquakes are scaled to get a displacement response spectrum that matches the soil type C design displacement spectrum with 5% damping from EC8 (CEN 2004) and are shown in Figure 4.23 and Figure 4.24.

7.4.3 Comparison of results from NLTHA and DDBD

7.4.3.1 Using artificially adjusted earthquakes

For the 4-storey and the 12-storey CBF structures, the maximum floor displacements, taking into account the higher modes effect, are found during nonlinear time-history analyses for the eight artificially adjusted accelerograms for the 4-storey and the 12-storey buildings. These are compared with the design displacement profile obtained from the DDBD method, as shown in Figure 7.6 and Figure 7.7, respectively. Similarly, the average of the maximum recorded displacement during time-history analyses for the eight artificially adjusted accelerograms and the design displacement profile are shown in Figure 7.8 and Figure 7.9 for the 4-storey and the 12-storey buildings, respectively. It is apparent that the maximum displacements recorded from the time history analyses for the 4-storey and the 12-storey buildings are conservatively representing the linear design displacements assumed. One possible reason is that in the design it was assumed that the tension brace only resists the earthquakes. However, it is found that the compression brace also contributes to the lateral resistance in CBFs (Goggins 2004). Furthermore, 10% of the base shear was assigned to be resisted by top floor to account for the higher mode effects, which leads to stronger upper storeys. While trying to account for the compression brace in the design, it is found that in some storeys failure of one of the

braces occurred causing soft storey. So it was decided to be safe and conservative and assume all the lateral braces are resisted by the tension braces only, which is also a requirement in EC8 (CEN 2004).

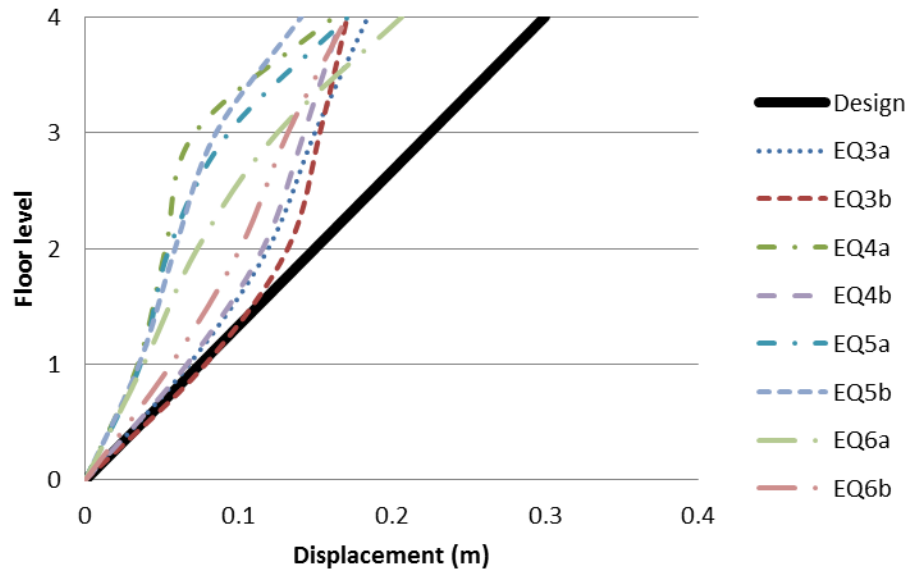


Figure 7.6: Maximum recorded displacements for eight spectrum compatible accelerograms compared with the design displacements for a 4-storey CBF.

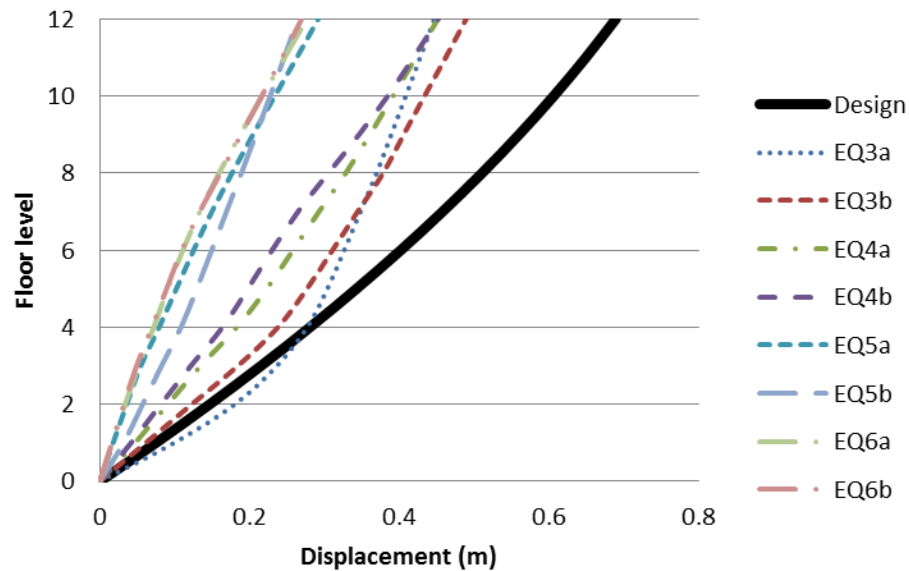


Figure 7.7: Maximum recorded displacements for eight spectrum compatible accelerograms compared with the design displacements for a 12-storey CBF.

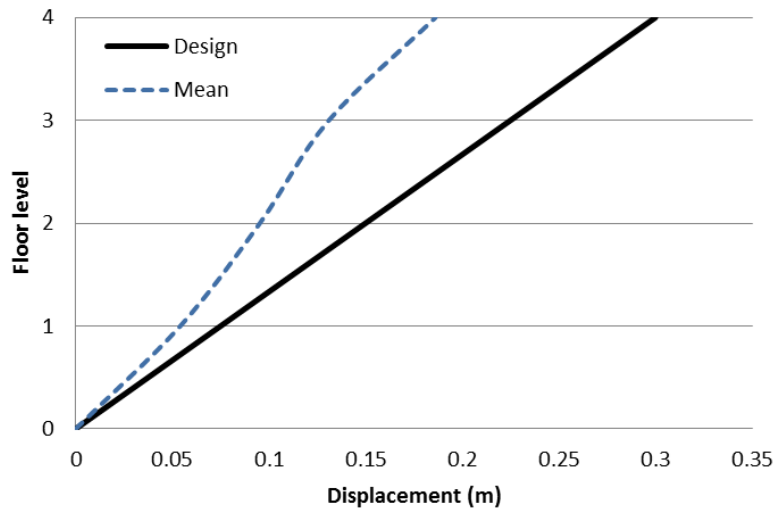


Figure 7.8: Average of the maximum recorded displacements for eight spectrum compatible accelerograms compared with the design displacements for the 4-storey CBFs.

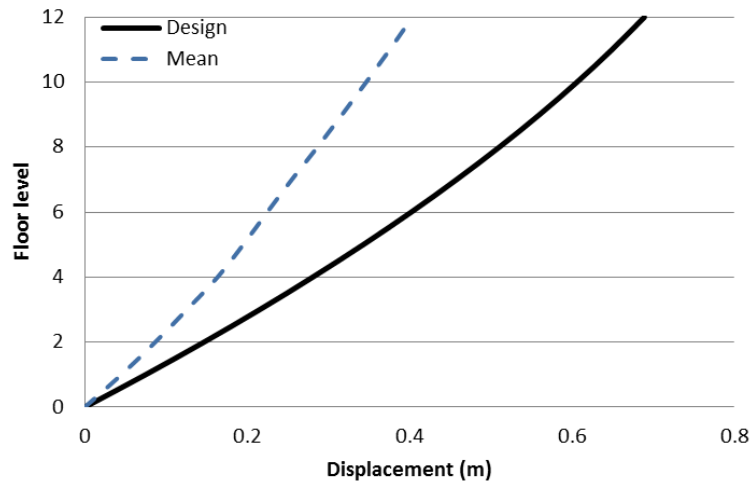


Figure 7.9: Average of the maximum recorded displacements for eight spectrum compatible accelerograms compared with the design displacements for the 12-storey CBFs.

The average of the maximum storey drifts recorded during time-history analyses using the eight accelerograms compared with the linear displacement design drift profile assumed for the case studies are shown in Figure 7.10 and Figure 7.11 for the 4-storey and 12-storey buildings, respectively. It is found that the average of the maximum recorded storey drifts for the eight artificially adjusted accelerograms for the 4-storey and

12-storey buildings are conservatively less than the design storey drift profile for the reasons mentioned earlier.

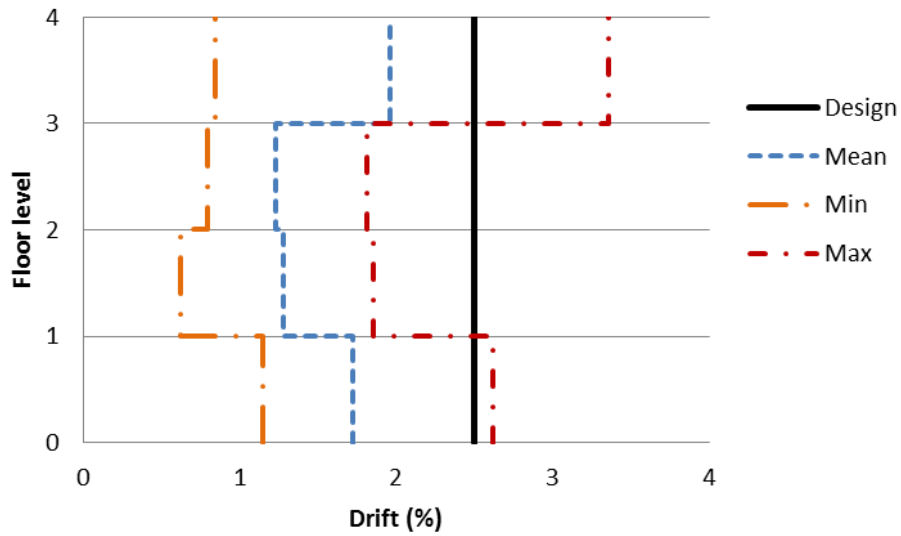


Figure 7.10: Average of the maximum recorded storey drifts for eight spectrum compatible accelerograms compared with the design storey drifts for the 4-storey CBF.

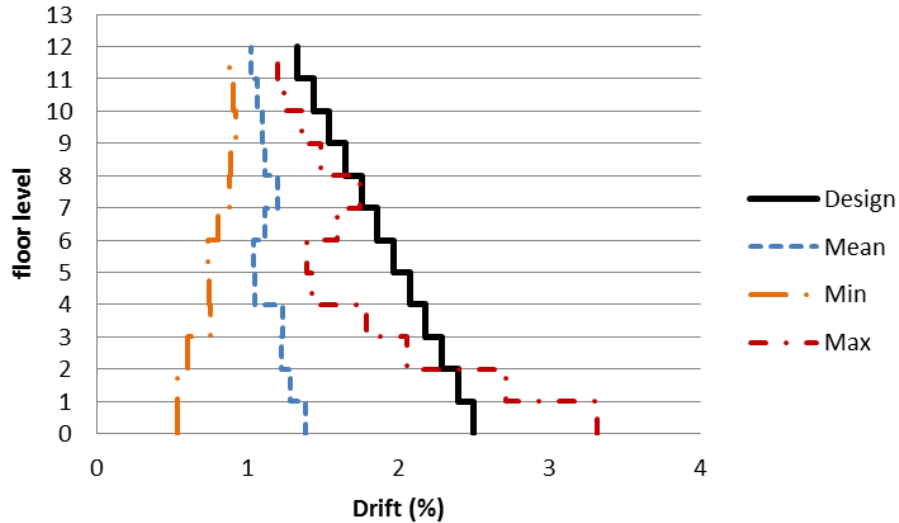


Figure 7.11: Average of the maximum recorded storey drifts for eight spectrum compatible accelerograms compared with the design storey drifts for the 12-storey CBF.

The maximum recorded ductility values are found during nonlinear time-history analyses for the eight artificially adjusted accelerograms for the 4-storey and the 12-storey

buildings. These are compared with the design ductility values obtained from the DDBD method as shown in Figure 7.12. It is found that the maximum ductility found from the time history analyses for the 4-storey and the 12-storey CBFs are in general less than the ductility used in the design. The main reason for this is that in the design, the lateral forces in the structure induced by the earthquakes were assumed to be resisted by the tension brace members only. However, as noted later the base shear is resisted by braces in both tension and compression, albeit the contribution of the compression member is significantly less than that of the tension member.

The average of the maximum recorded ductility during time-history analyses for the eight artificially adjusted accelerograms is shown in Figure 7.13 for the 4-storey and the 12-storey buildings. This is compared to the design ductility obtained from the DDBD method, ductility expressions established by Nip et al. (2010) for hot-rolled and cold-formed steel shown in Equations [2.6] and [2.7], respectively and ductility expression established by Tremblay (2002) shown in Equation [2.2]. It is apparent that the average of the maximum ductility values recorded from the time history analyses for the 4-storey and the 12-storey buildings are lower than the design ductility from the DDBD method and ductility expressions established by Nip et al. (2010) and Tremblay (2002).

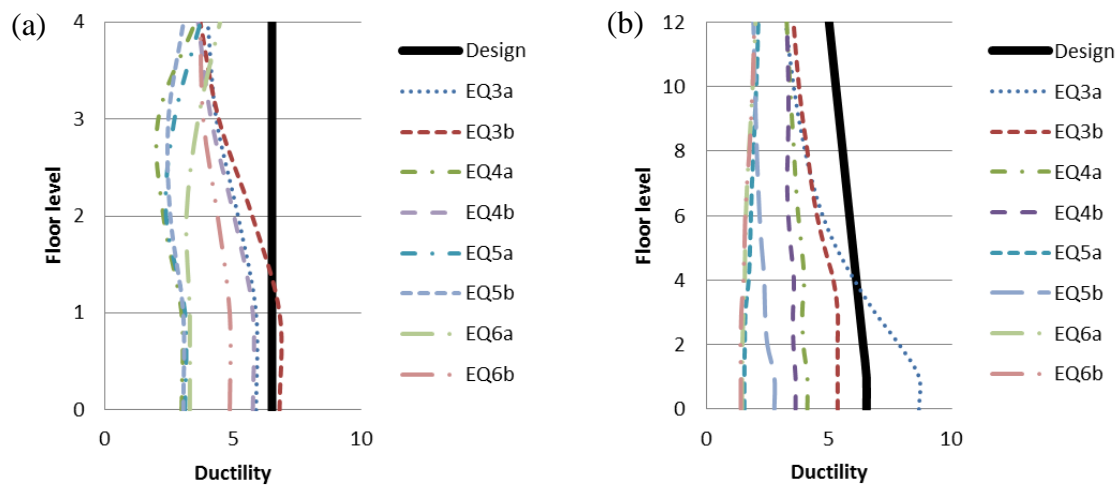


Figure 7.12: Maximum recorded ductility for eight spectrum compatible accelerograms compared with the design ductility for (a) 4-storey CBF and (b) 12-storey CBF.

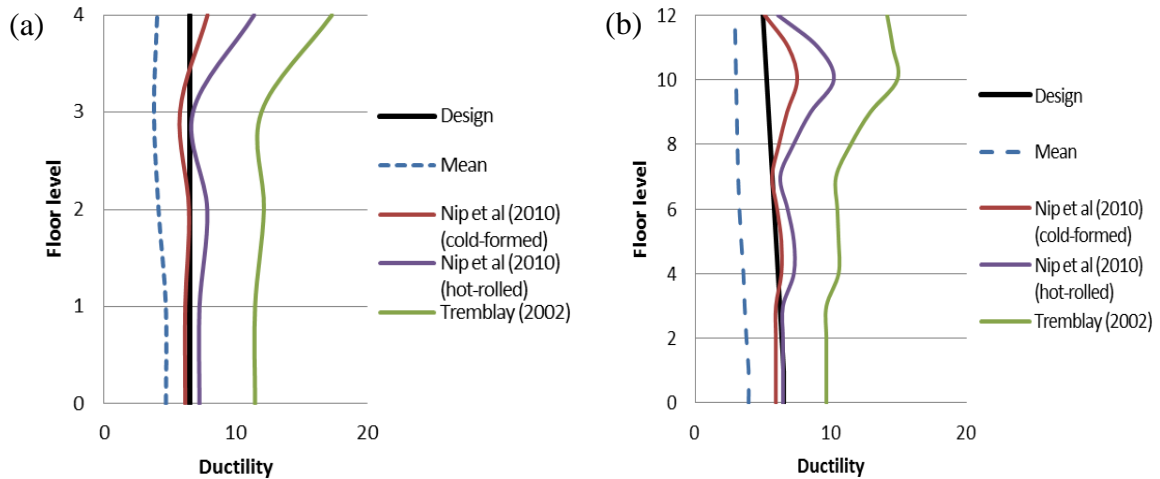


Figure 7.13: Average of the maximum recorded ductility for eight spectrum compatible accelerograms compared to the design ductility, ductility expressions of Nip et al (2010) for cold-formed and hot-rolled carbon steel and ductility expression of Tremblay (2002) for (a) 4-storey CBF and (b) 12-storey CBF.

As described in Section 7.3.1, the design base shear was distributed to the floors and assumed to be resisted by tension braces only in the DDBD of the case study buildings. Compression members were assumed not to resist any load as suggested by EC8 (CEN 2004). The design shear force from the DDBD procedure outlined in Section 7.3 and the shear force resisted by every brace at the instance when maximum displacement occurs in the NLTHA for the 4-storey and 12-storey CBF structures are shown from Figure 7.14 and Figure 7.15, respectively. As discussed previously, the compression member braces also resisted lateral forces and, thus, the predicted displacement and drift profiles were conservative as the system had a higher lateral resistance than assumed in the design. The mean of the shear forces resisted by both of the braces at the maximum displacement demand during the eight earthquakes are compared to the design shear forces in Figure 7.16 for the 4-storey and 12-storey CBF. Braces with low slenderness ratio are found to have more compressive strength capacity compared to slender braces, as observed in the lower floor shears that have stocky members. It is noted that compression shear resisted at the maximum displacement was less than the shear at the first buckling load due to residual deformation and Bauschinger effect. As discussed previously,

applying a percentage between 10% and 30% of the lateral force to be resisted by compression brace members led to fracture occurring in most of the slender braces located at the top floors. Thus, it was decided to adopt the design philosophy that lateral forces are resisted only by tension bracing members and the contribution to the lateral resistance of the system by the compression member is ignored.

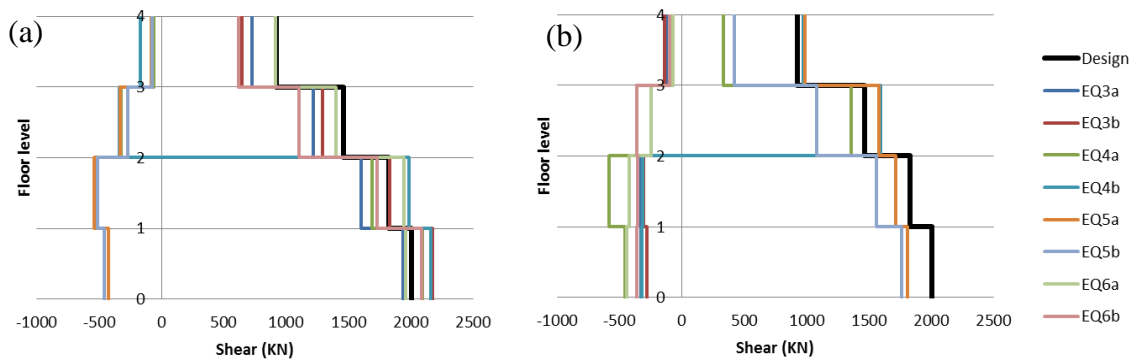


Figure 7.14: 4-storey CBF shear force design values compared to shear at the maximum displacement from NLTHA using artificially adjusted earthquakes resisted by (a) first brace and (b) second brace. Negative sign represents compression resistance and positive sign represents tension.

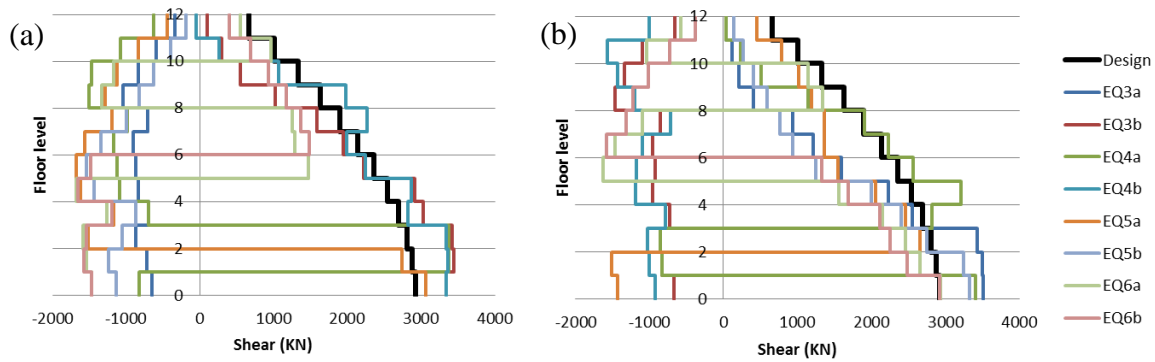


Figure 7.15: 12-storey CBF shear force design values compared to shear at the maximum displacement from NLTHA using artificially adjusted earthquakes resisted by (a) first brace and (b) second brace. Negative sign represents compression resistance and positive sign represents tension.

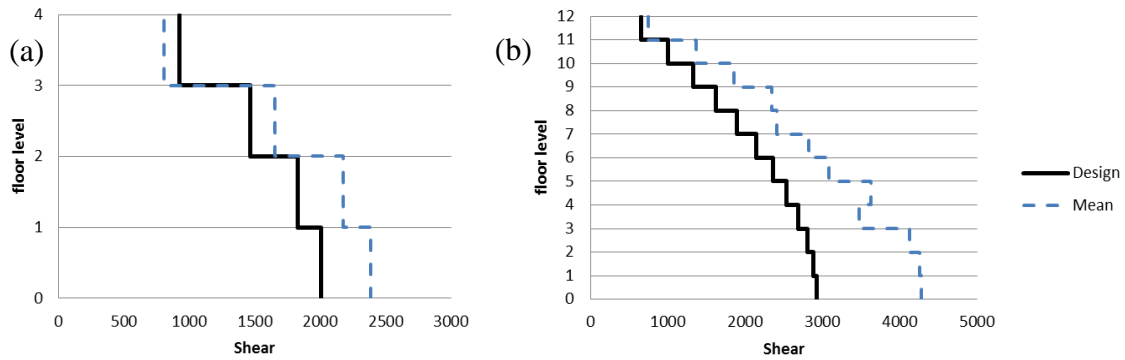


Figure 7.16: Average total shear forces resisted by both compression and tension braces from NLTHA using artificially adjusted earthquakes compared to the design shear forces of (a) 4-storey CBF (b) 12-storey CBF.

7.4.3.2 Using real earthquakes

NLTHA is carried out again for the 4-storey and 12-storey CBF structures using eight different real earthquakes to investigate the sensitivity of the analysis to the chosen earthquake records. The maximum floor displacements obtained from NLTHA for the real eight accelerograms for the 4-storey and the 12-storey buildings are compared with the design displacement profile obtained from the DDBD procedure in Figure 7.17 and Figure 7.18, respectively. Similarly, the average of the maximum recorded displacement during nonlinear time-history analyses for the real eight accelerograms and the design displacement profile are shown in Figure 7.19 and Figure 7.20 for the 4-storey and the 12-storey buildings, respectively. It is apparent that the average of the maximum displacements recorded from the time history analyses for the first floor of the 4-storey and the 12-storey buildings are close to the design displacement. However, the average of the maximum displacements recorded from the time history analyses for the upper storeys are conservatively representing the linear design displacements assumed, which were designed to resist additional 10% of the base shear to account for the higher mode effects. During design, shear resistance was assumed to be resisted by tension braces only as required by EC8 (CEN 2004) but both of the braces were found to resist shear which could be the reason of the conservative behaviour as found earlier. For the 4-storey structure, higher displacement was found in the first floor. For this 4-storey structure, the

effective period, T_e , equal to 2.84 s and equivalent viscous damping, ξ_{eq} , equal to 16.4%. At this period, the average of the 16.4% damping displacement spectra from the scaled accelerograms was 8.6% above the design displacement spectrum and this may be an explanation for exceeding the design displacement.

The average of the maximum storey drifts recorded during time-history analyses using the real eight accelerograms compared with the linear displacement design drift profile assumed for the case studies are shown in Figure 7.21 and Figure 7.22 and for the 4-storey and 12-storey buildings, respectively. It is found that the average of the maximum recorded storey drifts for the eight accelerograms for the 4-storey and 12-storey buildings are conservatively less than the design storey drift profile for the reasons mentioned earlier. However, for the 4-storey structure, higher drift concentration was found in the first floor (the average drift ratio from NLTHA is 10% above the design drift ratio for the first floor). As explained earlier, at the effective period of this structure, the average of the 16.4% damping displacement spectra from the scaled accelerograms was 8.6% above the design displacement spectrum and this may be an explanation for exceeding the design drift.

The average of the maximum recorded displacements and drifts during NLTHA for the real eight accelerograms were higher than the ones from the artificially adjusted eight accelerograms, despite all records being scaled to the same displacement response spectrum. A possible explanation is that the spectra of the real accelerograms were not matching perfectly to the EC8 displacement spectrum at the periods investigated. Furthermore, the real earthquakes were recorded at locations with soil type A, which would typically have different characteristics than those recorded at locations with soil type C. However, these records were scaled to the EC8 type C spectrum which was used in the DDBD for the case studies.

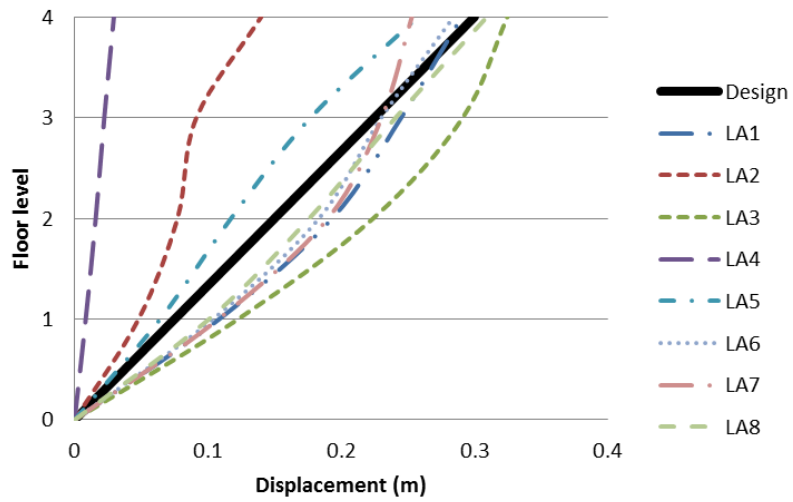


Figure 7.17: Maximum recorded displacements for real eight spectrum compatible accelerograms compared with the design displacements for the 4-storey CBF.

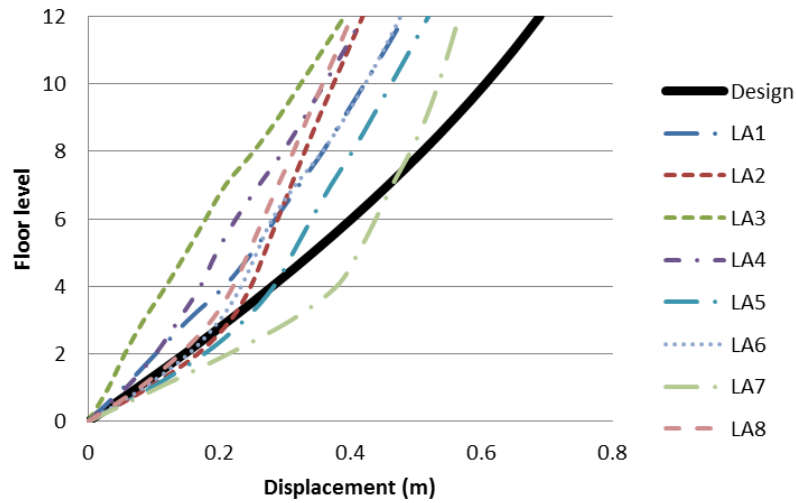


Figure 7.18: Maximum recorded displacements for real eight spectrum compatible accelerograms compared with the design displacements for the 12-storey CBF.

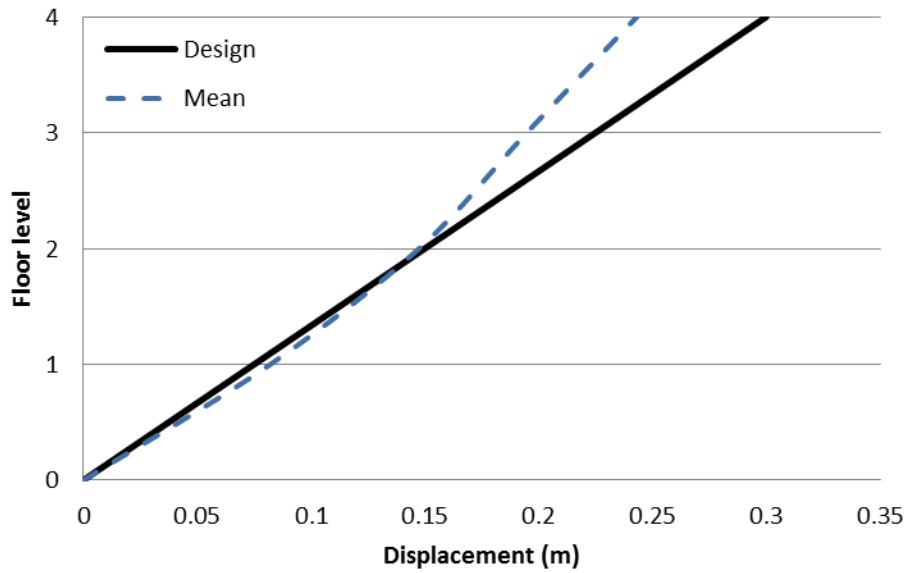


Figure 7.19: Average of the maximum recorded storey drifts for real eight spectrum compatible accelerograms compared with the design storey drifts for the 4-storey CBF.

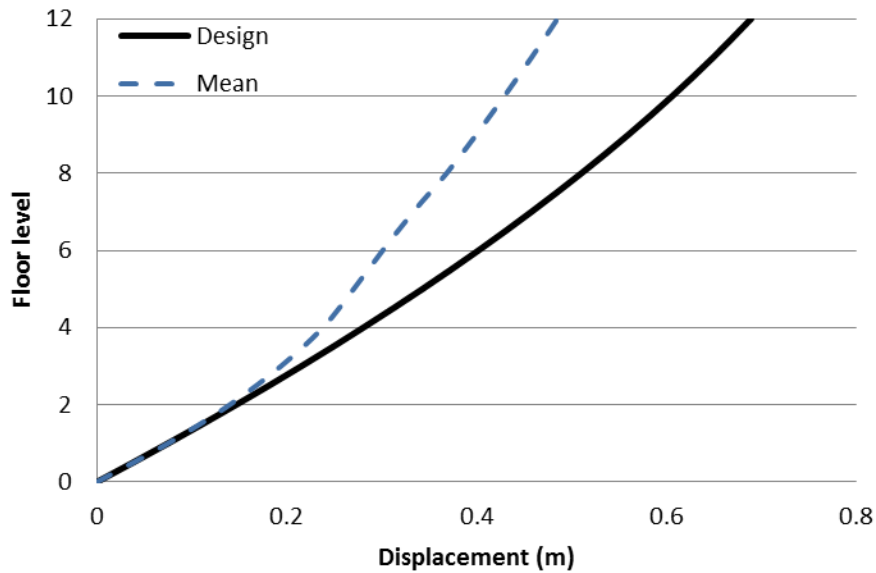


Figure 7.20: Average of the maximum recorded storey drifts for real eight spectrum compatible accelerograms compared with the design storey drifts for the 12-storey CBF.

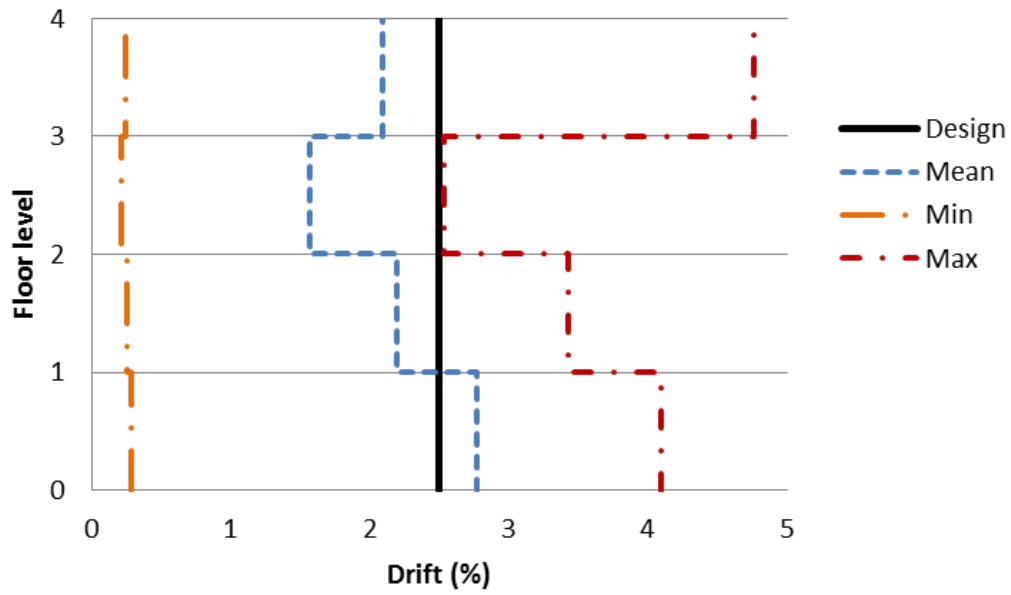


Figure 7.21: Average of the maximum recorded storey drifts for real eight spectrum compatible accelerograms compared with the design storey drifts for the 4-storey CBF.

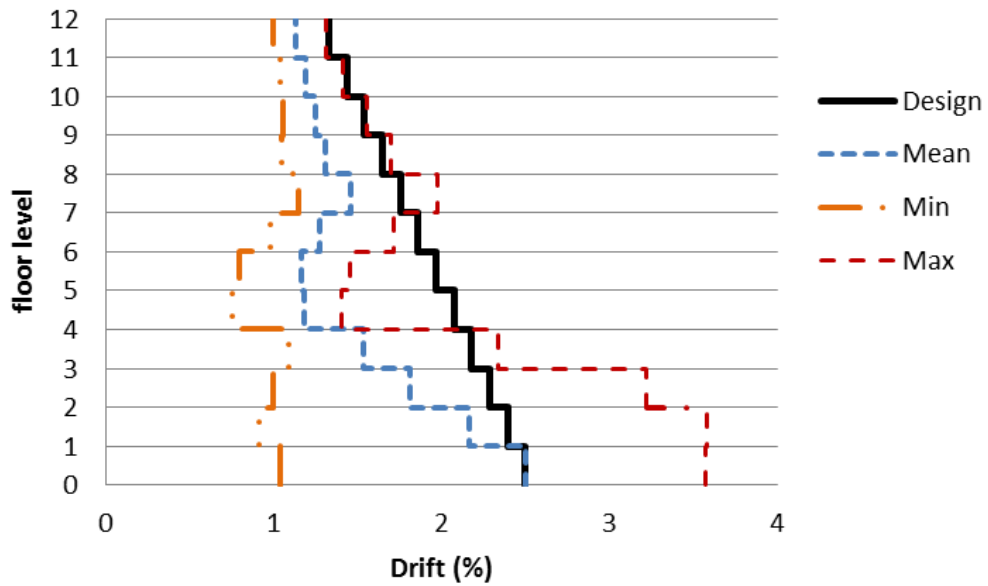


Figure 7.22: Average of the maximum recorded storey drifts for real eight spectrum compatible accelerograms compared with the design storey drifts for the 12-storey CBF.

The maximum recorded ductility values are found during nonlinear time-history analyses for the eight real accelerograms for the 4-storey and the 12-storey buildings and compared with the design ductility profile obtained from the DDBD method in Figure 7.23. Moreover, the average of the maximum recorded ductility values during time-history analyses for the eight real accelerograms are shown in Figure 7.24 for the 4-storey and the 12-storey buildings and compared to the design ductility obtained from the DDBD method, ductility expressions established by Nip et al. (2010) for hot-rolled and cold-formed steel shown in Equations [2.6] and [2.7] and ductility expression established by Tremblay (2002) shown in Equation [2.2]. It is found that the maximum ductility values recorded from the time history analyses for the 4-storey and the 12-storey buildings are close to the design ductility from the DDBD method and ductility expression established by Nip et al. (2010) for cold-formed steel. However, they were less than the values obtained from ductility expression established by Nip et al. (2010) for hot-rolled steel and the expression established by Tremblay (2002).

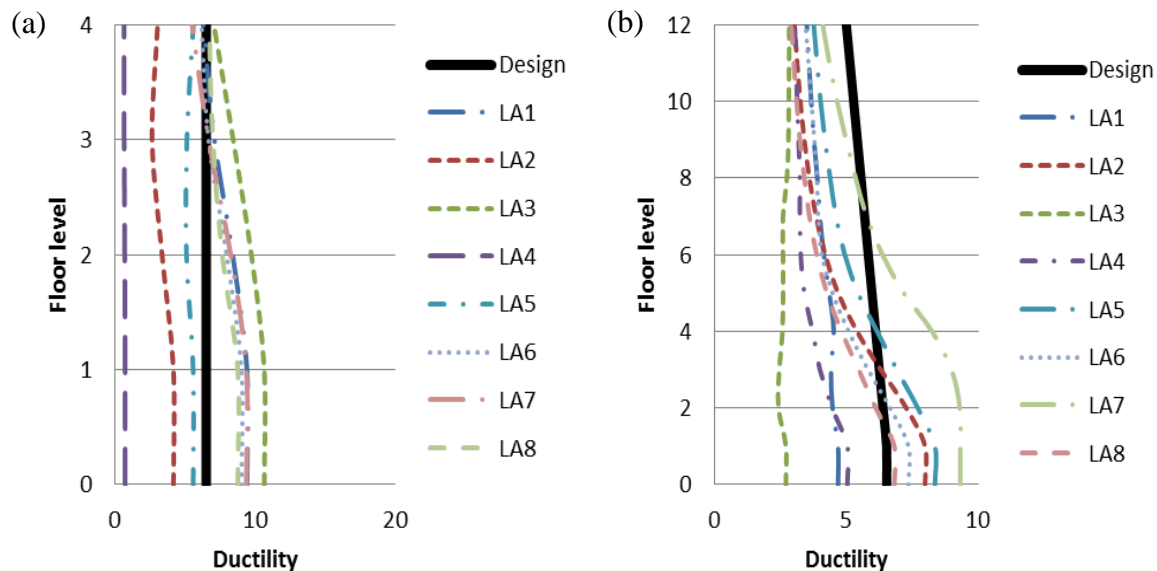


Figure 7.23: Maximum recorded ductility for real eight spectrum compatible accelerograms compared with the design ductility for (a) 4-storey CBF and (b) 12-storey CBF.

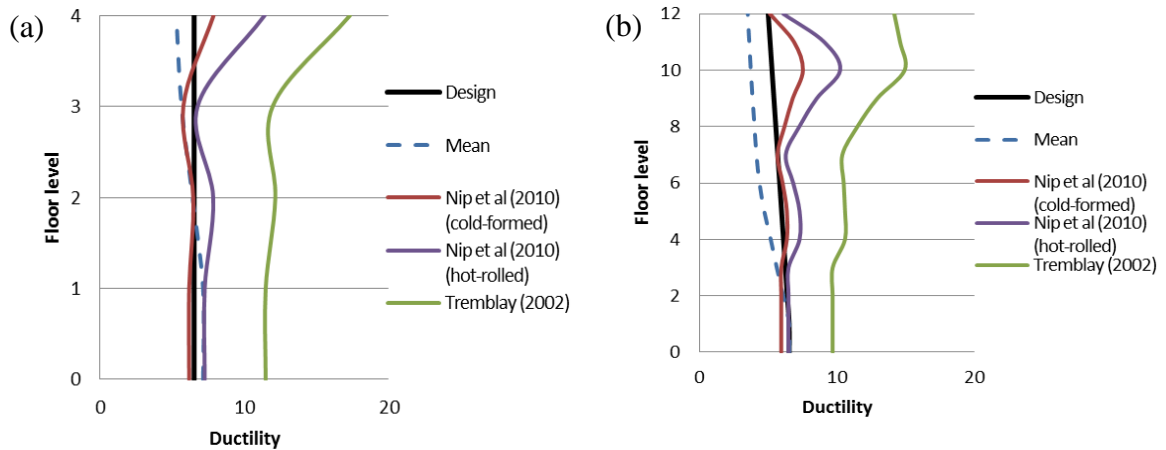


Figure 7.24: Average of the maximum recorded ductility for real eight spectrum compatible accelerograms compared with the design ductility, ductility expression of Nip et al (2010) for cold-formed and hot-rolled steel and ductility expression of Tremblay (2002) for (a) 4-storey CBF and (b) 12-storey CBF.

The shear force resisted by both of the braces during the real earthquakes in the NLTHA compared to the design shear force in Figure 7.25 and Figure 7.26 for the 4-storey and 12-storey CBF, respectively. Similar to the case of NLTHA using artificially adjusted earthquakes, it is found that compression member braces also resisted shear forces. Because of that the average shear resisted by both of the braces from NLTHA are significantly higher than the design shear, as shown in Figure 7.27.

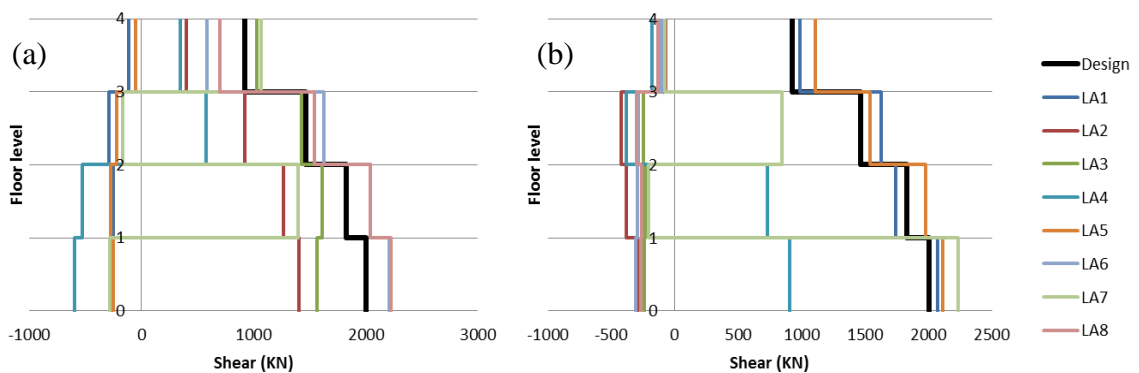


Figure 7.25: 4-storey CBF shear force design values compared to shear at the maximum displacement from NLTHA using real earthquakes resisted by (a) first brace and (b) second brace. Negative sign represents compression resistance and positive sign represents tension.

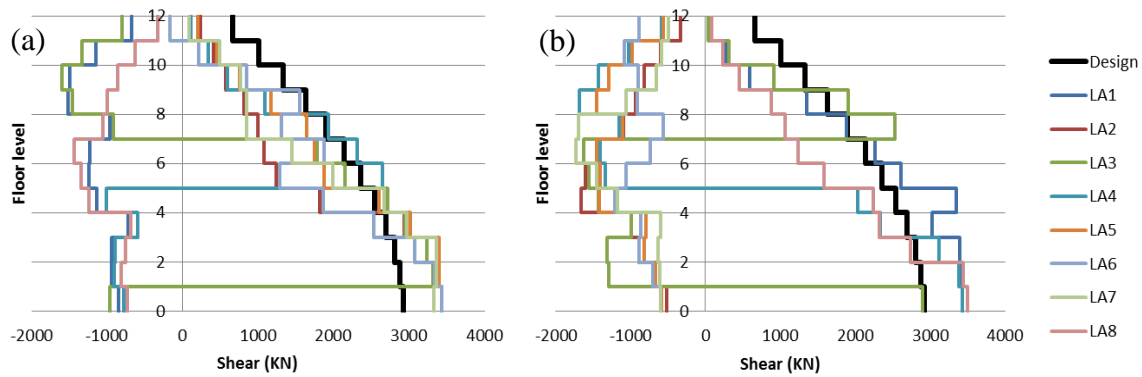


Figure 7.26: 12-storey CBF shear force design values compared to shear at the maximum displacement from NLTH using artificially adjusted earthquakes resisted by (a) first brace and (b) second brace. Negative sign represents compression resistance and positive sign represents tension.

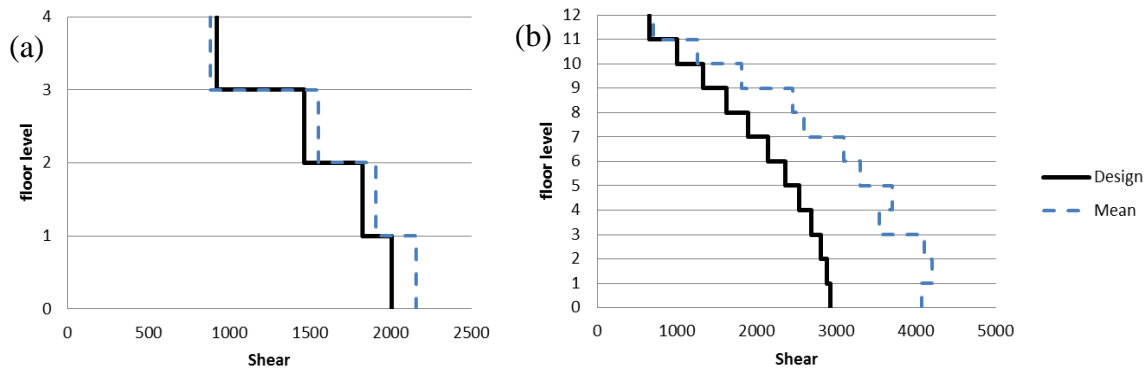


Figure 7.27: Average total shear forces resisted by both compression and tension braces from NLTH using artificially adjusted earthquakes compared to the design shear forces of (a) 4-storey CBF (b) 12-storey CBF.

7.5 Design of CBFs according to FBD

In this section an investigation of the seismic performance of CBFs is carried out when designed according to the forced based design (FBD) approach outlined in EC8 (CEN 2004) and explained in Section 2.6. To do this, the case study 4-storey CBF building detailed in Section 7.3 is re-designed using FBD approach, and then the performance is gauged with NLTH analyses and compared with the DDBD solution.

7.5.1 Design response spectrum and seismic forces

EC8 (CEN 2004) type 1 elastic response spectrum for soil type C and peak ground acceleration (PGA) of 0.3g is chosen. The importance factor γ_I for ordinary building is taken as 1, as shown in Table 1.1. Therefore, the design ground acceleration on type C ground ($a_g = \gamma_I a_{gR}$) is 0.3g.

The fundamental period of vibration of the building for lateral motion in the direction considered, T_1 , can be found by the following:

$$T_1 = C_t H^{3/4} \quad [7.35]$$

where C_t is 0.050 for CBFs and H is the height of the building, in metres, from the foundation or from the top of a rigid basement. The height of the building is 12m, and, thus, T_1 is equal to

$$T_1 = 0.05 * 12^{(3/4)} = 0.32 \text{ sec.} \quad [7.36]$$

To take into account the capacity of the structure to dissipate energy, FBD uses the design spectrum, S_d . This can be obtained by reducing the ordinates of the reference elastic spectrum, S_e , by means of a behaviour (reduction) factor, q , which allows for the ductility expected for the structural system. EC8 (CEN 2004) specify a value of 4 for the behaviour factor, q , for diagonal CBFs. From Table 2.4, the values of the periods T_B , T_C , T_D and the soil factor S describing the shape of the elastic response spectrum for ground type C for type 1 are found and summarised in Table 7.7.

Table 7.7: Values of the parameters describing the recommended Type 1 elastic response spectra for ground type C, EC8 (CEN 2004).

Ground Type	S	T_B	T_C	T_D
C	1.15	0.20	0.6	2.0

As $T_B \leq T_1 \leq T_C$, then the ordinate of the design spectrum at period T_1 is as follows

$$S_d(T_1) = a_g * S * \frac{2.5}{q} = 0.3 * 9.81 * 1.15 * \frac{2.5}{4} = 2.12 \text{ m/s}^2 \quad [7.37]$$

The seismic base shear, F_b , can be found by the following

$$F_b = S_d(T_1) \cdot m \cdot \lambda \quad [7.38]$$

where m is the total mass of the building above the foundation or above the top of a rigid basement, which is computed as the addition of the gravity dead load and 0.3 of the gravity live load. λ is the correction factor, the value of which is equal to 0.85 if $T_1 < 2T_c$ and the building has more than two storeys, where T_c is the upper limit of the period of the constant spectral acceleration branch, or $\lambda = 1.0$ otherwise. The seismic base shear, F_b , for the case study is as follows

$$F_b = 2.12 * 1843.2 * 0.85 = 3314 \text{ KN} \quad [7.39]$$

When the fundamental mode shape is approximated by horizontal displacements increasing linearly along the height, the horizontal forces, F_i , can be given at each storey i as follows:

$$F_i = F_b \frac{m_i z_i}{\sum m_j z_j} \quad [7.40]$$

where z_i, z_j are the heights of the masses m_i, m_j above the level of application of the seismic action. Storey forces and design shear are shown in Table 7.8.

Table 7.8: Storey forces and design shear for the 4-storey case study structure.

Level	Height (m)	Mass, m_i (ton)/frame	$m_i z_i$ (ton.m)	F_i (kN)	V_i (kN)
4	12	460.8	5530	1326	1326
3	9	460.8	4147	994	2320
2	6	460.8	2765	663	2983
1	3	460.8	1382	331	3314
Sum		1843.2	13824	3314	

7.5.2 Design of braces

EC8 (CEN 2004) assumes that storey shear at all floor levels are entirely resisted by axial forces in braces and only tension diagonal bracings resisting the shear forces. Thus, the axial force in the brace, $N_{Ed,i}$, is found by the following

$$N_{Ed,i} = \frac{V_i}{\cos\alpha} \quad [7.41]$$

where V_i is the floor shear assigned to the brace and α is the angle of the brace with the horizontal. The brace area is found by dividing the axial force in the brace, $N_{Ed,i}$, by the yield strength, f_y , which is taken as 355N/mm^2 in this case study. All braces are chosen to be Class 1 with a slenderness ratio $\bar{\lambda} \leq 2$, as suggested by EC8 (CEN 2004), where slenderness ratio, $\bar{\lambda}$, is found by

$$\bar{\lambda} = \frac{L_{cr}}{i} \frac{1}{\lambda_1} \quad [7.42]$$

where L_{cr} is the length of the brace, i is radius of gyration and $\lambda_1 = 93.9\varepsilon$, where $\varepsilon = \sqrt{235/f_y}$.

A check for the brace overstrength, Ω , is carried out as the following

$$\Omega_i = \frac{N_{pl,Rd,i}}{N_{Ed,i}} \quad [7.43]$$

where $N_{pl,Rd,i}$ is the design resistance of diagonal i and $N_{Ed,i}$ is the design value of the axial force in the same diagonal i in the seismic design situation. This check is carried out assuring that it satisfies the EC8 (CEN 2004) requirements that the maximum brace overstrength does not differ from the minimum value by more than 25% in order to satisfy the homogeneous dissipative behaviour of the diagonals, as shown in Table 7.9.

Table 7.9: Calculation of brace axial forces and the design of brace elements.

level	$N_{Ed,i}$ (kN)	proposed area, A_b (cm ²)	section size	$\bar{\lambda}$	Real A_b (cm ²)	$N_{pl,i}$ (kN)	Ω_i
4	1657	46.68	140X140X10	1.26	48.6	1725	1.04
3	2900	81.68	200X200X12	0.87	84.1	2986	1.03
2	3728	105.02	250X250X12	0.69	108	3834	1.03
1	4143	116.69	300X300X12	0.56	132	4686	1.13

7.5.3 Beams and columns design

Columns and beams are capacity designed to behave elastically ensuring that dissipative behaviour is provided primarily by the braces. This is achieved by following the combination from EC8 (CEN 2004). Thus, equations from [7.32] to [7.34] are employed in the design of columns and beams from EC8 (CEN 2004).

The selected beams and columns for the 4-storey building under consideration are shown in Table 7.5.

Table 7.10: Column and Beam designed sections from capacity design principles.

Level	Columns	Beams
4	HD 320X127	HE 320 B
3	HD 400X237	HE320 M
2	HD 400X287	HE 340 M
1	HD 400X314	HE 400 M

7.5.4 Inter-storey drift limitation

EC8 (CEN 2004) suggests that the displacements induced by the design seismic action shall be calculated on the basis of the elastic deformations of the structure by the following expression:

$$d_s = q_d \cdot d_e \quad [7.44]$$

where d_s is the displacement of a point of the structure induced by the design seismic action, q_d is the displacement behaviour factor assumed equal to q , d_e is the elastic displacement of the same point of the structure.

The elastic displacement is found using the software SAP2000 (SAP2000 2002). The design lateral displacement, d_s , is found from Equation [7.44] and as shown in Table 7.11.

Table 7.11: Calculations of elastic displacement, design displacement and drift.

Level	d_e (m)	d_s (m)	Drift (%)
4	0.0302	0.1208	0.97
3	0.0229	0.0916	1.08
2	0.0148	0.0592	1.04
1	0.007	0.028	0.93

From Table 7.11 it is found that the design drift is less than the maximum allowable drift assumed (2.5% which was used for the DDBD). Therefore, the sections sizes found using FBD are acceptable.

7.5.5 P-Δ effect

EC8 (CEN 2004) suggests that P-Δ effects need not be taken into account if the following condition is fulfilled in all storeys

$$\theta = \frac{P_{tot} d_r}{V_{tot} h} \leq 0.1 \quad [7.45]$$

where θ is the inter-storey drift sensitivity coefficient, P_{tot} is the total gravity load at and above the storey considered in the seismic design situation, d_r is the design inter-storey drift, d_r , and evaluated as the difference of the lateral displacements d_s at the top and bottom of the storey under consideration, V_{tot} is the total seismic storey shear and h is the inter-storey height.

EC8 (CEN 2004) suggests that if $0.1 < \theta \leq 0.2$, the P-Δ effects may approximately be taken into account by multiplying the relevant seismic action effects by a factor equal to $1/(1 - \theta)$. The maximum acceptable value of the coefficient θ is 0.3.

Calculations of the inter-storey drift sensitivity coefficients, θ , are shown in Table 7.12 for each level of the building. It is found that θ is less than 0.1 for all storeys, so it is not necessary to take into account P-Δ effects.

Table 7.12: Calculation of the inter-storey drift sensitivity coefficient

Level	P_{tot}	V_{tot}	d_r	θ
4	460.80	1325.62	0.0292	0.003
3	921.60	2319.84	0.0324	0.004
2	1382.40	2982.65	0.0312	0.005
1	1843.20	3314.05	0.028	0.005

7.6 Comparison of FBD approach with DDBD and NLTHA

In this section a comparison is carried out between the 4-storey structure designed using the DDBD approach in Section 7.3 with that designed using the FBD approach in Section 7.5. Furthermore, the predicted performance of the structure designed using the FBD approach will be obtained using NLTHA and salient response parameters are discussed.

The NLTHA numerical model used to verify the DDBD procedure is used here to verify the FBD approach. Eight artificially adjusted accelerograms from four different earthquakes (2 components in orthogonal direction for each earthquake) taken from Pennucci et al. (2009) are used in the NLTHA, as outlined in Section 4.3.1.

Time history accelerograms are scaled to get a displacement response spectrum that matches the soil type C design displacement spectrum with 5% damping from EC8 (CEN 2004), which was used in the FBD approach for the case study. Response spectra for the scaled accelerograms are found using the programme SeismoSignal (SeismoSoft 2007) for the elastic response spectra with 5% damping, as shown in Figure 4.13 and Figure 4.14.

When comparing the 4-storey case study designed using both the DDBD and FBD approaches, it is found that the seismic base shear, F_b , from the FBD is larger than the base shear obtained from DDBD. This leads to the use of bigger sections for the structure designed by FBD approach to resist the lateral forces. Because of that, the lateral displacements the structure endures in the FBD approach are less than the design lateral

displacements used to design the structure in DDBD approach. Furthermore, the larger base shear forces experienced in the structure designed using the FBD approach will lead to higher demands on foundations.

The maximum floor displacements are found during nonlinear time-history analyses for the eight artificially adjusted accelerograms for the 4-storey case study. These are compared with the design displacement profile obtained from the FBD approach and the displacement profile used in DDBD, as shown in Figure 7.28. Similarly, the average of the maximum recorded displacement during time-history analyses for the eight artificially adjusted accelerograms and the design displacement profile from DDBD and the displacement profile obtained from FBD are shown in Figure 7.29. It is apparent that the maximum displacements recorded from the time history analyses and from the FBD approach are less than the linear design displacements assumed for the DDBD procedure.

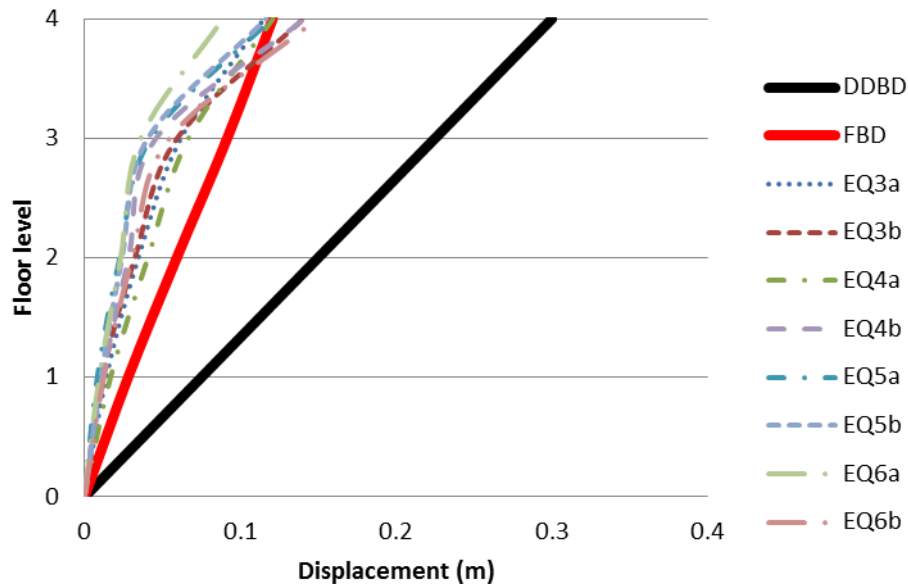


Figure 7.28: Maximum recorded displacements for eight spectrum compatible accelerograms compared with the design displacements used for the DDBD and the displacements obtained from FBD approach for a 4-storey CBFs.

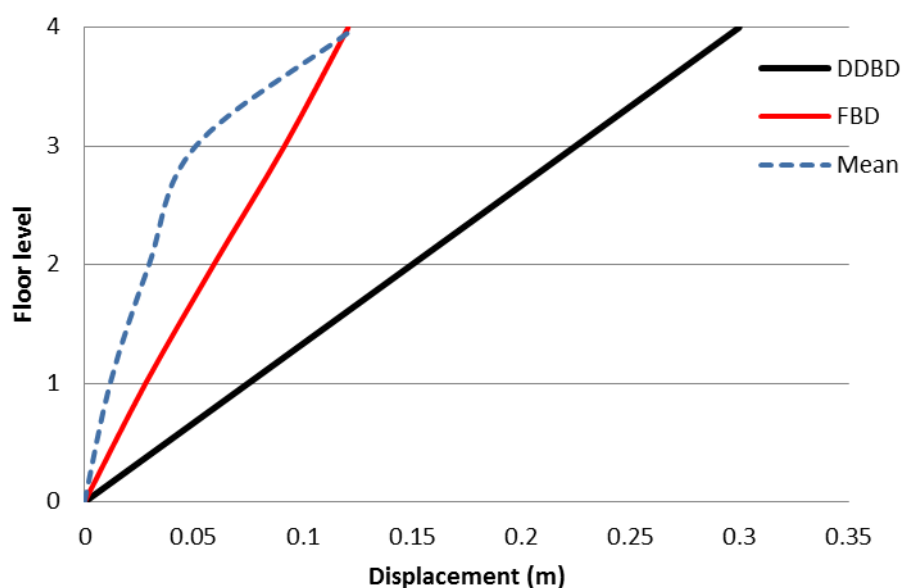


Figure 7.29: Average of the maximum recorded displacements for eight spectrum compatible accelerograms compared with the design displacements used for the DDBD and the displacements obtained from FBD approach for a 4-storey CBFs.

The average of the maximum storey drifts recorded during time-history analyses using the eight accelerograms compared with the linear displacement design drift profile assumed for the case study and the drift profile obtained for FBD are shown in Figure 7.30. It is found that the average of the maximum recorded storey drifts for the eight artificially adjusted accelerograms for the 4-storey building are less than the design storey drift profile obtained from FBD and used in DDBD for the first 3 storeys. This is due to the design assumption that the tension brace member only is assumed to contribute to the lateral resistance of the system. On the other hand, the drift obtained from the NLTHA was more than the design drift for the top storey due to higher mode effects. Because of that and in order to take into account the higher modes effect, 10% of the base shear force should be allocated for to the roof level and the remaining 90% of the base shear force should be distributed to all floor levels including the roof in proportion to the product of mass and displacement as shown in Equation [7.19] as suggested by Priestley et al. (2007). This is the approach taken in the DDBD method outlined in Section 7.2.

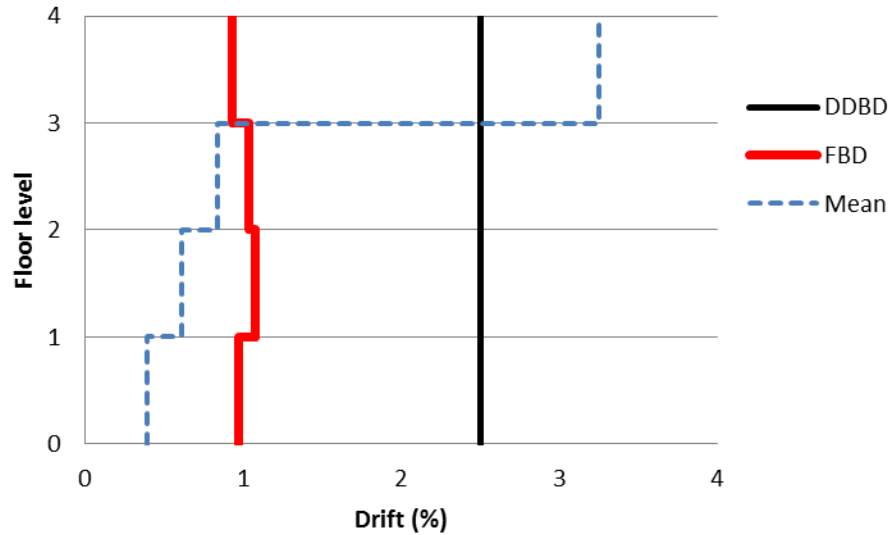


Figure 7.30: Average of the maximum recorded storey drifts for eight spectrum compatible accelerograms compared with the design storey drifts used for the DDBD and the drifts obtained from FBD approach for the 4-storey CBFs.

The maximum recorded ductility values are found during nonlinear time-history analyses for the eight artificially adjusted accelerograms for the 4-storey CBF. These are compared with the design ductility values obtained from the DDBD and FBD method as shown in Figure 7.31. It is found that the maximum ductility demand estimated from the time history analyses for the case study is in general very close to the ductility found from FBD approach and less than the ductility used in the DDBD. This is due to the larger section sizes required in the structure designed using the FBD approach.

The average of the maximum recorded ductility during time-history analyses for the eight artificially adjusted accelerograms is shown in Figure 7.32 for the case study building. This is compared to the design ductility obtained from the FBD and the DDBD methods, as well as ductility expressions established by Nip et al. (2010) for hot-rolled and cold-formed steel shown in Equations [2.6] and [2.7], respectively and ductility expression established by Tremblay (2002) shown in Equation [2.2]. It is apparent that the average of the maximum ductility values recorded from the time history analyses for the case study building are close to the design ductility obtained from FBD and lower than the design ductility from the DDBD method and ductility expressions established by Nip et al. (2010) and Tremblay (2002).

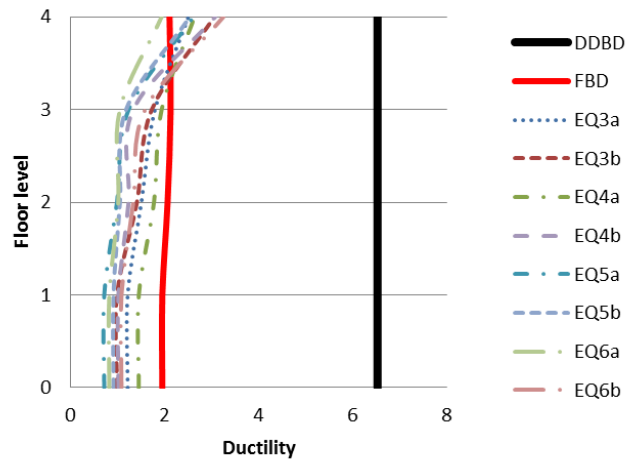


Figure 7.31: Maximum recorded ductility for eight spectrum compatible accelerograms compared with the design ductility from DDBD and FBD method for the 4-storey CBFs.

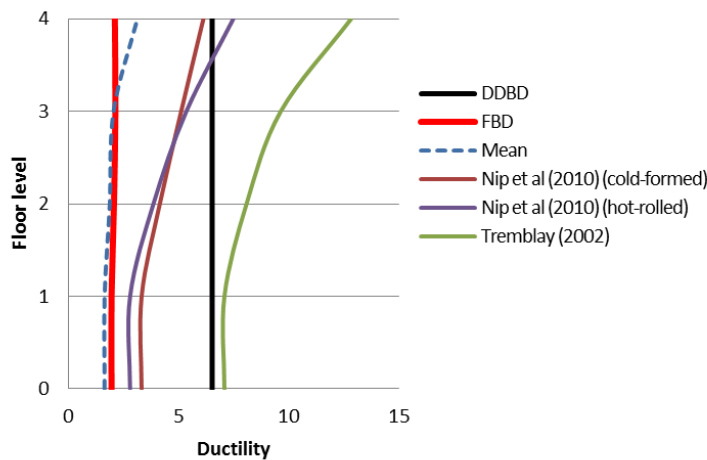


Figure 7.32: Average of the maximum recorded ductility for eight spectrum compatible accelerograms compared to the design ductility from DDBD and FBD approach, ductility expressions of Nip et al (2010) for cold-formed and hot-rolled carbon steel and ductility expression of Tremblay (2002) for the 4-storey CBFs.

The design base shear was distributed to the floors by Equation [7.40] and assumed to be resisted by tension braces only in the FBD case study building. Compression members were assumed not to resist any load as suggested by EC8 (CEN 2004). The design shear force from the FBD procedure and the shear force resisted by every brace at the instance when maximum displacement occurs in the NLTHA for the 4-storey CBF structure are

shown in Figure 7.33. As discussed previously in the DDBD approach, the compression member braces also resisting lateral forces. The mean of the shear forces resisted by both of the braces at the maximum displacement demand during the eight earthquakes are compared to the design shear forces in Figure 7.34 for the 4-storey building.

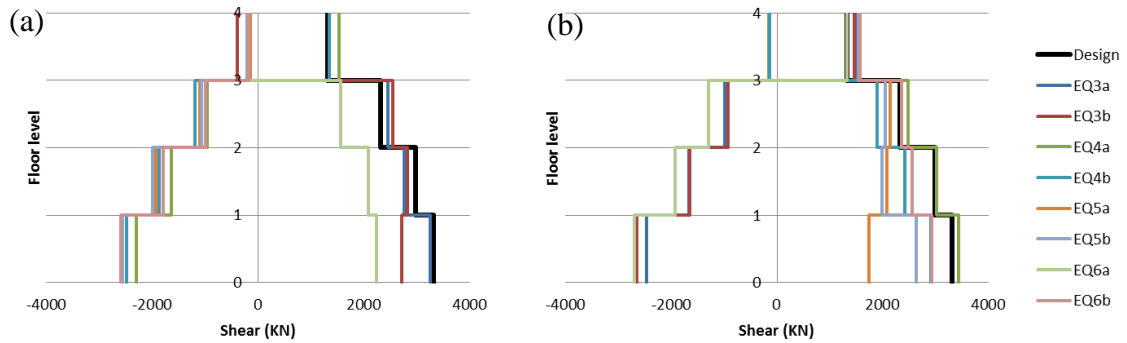


Figure 7.33: 4-storey CBF shear force design values compared to shear at the maximum displacement from NLTHA using artificially adjusted earthquakes resisted by (a) first brace and (b) second brace. Negative sign represents compression resistance and positive sign represents tension.

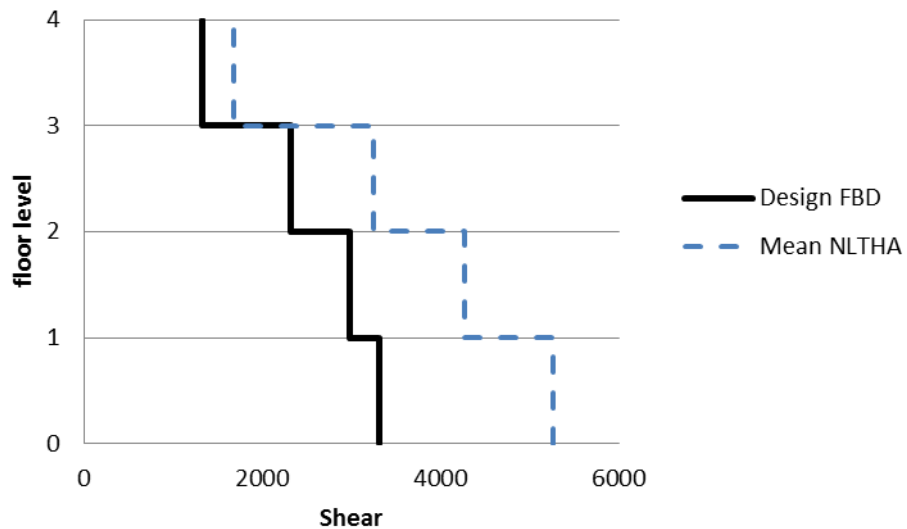


Figure 7.34: Average total shear forces resisted by both compression and tension braces from NLTHA using artificially adjusted earthquakes compared to the design shear forces obtained from FBD approach for the 4-storey CBF.

7.7 Summary and conclusion

A DDBD methodology for steel multi-storey CBFs has been validated. A linear displacement profile shape was found to give conservatively adequate approximation for the displaced shape of multi-storey CBFs. In this design methodology, columns and beams were capacity designed to behave elastically and all the lateral forces were considered to be resisted by tension brace members only. Columns were chosen to be continuous along the building height and pinned at the base. The connections between columns and beams were considered to be pinned. Furthermore, bracing end conditions were considered to be pinned in both ends.

Two case studies of 4-storey and 12-storey CBFs were carried out to verify the DDBD procedure. NLTHA, which was advanced using shake table tests for real one-storey-one-bay CBFs, was used to check the validity of the method on the case studies using two different sets of earthquakes. Each set consists of eight different accelerograms with displacement spectra matching the design displacement spectrum. In the first set, artificially adjusted earthquakes were used. In the second set, real earthquakes were used. The results indicated that the method is conservative for displacement shapes and storey drifts. Brace ductility results were satisfactory and total shear forces resisted by tension and compression members obtained from NLTHA were found to be greater than the design shear forces as the compression members contributed also in resisting the seismic lateral forces.

An investigation of the forced based design (FBD) approach of CBFs is carried out using EC8 (CEN 2004). A case study of 4-storey CBF building is designed using FBD approach, and then the performance is gauged with NLTH analyses and compared with the DDBD solution. The results showed that FBD approach gives larger section sizes for the same earthquake demand on the building. This leads to lower displacement shapes and storey drifts than the DDBD approach. Moreover, the NLTHA indicated that FBD is conservative for displacement shapes and storey drifts for all storeys except the top floor which leads to the need of taking into account the higher mode effects on FBD. Total shear forces resisted by tension and compression members obtained from NLTHA were

found to be greater than the design shear forces obtained from FBD, as the compression members contributed also in resisting the seismic lateral forces.

Chapter 8

Summary, conclusions and future work

8.1 Introduction

This chapter summarises the findings and conclusions from the study and discusses areas which may need further investigation in future work. This dissertation had five specific goals. These were to 1) validate a numerical model for brace members by using pseudo-static cyclic tests; 2) validate a fatigue model to be used for bracing members; 3) develop an improved numerical model for single-degree-of-freedom concentrically braced frames by using shake table tests and non-linear time history analysis; 4) develop a DDBD procedure for single-degree of freedom concentrically braced frames and validate it using shake table tests and non-linear time history analysis; 5) develop a DDBD procedure for multi-storey concentrically braced frames and validate it using non-linear time history analysis.

8.2 Summary and conclusions

This section gives a brief summary of the previous chapters which shows significant improvements to the understanding of CBF behaviour and existing design methodologies.

8.2.1 Validating of a numerical model for steel brace members incorporating a fatigue model

The behaviour of braces, which are the main elements to dissipate energy in concentrically braced frames, is studied. A numerical model is developed and found to be capable of simulating the hysteretic behaviour of braces. Nonlinear beam-column

elements with distributed plasticity are used where the cross section of the brace is divided into fibres along the perimeter and across the thickness. It was found that dividing the brace into a minimum of two elements using ten integration points per element was most appropriate for this model. An initial camber on the middle of the brace is used to instigate the overall buckling. A value between 0.1 and 1% of the length of the brace was found to give the most accurate prediction of the first buckling load when compared to physical test data. A low cyclic fatigue model with new parameters is also proposed and is used to wrap the fibre-based nonlinear beam-column element in order to capture fracture in the braces. It has been shown in this study that this model can accurately predict the maximum displacement ductility demand of the brace members when fracture occurs.

In general, good agreement was found between the main response parameters of the numerical and physical tests, including the maximum tensile force (F_{\max}), initial buckling load (F_c), number of cycles to fracture, the total energy dissipated by the specimens (W_{tot}) and the energy dissipated by the specimens at the first cycle of ductility of four ($W_{\mu=4}$). However, there was a difference in the response between the numerical model and some tests in the post buckling range and the hysteretic loops were fatter. One possible reason for this is that the model does not account for local buckling and this should be taken into account in future research.

8.2.2 Validation of NLTHA model for single storey CBFs

The developed numerical model simulating the real behaviour of braces is extended to represent a single storey CBF system. This model is validated by shake table tests and a large range of nonlinear time history analyses (NLTHA). The experimental response of single-storey concentrically braced frames (CBFs) to earthquakes measured in real-time shake table tests was compared with the results of NLTHA. The test frames considered a range of brace slenderness. Furthermore, in the NLTHA four of the test frames were subjected to eight earthquake records that had been scaled to the record used in the shake table tests.

The comparison of experimental and numerical results showed that the use of inelastic fibre elements with a bilinear material relationship to represent the behaviour of bracing members leads to accurate modelling of the response of brace elements to earthquake excitations. The model captured the displacement response, the axial forces, energy dissipated and the equivalent viscous damping relatively well.

The prediction of structural collapse using earthquake analysis relies upon an accurate assessment of structural displacements, leading to a quantification of the ductility demand experienced by dissipative elements such as bracing members. This study has highlighted the sensitivity of the response of concentrically braced frames to the earthquake input motion, even when the accelerograms are scaled to have compatible displacement response spectrums.

It is important that numerical models used to develop seismic design methodologies are validated through full scale experimental testing. The results of this study suggest that the equivalent viscous damping values developed by Wijesundara (2009) can be used in the direct displacement based design (DDBD) of single storey CBFs.

There is a strong role to be played by NLTHA in providing parametric studies for examining the likely response of different structural configurations to a variety of ground motions. The comparative assessments presented in this work indicate that numerical tools which incorporate material and geometric nonlinearities can largely capture the main features related to the seismic behaviour of CBF systems. Particular attention should however be placed on interpreting the inter-storey drift results in time-history analyses by careful consideration of material idealisation and characteristics of the selected seismic excitations.

8.2.3 DDBD for single storey CBFs

A direct displacement based design (DDBD) procedure for single-storey concentrically braced frames (CBFs) was presented. DDBD was performed for all the shake table tests with a target displacement equal to the maximum displacement from the shake table tests. It was found that the estimated base shear forces and the required brace cross sectional

sizes predicted by the DDBD methodology match very closely to the actual values obtained from shake table tests.

The numerical model employed in NLTHA of single storey CBFs and validated using shake table tests was also used to verify the DDBD methodology. This was achieved by subjecting each CBF to eight different accelerograms scaled to have displacement spectrum equal to displacement spectrums used for the DDBD. It was found that the average of the displacements and base shear obtained from NLTHA and those obtained from DDBD are very similar.

Thus, the DDBD methodology presented in this chapter has been shown to give accurate and reliable results, which was proved by comparing them to data from shake table tests and a large range of NLTHA.

8.2.4 DDBD for multi-storey CBFs

The DDBD procedure developed for single storey steel CBF systems was then further developed for multi-storey steel CBF systems. This procedure was validated using NLTHA of two case study buildings. A linear displacement profile shape was found to give a conservatively adequate approximation for the displaced shape of CBFs. In this design methodology, columns and beams were capacity designed according to EC8 (CEN 2004) to behave elastically and all the lateral forces were considered to be resisted by tension member braces only. Columns were chosen to be continuous along their height and pinned at the base. The connections between columns and beams are considered to be pinned. Furthermore, bracing end conditions are considered to be pinned at both ends.

Two case studies of 4-storey and 12-storey CBF buildings were carried out. NLTHA, advanced using shake table tests for real one-storey-one-bay CBFs, was used to check the validity of the method on the case studies using two different sets of earthquakes. Each set consisted of eight different accelerograms with displacement spectra matching the design displacement spectrum. In the first set artificially adjusted earthquakes were used. In the second set real earthquakes were used. The results indicated that the method is conservative for displacement shapes and storey drifts. Total shear forces resisted by

tension and compression members obtained from NLTHA were found to be more than the design shear forces as the compression members also contributed in resisting the seismic lateral forces.

An investigation of the forced based design (FBD) approach of CBFs is carried out using EC8 (CEN 2004). A case study of 4-storey CBF building is designed using FBD approach, and then the performance is gauged with NLTH analyses and compared with the DDBD solution. The results showed that FBD approach gives larger section sizes for the same earthquake demand on the building. This leads to lower displacement shapes and storey drifts than the DDBD approach. Moreover, the NLTHA indicated that FBD is conservative for displacement shapes and storey drifts for all storeys except the top floor which leads to the need of taking into account the higher mode effects on FBD. Total shear forces resisted by tension and compression members obtained from NLTHA were found to be greater than the design shear forces obtained from FBD, as the compression members contributed also in resisting the seismic lateral forces.

8.2.5 Potential impact of this research project

A robust numerical model incorporating a fatigue model for CBF systems has been developed. This numerical model gave accurate simulation of the response of CBFs to strong earthquake loading. It can be used by researchers and designers to predict the real behaviour of CBF systems. Furthermore, this model can be used to represent different configurations of CBFs.

CBFs are widely employed in many regions of Europe, and are frequently relied upon to provide adequate earthquake resistance for buildings and other structures. This implies that their design, construction and seismic performance have important consequences for public safety during seismic events. However, recent research has shown that current design practice for these structures may lead to sub-optimum seismic performance. This has implications for new construction and for the assessment of existing buildings. The DDBD procedure validated in this work can be used by engineers to design CBFs in seismic regions. This design methodology is simple to apply and provides reliable and satisfactory displacement solutions to seismic design problems.

8.3 Future work

The research presented herein focussed on the general behaviour and design of CBFs. Many details, factors, and configurations can be added and taken into account in future research. These include:

1. A beam-column brace model that can take into account local buckling should be developed. This can be achieved by developing a numerical model that wraps around the parental material. The concept for this model is similar to the fatigue model presented in this thesis, in so far as it does not affect the properties of the parental material. It captures local buckling by reducing the capacity of the parental material where local buckling is detected. Moreover, this can be achieved by incorporating modified zero length elements that represent the expected local buckling behaviour in the vulnerable locations of the brace to local buckling.
2. The development of an accurate node, or zero length element, that represents the real behaviour of brace connections, such as gusset plates, that can be incorporated into the physical theory model.
3. The work presented herein used a limited number of shake table tests. Further shake table tests on CBFs are planned for the BRACED project, which is part of an EU FP7 TNA programme known as SERIES (Broderick 2010). These are expected to be carried out on the Azalee shake table at the Tamaris facility in CEA, Saclay in August 2012. These shake table tests will expand the rich source of physical experimental data on the behaviour of brace elements to real-time earthquake loadings. Additional features of these tests to those carried out by Elghazouli et al (2005) include realistic end connections (e.g. gusset plates), a broader range of normalised slenderness ratios and larger displacement demands on the CBF system. Furthermore, accurate data acquisition systems that can record the local and global deformations of the brace behaviour in real-time will be employed. Thus, this data can be used to develop and validate numerical models, such as that identified in item 1 above.

4. Numerous additional case studies and CBF configurations should be investigated, especially buildings containing irregularities in plans and vertical structural configurations. Many types of structures can feature irregularities due to functional, aesthetic, or economic reasons.
5. Development and investigation of guidelines for the capacity design of CBF systems must be carried out.
6. An investigation of the behaviour of CBF structures should be carried out for the cases of irregular structures with a view to developing appropriate performance based design guidance for these configurations.
7. Residual drifts should be accounted for in the seismic design methodology, as they could be important performance parameters for CBF systems.
8. A dual system of concentrically braced frames and moment resisting frames are often used to resist the seismic actions. Thus, a study on their behaviour and the verification of suitable DDBD procedure for these systems could be carried out.
9. The development of robust and reliable analysis and design methodologies for retrofitting existing buildings with CBF systems in order to improve their sustainability and reliability in earthquakes.

References

- ABAQUS (2006). User manual, version 6.5. Hibbitt, Karlsson and Sorensen Inc.
- AISC (2005). Seismic provisions for structural steel buildings. Chicago (IL), American Institute of Steel Construction.
- Andreas, U. and P. Gaudenzi (1989). "Modeling of Cyclic Behavior of Steel Braces." International Journal of Structural Mechanics and Materials Science **26**(3): 267–288.
- ANSYS (2002). Version 6.1, ANSYS Inc.
- Antoniou, S. and R. Pinho (2004). "DEVELOPMENT AND VERIFICATION OF A DISPLACEMENT-BASED ADAPTIVE PUSHOVER PROCEDURE." Journal of Earthquake Engineering **8**(5): 643-661.
- Archambault, M. H. (1995). Etude du comportement séismique des contreventements ductiles en X avec profils tubulaires en acier, EPM/GCS-1995-09, Department of Civil Engineering, école Polytechnique, Montréal, Que.
- ARUP (2007). A Guide to the Match Graphical User Interface. Match User Manual. London, UK.
- ASCE (2006). Minimum design loads for buildings and other structures. ASCE Standard ASCE/SEI 7-05. A. S. o. C. Engineers. Reston, Virginia.
- Astaneh-Asl, A., S. Goel and R. D. Hanson (1985). Cyclic out-of-plane buckling of double-angle bracing, ASCE Jtpl/rllt;f of structural Engineering. **111**(5): 1135-1153.
- Astaneh-Asl, A. and S. C. Goel (1984). "Cyclic in-plane buckling of double-angle bracing." J Struct Engng, ASCE **109**: 2036–2055.
- ASTM (2003). ASTM E-1049 -Standard Practices for Cycle Counting in Fatigue Analysis. West Conshohocken, PA.
- ASTM (2005). E 1049-85, Standard practices for cycle counting in fatigue analysis, ASTM International.
- Ballio, G. and F. Perotti (1987). "Cyclic Behavior of Axially Loaded Members - Numerical-Simulation and Experimental-Verification." Journal of Constructional Steel Research **7**(1): 3-41.

- Black, G. R., B. A. Wenger and E. P. Popov (1980). Inelastic Buckling of Steel Struts Under Cyclic Load Reversals, UCB/EERC-80/40, Earthquake Engineering Research Center, Berkeley, CA.
- Blandon, C. A. and M. J. N. Priestley (2005). "EQUIVALENT VISCOUS DAMPING EQUATIONS FOR DIRECT DISPLACEMENT BASED DESIGN." Journal of Earthquake Engineering **9**(sup2): 257-278.
- Broderick, B. M. (2010). Improved european design and assessment method of concentrically braced frames (BRACED), seismic engineering research infrastructures for european synergies series. E. C. 7th Framework Programme. Dublin, Ireland.
- Broderick, B. M., A. Y. Elghazouli and J. Goggins (2008). "Earthquake testing and response analysis of concentrically-braced sub-frames." Journal of Constructional Steel Research **64**: 997-1007.
- Broderick, B. M., J. M. Goggins and A. Y. Elghazouli (2005). "Cyclic performance of steel and composite bracing members." Journal of Constructional Steel Research **61**(4): 493-514.
- Bruneau, M., C. Clifton, G. A. MacRae, R. Leon and A. Fussell. (2011). "Steel Building Damage from the Christchurch Earthquake of February 22, 2011, NZST." MCEER Information Service. http://mceer.buffalo.edu/research/Reconnaissance/New_Zealand2-21-11/CHCH_EQ_Steel_damage_2011-03-11.pdf.
- Bruneau, M., C. M. Uang and A. Whittaker (1998). "Ductile Design of Steel Structures." McGraw-Hill, Boston.
- Bungale, S. T. (2004). Wind and Earthquake Resistant Buildings Structural Analysis and Design. Boca Raton, FL., CRC Press.
- California State University Northridge. (1994). "Oviatt Library earthquake damage, 1994 ", from <http://digital-library.csun.edu/u?/SFVH,1643>.
- Calvi, G. M. and T. J. Sullivan (2009). Development of a Model Code for Direct Displacement Based Seismic Design. G. Manfredi, M. Dolce (eds), The state of Earthquake Engineering Research in Italy: the ReLUIIS-DPC 2005-2008 Project. Napoli, Italy.
- Calvi, G. M. and T. J. Sullivan (2009). A model code for the Displacement-Based Seismic Design of Structures. Pavia, Italy, IUSS Press.
- Celik, O., C., J. W. Bermnn and M. Bruneau (2004). Cyclic testing of braces laterally restrained by steel studs to enhance performance during earthquakes. New York, MCEER-04-0003, Multidisciplinary Center for Earthquake Engineering Research, Buffalo,.
- CEN (1997). Cold formed welded structural hollow sections of non-alloy and fine grain steels. 1. Technical delivery requirement. 2. Tolerances, dimensions & section properties., EN10219-1:1997.
- CEN (1998). Eurocode 8, design of structures for earthquake resistance – Part 1: General rules, seismic actions and rules for buildings, Pr-EN 1998-1. Draft.
- CEN (2004). Eurocode 1.General actions. Part 1-1: Densities, self-weight, imposed loads for buildings. EN 1991-1-1.
- CEN (2004). Eurocode 8, design of structures for earthquake resistance – Part 1: General rules, seismic actions and rules for buildings, EN 1998-1:2004/AC:2009.
- CEN (2005). Eurocode 3: Design of steel structures - Part 1-1: General rules and rules for buildings, EN 1993-1-1:2005/AC:2009.

- CEN (2006). Eurocode 3 - Design of steel structures - Part 1-3: General rules - Supplementary rules for cold-formed members and sheeting, EN 1993-1-3:2006/AC:2009.
- Chopra, A. K. and R. K. Goel (2001). "Direct displacement-based design: use of inelastic design spectra versus elastic design spectra." Earthquake Spectra **17**(1): pp 47-65.
- Coffin, L. (1954). "A study of the effect of cyclic thermal stresses on a ductile metal." Trans ASME 1954;76:931-50.
- Della Corte, G., R. Landolfo and F. M. Mazzolani (2010). "Displacement-based seismic design of braced steel structures." Steel Construction **3**(3): 134-139.
- Della Corte, G. and F. M. Mazzolani (2008). Theoretical developments and numerical verification of a displacement-based design procedure for steel braced structures. 14th World Conference on Earthquake Engineering, Beijing, China.
- Duggan, T. V. and J. Byrne (1977). Fatigue as a design criterion, The Macmillan press LTD.
- ECCS (1986). —Technical Committee 1. Structural Safety and Loadings—Technical Working Group 1.3. Seismic design recommended testing procedure for assessing the behaviour of structural steel elements under cyclic loads, 1st ed. Brussels; 1986.
- Elchalakani, M., X.-L. Zhao and R. Grzebieta (2003). "Tests of Cold-Formed Circular Tubular Braces under Cyclic Axial Loading." Journal of Structural Engineering **129**(4): 507-514.
- Elghazouli, A. Y., B. M. Broderick, J. Goggins, H. Mouzakis, P. Carydis, J. Bouwkamp and A. Plumier (2005). "Shake table testing of tubular steel bracing members." Proceedings of the Institution of Civil Engineers-Structures and Buildings **158**(4): 229-241.
- Elnashai, A. S. and L. Sarno (2008). Fundamentals of Earthquake Engineering, John Wiley & Sons.
- EM-DAT (2011). The OFDA/CRED International Disaster Database. Universite catholique de Louvain, Brussels, Belgium.
- Encyclopædia Britannica. (2010). "Mexico City earthquake of 1985." from <http://www.britannica.com/EBchecked/topic/1421132/Mexico-City-earthquake-of-1985>.
- Fell, B. V., A. M. Kanvinde, G. G. Deierlein and A. T. Myers (2009). "Experimental investigation of inelastic cyclic buckling and fracture of steel braces." Journal of Structural Engineering **135**(1): 19-22.
- Filippou, F. C. and G. L. Fenves (2004). Methods of analysis for earthquake-resistant structures, Chapter 6 in Earthquake Engineering: From Engineering Seismology to Performance-Based Engineering.
- Fisher, J., G. Kulak and I. Smith (1997). A fatigue primer for structural engineers. ATLSS Report No. 97-11.: National Steel Bridge Alliance, AISC. Chicago, IL.
- Foutch, D. A., S. C. Goel and C. W. Roeder (1987). "Seismic Testing of Full-Scale Steel Building---Part I." Journal of Structural Engineering **113**(11): 2111-2129.
- Fukuta, T., I. Nishiyama, H. Yamanouchi and B. Kato (1989). "Seismic Performance of Steel Frames with Inverted V Braces." Journal of Structural Engineering, ASCE **115**(8): 2016-2028.
- Ger, J. F., F. Y. Cheng and L. W. Lu (1993). "Collapse behavior of Pino Suarez Building during 1985 Mexico City earthquake." Journal of Structural Engineering **119**(3): 852-870.

- Ghanaat, Y. (1980). Study of X-Braced Steel Frame Structures Under Earthquake Simulation, UCB/EERC-80/08 University of California, Berkeley, California.
- Goel, S. C. and A. A. El-Tayem (1986). "Cyclic Load Behavior of Angle X-Bracing." Journal of Structural Engineering **112**(11): 2528-2539.
- Goggins, J. (2004). Earthquake resistant hollow and filled steel braces. Doctoral dissertation, Ph.D. thesis, Trinity College, University of Dublin.
- Goggins, J., B. M. Broderick and A. Y. Elghazouli (2006b). "Recommendations for the earthquake resistant design of braced steel frames." Proc. of First European Conference on Earthquake Engineering and Seismology, Geneva, Switzerland; Paper 966.
- Goggins, J. and T. Sullivan (2009). "Displacement-based seismic design of SDOF concentrically braced frames." Proc. of STESSA 2009, Philadelphia, US. Paper 141.
- Goggins, J. M., B. M. Broderick, A. Y. Elghazouli and A. S. Lucas (2005). "Experimental cyclic response of cold-formed hollow steel bracing members." Engineering Structures **27**(7): 977-989.
- Goggins, J. M., B. M. Broderick, A. Y. Elghazouli and A. S. Lucas (2006). "Behaviour of tubular steel members under cyclic axial loading." Journal of Constructional Steel Research **62**(1-2): 121-131.
- Grant, D. N., P. D. Greening, M. Taylor and B. Gosh (2008). Seed Record Selection for Spectral Matching with RSPMatch. The 14th World Conference on Earthquake Engineering, Beijing, China.
- Gugerli, H. (1982). Inelastic cyclic behavior of steel members. Doctoral Thesis, University of Michigan.
- Gugerli, H. and S. C. Goel (1982). "Inelastic Cyclic Behavior of Steel Bracing Members." UMEE 82R1, University of Michigan, Dept. of Civil Engineering.
- Gulkan, P. and M. A. Sozen (1974). "Inelastic responses of reinforced concrete structures to earthquakes motions." Proceedings of the ACI, Vol. 71, No. 12, pp. 604-610.
- Haddad, M., T. Brown, N. Shrive and R.-P. 3D (2004). Finite Element Modelling of Concentrically Braced Frames for Earthquakes. 13th World Conference on Earthquake Engineering, Vancouver, B.C., Canada.
- Hassan, O. F. and S. C. Goel (1991). Modeling of Bracing Members and Seismic Concentrically Braced Frames. UMCE 91-1. C. o. E. University of Michigan. Ann Arbor, MI.
- Higginbotham, A. B. and R. D. Hanson (1976). "Axial hysteretic behavior of steel members." J. Struct. Div., ASCE **102**(7): 1365-1381.
- Ikeda, K. and S. A. Mahin (1986). "Cyclic Response of Steel Braces." ASCE Journal of Structural Engineering **112**(2): 342-361.
- INGV. (2004). "National Institute for Geophysics and Volcanology." <http://zonesismiche.mi.ingv.it/>.
- Jacobsen, L. S. (1960). Damping in Composite Structures. 2nd World Conference on Earthquake Engineering, Japan: pp1029-1044.
- Jain, A. K., R. K. Goel and R. D. Hanson (1977). Static and dynamic hysteresis behaviour of steel tubular members with welded gusset plates. Ann Arbor, UMEE 77R3, University of Michigan.

- Jain, A. K. and S. C. Goel (1979). Cyclic end moments and buckling in steel members. the 2nd U.S. Nat. Conf. of Earthq. Engng, Stanford University, Stanford, CA.
- Jain, A. K., S. C. Goel and R. D. Hanson (1978). "Inelastic response of restrained steel tubes." Journal of the Structural Division, ASCE **102**(ST1): 1-18.
- Jain, A. K., S. C. Goel and R. D. Hanson (1980). "Hysteretic Cycles of Axially Loaded Steel Members." Journal of the Structural Division-Asce **106**(8): 1777-1795.
- Jin, J. and S. El-Tawil (2003). "Inelastic Cyclic Model for Steel Braces." Journal of Engineering Mechanics, ASCE **129**(5): 548-557.
- Judi, H. J., B. J. Davidson and R. C. Fenwick (2000). The direct displacement based design — A damping perspective. the 12th World Conference on Earthquake Engineering, Auckland, New Zealand, Paper No. 0330.
- Kahn, L. F. and R. D. Hanson (1976). "Inelastic Cycles of Axially Loaded Steel Members." Journal of the Structural Division-Asce **102**(5): 947-959.
- Kelly, D. J., D. R. Bonneville and S. J. Bartoletti (2000). 1994 Northridge Earthquake: Damage to a Four-Story Steel Braced Frame Building and Its Subsequent Upgrade. 12th World Conference on Earthquake Engineering, Upper Hutt, New Zealand.
- Khatib, F., S. A. Mahin and K. S. Pister (1988). Seismic behavior of concentrically braced steel frames. UCB/EERC-88/01. U. o. C. Earthquake Engineering Research Center. Berkeley, CA.
- Kitagawa, Y. and H. Hiraishi (2004). "Overview Of The 1995 Hyogo-Ken Nanbu Earthquake And Proposals For Earthquake Mitigation Measures." Journal of Japan Association for Earthquake Engineering **Vol.4, No.3(Special Issue)**.
- Kowalsky, M. J. (1994). Displacement-based design-a methodology for seismic design applied to RC bridge columns. Master's thesis, University of California at San Diego.
- Kramer, S. L. (1996). Geotechnical Earthquake Engineering, Prentice Hall.
- Kwan, W.-P. and S. L. Billington (2003). "Influence of Hysteretic Behavior on Equivalent Period and Damping of Structural Systems." Journal of Structural Engineering **129**(5): 576-585.
- Lee, K. and M. Bruneau (2005). "Energy Dissipation of Compression Members in Concentrically Braced Frames: Review of Experimental Data." Journal of Structural Engineering and Structural Dynamics **131**(4): 552-559.
- Lee, S. and S. Goel (1987). Seismic behavior of hollow and concrete-filled square tubular bracing members., UMCE 87-11. Ann Arbor, MI: Department of Civil Engineering, University of Michigan.
- Lee, S. J. and L. W. Lu (1989). "Quasi-Static Tests of Scaled Model Building." Journal of Structural Engineering, ASCE **115**(8): 1895–1916.
- Lotfollahi, M. and M. M. Alinia (2009). "Effect of tension bracing on the collapse mechanism of steel moment frames." Journal of Constructional Steel Research **65**(10-11): 2027-2039.
- Maison, B. F. and E. P. Popov (1980). "Cyclic Response Prediction for Braced Steel Frames." ASCE J Struct Div **106**(7): 1401-1416.
- Maley, T., R. Roldán, A. Lago and T. J. Sullivan (2012). Effects of response spectrum shape on the response of steel frame and frame-wall structures. I. P. Research Report ROSE-2012/01 (to be published). Pavia, Italy.

- Mamaghani, I. H. P., T. Usami and E. Mizuno (1996). "Inelastic large deflection analysis of structural steel members under cyclic loading." Engineering Structures **18**(9): 659-668.
- Manson, S. S. (1953). "Behaviour of materials under conditions of thermal stress. Heat Transfer Symposium." University of Michigan Engineering Research Institute, pp. 9-75.
- McCormick, J., R. DesRoches, D. Fugazza and F. Auricchio (2007). "Seismic assessment of concentrically braced steel frames with shape memory alloy braces." Journal of Structural Engineering **133** (6): 862-870.
- McKenna, F., G. L. Fenves and M. H. Scott (2000). Object oriented program, OpenSees; Open system for earthquake engineering simulation., <http://opensees.berkeley.edu>.
- Medhekar, M. S. and D. J. L. Kennedy (2000). "Displacement-based seismic design of buildings--application." Engineering Structures **22**(3): 210-221.
- Medhekar, M. S. and D. J. L. Kennedy (2000). "Displacement-based seismic design of buildings--theory." Engineering Structures **22**(3): 201-209.
- Moghaddam, H. and I. Hajirasouliha (2006). "An investigation on the accuracy of pushover analysis for estimating the seismic deformation of braced steel frames." Journal of Constructional Steel Research **62**(4): 343-351.
- Nakashima, M., K. Inoue and M. Tada (1998). "Classification of damage to steel buildings observed in the 1995 Hyogoken-Nanbu earthquake." Engineering Structures **20**(4-6): 271-281.
- Nip, K. H., L. Gardner and A. Y. Elghazouli (2010). "Cyclic testing and numerical modelling of carbon steel and stainless steel tubular bracing members." Engineering Structures **32**(2): 424-441.
- Osteraas, J. and H. Krawinkler (1989). "The Mexico Earthquake of September 19, 1985 - Behavior of Steel Buildings." Earthquake Spectra **5**(1): 51-88.
- Paulay, T. and M. N. J. Priestley (1992). Seismic Design of Reinforced Concrete and Masonry Buildings. Wiley, New York.
- PEER (2008). "On Line Strong Motion Database." University of California. peer.berkeley.edu.
- PEER (2011). "Pacific Earthquake Engineering Research. PEER Strong Motion Database." Available at <http://peer.berkeley.edu/smcat/>.
- Pennucci, D., G. M. Calvi and T. Sullivan (2009). "Displacement Based Design of Precast Walls with Additional Dampers." Journal of Earthquake Engineering **Vol. 13, No. 1**.
- Pennucci, D., T. J. Sullivan and G. M. Calvi (2011). "Displacement Reduction Factors for the Design of Medium and Long Period Structures." Journal of Earthquake Engineering **15**(sup1): 1-29.
- Popov, E. P. and R. G. Black (1981). "Steel Struts under Severe Cyclic Loadings." Journal of the Structural Division-Asce **107**(9): 1857-1881.
- Popov, E. P., V. A. Zayas and S. A. Mahin (1979). "Cyclic inelastic buckling of thin tubular columns." J. Struct. Div., ASCE, **105**(ST11): 2261-2277.
- Priestley, M. J. N. (1993). "Myths and fallacies in earthquake engineering.-conflicts between design and reality." Bulletin of the NZ National Society for Earthquake Engineering **26**(3) 329-334.

- Priestley, M. J. N. (2003). Myths and fallacies in earthquake engineering, revisited. Mallet Milne lecture. IUSS Press. Pavia, Italy.
- Priestley, M. J. N., G. M. Calvi and M. J. Kowalsky (2007). Displacement-Based Seismic Design of Structures, , IUSS Press, Pavia, Italy.
- RAM-Perform 3D Element Description Manual, Version 1.19. Graham H. Powell Inc. 2003.
- RAM-Perform 3D (2003). Element Description Manual, Version 1.19. Graham H. Powell Inc.
- Remennikov, A. M. and W. R. Walpole (1997a). "Analytical prediction of seismic behaviour for concentrically-braced steel systems." Earthquake Engineering & Structural Dynamics **26**(8): 859-874.
- Remennikov, A. M. and W. R. Walpole (1997b). "Modeling the inelastic cyclic behavior of a bracing member for work-hardening material." Int. J. Solids Struct. **34**: 3491–3515.
- Remennikov, A. M. and W. R. Walpole (1998). "A note on compression strength reduction factor for a buckled strut in seismic-resisting braced system." Engineering Structures **20**(8): 779-782.
- Roeder, C. W., D. A. Foutch and S. C. Goel (1987). "Seismic Testing of Full-Scale Steel Building---Part II." Journal of Structural Engineering **113**(11): 2130-2145.
- Rofooeia, F. R., N.K. Attaria, A. Rasekhhb and A. H. Shodjaa (2007). "Adaptive pushover analysis." Asian journal of civil engineering (building and housing) **8**(3): 343-358.
- Sabelli, R. (2001). "Research on improving the design and analysis of earthquake resistant steel braced frames." FEMA / EERI.
- SAP2000 (2002). A General Structural Analysis Program. Computers and Structures, Inc. University of California, Berkeley.
- SeismoSoft (2007). SeismoStruct—A computer program for static and dynamic analysis for framed structures, Available from URL: www.seismosoft.com (online).
- Shaback, B. and T. Brown (2003). "Behaviour of square hollow structural steel braces with end connections under reversed cyclic axial loading." Canadian Journal of Civil Engineering **30**(4): 745-753.
- Sharpe, R. D. (1974). The Seismic Response of Inelastic Structures. Ph.D Thesis, University of Canterbury.
- Shermann, D. (1996). "Designing with structural tubing. ." Engng JI, AISC 1996;3rd Quarter:101–9.
- Shibata, A. and M. A. Sozen (1976). "Substitute-Structure Method for Seismic Design in R/C." Journal of the Structural Division, ASCE, Vol. 102, No. ST1, pp. 1-18.
- Shibata, M. and M. Wakabayashi (1984). Hysteretic behaviour of K-type braced frame. 8th World Conf. Earthq. Engng, San Francisco, CA.
- Spacone, E., F. C. Filippou and F. F. Taucer (1996). "Fiber Beam-Column Model for Nonlinear Analysis of R/C Frames. I: Formulation." Earthquake Engineering and Structural Dynamics **25**(7): 711-725.
- Stephens, R. I., A. Fatemi, R. R. Stephens and H. O. Fuchs (2001). Metal Fatigue in Engineering, John Wiley & Sons, Inc.

- Tanaka, A., K. Morita and Y. H. (1980). Damage of braced steel frames due to the 1978 Miyagiken-oki earthquake. SEVENTH WORLD CONFERENCE ON EARTHQUAKE ENGINEERING. ISTANBUL, TURKEY.
- Tang, X. and S. C. Goel (1989). "Brace fractures and analysis of phase I structures." J. Struct. Eng. **115**(8): 1960–1976.
- Tremblay, R. (2002). "Inelastic seismic response of steel bracing members." Journal of Constructional Steel Research **58**(5-8): 665-701.
- Tremblay, R., M. H. Archambault and A. Filiatrault (2003). "Seismic response of concentrically braced steel frames made with rectangular hollow bracing members." Journal of Structural Engineering **129**: 1626-1636.
- Tremblay, R., A. Filiatrault, M. Bruneau, M. Nakashima, H. G. L. Prion and R. DeVal (1996). "Seismic design of steel buildings: lessons from the 1995 Hyogo-ken Nanbu earthquake." Canadian Journal of Civil Engineering **23**(3): 727-756.
- Tremblay, R., Timler P, Bruneau M and A. Filiatrault (1995). "Performance of steel structures during the 1994 Northridge earthquake." Canadian Journal of Civil Engineering **22**(2): 338-360.
- UNDP (2004). Reducing Disaster Risk a Challenge for Development. United Nations Development Programme, Bureau for Crisis Prevention and Recovery www.undp.org/bcpr. New York, NY 10017, USA.
- Uriz, P. (2005). Towards earthquake resistant design of concentrically braced steel buildings. Doctoral Dissertation, University of California, Berkeley.
- Wakabayashi, M., T. Nonaka, T. Nakamura, S. Morino and N. Yoshida (1973). Experimental Studies on the behavior of Steel Bars Under Repeated Axial Loading. Bulletin Disaster Prevention Research Institute in Kyoto University. Kyoto, Japan.
- Wakabayashi, M., N. T. and N. Yoshida (1977). "Experimental studies on the elastic-plastic behaviour of braced frames under repeated horizontal loading." Bull. Disas. Prev. Inst., Kyoto Univ **27** 121–154.
- Walpole, W. R. (1995). Behaviour of cold-formed steel RHS members under cyclic loading. The NZNSEE Conference, Rotorua, New Zealand.
- Walpole, W. R. and L. S. Leowardi (1995). The behaviour of brace members under cyclic loading. Conf. Struct. Stability Des.
- Wijesundara, K. K. (2009). Design of concentrically braced steel frames with RHS shape braces. Doctoral dissertation, Ph.D. thesis, European Centre for Training and Research in Earthquake Engineering (EUCENTRE).
- Xue, L. (2008). "A unified expression for low cycle fatigue and extremely low cycle fatigue and its implication for monotonic loading." International Journal of Fatigue **30**(10-11): 1691-1698.
- Yamanouchi, H., M. Midorikawa, I. Nishiyama and M. Watabe (1989). "Seismic Behaviour of Full Scale Concentrically Braced Steel Building Structure." Journal of Structural Engineering, ASCE **115**(8): 1917-1929.
- Yoo, J. H., C.W. Roeder and D.E. Lehman (2006). Finite element simulation of Special Concentrically Braced Frame Tests. STESSA 2006-Fifth International Conference: Behavior of Steel Structures in Seismic Areas, Yokohama, Japan,.

- Zayas, V. A., E. P. Popop and S. A. Mahin (1980). Cyclic inelastic buckling of tubular steel braces. UCB/EERC-80/16. U. o. C. Earthquake Engineering Research Center. Berkeley, CA.
- Zhao, X. L., R. H. Grzebieta and C. Lee (2002). "Void Filled Cold-Formed RHS Braces subjected to Large Deformation Cyclic Axial Loading." Journal of Structural Engineering, ASCE **128** (6): 747-753.

Appendix A

NLTHA results for shake table tests

This appendix shows the comparison of the hysteretic axial displacement and axial force for the experimental and numerical results for all the shake table tests explained in Chapter 5.

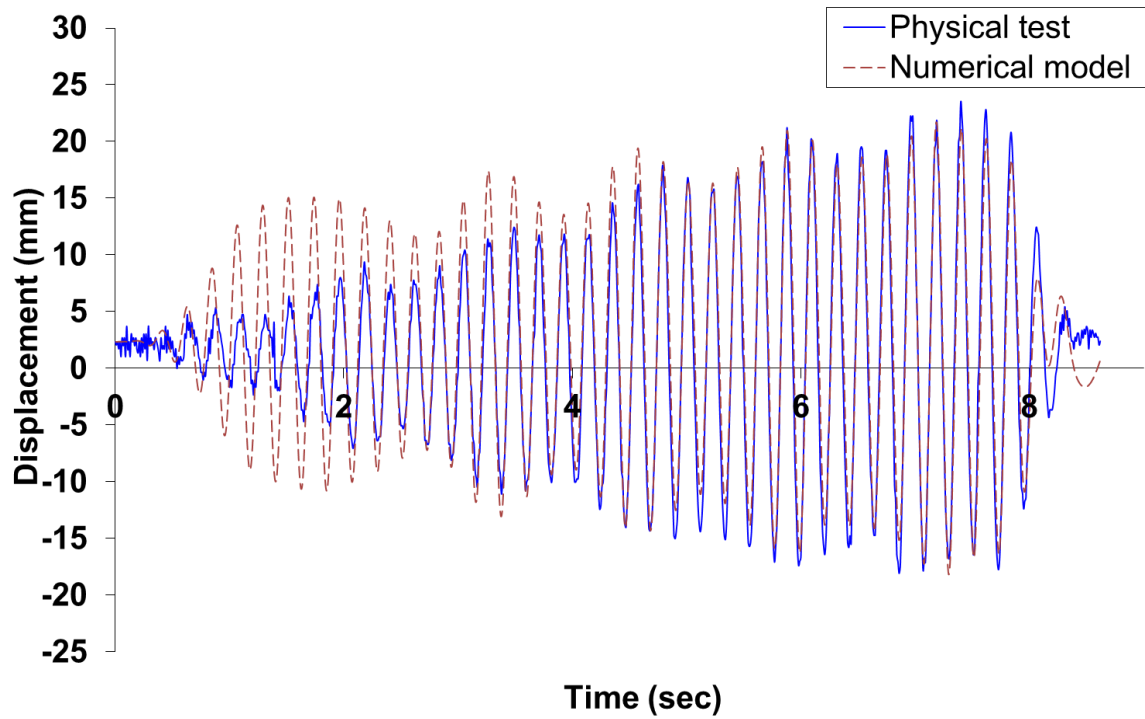


Figure A.1: Comparison for the displacement time-history response of test ST1-R50H and the numerical model in OpenSees.

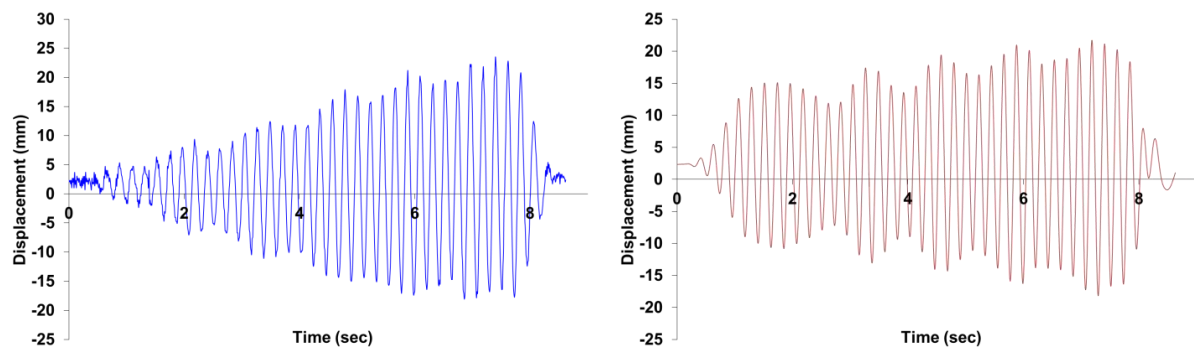


Figure A.2: Measured displacement time-history response of test ST1-R50H in (a) physical test and (b) numerical model.

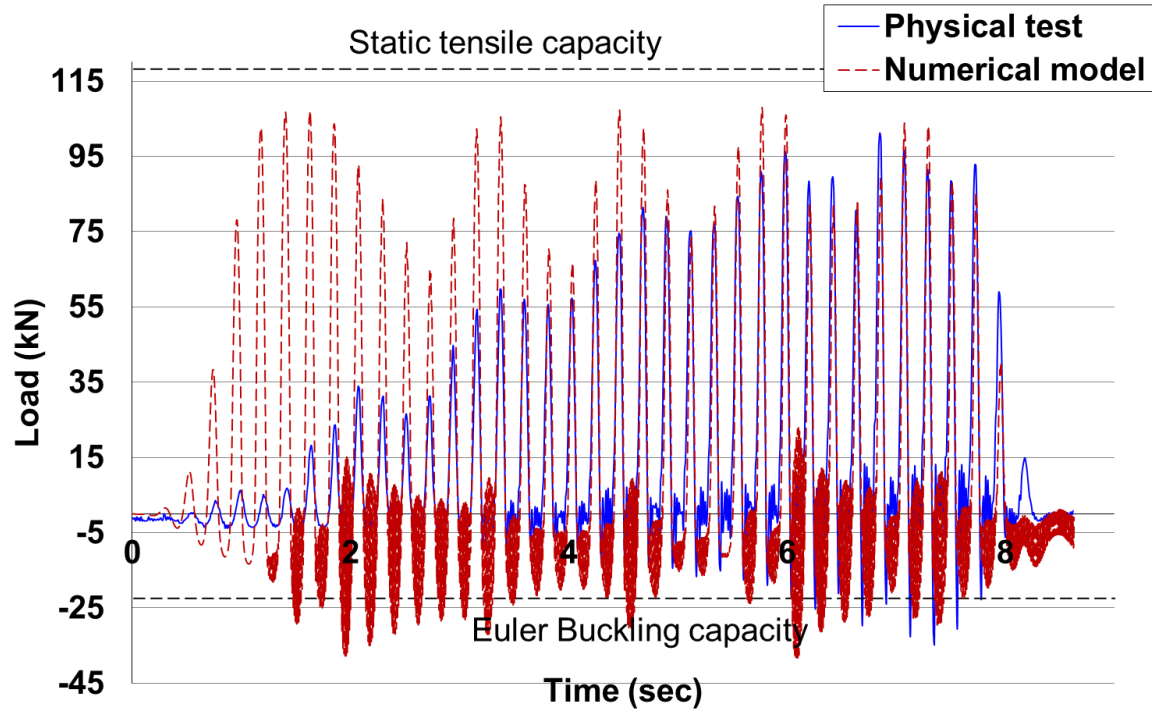


Figure A.3: Comparison for the axial load time-history response of the first brace specimen of test ST1-R50H and the numerical model in OpenSees.

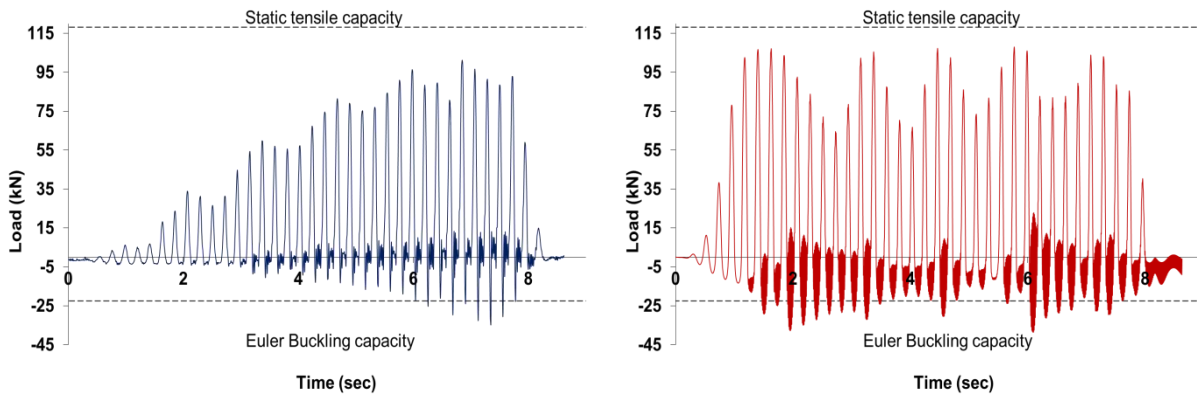


Figure A.4: Axial load time-history response of the first brace of test ST1-R50H in (a) physical test and (b) numerical model.

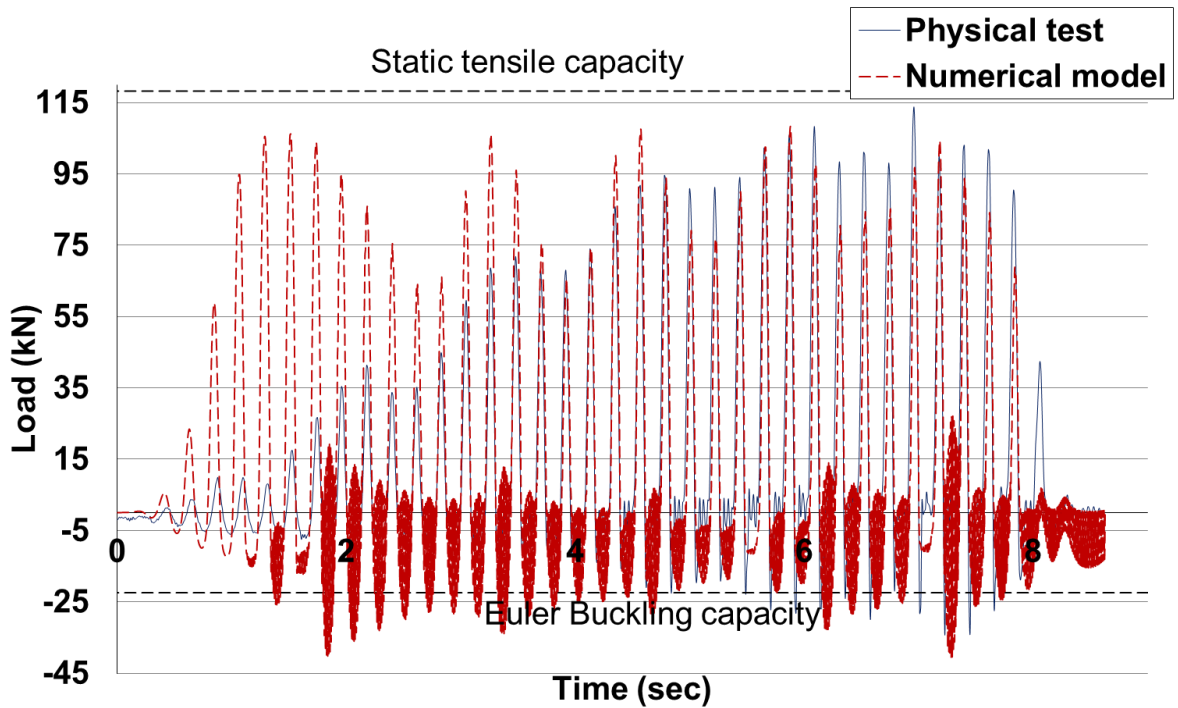


Figure A.5: Comparison for the axial load time-history response of the second brace specimen of test ST1-R50H and the numerical model in OpenSees.

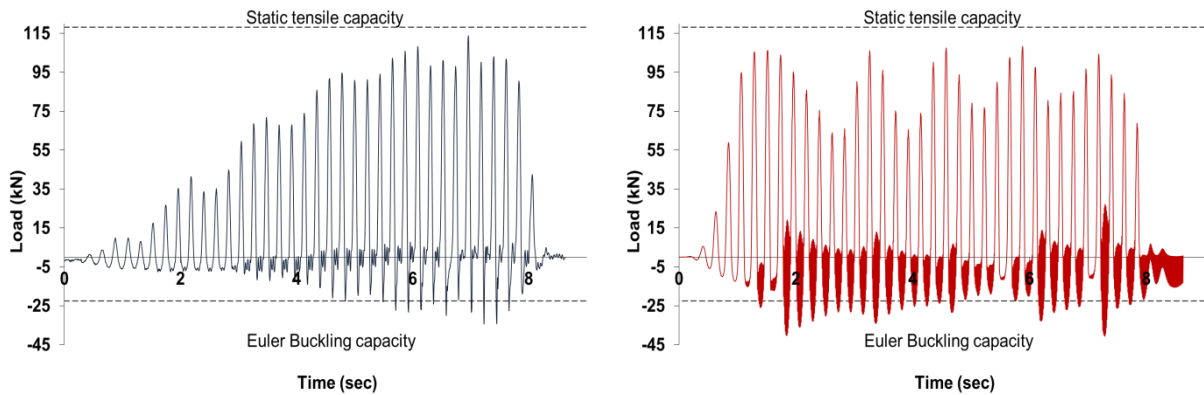


Figure A.6: Axial load time-history response of the second brace of test ST1-R50H in (a) physical test and (b) numerical model.

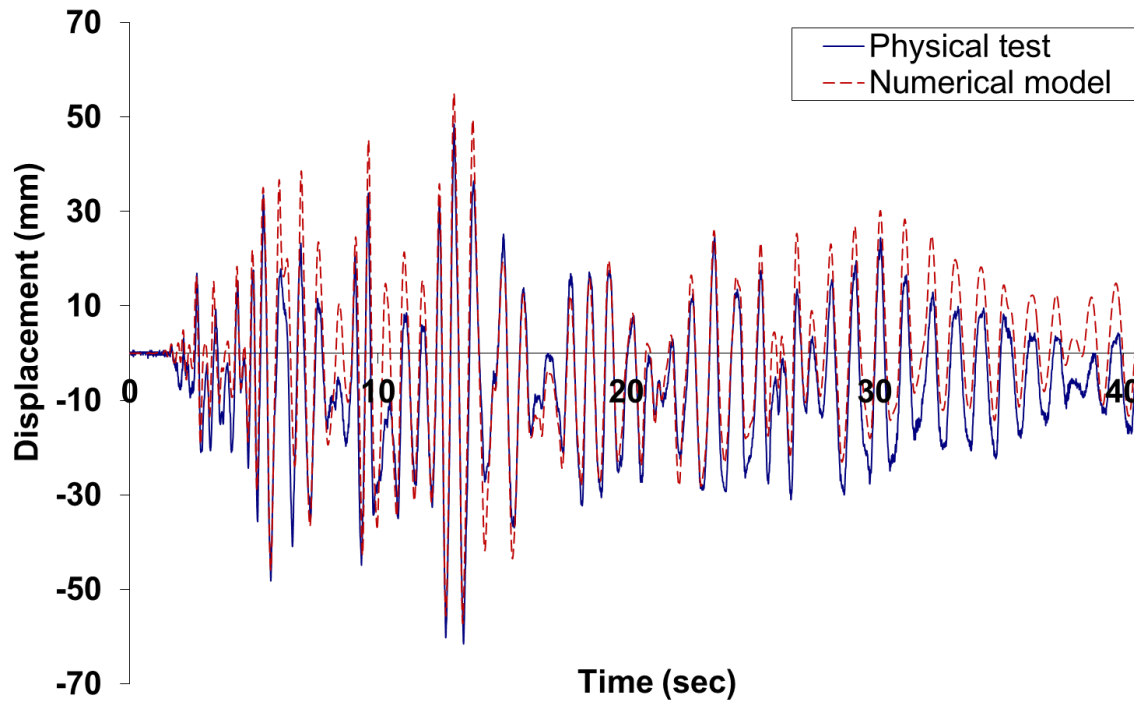


Figure A.7: Comparison for the displacement time-history response of test ST2-E50H and the numerical model in OpenSees.

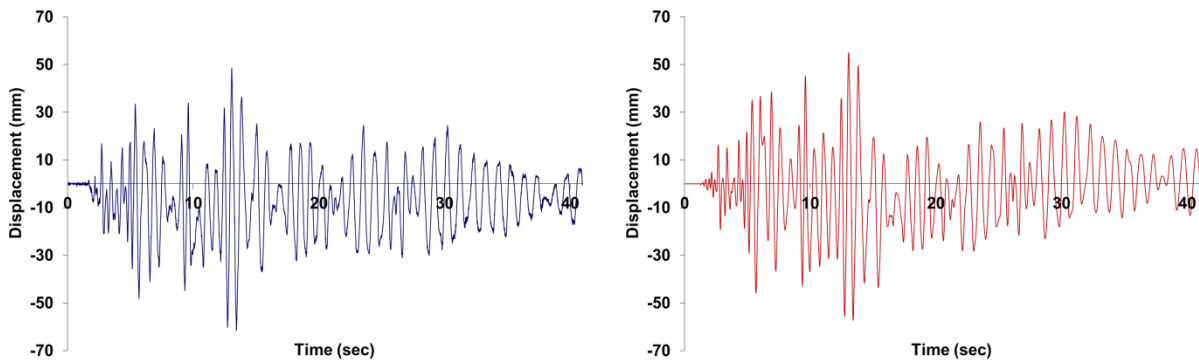


Figure A.8: Measured displacement time-history response of test ST2-E50H in (a) physical test and (b) numerical model.

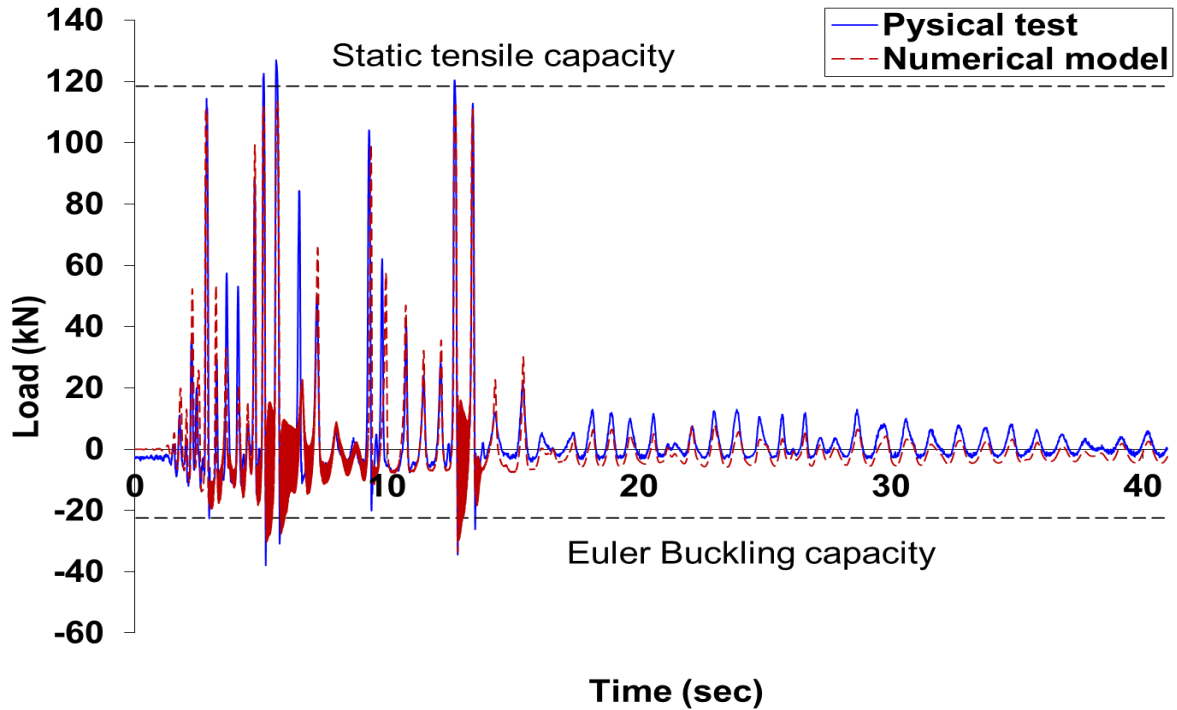


Figure A.9: Comparison for the axial load time-history response of the first brace specimen of test ST2-E50H and the numerical model in OpenSees.

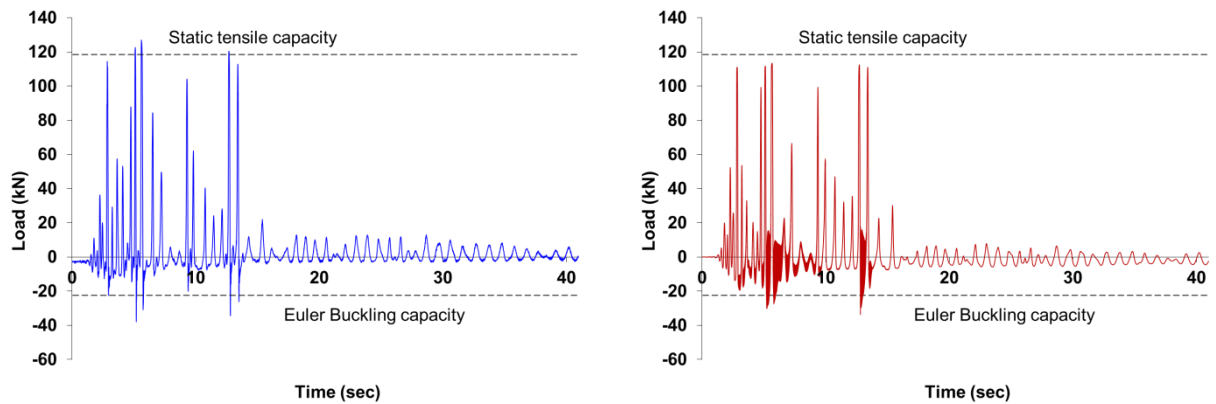


Figure A.10: Axial load time-history response of the first brace of test ST2-E50H in (a) physical test and (b) numerical model.

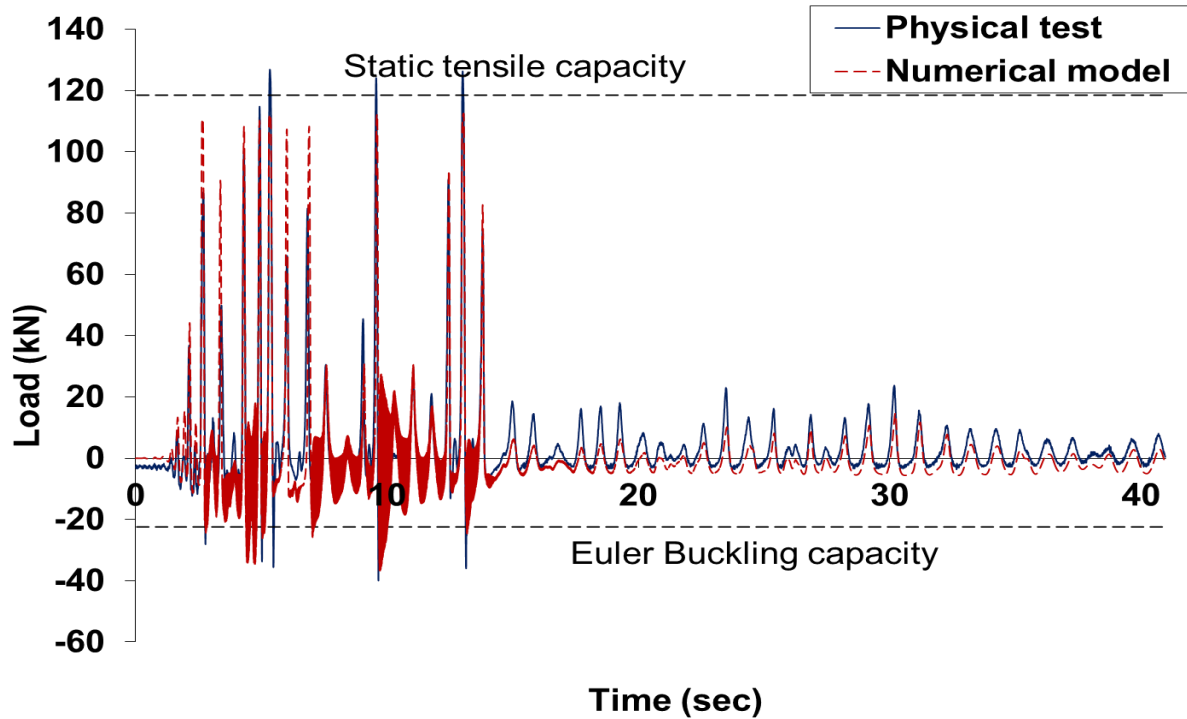


Figure A.11: Comparison for the axial load time-history response of the second brace specimen of test ST2-E50H and the numerical model in OpenSees.

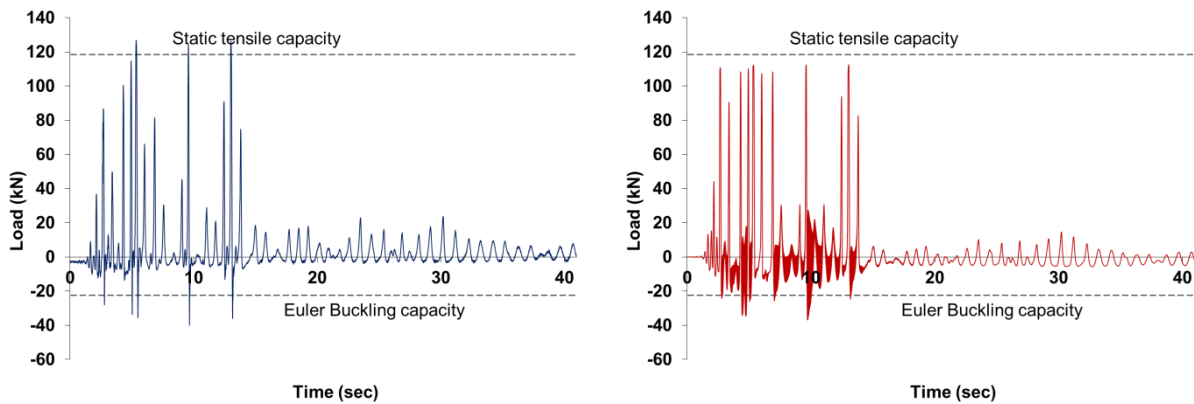


Figure A.12: Axial load time-history response of the second brace of test ST2-E50H in (a) physical test and (b) numerical model.

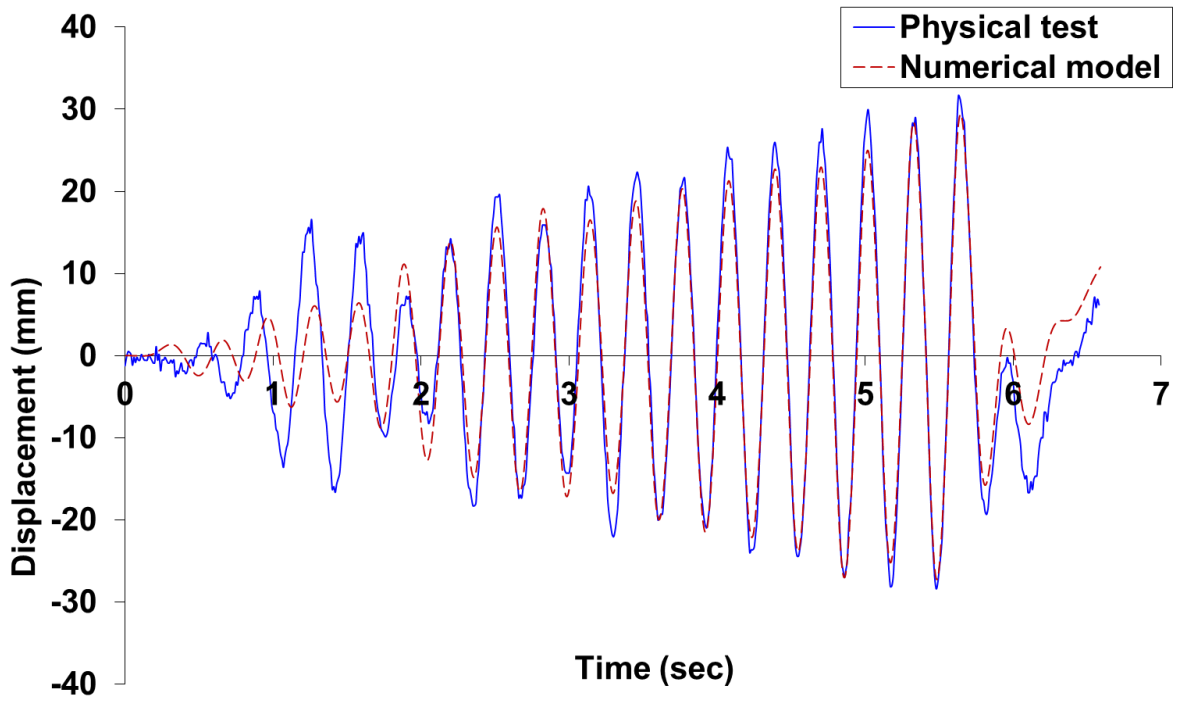


Figure A.13: Comparison for the displacement time-history response of test ST4-R20H and the numerical model in OpenSees.

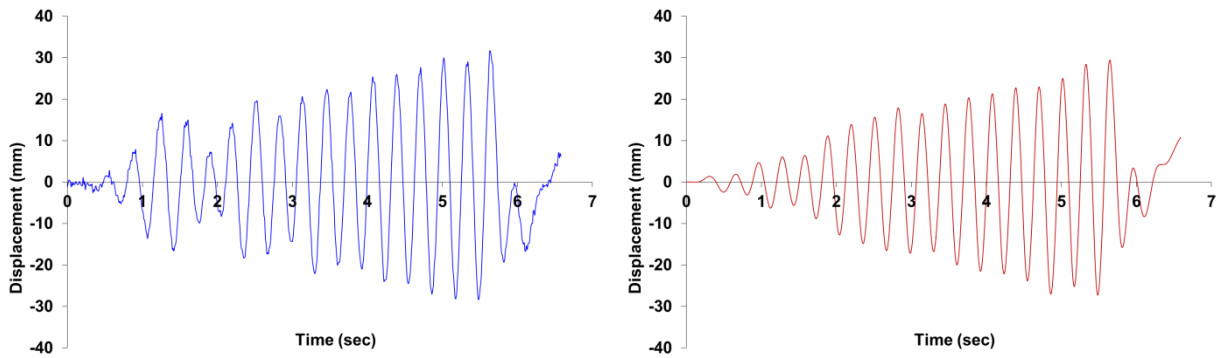


Figure A.14: Measured displacement time-history response of test ST4-R20H in (a) physical test and (b) numerical model.

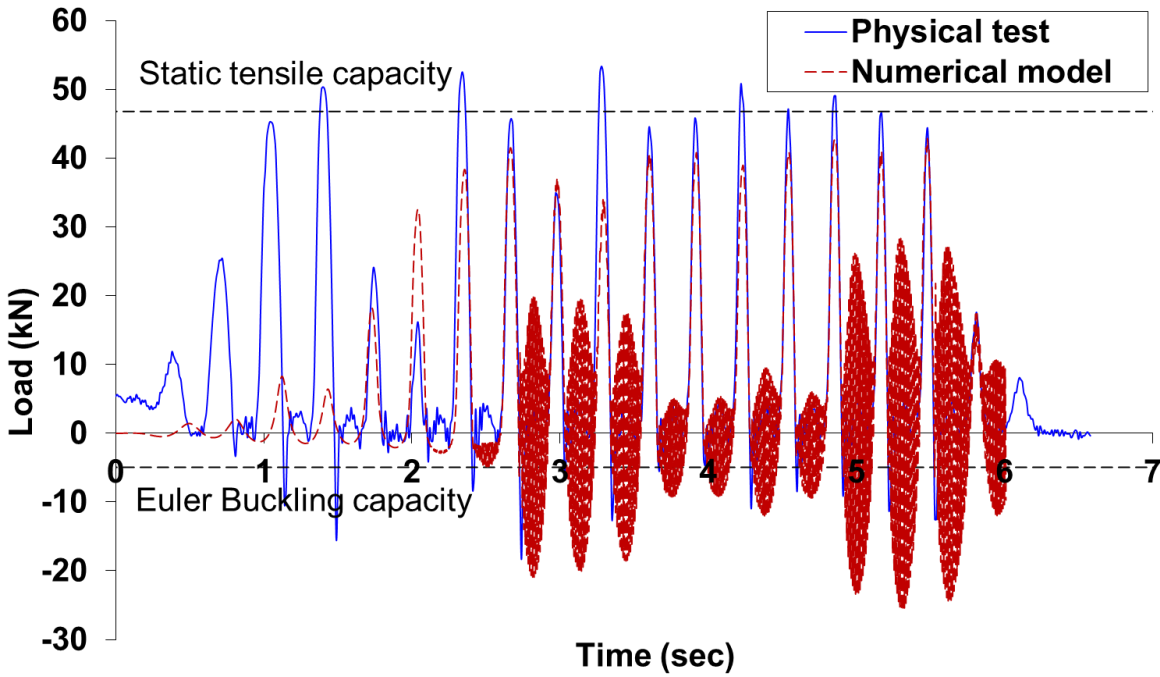


Figure A.15: Comparison for the axial load time-history response of the first brace specimen of test ST4-R20H and the numerical model in OpenSees.

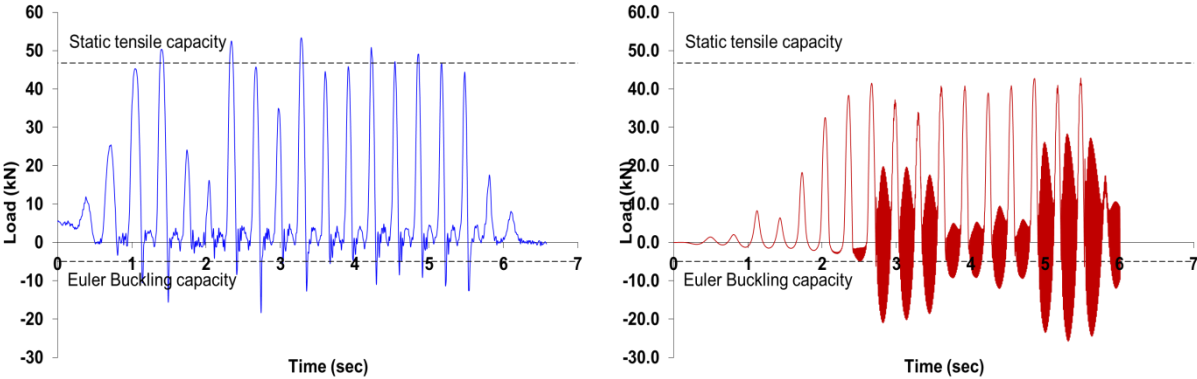


Figure A.16: Axial load time-history response of the first brace of test ST4-R20H in (a) physical test and (b) numerical model.

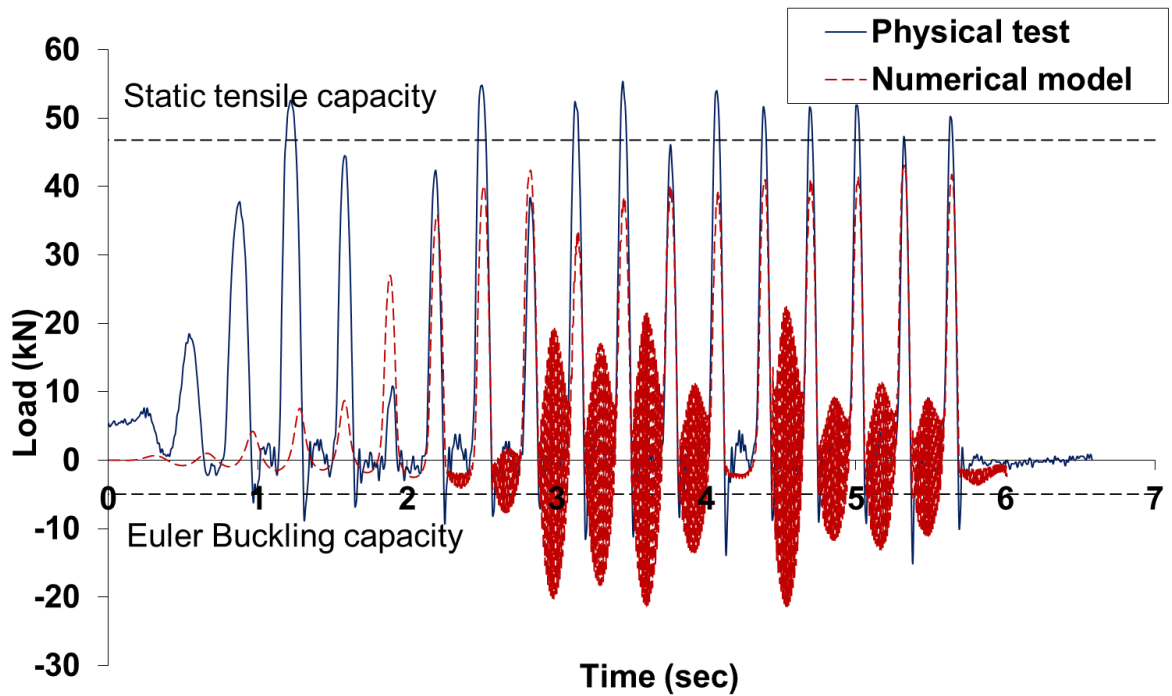


Figure A.17: Comparison for the axial load time-history response of the second brace specimen of test ST4-R20H and the numerical model in OpenSees.

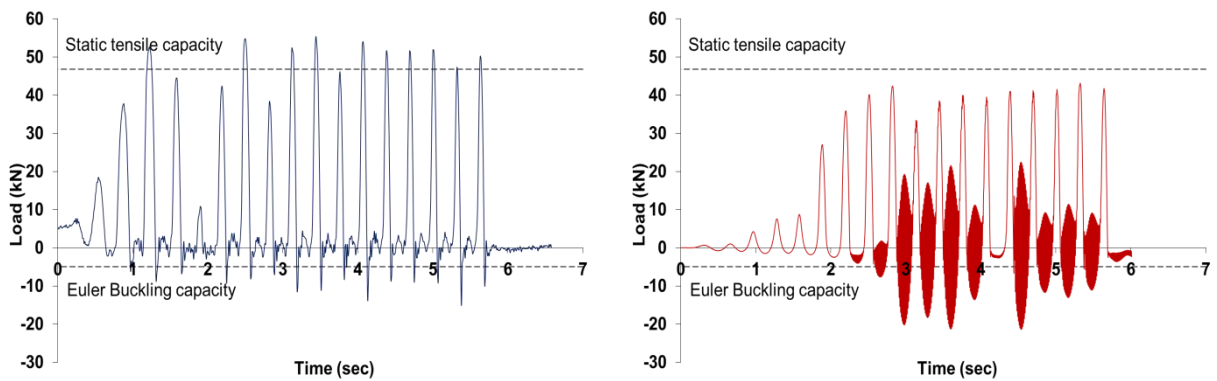


Figure A.18: Axial load time-history response of the second brace of test ST4-R20H in (a) physical test and (b) numerical model.

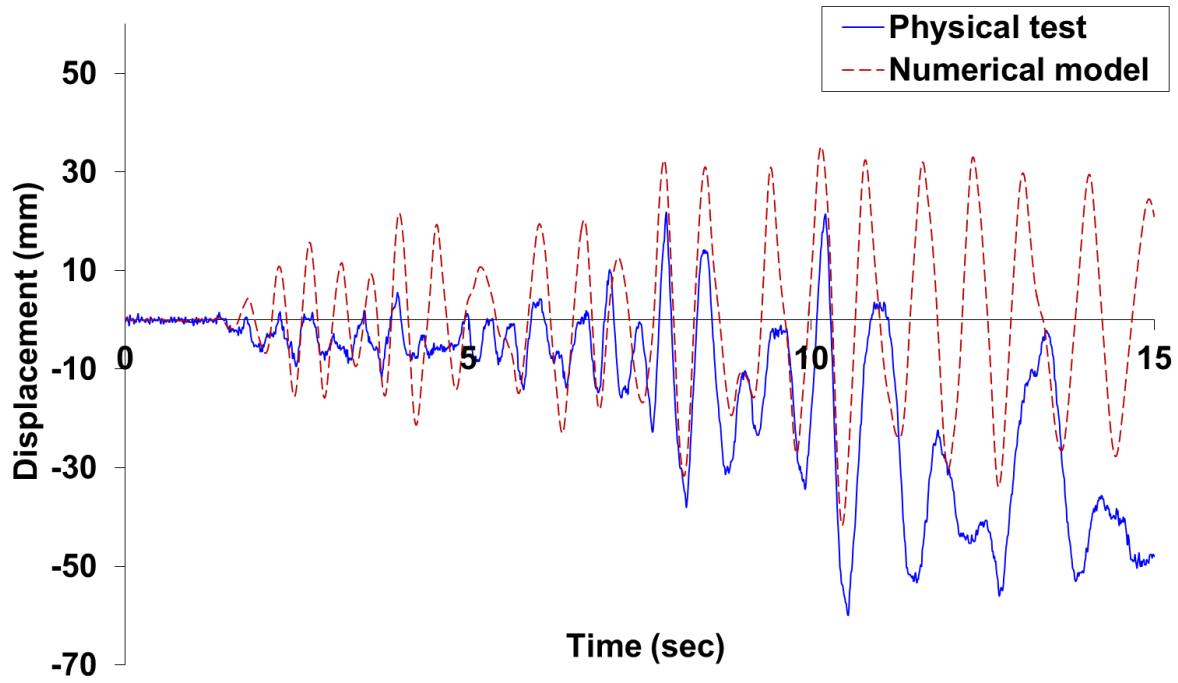


Figure A.19: Comparison for the displacement time-history response of test ST5-E20H and the numerical model in OpenSees.

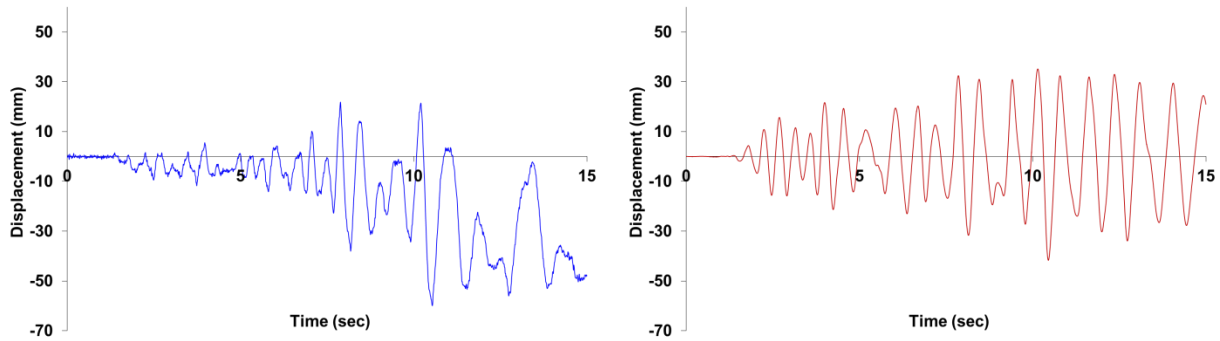


Figure A.20: Measured displacement time-history response of test ST5-E20H in (a) physical test and (b) numerical model.

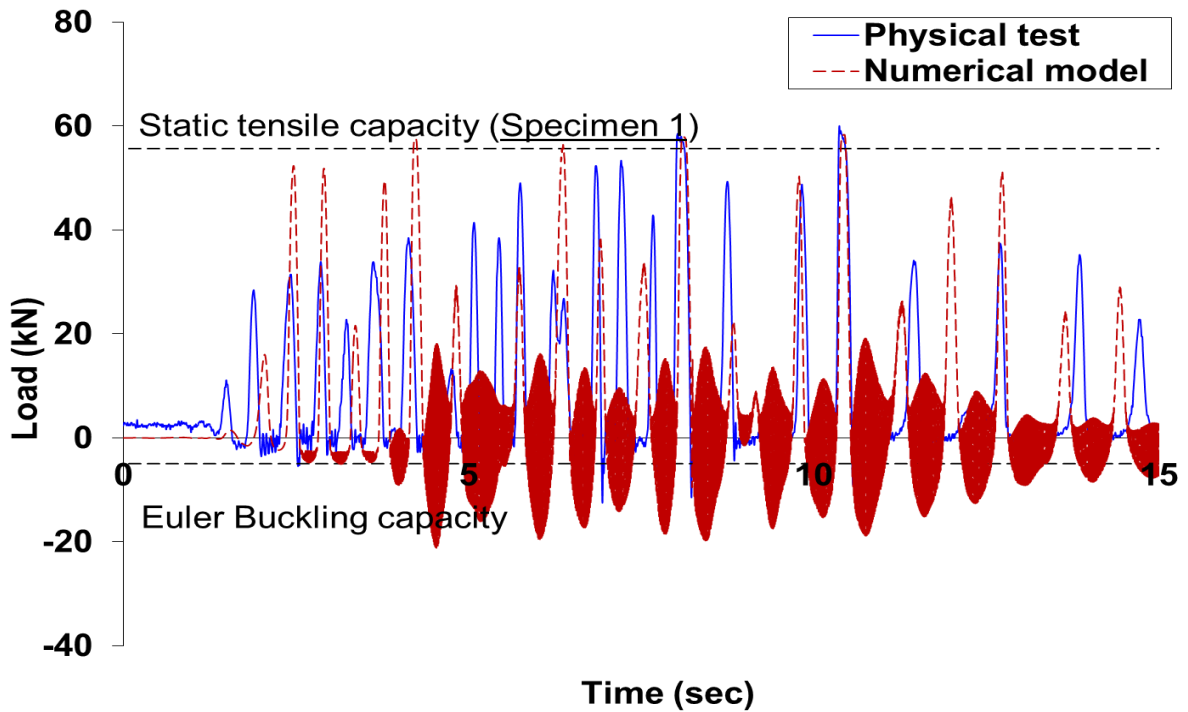


Figure A.21: Comparison for the axial load time-history response of the first brace specimen of test ST5-E20H and the numerical model in OpenSees.

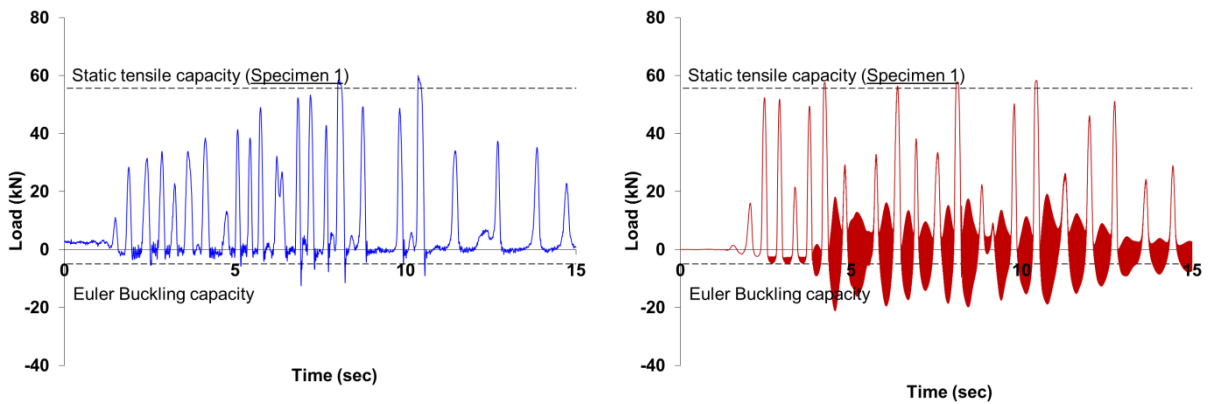


Figure A.22: Axial load time-history response of the first brace of test ST5-E20H in (a) physical test and (b) numerical model.

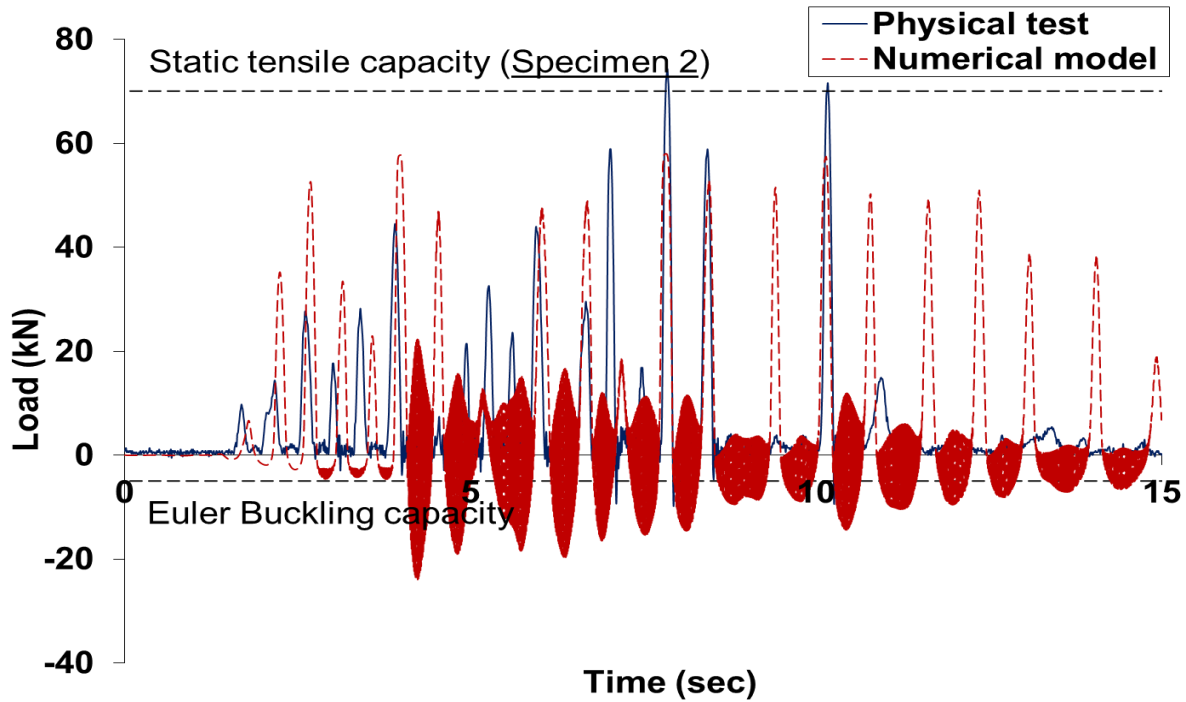


Figure A.23: Comparison for the axial load time-history response of the second brace specimen of test ST5-E20H and the numerical model in OpenSees.

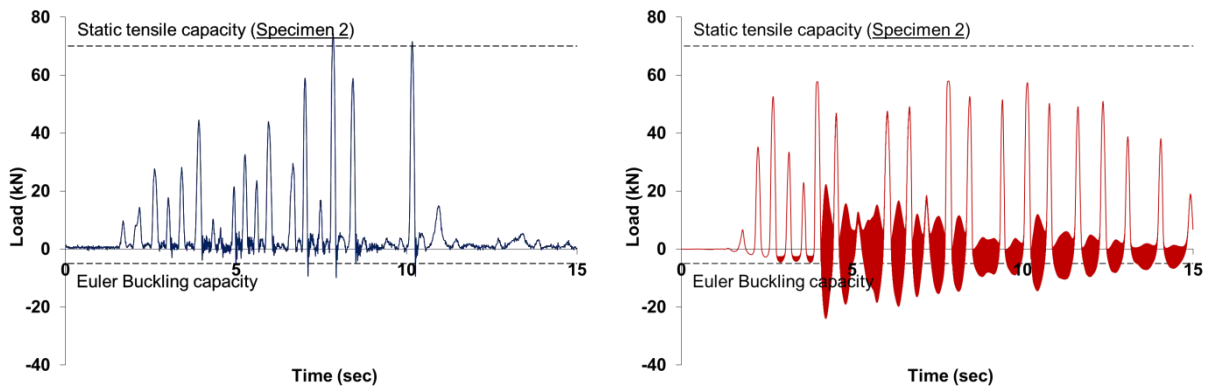


Figure A.24: Axial load time-history response of the second brace of test ST5-E20H in (a) physical test and (b) numerical model.

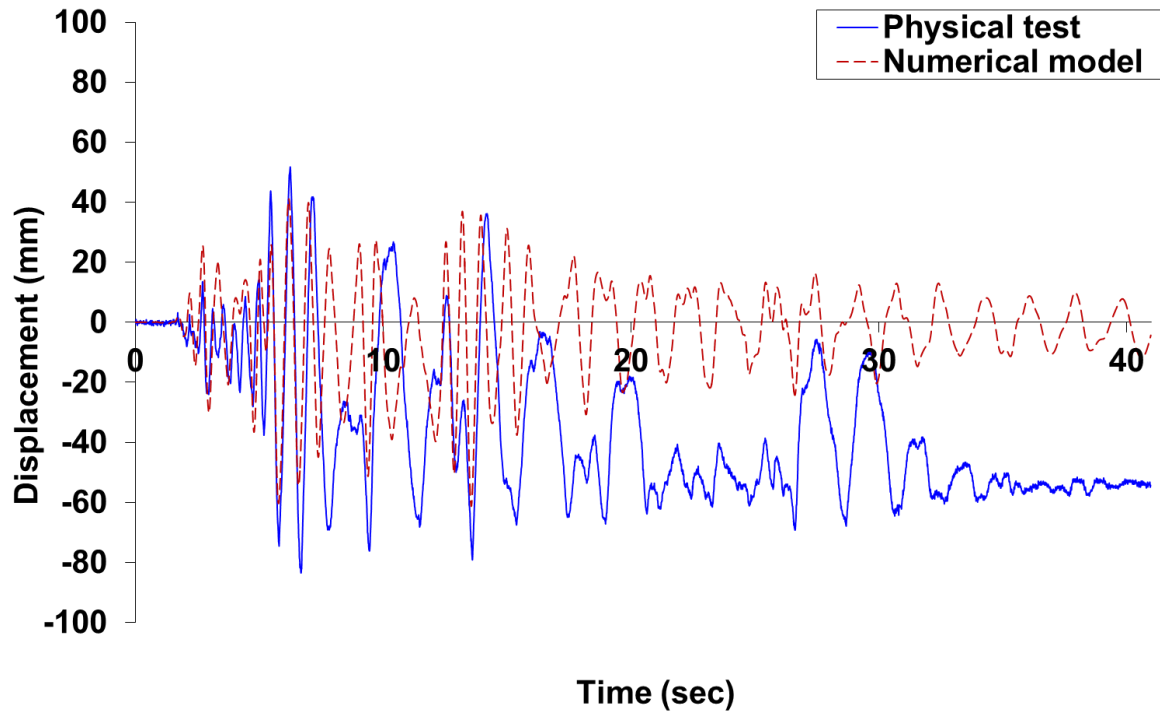


Figure A.25: Comparison for the displacement time-history response of test ST5-E20H-B and the numerical model in OpenSees.

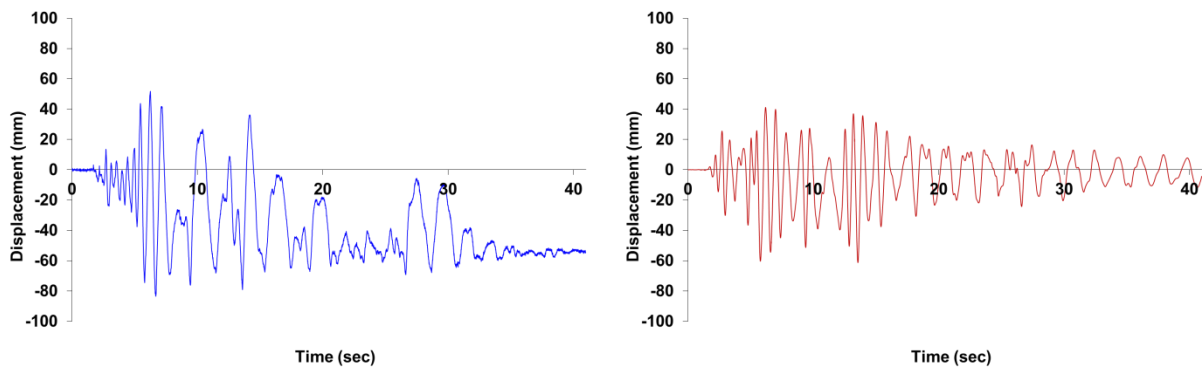


Figure A.26: Measured displacement time-history response of test ST5-E20H-B in (a) physical test and (b) numerical model.

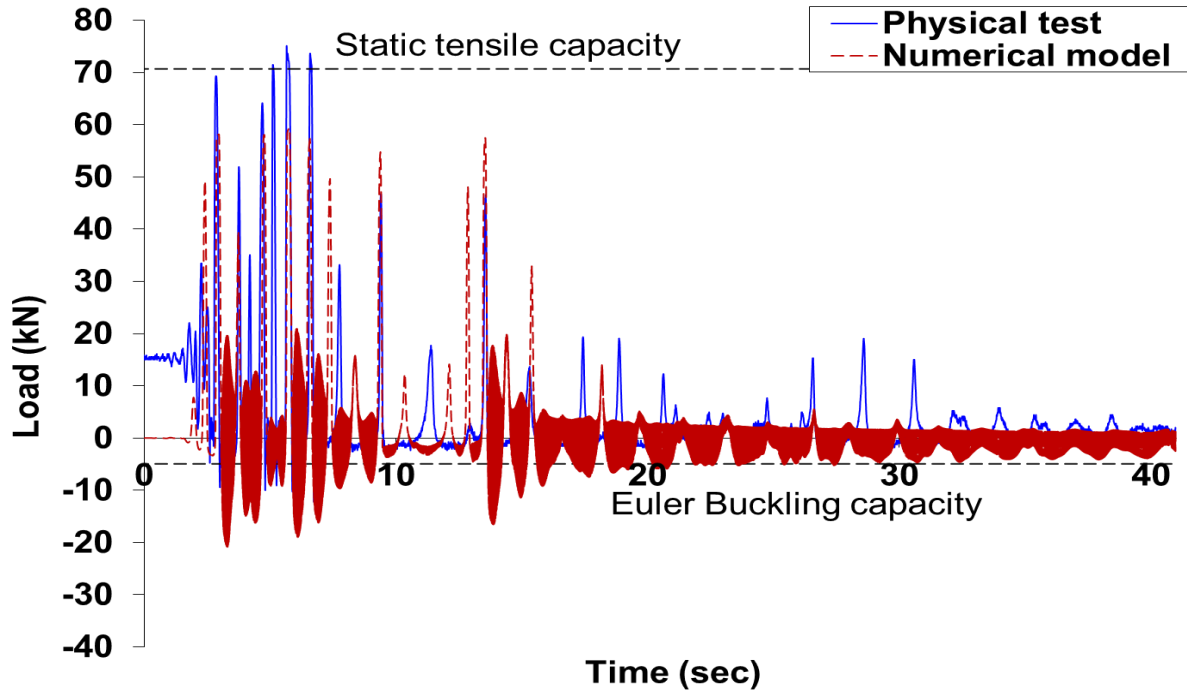


Figure A.27: Comparison for the axial load time-history response of the first brace specimen of test ST5-E20H-B and the numerical model in OpenSees.

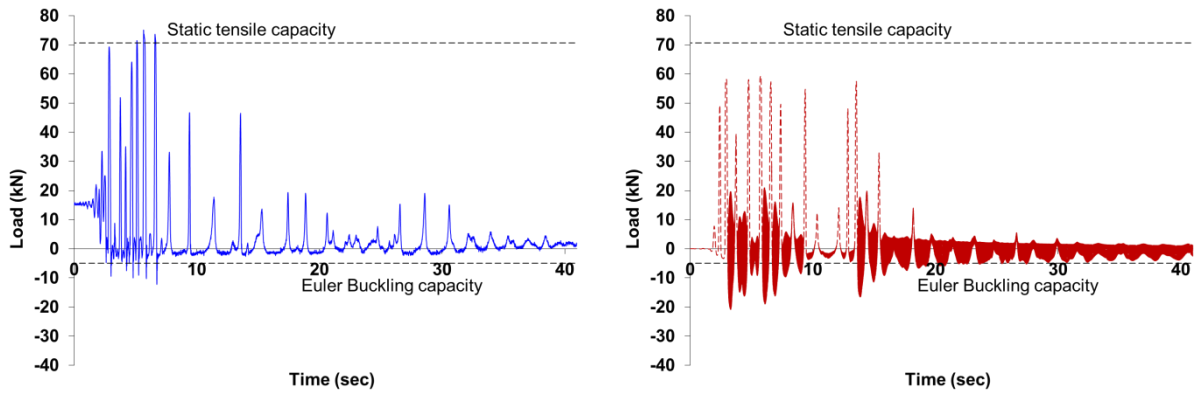


Figure A.28: Axial load time-history response of the first brace of test ST5-E20H-B in (a) physical test and (b) numerical model.

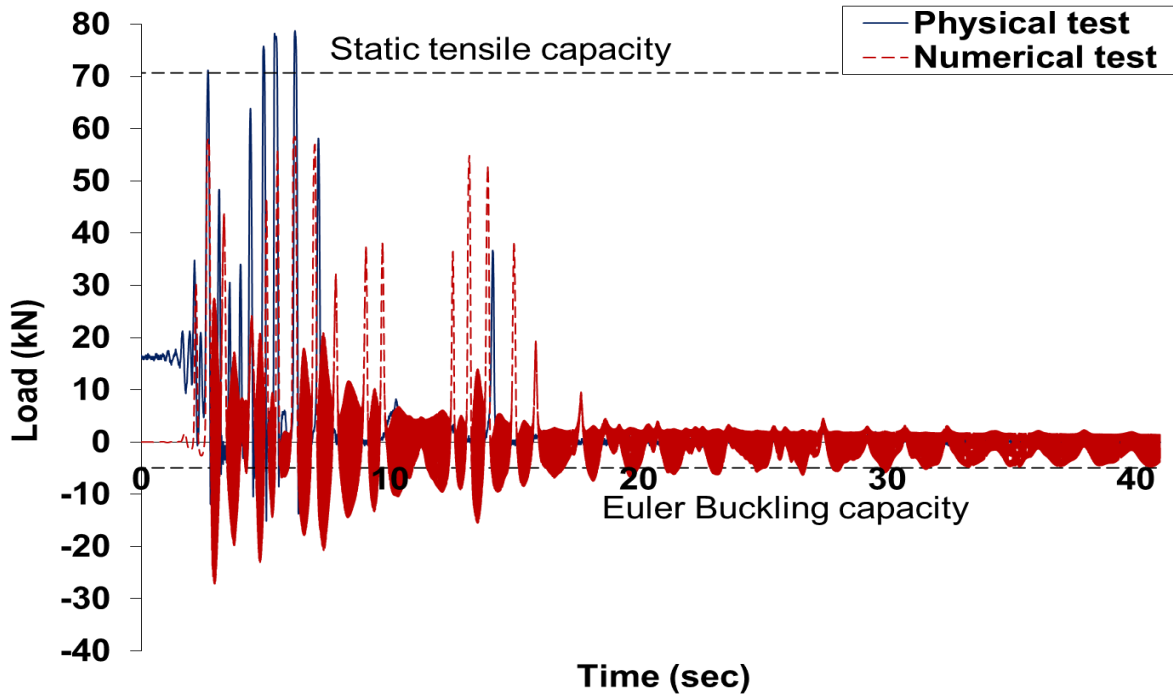


Figure A.29: Comparison for the axial load time-history response of the second brace specimen of test ST5-E20H-B and the numerical model in OpenSees.

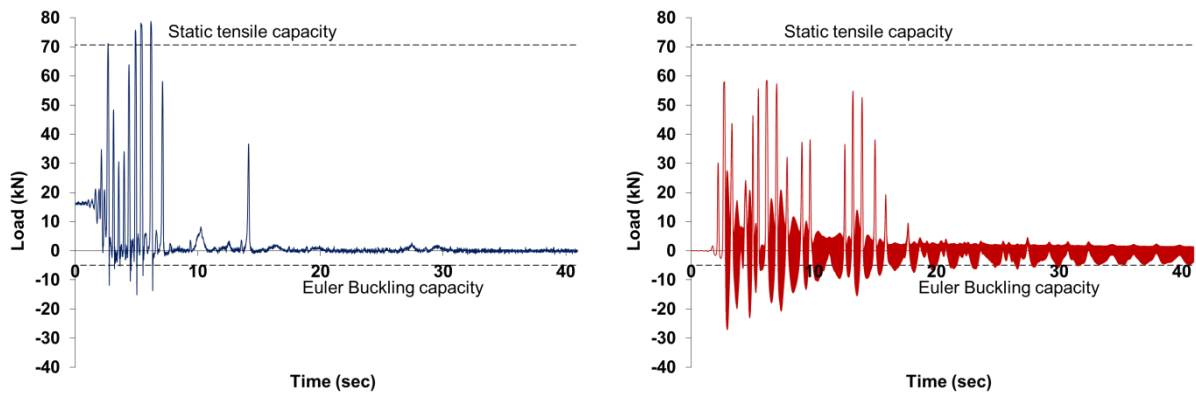


Figure A.30: Axial load time-history response of the second brace of test ST5-E20H-B in (a) physical test and (b) numerical model.

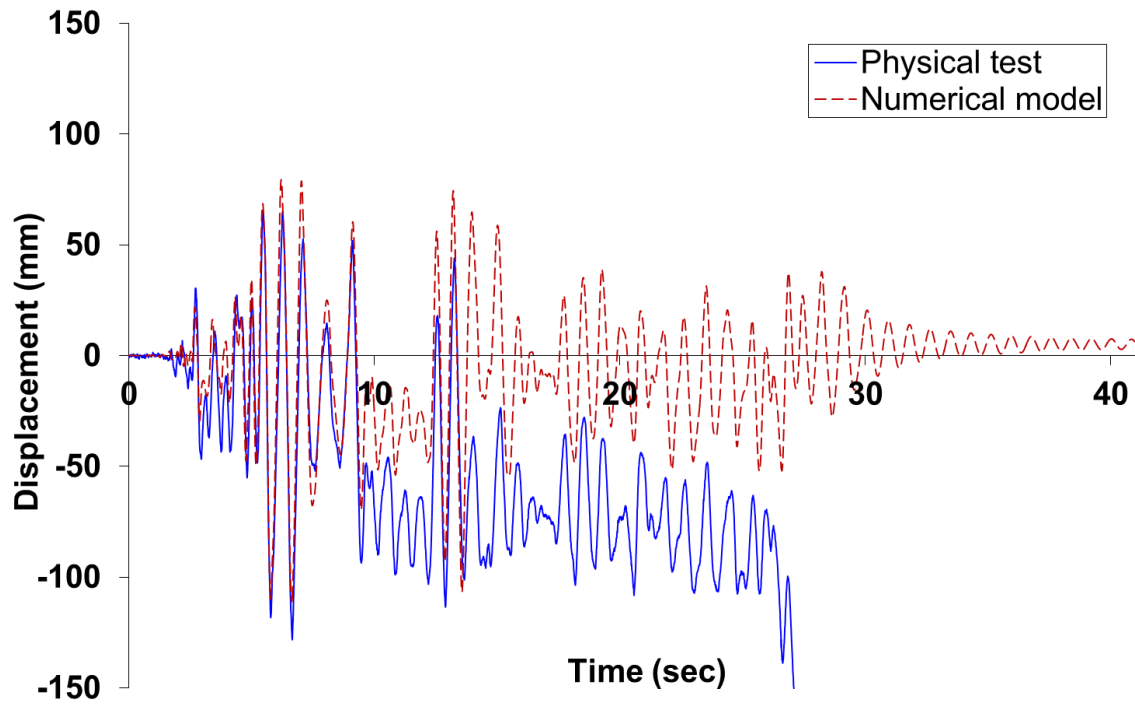


Figure A.31: Comparison for the displacement time-history response of test ST7-E40H and the numerical model in OpenSees.

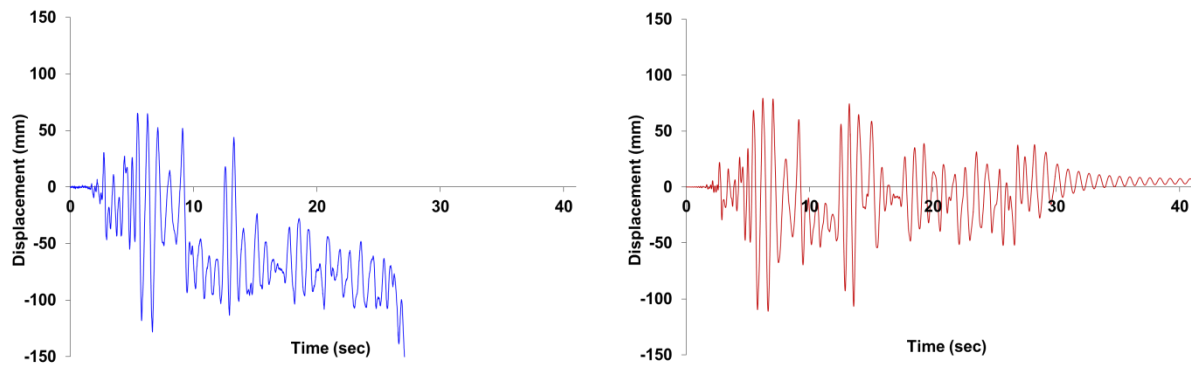


Figure A.32: Measured displacement time-history response of test ST7-E40H in (a) physical test and (b) numerical model.

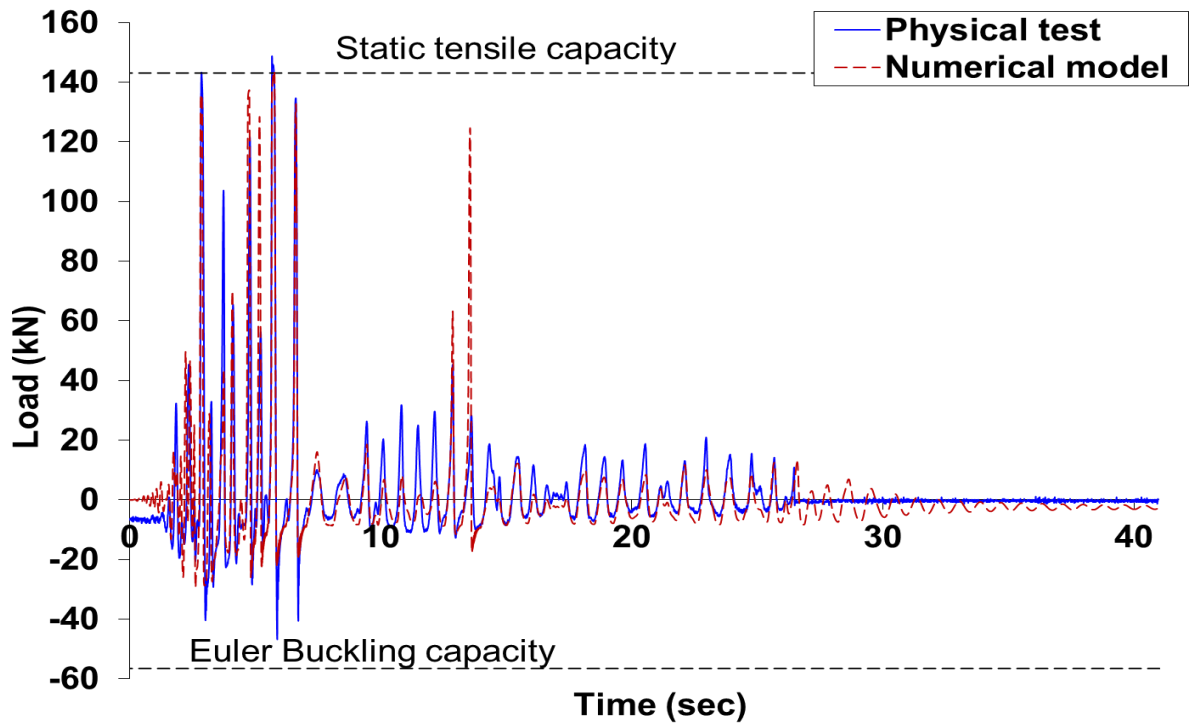


Figure A.33: Comparison for the axial load time-history response of the first brace specimen of test ST7-E40H and the numerical model in OpenSees.

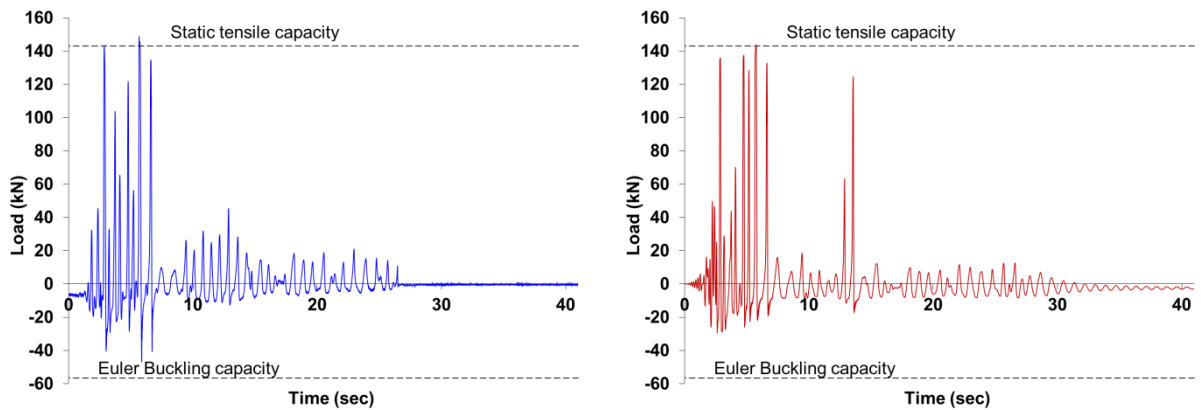


Figure A.34: Axial load time-history response of the first brace of test ST7-E40H in (a) physical test and (b) numerical model.

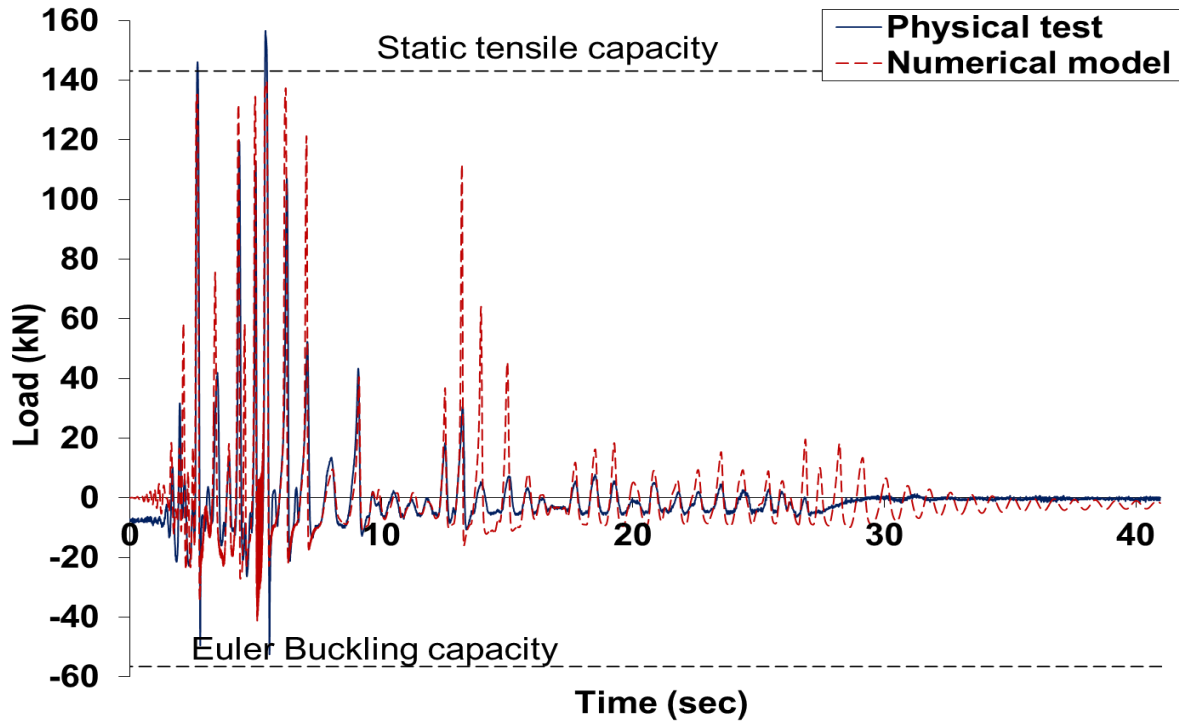


Figure A.35: Comparison for the axial load time-history response of the second brace specimen of test ST7-E40H and the numerical model in OpenSees.

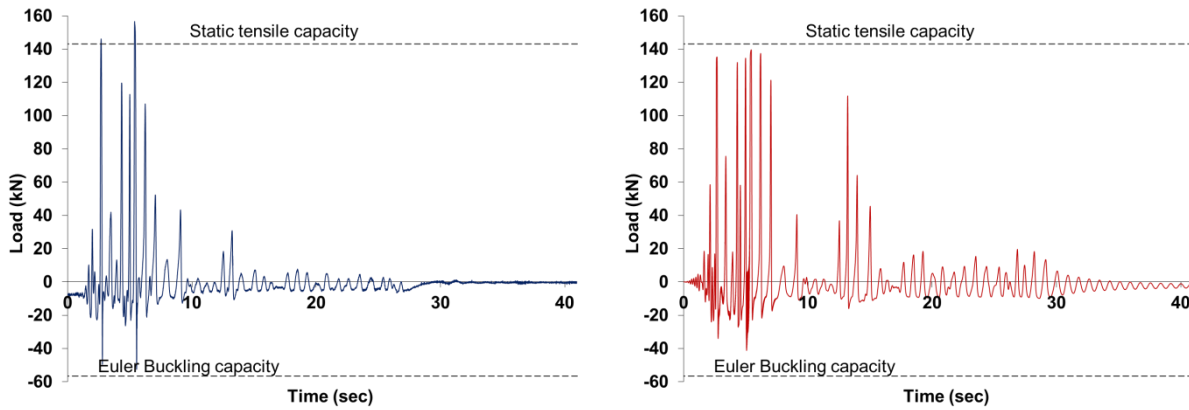


Figure A.36: Axial load time-history response of the second brace of test ST7-E40H in (a) physical test and (b) numerical model.

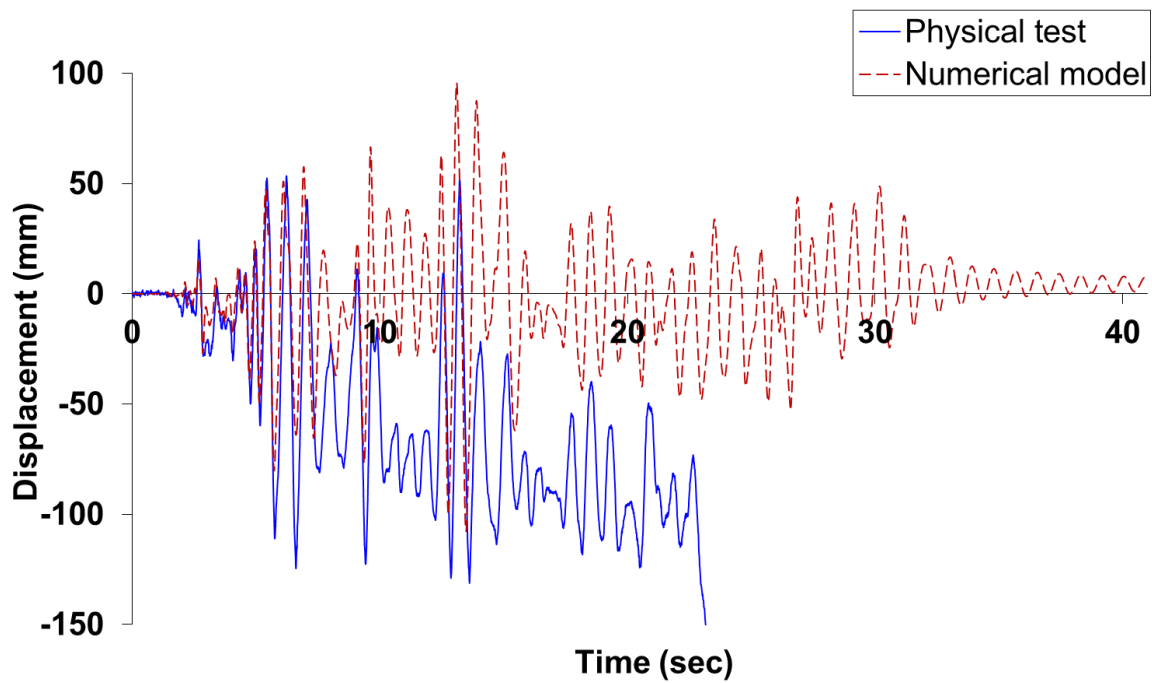


Figure A.37: Comparison for the displacement time-history response of test ST8-E40H and the numerical model in OpenSees.

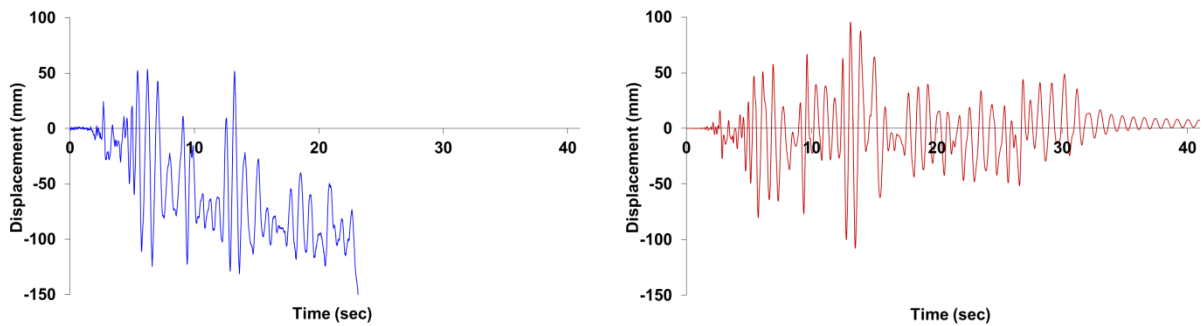


Figure A.38: Measured displacement time-history response of test ST8-E40H in (a) physical test and (b) numerical model.

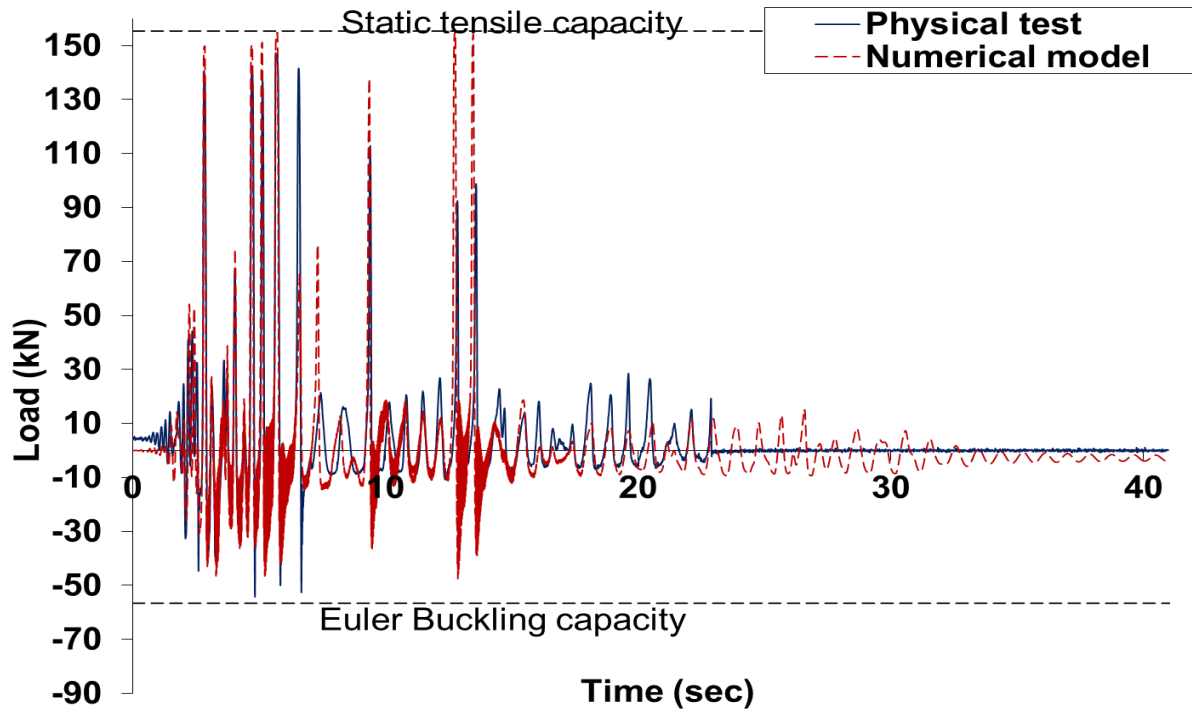


Figure A.39: Comparison for the axial load time-history response of the first brace specimen of test ST8-E40H and the numerical model in OpenSees.

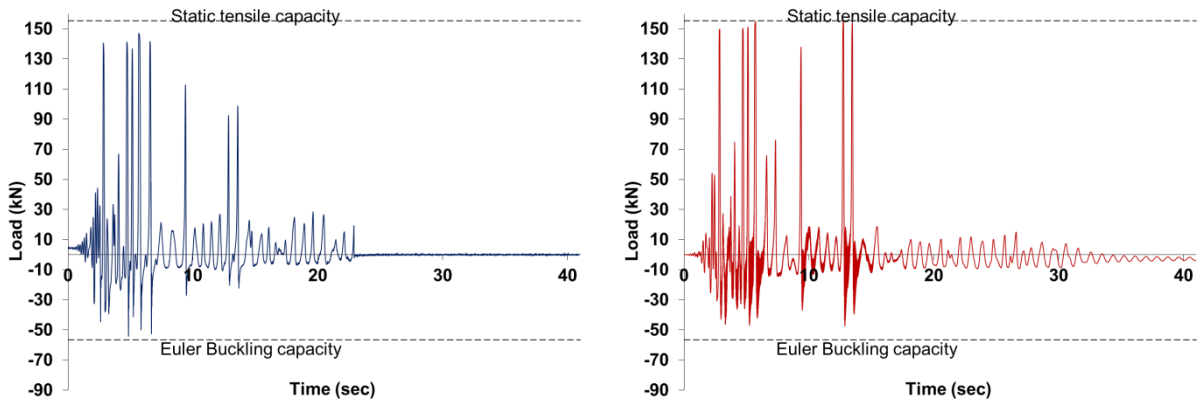


Figure A.40: Axial load time-history response of the first brace of test ST8-E40H in (a) physical test and (b) numerical model.

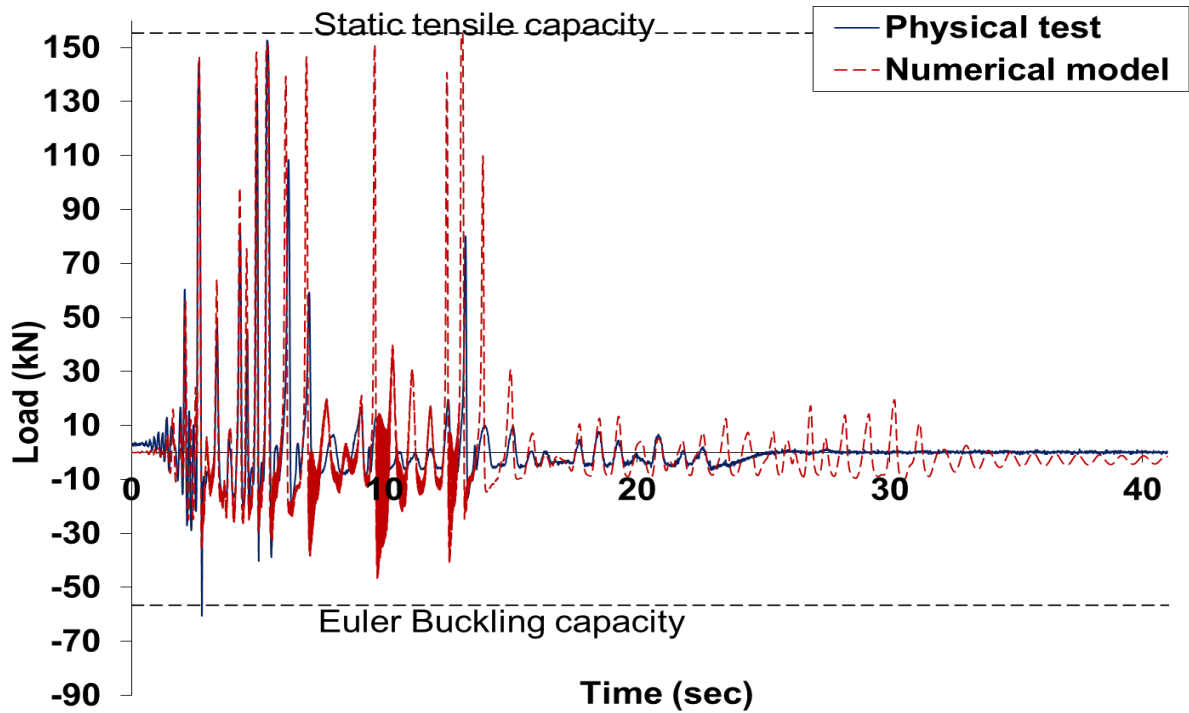


Figure A.41: Comparison for the axial load time-history response of the second brace specimen of test ST8-E40H and the numerical model in OpenSees.

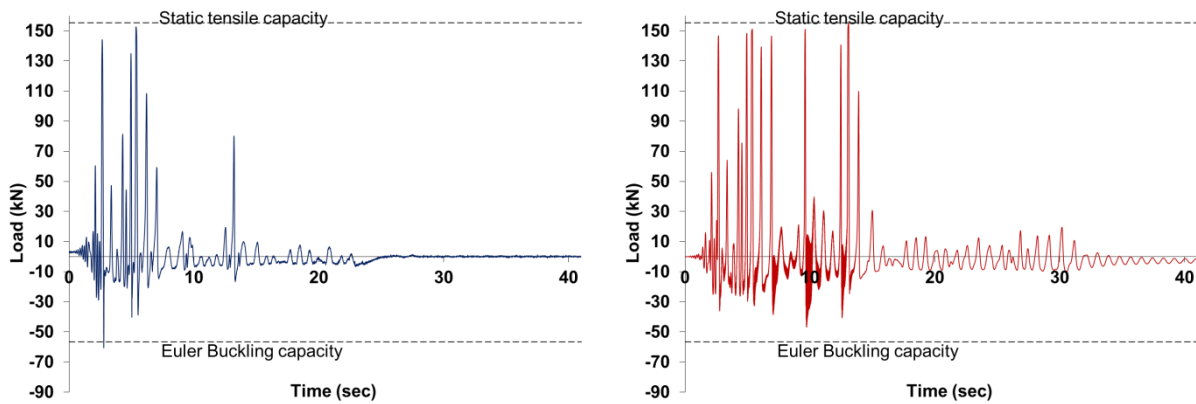


Figure A.42: Axial load time-history response of the second brace of test ST8-E40H in (a) physical test and (b) numerical model.

Appendix B

DDBD for 12-storey CBF case study

This appendix describes the design procedure of the 12-storey concentrically braced frame used to validate the direct displacement based design method.

The building dimension is 32X32m in plan consisting of two CBFs in each direction as the lateral resistant frames. It is chosen to be symmetric in plan and elevation with a uniform storey height of 3m. Stiffness and strength contributions of the interior partitions and the exterior cladding are ignored and the accidental torsion is neglected. Plan view and elevation for the 12-storey structure is shown in Figure B.1 and Figure B.2, respectively.

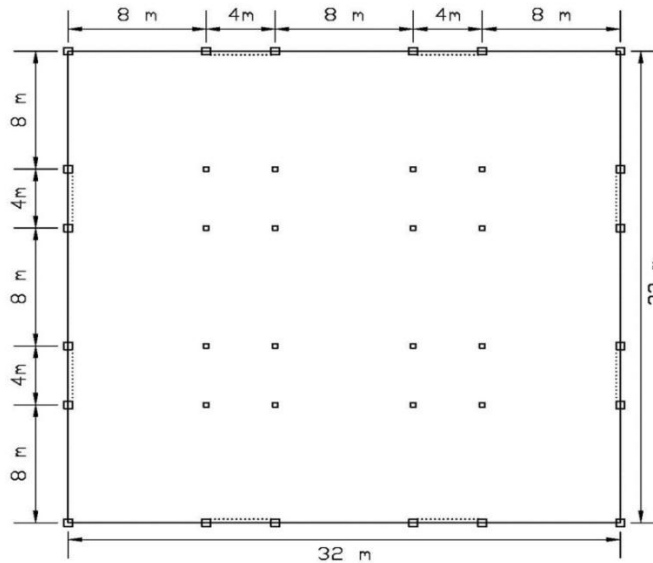


Figure B.1: Plan view of the 12-storey CBF case study.

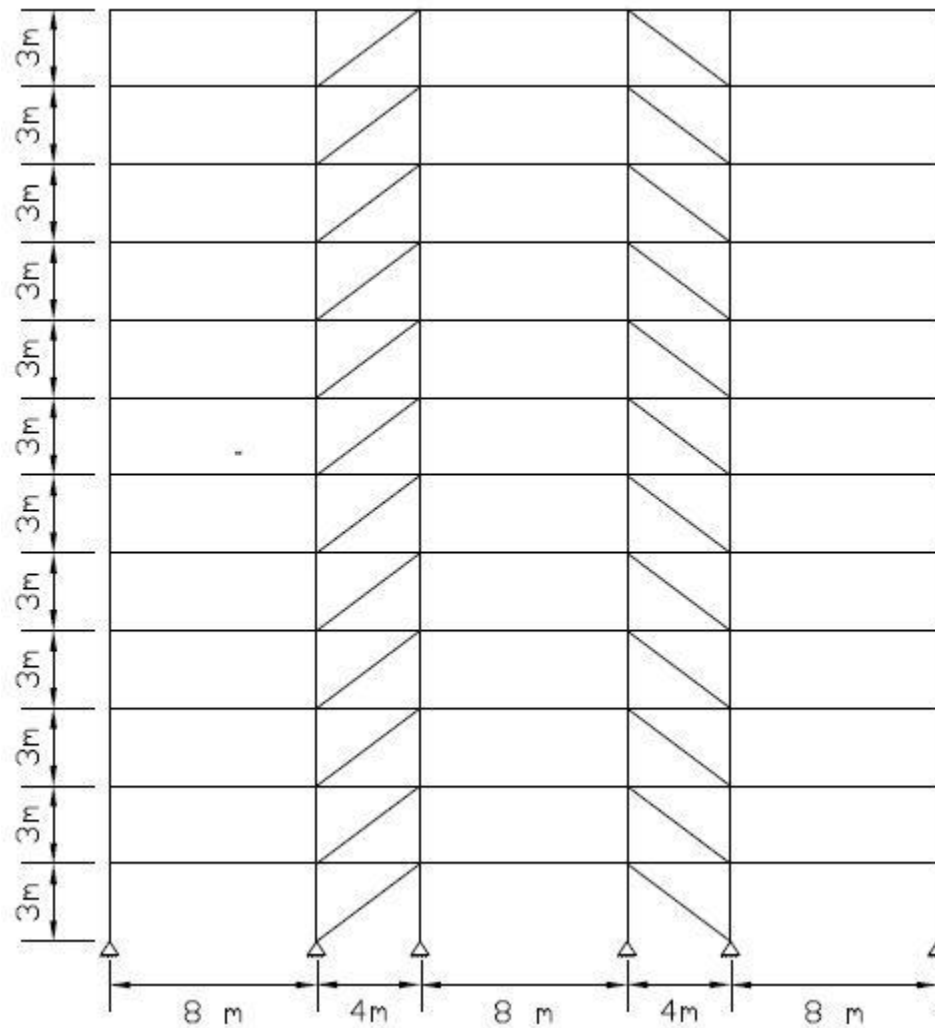


Figure B.2: Elevation of the 12-storey CBF.

Columns are assumed to be continuous along the height and pinned at the base. The connections between columns and beams are assumed to be pinned and the lateral forces are assumed to be resisted by the braces on the 4m bays represented in the dashed line. Bracing end conditions are considered to be pinned in both ends. Dead Load of 8.1KPa and live load of 3KPa were selected using provisions of EC1 (CEN 2004). Seismic load was taken as 9KPa. Grade S355 steel with nominal yield strength of 355N/mm² is chosen. Eurocode 8 (CEN 2004) type 1 elastic response spectrum for soil type C and

peak ground acceleration (PGA) of 0.3g is chosen. Design storey drift of 2.5% is chosen to control damage of non-structural elements.

B.1 Calculation of design displacement and effective height

(a) The inelastic mode shape δ_i in column 4 at Table B.1, is found by

$$\delta_i = \frac{4}{3} \left(\frac{H_i}{H_n} \right) \left(1 - \frac{H_i}{4H_n} \right)$$

where H_i is the storey height of the i^{th} level shown at column 2 of Table B.1, and H_n is the roof height. The design storey displacements, Δ_{Di} , is found from the following equation

$$\Delta_{Di} = \delta_i \left(\frac{\Delta_C}{\delta_C} \right)$$

where Δ_C is the displacement of the critical storey and δ_C is the normalised inelastic mode shape of the critical storey. The shape implies that the maximum drift occurs between the ground and the first floor. So, the design displacement of the first floor is the critical storey and $\Delta_1 = 0.025 * 3 = 0.075\text{m}$ and the design displacement profile in column 5 of Table B.1 is found by

$$\Delta_{Di} = \delta_i \left(\frac{\Delta_C}{\delta_C} \right) = \delta_i \left(\frac{0.075}{0.11} \right) = 0.689\delta_i$$

(b) Substitute structure design displacement can be found by dividing the sum of column 7 and the sum of column 6 in Table B.1 as the following

$$\Delta_D = \frac{\sum m_i \Delta_{Di}^2}{\sum m_i \Delta_{Di}} = \frac{1143.16}{2275.08} = 0.503\text{m}$$

(c) Substitute structure effective height can be found by dividing the sum of column 8 and the sum of column 6 in Table B.1 as the following

$$H_e = \frac{\sum m_i \Delta_{Di} H_i}{\sum m_i \Delta_{Di}} = \frac{55404.83}{2275.08} = 24.35 \text{ m}$$

(d) Effective mass can be found by dividing the sum of column 6 in Table B.1 and substitute structure design displacement, Δ_D .

$$m_e = \frac{\sum m_i \Delta_{Di}}{\Delta_D} = \frac{2275.08}{0.503} = 4523 \text{ tons}$$

Table B.1: Calculations for design displacement and effective height.

1	2	3	4	5	6	7	8
Level	H _i (m)	m _i (ton)/fr	δ _i	Δ _{id}	m _i Δ _{id}	m _i Δ _{id} ²	m _i Δ _{id} H _i
12	36	460.80	1.00	0.69	317.66	218.98	11435.68
11	33	460.80	0.94	0.65	299.27	194.37	9876.07
10	30	460.80	0.88	0.61	279.42	169.44	8382.64
9	27	460.80	0.81	0.56	258.10	144.56	6968.62
8	24	460.80	0.74	0.51	235.30	120.15	5647.25
7	21	460.80	0.66	0.46	211.04	96.65	4431.77
6	18	460.80	0.58	0.40	185.30	74.51	3335.41
5	15	460.80	0.50	0.34	158.09	54.24	2371.40
4	12	460.80	0.41	0.28	129.42	36.35	1552.99
3	9	460.80	0.31	0.22	99.27	21.38	893.41
2	6	460.80	0.21	0.15	67.65	9.93	405.90
1	3	460.80	0.11	0.08	34.56	2.59	103.68
Sum		5529.60			2275.08	1143.16	55404.83

(e) To find the yield displacement at the i^{th} floor, Δ_{yi} , the lateral drift from yielding of the brace and column deformation can be obtained from

$$\Delta_{yi} = \sum_{j=1}^i \left(\frac{\varepsilon_{br,y}}{\sin \alpha \cos \alpha} h_j + \varepsilon_{col,y} h_j \tan \alpha \right)$$

where $\varepsilon_{br,y}$ is the brace axial strain taken as f_y of the brace divided by young modulus as the following

$$\varepsilon_{br} = \frac{f_y}{E} = \frac{355}{210000} = 1.69 \times 10^{-3}$$

α is angle of the brace with the horizontal axis equal to 36.9° , h_j is the storey height which is 3m and $\varepsilon_{col,y}$ is the column axial strain taken as $f_{y,col}/E$ which is equal to 1.69×10^{-3} .

Substitute structure yield displacement, Δ_y , can be found by dividing the sum of column 11 and the sum of column 10 in Table B.2 as the following

$$\Delta_y = \frac{\sum m_i \Delta_{yi}^2}{\sum m_i \Delta_{yi}} = \frac{61.84}{516.46} = 0.12 \text{ m}$$

Table B.2: Calculations for yield displacement.

	9	10	11
Level	Δ_{iy}	$m_i \Delta_{iy}$	$m_i \Delta_{iy}^2$
12	0.17	79.46	13.70
11	0.16	72.83	11.51
10	0.14	66.21	9.51
9	0.13	59.59	7.71
8	0.11	52.97	6.09
7	0.10	46.35	4.66
6	0.09	39.73	3.43
5	0.07	33.11	2.38
4	0.06	26.49	1.52
3	0.04	19.86	0.86
2	0.03	13.24	0.38
1	0.01	6.62	0.10
Sum		516.46	61.84

(f) The design displacement ductility, μ , is found by dividing the design displacement, Δ_D , by the yield displacement, Δ_y , as the following

$$\mu = \frac{\Delta_D}{\Delta_y} = \frac{0.503}{0.12} = 4.19$$

The equivalent viscous damping (EVD) equations suggested by Wijesundara (2009) are a function of ductility, μ , and non-dimensional slenderness ratio, $\bar{\lambda}$. The first variable which is the ductility is found. However, the slenderness ratio is unknown at this stage of design, because of that an initial assumption of slenderness ratio is assumed to get the EVD, which will be checked in the next steps of the design procedure. Initial design of braces is carried out, number of trials should be done in which new shear forces and designed braces are found and these trials stop when the same braces are found to be

adequate for the last two trials as will be explained in the following. A slenderness ratio, $\bar{\lambda}$, is first assumed as 1.3 giving a damping ratio of 17.33% as the following

$$\xi = 0.03 + \left(0.23 - \frac{1.3}{15}\right) = 0.1733$$

Following the EC8 (CEN 1998) recommendation for relationship between damping and displacement reduction. The reduction factor to be applied to the 5% displacement spectrum to get the 17.33% displacement spectrum is given by

$$R_{\xi} = \left(\frac{0.07}{(0.02 + 0.1733)}\right)^{0.5} = 0.602$$

The displacement spectra for the design example are shown in Figure 7.5 from which the effective period, T_e , corresponds to the design displacement, Δ_D , can be read and found to be 6.49 seconds.

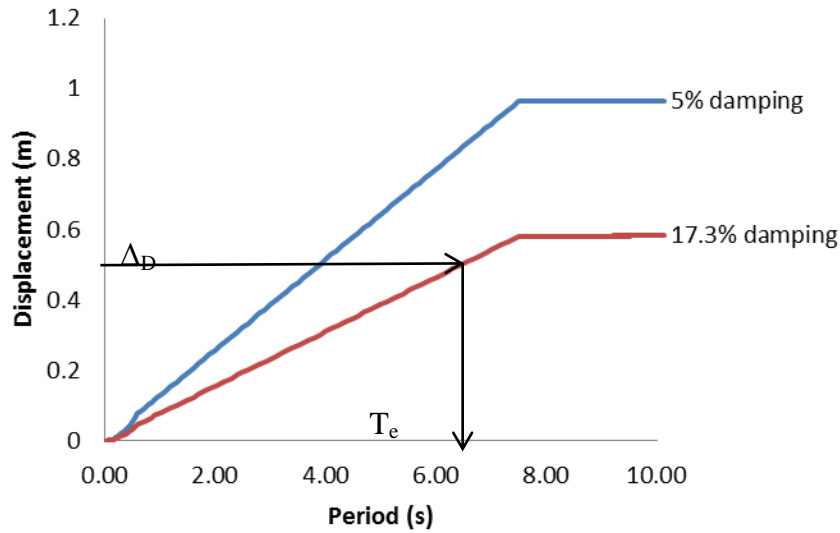


Figure B.3: Displacement response spectra for the 5% and 17.3% damping.

By knowing the effective mass, m_e , and the effective period, T_e , the effective stiffness can be found by

$$K_e = \frac{4\pi^2 m_e}{T_e^2} = \frac{4\pi^2 * 4523}{(6.49)^2} = 4239.3 \text{ KN/m}$$

Then the base shear, F_b , can be found by

$$F_b = \left(K_e + \frac{m_e g}{H_e} \right) \Delta_D = 3046 \text{ KN}$$

This base shear, F_b , is distributed to the floors as shown in Table B.3 by the following equation

$$F_i = F_t + 0.9F_b \frac{m_i \Delta_i}{\sum m_i \Delta_i}$$

where $F_t = 0.1F_b = 0.1 \cdot 3046 = 304.6 \text{ KN}$ at roof level and $F_t = 0$ at all other levels.

Storey shear forces are found by summing the floor forces above the storey considered as shown in column 13 in Table B.3. Assuming only tension diagonal bracings resisting the shear as suggested by EC8 (CEN 2004), the axial force in the brace, $N_{Ed,i}$, is found by dividing the amount of floor shear assigned to this brace by cosine of the angle of the brace with the horizontal. By dividing the axial force in the brace, $N_{Ed,i}$, by the yield force the proposed area of the braces are found and a suitable brace can be chosen taking into account the following:

All braces should be chosen to be class 1 with a slenderness ratio $\bar{\lambda} \leq 2$, as suggested by EC8 (CEN 2004), where slenderness ratio, $\bar{\lambda}$, is found by

$$\bar{\lambda} = \frac{L_{cr}}{i} \frac{1}{\lambda_1}$$

where L_{cr} is the length of the brace, i is radius of gyration and $\lambda_1 = 93.9\varepsilon$, where $\varepsilon = \sqrt{(235/f_y)}$.

A check for the brace overstrength, Ω , is carried out as the following

$$\Omega_i = \frac{N_{pl,Rd,i}}{N_{Ed,i}}$$

where $N_{pl,Rd,i}$ is the design resistance of diagonal i and $N_{Ed,i}$ is the design value of the axial force in the same diagonal i in the seismic design situation where $N_{Ed,i} \leq N_{pl,Rd,i}$. This check is carried out assuring that it satisfies the EC8 (CEN 2004) requirements that the maximum brace overstrength does not differ from the minimum value by more than

25% in order to satisfy the homogeneous dissipative behaviour of the diagonals as shown in Table B.3 for the first iteration ($n = 1$).

Table B.3: Base shear distribution and brace section selection ($n = 1$).

	12	13	14	15	16	17	18	19	20
Level	$F_{i,n}$ (kN)	$V_{i,n}$ (kN)	$N_{Ed,i,n}$ (kN)	proposed area, $A_{b,n}$ (cm^2)	section size	Real $A_{b,n}$ (cm^2)	$N_{pl,i,n}$ (kN)	$\Omega_{i,n}$	$\bar{\lambda}_n$
12	687	687	859	24.21	120X120X6.3	28.2	1001.1	1.16	1.42
11	361	1048	1310	36.91	120X120X10	42.9	1522.95	1.16	1.47
10	337	1385	1731	48.76	120X120X12.5	52.1	1849.55	1.07	1.51
9	311	1696	2120	59.71	140X140X12.5	62.1	2204.55	1.04	1.27
8	284	1979	2474	69.70	160X160X12.5	72.1	2559.55	1.03	1.09
7	254	2234	2792	78.65	180X180X12.5	82.1	2914.55	1.04	0.96
6	223	2457	3071	86.52	180X180X14.2	92	3266	1.06	0.97
5	190	2648	3309	93.23	180X180X16	102	3621	1.09	0.99
4	156	2804	3504	98.72	180X180X16	102	3621	1.03	0.99
3	119	2923	3654	102.93	200X200X16	115	4082.5	1.12	0.88
2	82	3005	3755	105.80	200X200X16	115	4082.5	1.09	0.88
1	42	3046	3807	107.27	200X200X16	115	4082.5	1.07	0.88
Sum	3046								

By knowing the ductility, μ , and the non-dimensional slenderness ratio, $\bar{\lambda}$, for every brace, the equivalent viscous damping values for every floor are found as shown in column 21 in Table B.4 from the following equations

$$\xi_i = 0.03 + \left(0.23 - \frac{\bar{\lambda}_i}{15}\right)(\mu - 1) \quad \mu \leq 2$$

$$\xi_i = 0.03 + \left(0.23 - \frac{\bar{\lambda}_i}{15}\right) \quad \mu \geq 2$$

The system equivalent viscous damping, ξ_{sys} , can be found by dividing column 22 over column 23 of Table B.4 as the following

$$\xi_{\text{sys}} = \frac{\sum V_i \Delta_{D,i} \xi_i}{\sum V_i \Delta_{D,i}} = \frac{1662.87}{8961.20} = 0.1855 = 18.55\%$$

Table B.4: Equivalent viscous damping calculations (n=1)

	21	22	23
Level	$\xi_{i,n+1}$	$V_{i,n} * \Delta_{D,i}$	$V_{i,n} * \Delta_{D,i} * \xi_{i,n+1}$
12	0.17	473.90	78.46
11	0.16	680.72	110.39
10	0.16	839.75	133.91
9	0.18	949.88	166.65
8	0.19	1010.79	189.06
7	0.20	1023.02	200.35
6	0.20	988.06	192.74
5	0.19	908.36	176.49
4	0.19	787.39	152.98
3	0.20	629.73	126.90
2	0.20	441.12	88.89
1	0.20	228.48	46.04
Sum		8961.20	1662.87

The revised equivalent viscous damping value for the first trial is 18.55% and it is 6.6% above the initial value. For that, the above procedure should be done again using the new equivalent viscous damping and finding adequate braces. The trials are finished when the same braces are adequate to be used for the last two trials. Using the revised equivalent viscous damping, new effective period, $T_e = 6.7$ sec is found leading to new effective stiffness, $K_e = 3987$ KN/m, and base shear, $F_b = 2920$ KN. The distribution of base shear to floors and the chosen braces are shown in Table B.5. The braces selected for this trial was the same as the braces used for the first trial, repetition is stopped and the selected braces are considered as the design braces. The selected braces for each trial should be checked to satisfy the requirements of EC8 (CEN 2004) that it should be chosen to be class 1 with a slenderness ratio $\bar{\lambda} \leq 2$, and the brace overstrength, Ω , is checked to assure

the requirements that the overstrength factor should be greater than 1 and the maximum brace overstrength does not differ from the minimum value by more than 25% in order to satisfy the homogeneous dissipative behaviour of the diagonals.

Table B.5: Revised base shear distribution and brace section selection (n = 2)

	24	25	26	27	28	29	30	31
Level	$F_{i,n}$ (kN)	$V_{i,n}$ (kN)	$N_{Ed,i,n}$ (kN)	Proposed $A_{b,n}$ (cm ²)	section size	Real $A_{b,n}$ (cm ²)	$N_{pl,i,n}$ (kN)	$\Omega_{i,n}$
12	658.86	658.86	823.57	23.20	120X120X6.3	28.2	1001.1	1.22
11	345.66	1004.52	1255.65	35.37	120X120X10	42.9	1522.95	1.21
10	322.73	1327.25	1659.06	46.73	120X120X12.5	52.1	1849.55	1.11
9	298.10	1625.35	2031.69	57.23	140X140X12.5	62.1	2204.55	1.09
8	271.77	1897.12	2371.40	66.80	160X160X12.5	72.1	2559.55	1.08
7	243.75	2140.87	2676.08	75.38	180X180X12.5	82.1	2914.55	1.09
6	214.02	2354.89	2943.61	82.92	180X180X14.2	92	3266	1.11
5	182.60	2537.48	3171.86	89.35	180X180X16	102	3621	1.14
4	149.47	2686.96	3358.70	94.61	180X180X16	102	3621	1.08
3	114.65	2801.61	3502.02	98.65	200X200X16	115	4082.5	1.17
2	78.13	2879.75	3599.68	101.40	200X200X16	115	4082.5	1.13
1	39.92	2919.66	3649.58	102.81	200X200X16	115	4082.5	1.12
Sum	2919.66							

B.2 Columns and beams capacity design

Columns and beams are capacity designed to behave elastically ensuring that dissipative behaviour is provided primarily by the braces by the following combination from EC8 (CEN 2004)

$$N_{pl,Rd} \geq N_{Ed,G} + 1.1\gamma_{ov}\Omega N_{Ed,E}$$

$$M_{pl,Rd} \geq M_{Ed,G} + 1.1\gamma_{ov}\Omega M_{Ed,E}$$

$$V_{pl,Rd} \geq V_{Ed,G} + 1.1\gamma_{ov}\Omega V_{Ed,E}$$

where

$N_{pl,Rd}$, $M_{pl,Rd}$ is the design buckling resistance, moment resistance and shear resistance respectively of the beam or the column in accordance with EC3 (CEN 2006), taking into account the interaction of the buckling resistance with the bending moment.

$N_{Ed,G}$, $M_{Ed,G}$ is the axial force, bending moment and shear respectively in the beam or in the column due to the non-seismic actions included in the combination of actions for the seismic design situation.

$N_{Ed,E}$, $M_{Ed,E}$ is the axial force, bending moment and shear respectively in the beam or in the column due to the design seismic action

γ_{ov} is the overstrength factor taken as 1.25.

Ω The brace overstrength taken as the minimum of Ω_i .

The selected beams and columns are shown in Table B.6.

Table B.6: Column and Beam designed sections from capacity design principles.

Level	Columns	Beams
12	HD 320X198	HE 400 M
11	HD 320X198	HE 400 M
10	HD 320X198	HE 400 M
9	HD 400X314	HE 400 M
8	HD 400X314	HE 550 M
7	HD 400X314	HE 550 M
6	HD 400X421	HE 550 M
5	HD 400X421	HE 550 M
4	HD 400X421	HE650X340
3	HD 400X509	HE650X341
2	HD 400X509	HE650X342
1	HD 400X509	HE650X343

Appendix C

OpenSees input files

C.1 OpenSee input file for a brace element

```
model BasicBuilder -ndm 2 -ndf 3
```

```
set H 0.05
```

```
set W 0.025
```

```
set t 0.0025
```

```
set tt 0.008
```

```
set d1 [expr $H/2]
```

```
set d2 [expr $W/2-$t]
```

```
set d3 [expr $H/2-$t]
```

```
set d4 [expr $W/2]
```

```
set d5 [expr $d4+0.03]
```

```
set d6 [expr $tt/2]
```

```
set nfd 17
```

```
set nfW 9
```

```
set nft 3
```

```
node 1 0.0 0.0
```

```

node 2 0.125 0.0
node 4 0.55 0.004
node 6 0.975 0.0
node 5 1.1 0.0
fix 1 1 1 1
fix 5 0 1 1
uniaxialMaterial Steel02 1 300000 200000000 0.008 18.5 0.925 0.15 0.0005 0.01
0.0005 0.01
uniaxialMaterial Fatigue 5 1 -E0 0.095 -m -0.5
section Fiber 1 {
patch quad 1 $nfW $nft -$d2 +$d3 +$d2 +$d3 +$d4 +$d1 -$d4 +$d1
patch quad 1 $nft $nfd +$d2 -$d3 +$d4 -$d1 +$d4 +$d1 +$d2 +$d3
patch quad 1 $nfW $nft -$d4 -$d1 +$d4 -$d1 +$d2 -$d3 -$d2 -$d3
patch quad 1 $nft $nfd -$d4 -$d1 -$d2 -$d3 -$d2 +$d3 -$d4 +$d1
}
section Fiber 2 {
patch quad 1 $nfW $nft -$d2 +$d3 +$d2 +$d3 +$d4 +$d1 -$d4 +$d1
patch quad 1 $nft $nfd +$d2 -$d3 +$d4 -$d1 +$d4 +$d1 +$d2 +$d3
patch quad 1 $nfW $nft -$d4 -$d1 +$d4 -$d1 +$d2 -$d3 -$d2 -$d3
patch quad 1 $nft $nfd -$d4 -$d1 -$d2 -$d3 -$d2 +$d3 -$d4 +$d1
patch quad 1 $nfW $nft -$d5 -$d6 -$d4 -$d6 -$d4 +$d6 -$d5 +$d6
patch quad 1 $nfW $nft -$d2 -$d6 +$d2 -$d6 +$d2 +$d6 -$d2 +$d6
patch quad 1 $nfW $nft +$d4 -$d6 +$d5 -$d6 +$d5 +$d6 +$d4 +$d6
}

```

```
geomTransf Corotational 1
element nonlinearBeamColumn 1 2 4 10 1 1
element nonlinearBeamColumn 3 4 6 10 1 1
element nonlinearBeamColumn 5 1 2 10 2 1
element nonlinearBeamColumn 6 6 5 10 2 1
pattern Plain 1 Linear -factor 1 [ load 5 1.0 0.0 0.0 ]
recorder Node -file LoadDisp170903.txt -time -node 5 -dof 1 disp
test EnergyIncr 1.0e-8 30 0
algorithm Newton
system UmfPack
numberer RCM
constraints Plain
analysis Static
integrator DisplacementControl 5 1 -0.00001
analyze 57
integrator DisplacementControl 5 1 +0.00001
analyze 57
integrator DisplacementControl 5 1 +0.00001
analyze 57
integrator DisplacementControl 5 1 -0.00001
analyze 57
integrator DisplacementControl 5 1 -0.00001
analyze 115
integrator DisplacementControl 5 1 +0.00001
```

analyze 115

integrator DisplacementControl 5 1 +0.00001

analyze 115

integrator DisplacementControl 5 1 -0.00001

analyze 115

integrator DisplacementControl 5 1 -0.00001

analyze 174

integrator DisplacementControl 5 1 +0.00001

analyze 174

integrator DisplacementControl 5 1 +0.00001

analyze 174

integrator DisplacementControl 5 1 -0.00001

analyze 174

integrator DisplacementControl 5 1 -0.00001

analyze 232

integrator DisplacementControl 5 1 +0.00001

analyze 232

integrator DisplacementControl 5 1 +0.00001

analyze 232

integrator DisplacementControl 5 1 -0.00001

analyze 232

integrator DisplacementControl 5 1 -0.00001

analyze 468

integrator DisplacementControl 5 1 +0.00001

analyze 468

integrator DisplacementControl 5 1 +0.00001

analyze 468

integrator DisplacementControl 5 1 -0.00001

analyze 468

integrator DisplacementControl 5 1 -0.00001

analyze 469

integrator DisplacementControl 5 1 +0.00001

analyze 469

integrator DisplacementControl 5 1 +0.00001

analyze 469

integrator DisplacementControl 5 1 -0.00001

analyze 469

integrator DisplacementControl 5 1 -0.00001

analyze 469

integrator DisplacementControl 5 1 +0.00001

analyze 469

integrator DisplacementControl 5 1 +0.00001

analyze 469

integrator DisplacementControl 5 1 -0.00001

analyze 469

integrator DisplacementControl 5 1 -0.00001

analyze 940

integrator DisplacementControl 5 1 +0.00001

analyze 940

integrator DisplacementControl 5 1 +0.00001

analyze 940

integrator DisplacementControl 5 1 -0.00001

analyze 940

integrator DisplacementControl 5 1 -0.00001

analyze 940

integrator DisplacementControl 5 1 +0.00001

analyze 940

integrator DisplacementControl 5 1 +0.00001

analyze 940

integrator DisplacementControl 5 1 -0.00001

analyze 940

integrator DisplacementControl 5 1 -0.00001

analyze 940

integrator DisplacementControl 5 1 +0.00001

analyze 940

integrator DisplacementControl 5 1 +0.00001

analyze 940

integrator DisplacementControl 5 1 -0.00001

analyze 940

integrator DisplacementControl 5 1 -0.00001

analyze 1411

integrator DisplacementControl 5 1 +0.00002

analyze 1411

integrator DisplacementControl 5 1 -0.00001

analyze 1411

integrator DisplacementControl 5 1 -0.00001

analyze 1417

integrator DisplacementControl 5 1 +0.00002

analyze 1417

integrator DisplacementControl 5 1 -0.00001

analyze 1417

integrator DisplacementControl 5 1 -0.00001

analyze 1414

integrator DisplacementControl 5 1 +0.00002

analyze 1414

integrator DisplacementControl 5 1 -0.00001

analyze 1414

integrator DisplacementControl 5 1 -0.00001

analyze 1880

integrator DisplacementControl 5 1 +0.00002

analyze 1880

integrator DisplacementControl 5 1 -0.00001

analyze 1880

integrator DisplacementControl 5 1 -0.00001

analyze 1888

integrator DisplacementControl 5 1 +0.00002

```
analyze 1888
integrator DisplacementControl 5 1 -0.00001
analyze 1888
integrator DisplacementControl 5 1 -0.00001
analyze 1885
integrator DisplacementControl 5 1 +0.00002
analyze 1885
integrator DisplacementControl 5 1 -0.00001
analyze 1885
integrator DisplacementControl 5 1 -0.00001
analyze 2354
integrator DisplacementControl 5 1 +0.00002
analyze 2354
integrator DisplacementControl 5 1 -0.00001
analyze 2354
```

C.2 OpenSees input file for SDOF CBF

In this Appendix the input file used to mimic the ST2-E50H shake table test in the software OpenSees is presented:

```
model BasicBuilder -ndm 2 -ndf 3
#Definition of geometric parameters
set H 0.025          # height of the RHS
set W 0.05           #width of the RHS
set t 0.0025        #thickness of the wall of RHS
set y1 [expr $H/2]
```

```
set y2 [expr $H/2-$t]
set z1 [expr $W/2]
set z2 [expr $W/2-$t]

set nfH 10          # number of fibres along depth
set nfW 20          # number of fibres along width
set nft 3           # number of fibres along thickness

node 1 0.00 0.00
node 2 0.00 2.891
node 102 0.00 2.891
node 3 2.70 2.891
node 103 2.70 2.891
node 4 2.70 0.00
node 5 1.38 1.4755
node 101 0.00 0.00
node 104 2.70 0.00
node 105 1.32 1.4755

fix 1 1 1 0
fix 4 1 1 0
fix 101 1 1 1
fix 104 1 1 1

uniaxialMaterial Steel02 1 315000 200000000 0.008 18.5 0.925 0.15
uniaxialMaterial Fatigue 5 1 -E0 0.2 -m -0.5

# Definition of elements

section Fiber 1 {
```

```

patch quad    5  $nfW  $nft -$y1 +$z1 -$y1 -$z1 -$y2 -$z2 -$y2 +$z2
patch quad    5  $nft  $nfH -$y2 -$z2 -$y1 -$z1 +$y1 -$z1 +$y2 -$z2
patch quad    5  $nfW  $nft +$y2 +$z2 +$y2 -$z2 +$y1 -$z1 +$y1 +$z1
patch quad    5  $nft  $nfH -$y1 +$z1 -$y2 +$z2 +$y2 +$z2 +$y1 +$z1
}

geomTransf Linear 1
geomTransf Linear 2
geomTransf Corotational 3
geomTransf Corotational 4

element elasticBeamColumn    1    1    2    0.00971 200000000 5.10E-05    1
element elasticBeamColumn    2    4    3    0.00971 200000000 5.10E-05    1
element elasticBeamColumn    3   103   102    0.00453 200000000 2.51E-05    2
element nonlinearBeamColumn   4    101   105    10    1    3
element nonlinearBeamColumn   5    105   103    10    1    3
element nonlinearBeamColumn   6    104    5     10    1    4
element nonlinearBeamColumn   7     5    102    10    1    4

uniaxialMaterial Elastic    2 200000000 0
uniaxialMaterial Elastic    3 10 0

element zeroLength 8 2 102 -mat 2 2 3 -dir 1 2 6
element zeroLength 9 3 103 -mat 2 2 3 -dir 1 2 6

# Definition of Node Mass

mass    2    5 0 0 0
mass    3    5 0 0 0

# Dynamic ground-motion analysis

```

```
set ST2EQ "Series -filePath ST2EQ.txt -dt 0.01 -factor 9.81"

# load pattern

pattern UniformExcitation 2 1 -accel $ST2EQ

# Damping

set Damp 0.03

eigen 1

set lambda [eigen 1]

set omega [expr pow($lambda,0.5)]

set PI [expr 2*asin(1.0)]

set Tperiod [expr 2*$PI/$omega];

puts $Tperiod

set beta [expr 2*$Damp/$omega]

rayleigh 0.0 0.0 0.0 $beta

# Recorders

recorder Node -file node2st2.out -time -node 2 -dof 1 disp
recorder Node -file accelnode2st2.out -time -node 2 -dof 1 accel
recorder Element -file axialsection1st2.out -time -ele 5 section 5 force
recorder Element -file axialsection2st2.out -time -ele 7 section 5 force
recorder plot node2st2.out Displacement_Time_History 300 200 800 400 -columns 1 2

# Analysis parameters

constraints Transformation

set DtAnalysis 0.005;

set TmaxAnalysis 40.97;

set Nsteps [expr int($TmaxAnalysis/$DtAnalysis)];
```

```
numberer RCM
system UmfPack
set TestType NormDispIncr
set Tol 1.e-12
set maxNumIter 1000
test NormDispIncr 1.e-12 1000
set algorithmType KrylovNewton
algorithm $algorithmType
integrator Newmark 0.5 0.25
analysis Transient
set ok [analyze $Nsteps $DtAnalysis]
```